Advanced Modeling, Estimation, and Control for Electrified Vehicles

Lead Guest Editor: Xianjian Jin
Guest Editors: Guodong Yin, Chuan Hu, Haiping Du, and Chongfeng Wei
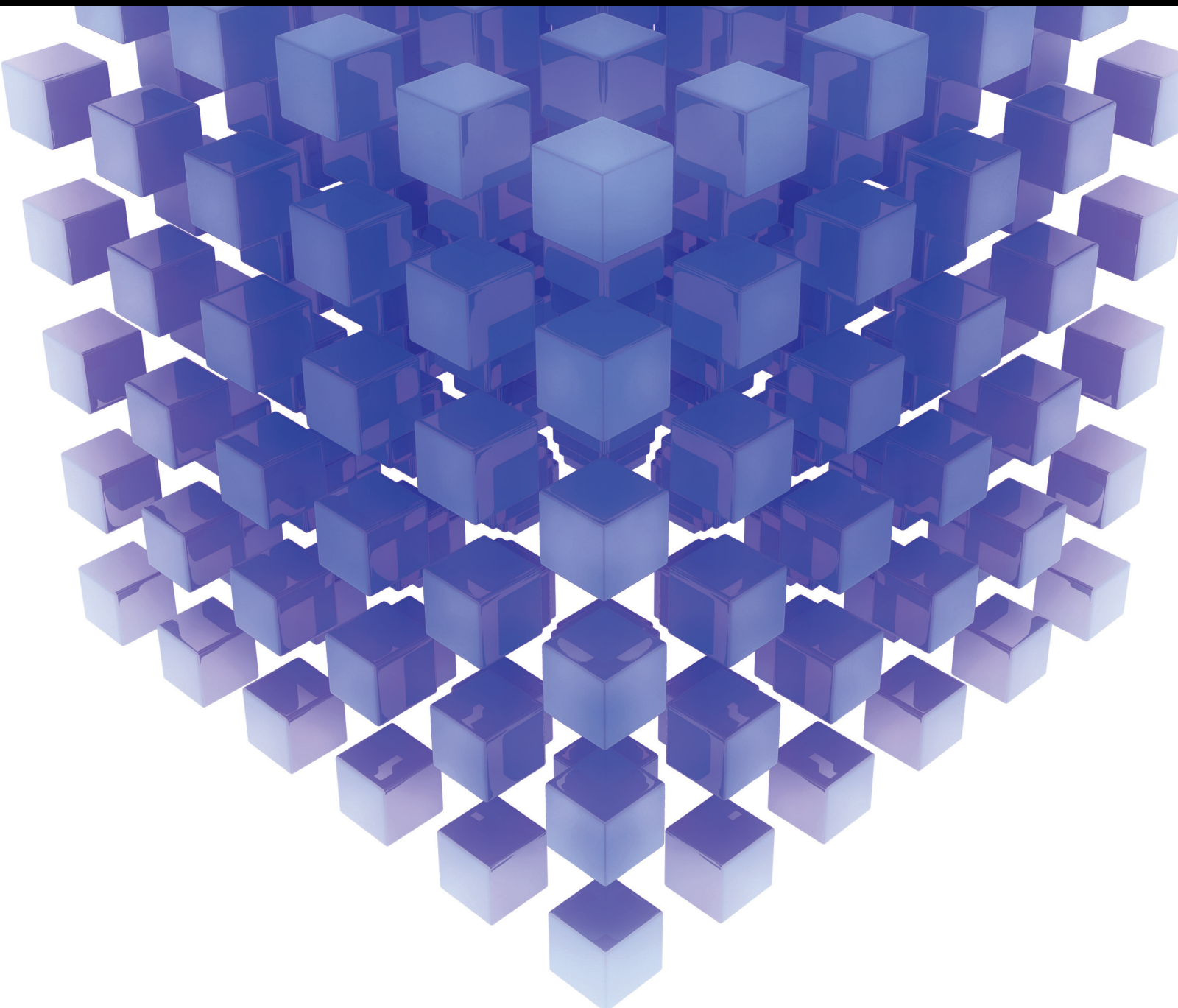
Advanced Modeling, Estimation, and Control for Electrified Vehicles

Advanced Modeling, Estimation, and Control for Electrified Vehicles

Lead Guest Editor: Xianjian Jin
Guest Editors: Guodong Yin, Chuan Hu, Haiping Du, and Chongfeng Wei

Paolo Boscariol, Italy
Daniela Boso (iD), Italy
Guillermo Botella-Juan, Spain
Abdesselem Boulkroune (iD), Algeria
Boulaïd Boulkroune, Belgium
Fabio Bovenga (iD), Italy
Francesco Braghin (iD), Italy
Ricardo Branco, Portugal
Julien Bruchon (iD), France
Matteo Bruggi (iD), Italy
Michele Brun (iD), Italy
Maria Elena Bruni, Italy
Maria Angela Butturi (iD), Italy
Bartłomiej Błachowski (iD), Poland
Dhanamjayulu C (iD), India
Raquel Caballero-Águila (iD), Spain
Filippo Cacace (iD), Italy
Salvatore Caddemi (iD), Italy
Zuowei Cai (iD), China
Roberto Caldelli (iD), Italy
Francesco Cannizzaro (iD), Italy
Maosen Cao (iD), China
Ana Carpio, Spain
Rodrigo Carvajal (iD), Chile
Caterina Casavola, Italy
Sara Casciati, Italy
Federica Caselli (iD), Italy
Carmen Castillo (iD), Spain
Inmaculada T. Castro (iD), Spain
Miguel Castro (iD), Portugal
Giuseppe Catalanotti (iD), United Kingdom
Alberto Cavallo (iD), Italy
Gabriele Cazzulani (iD), Italy
Fatih Vehbi Celebi, Turkey
Miguel Cerrolaza (iD), Venezuela
Gregory Chagnon (iD), France
Ching-Ter Chang (iD), Taiwan
Kuei-Lun Chang (iD), Taiwan
Qing Chang (iD), USA
Xiaoheng Chang (iD), China
Prasenjit Chatterjee (iD), Lithuania
Kacem Chehdi, France
Peter N. Cheimets, USA
Chih-Chiang Chen (iD), Taiwan
He Chen (iD), China

Kebing Chen (iD), China
Mengxin Chen (iD), China
Shyi-Ming Chen (iD), Taiwan
Xizhong Chen (iD), Ireland
Xue-Bo Chen (iD), China
Zhiwen Chen (iD), China
Qiang Cheng, USA
Zeyang Cheng, China
Luca Chiapponi (iD), Italy
Francisco Chicano (iD), Spain
Tirivanhu Chinyoka (iD), South Africa
Adrian Chmielewski (iD), Poland
Seongim Choi (iD), USA
Gautam Choubey (iD), India
Hung-Yuan Chung (iD), Taiwan
Yusheng Ci, China
Simone Cinquemani (iD), Italy
Roberto G. Citarella (iD), Italy
Joaquim Ciurana (iD), Spain
John D. Clayton (iD), USA
Piero Colajanni (iD), Italy
Giuseppina Colicchio, Italy
Vassilios Constantoudis (iD), Greece
Enrico Conte, Italy
Alessandro Contento (iD), USA
Mario Cools (iD), Belgium
Gino Cortellessa, Italy
Carlo Cosentino (iD), Italy
Paolo Crippa (iD), Italy
Erik Cuevas (iD), Mexico
Guozeng Cui (iD), China
Mehmet Cunkas (iD), Turkey
Giuseppe D'Aniello (iD), Italy
Peter Dabnichki, Australia
Weizhong Dai (iD), USA
Zhifeng Dai (iD), China
Purushothaman Damodaran (iD), USA
Sergey Dashkovskiy, Germany
Adiel T. De Almeida-Filho (iD), Brazil
Fabio De Angelis (iD), Italy
Samuele De Bartolo (iD), Italy
Stefano De Miranda (iD), Italy
Filippo De Monte (iD), Italy

José António Fonseca De Oliveira Correia, Portugal
Jose Renato De Sousa, Brazil
Michael Defoort, France
Alessandro Della Corte, Italy
Laurent Dewasme, Belgium
Sanku Dey, India
Gianpaolo Di Bona, Italy
Roberta Di Pace, Italy
Francesca Di Puccio, Italy
Ramón I. Diego, Spain
Yannis Dimakopoulos, Greece
Hasan Dinçer, Turkey
José M. Domínguez, Spain
Georgios Dounias, Greece
Bo Du, China
Emil Dumic, Croatia
Madalina Dumitriu, United Kingdom
Premraj Durairaj, India
Saeed Eftekhar Azam, USA
Said El Kafhali, Morocco
Antonio Elipe, Spain
R. Emre Erkmen, Canada
John Escobar, Colombia
Leandro F. F. Miguel, Brazil
FRANCESCO FOTI, Italy
Andrea L. Facci, Italy
Shahla Faisal, Pakistan
Giovanni Falsone, Italy
Hua Fan, China
Jianguang Fang, Australia
Nicholas Fantuzzi, Italy
Muhammad Shahid Farid, Pakistan
Hamed Faroqi, Iran
Yann Favennec, France
Fiorenzo A. Fazzolari, United Kingdom
Giuseppe Fedele, Italy
Roberto Fedele, Italy
Baowei Feng, China
Mohammad Ferdows, Bangladesh
Arturo J. Fernández, Spain
Jesus M. Fernandez Oro, Spain
Francesco Ferrise, Italy
Eric Feulvarch, France
Thierry Floquet, France

Eric Florentin, France
Gerardo Flores, Mexico
Antonio Forcina, Italy
Alessandro Formisano, Italy
Francesco Franco, Italy
Elisa Francomano, Italy
Juan Frausto-Solis, Mexico
Shujun Fu, China
Juan C. G. Prada, Spain
HECTOR GOMEZ, Chile
Matteo Gaeta, Italy
Mauro Gaggero, Italy
Zoran Gajic, USA
Jaime Gallardo-Alvarado, Mexico
Mosè Gallo, Italy
Akemi Gálvez, Spain
Maria L. Gandarias, Spain
Hao Gao, Hong Kong
Xingbao Gao, China
Yan Gao, China
Zhiwei Gao, United Kingdom
Giovanni Garcea, Italy
José García, Chile
Harish Garg, India
Alessandro Gasparetto, Italy
Stylianos Georgantzinos, Greece
Fotios Georgiades, India
Parviz Ghadimi, Iran
Ştefan Cristian Gherghina, Romania
Georgios I. Giannopoulos, Greece
Agathoklis Giaralis, United Kingdom
Anna M. Gil-Lafuente, Spain
Ivan Giorgio, Italy
Gaetano Giunta, Luxembourg
Jefferson L.M.A. Gomes, United Kingdom
Emilio Gómez-Déniz, Spain
Antonio M. Gonçalves de Lima, Brazil
Qunxi Gong, China
Chris Goodrich, USA
Rama S. R. Gorla, USA
Veena Goswami, India
Xunjie Gou, Spain
Jakub Grabski, Poland

Francisco J. Martos (iD), Spain
Elio Masciari (iD), Italy
Paolo Massioni (iD), France
Alessandro Mauro (iD), Italy
Jonathan Mayo-Maldonado (iD), Mexico
Pier Luigi Mazzeo (iD), Italy
Laura Mazzola, Italy
Driss Mehdi (iD), France
Zahid Mehmood (iD), Pakistan
Roderick Melnik (iD), Canada
Xiangyu Meng (iD), USA
Jose Merodio (iD), Spain
Alessio Merola (iD), Italy
Mahmoud Mesbah (iD), Iran
Luciano Mescia (iD), Italy
Laurent Mevel (iD), France
Constantine Michailides (iD), Cyprus
Mariusz Michta (iD), Poland
Prankul Middha, Norway
Aki Mikkola (iD), Finland
Giovanni Minafò (iD), Italy
Edmondo Minisci (iD), United Kingdom
Hiroyuki Mino (iD), Japan
Dimitrios Mitsotakis (iD), New Zealand
Ardashir Mohammadzadeh (iD), Iran
Francisco J. Montáns (iD), Spain
Francesco Montefusco (iD), Italy
Gisele Mophou (iD), France
Rafael Morales (iD), Spain
Marco Morandini (iD), Italy
Javier Moreno-Valenzuela (iD), Mexico
Simone Morganti (iD), Italy
Caroline Mota (iD), Brazil
Aziz Moukrim (iD), France
Shen Mouquan (iD), China
Dimitris Mourtzis (iD), Greece
Emiliano Mucchi (iD), Italy
Taseer Muhammad, Saudi Arabia
Ghulam Muhiuddin, Saudi Arabia
Amitava Mukherjee (iD), India
Josefa Mula (iD), Spain
Jose J. Muñoz (iD), Spain
Giuseppe Muscolino, Italy
Marco Mussetta (iD), Italy

Hariharan Muthusamy, India
Alessandro Naddeo (iD), Italy
Raj Nandkeolyar, India
Keivan Navaie (iD), United Kingdom
Soumya Nayak, India
Adrian Neagu (iD), USA
Erivelton Geraldo Nepomuceno (iD), Brazil
AMA Neves, Portugal
Ha Quang Thinh Ngo (iD), Vietnam
Nhon Nguyen-Thanh, Singapore
Papakostas Nikolaos (iD), Ireland
Jelena Nikolic (iD), Serbia
Tatsushi Nishi, Japan
Shanzhou Niu (iD), China
Ben T. Nohara (iD), Japan
Mohammed Nouari (iD), France
Mustapha Nourelfath, Canada
Kazem Nouri (iD), Iran
Ciro Núñez-Gutiérrez (iD), Mexico
Wlodzimierz Ogryczak, Poland
Roger Ohayon, France
Krzysztof Okarma (iD), Poland
Mitsuhiro Okayasu, Japan
Murat Olgun (iD), Turkey
Diego Oliva, Mexico
Alberto Olivares (iD), Spain
Enrique Onieva (iD), Spain
Calogero Orlando (iD), Italy
Susana Ortega-Cisneros (iD), Mexico
Sergio Ortobelli, Italy
Naohisa Otsuka (iD), Japan
Sid Ahmed Ould Ahmed Mahmoud (iD),
Saudi Arabia
Taoreed Owolabi (iD), Nigeria
EUGENIA PETROPOULOU (iD), Greece
Arturo Pagano, Italy
Madhumangal Pal, India
Pasquale Palumbo (iD), Italy
Dragan Pamučar, Serbia
Weifeng Pan (iD), China
Chandan Pandey, India
Rui Pang, United Kingdom
Jürgen Pannek (iD), Germany
Elena Panteley, France
Achille Paolone, Italy

Zaoli Yang (iD), China
Jun Ye (iD), China
Min Ye (iD), China
Luis J. Yebra (iD), Spain
Peng-Yeng Yin (iD), Taiwan
Muhammad Haroon Yousaf (iD), Pakistan
Yuan Yuan, United Kingdom
Qin Yuming, China
Elena Zaitseva (iD), Slovakia
Arkadiusz Zak (iD), Poland
Mohammad Zakwan (iD), India
Ernesto Zambrano-Serrano (iD), Mexico
Francesco Zammori (iD), Italy
Jessica Zangari (iD), Italy
Rafal Zdunek (iD), Poland
Ibrahim Zeid, USA
Nianyin Zeng (iD), China
Junyong Zhai (iD), China
Hao Zhang (iD), China
Haopeng Zhang (iD), USA
Jian Zhang (iD), China
Kai Zhang, China
Lingfan Zhang (iD), China
Mingjie Zhang (iD), Norway
Qian Zhang (iD), China
Tianwei Zhang (iD), China
Tongqian Zhang (iD), China
Wenyu Zhang (iD), China
Xianming Zhang (iD), Australia
Xuping Zhang (iD), Denmark
Yinyan Zhang, China
Yifan Zhao (iD), United Kingdom
Debao Zhou, USA
Heng Zhou (iD), China
Jian G. Zhou (iD), United Kingdom
Junyong Zhou (iD), China
Xueqian Zhou (iD), United Kingdom
Zhe Zhou (iD), China
Wu-Le Zhu, China
Gaetano Zizzo (iD), Italy
Mingcheng Zuo, China

Contents

Research Article

Development of Robust Guaranteed Cost Mixed Control System for Active Suspension of In-Wheel-Drive Electric Vehicles

Xianjian Jin (iD),[1,2] **Jiadong Wang,**[2] **and Junpeng Yang**[2]

[1]*School of Mechatronic Engineering and Automation, Shanghai Key Laboratory of Intelligent Manufacturing and Robotics, Shanghai University, Shanghai 200072, China*
[2]*State Key Laboratory of Automotive Simulation and Control, Jilin University, Changchun 130025, China*

Correspondence should be addressed to Xianjian Jin; xianjianjin@shu.edu.cn

This paper presents a mixed H_2/H_∞-based robust guaranteed cost control system design of an active suspension system for in-wheel-independent-drive electric vehicles considering suspension performance requirements and parameter variation. In the active suspension system model, parameter uncertainties of active suspension are described by the bounded method, and the perturbation bounds can be also limited; then, the uncertain quarter-vehicle active suspension model where in-wheel motor is suspended as a dynamic vibration absorber is established. The robust guaranteed cost mixed H_2/H_∞ feedback controller of the closed-loop active suspension system is designed using Lyapunov stability theory, in which the suspension working space, dynamic tire displacement, and the active control force are taken as H_∞ performance indices, the H_2 norm of body acceleration is selected as the output performance index to be minimized, and then a comprehensive solution is transformed into a convex optimization problem with linear matrix inequality constraints. Simulations on random and bump road excitations are implemented to verify and evaluate the performance of the designed controller. The results show that the active suspension with developed robust mixed H_2/H_∞ controller can effectively achieve better ride comfort and road-holding ability compared with passive suspension and alone H_∞ controller.

1. Introduction

Due to air pollution and the lack of fossil fuels, electric vehicles have developed rapidly in the world. The emerging in-wheel motor-driven electric vehicle (IWMD-EV) has become a promising vehicle architecture due to its advantages of low fuel consumption, less environmental pollution, clean electric power supply, and advanced vehicle dynamics control [1–3]. IWMD-EV uses hub motors to drive four wheels directly, which makes it easier to realize independent control and quick response of wheel torque, and provides greater flexibility and traffic mobility for the vehicle dynamic control (VDC) system. In order to improve the ride comfort and handling stability of vehicles, a great deal of research studies have been carried out on the VDC system in recent years, such as direct yaw moment control (DYC), active

front steering system (AFS), traction control system (TCS), and regenerative braking system (RBS) [4–9].

Most of the above studies are focused on the lateral and longitudinal VDC systems, while optimization, design, and application of topology are still open and immature, and few research on the vertical vibration control of the IWMD-EV active suspension system is carried out [10–13]. In practice, the suspension system of IWMD-EV mounts and integrates the motor, wheel hub, and speed reducer together, which causes the increase of unsprung mass of IWMD-EV. It will lead to the deterioration of the ride comfort of the vehicle and even affect the active safety. Therefore, it is necessary to develop an advanced suspension topology based on IWM with a dynamic-damper mechanism. In addition, special attention should be paid to the active control of the IWMD-EV active suspension system.

Robust control has been proved to be able to deal well with model uncertainties and external disturbances in practical engineering systems [14–27]. For instance, the work in [23] addressed the adaptive event-triggered neural control for nonaffine nonlinear multiagent systems. The unknown nonlinear function is approximated by radial basis function neural networks, and the unmodeled dynamics is also dealt with a dynamic signal. The integral barrier Lyapunov function-based adaptive control is adopted to solve the full state constraint problems for switched nonlinear systems [24].The distributed observer-based event-triggered bipartite tracking control is designed for stochastic nonlinear multiagent systems with input saturation, and a novel distributed reduced-order observer is constructed to estimate unknown states [25]. Some scholars have applied robust controller to active suspension dynamics systems, such as sliding mode control, fuzzy control, H_∞ control, and other nonlinear adaptive robust methods [14–19, 26–28]. In [14], an integral terminal sliding mode control method with strong robustness is designed for the multivariable nonlinear suspension system affected by model uncertainty, time-varying parameters, road roughness excitation, and other factors so that the system could converge quickly in a finite time away from the equilibrium point. The work in [15] presents the adaptive fuzzy control for active suspension by considering time delay and unknown nonlinear dynamics, A predictor-based compensation scheme is developed, and a fuzzy logic system is constructed to address the two issues, respectively. The transient suspension response can be enhanced via the parameter estimation error-based finite-time adaptive method. In study [16], a sufficient condition for the design of sliding motion asymptotically stable is proposed, which can be transformed into a convex optimization problem, and an adaptive sliding mode controller is developed to ensure the reachability of the specified switch surface. Because H_∞ control can well deal with the hard time-domain constraint problem of the suspension system, that is, on the premise of considering multiple constraint output indexes, it can maximize the suppression of vertical vibration, so the application of this method can better improve the ride comfort of suspension. For instance, the study in [17] introduced the auxiliary function-based integral inequality method and reciprocally convex approach into the H_∞ controller design of the active half-vehicle suspension system with time-varying input delay, and the controller can achieve good performance. The research in [18] designed a robust H_∞ controller for the electrorheological (ER) suspension system with sprung mass and time constant of the ER damper uncertainties, which achieved the expected performance. In [19], a multiobjective

control with wheelbase preview information is presented for vehicle active suspension, in which disturbances of the front wheel are used as preview, and the solution is derived through cone complementarity linearization. The research [26] proposed the codesign problem of decentralized dynamic event-triggered communication and active suspension control of IWMD-EV. The T-S fuzzy active suspension model is established, and a novel decentralized dynamic event-triggered communication mechanism is also developed. In [27], the problem of event-triggered scheduling and control for active suspension over the resource-constrained controller area network (CAN) is addressed. Two new dynamic event-triggered schedulers (DETSs) are developed to orchestrate the transmissions of sensor data packets.

It is worth noting that, different from some published studies that aimed at traditional vehicle suspension, the main contribution of this work is to research a mixed H_2/H_∞-based robust guaranteed cost strategy of the active suspension system for in-wheel-independent-drive electric vehicles (IWMD-EV) rather than traditional vehicle suspension, where motor, the wheel hub, and speed reducer of IWMD-EV are mounted and integrated so that vehicle ride comfort will be deteriorated; meanwhile, designing the mixed H_2/H_∞ robust guaranteed cost controller for such an active suspension system of IWMD-EV in Figure 1 is seldom treated; therefore, these theoretical design and results have the essential difference. The structure of this paper is arranged as follows: In Section 2, a quarter car suspension model of IWMD-EV is established. Section 3 presents the mixed H_2/H_∞ robust guaranteed cost controller design. The simulation results are provided in Section 4. Finally, Section 5 gives the conclusion.

2. Active Suspension System Model

Since the main research objective is to design the control strategy of the active suspension system of IWMD-EV, we only consider the vertical motion of the active suspension system, and the lateral dynamics (sideslip, yaw, and roll) behaviour of the vehicle is ignored. As shown in Figure 1 [29], although the quarter-car model is relatively simple, it can feature the fundamental characteristics of the suspension system. It is noted that the half-vehicle suspension model or the whole vehicle suspension model can also describe vehicle vertical motion, pitch motion, and roll motion whereas it can be often used to analyze vehicle handling stability and study vehicle integrated suspension control.

According to the laws of dynamics, the quarter-car active suspension model can be described as

$$
\begin{aligned}
Z_s m_s + k_s\left(Z_s - Z_u\right) + c_s\left(\dot{Z}_s - \dot{Z}_u\right) - F_a &= 0, \\
Z_u m_u - k_s\left(Z_s - Z_u\right) - c_s\left(\dot{Z}_s - \dot{Z}_u\right) + k_t\left(Z_u - Z_r\right) - k_h\left(Z_h - Z_u\right) - c_h\left(\dot{Z}_h - \dot{Z}_u\right) + F_a &= 0, \\
Z_h m_h + k_h\left(Z_h - Z_u\right) + c_h\left(\dot{Z}_h - \dot{Z}_u\right) &= 0,
\end{aligned}
\tag{1}
$$
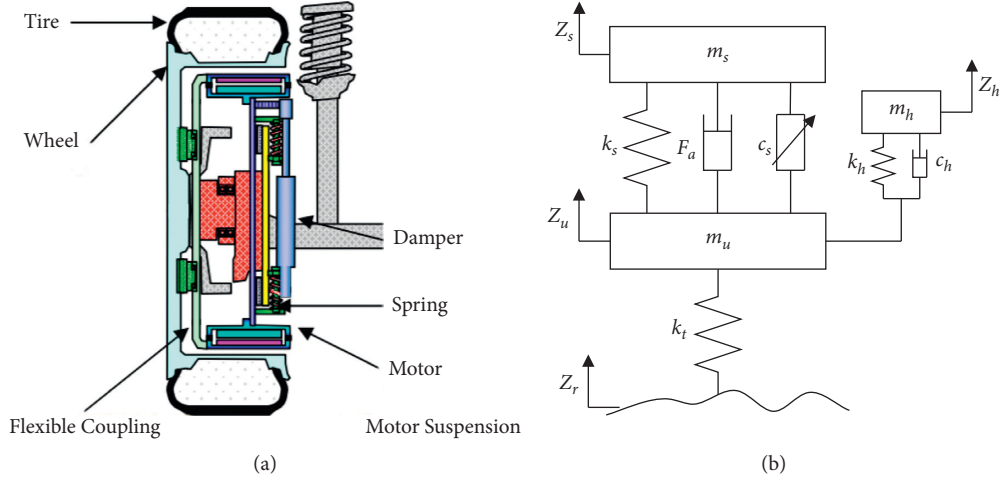
FIGURE 1: Quarter-car active suspension of IWMD-EV [29]. (a). Mechanical structure. (b). Suspension model.

where m_s, m_u, and m_h represent the sprung mass, the wheel mass, and the in-wheel-motor mass, respectively; k_s and c_s are the stiffness and damping of the suspension, respectively; k_h and c_h denote the stiffness and damping of the damping system between motor and wheel; k_t is the tire stiffness; F_a is the active control force; Z_s, Z_u, Z_h, and Z_r denote the vertical displacement of the vehicle body, wheel, motor, and road, respectively; the superscripts $\cdot$ and $\cdot\cdot$ stand for velocity and acceleration, respectively.

In this suspension system, the sprung mass m_s is an uncertain parameter due to the change of the vehicle load. For the convenience of the following description, let

$$M_{s0} = \frac{1}{m_{s0}}, \tag{2}$$

$$M_s = M_{s0}\left(1 + \alpha \delta_M(t)\right),$$

where m_{s0} is the m_s nominal value of the sprung mass, and α represents the perturbation of the uncertain parameter with bound $\delta_M(t) < 1$.

We choose the state variables of the active suspension system as follows:

$$X_1 = Z_s - Z_u, X_2 = \dot{Z}_s, X_3 = Z_u - Z_r,$$
$$X_4 = \dot{Z}_u, X_5 = Z_h - Z_r, X_6 = \dot{Z}_h. \tag{3}$$

In the process of active suspension system designing, four performance indicators should be considered as follows:

(1) Ride comfort. Vertical acceleration of the body can be used as an evaluation index of ride comfort, which is generally required to be minimized.

(2) Suspension working space (SWS). Due to the structural limitation of the suspension itself, the excessive suspension travel will lead to collision, so it should be limited as

$$Z_s - Z_u \ll S_{\max}. \tag{4}$$

(3) Steering stability. To satisfy the steering stability of the vehicle, it is required that the tires cannot leave the road in the process of driving. Obviously, only the dynamic load of the tire is less than the static load that satisfies the requirements. Otherwise, it may result in vibration of the driver seat in the vertical direction and cause the wheels to lift off the ground. That is,

$$k_t\left(Z_u - Z_r\right) < Mg, \tag{5}$$

where

$$M = m_s + m_u + m_h. \tag{6}$$

(4) Active control force. The output control force of the actuating motor cannot be infinite and should be limited as

$$\left|F_a\right| \ll F_{a\max}. \tag{7}$$

We consider that H_∞ control is good at the suppression of the energy bounded interference and has a good robustness, while H_2 control has a significant effect on suppressing the white noise interference and has a good dynamic characteristic. Therefore, we take the body acceleration (BA) $\ddot{Z}_s$ as H_2 index and take the other three performances including the suspension working space, dynamic tire displacement(DTD), and the active control force as the H_∞ index, that is,

$$z_2 = Z_s,$$

$$z_\infty = \left[\begin{array}{ccc} \dfrac{Z_s - Z_u}{S_{\max}} & \dfrac{k_t\left(Z_u - Z_r\right)}{\left(m_s + m_u + m_h\right)g} & \dfrac{F_a}{F_{a\max}} \end{array}\right]^T. \tag{8}$$

Combined with the above derivation and equation, the state space expression of the open loop suspension uncertain linear system is obtained as

$$\begin{cases} \dot{x}(t) = (A + \Delta A)x(t) + B_1 w(t) + (B_2 + \Delta B_2)u(t), \\ z_2(t) = C_2 x(t) + D_2 u(t), \\ z_\infty(t) = C_\infty x(t) + D_\infty u(t), \end{cases} \quad (9)$$

where A, B_1, B_2, C_2, D_2, C_∞, and D_∞ are known constant matrices that describe the nominal system model of the

suspension; ΔA and ΔB_2 are unknown real matrices of appropriate dimensions that represent time-varying parameter uncertainties of the system model. These matrices can be presented as follows:

$$A = \begin{bmatrix} 0 & 1 & 0 & -1 & 0 & 0 \\ -k_s M_{s0} & -c_s M_{s0} & 0 & c_s M_{s0} & 0 & 0 \\ 0 & 0 & 0 & 1 & 0 & 0 \\ k_s/m_u & c_s/m_u & c_s/m_u & -(c_s+c_h)/m_u & k_h/m_u & c_h/m_u \\ 0 & 0 & 0 & -1 & 0 & 1 \\ 0 & 0 & 0 & c_h/m_h & -k_h/m_h & -c_h/m_h \end{bmatrix},$$

$$\Delta A = \begin{bmatrix} 0 & 0 & 0 & 0 & 0 & 0 \\ -k_s M_{s0}\alpha\delta_M & -c_s M_{s0}\alpha\delta_M & 0 & c_s M_{s0}\alpha\delta_M & 0 & 0 \\ 0 & 0 & 0 & 0 & 0 & 0 \\ 0 & 0 & 0 & 0 & 0 & 0 \\ 0 & 0 & 0 & 0 & 0 & 0 \\ 0 & 0 & 0 & 0 & 0 & 0 \end{bmatrix},$$

$$B_1 = \begin{bmatrix} 0 & 0 & -1 & 0 & 0 & 0 \end{bmatrix}^T,$$

$$B_2 = \begin{bmatrix} 0 & M_{s0} & 0 & -1/m_u & 0 & 0 \end{bmatrix}^T,$$

$$\Delta B_2 = \begin{bmatrix} 0 & M_{s0}\alpha\delta_M & 0 & 0 & 0 & 0 \end{bmatrix}^T,$$

$$C_2 = \begin{bmatrix} -k_s M_{s0} & -c_s M_{s0} & 0 & c_s M_{s0} & 0 & 0 \end{bmatrix},$$

$$D_2 = \begin{bmatrix} M_{s0} \end{bmatrix},$$

$$C_\infty = \begin{bmatrix} 1/S_{max} & 0 & 0 & 0 & 0 & 0 \\ 0 & 0 & k_t/Mg & 0 & 0 & 0 \\ 0 & 0 & 0 & 0 & 0 & 0 \end{bmatrix},$$

$$D_\infty = \begin{bmatrix} 0 & 0 & 1/F_{a\,max} \end{bmatrix}^T.$$

(10)

The uncertain matrices ΔA and ΔB_2 can be expressed as

$$\begin{bmatrix} \Delta A(t) & \Delta B_2(t) \end{bmatrix} = H\delta_M(t)\begin{bmatrix} E_1 & E_2 \end{bmatrix}, \quad (11)$$

where H, E_1, and E_2 are known real matrices of appropriate dimensions which represent the structural information of uncertain parameters, that is,

$$H = \begin{bmatrix} 0 & 1 & 0 & 0 & 0 & 0 \end{bmatrix}^T,$$

$$E_1 = \begin{bmatrix} -\alpha k_s M_{s0} & -\alpha c_s M_{s0} & 0 & \alpha c_s M_{s0} & 0 & 0 \end{bmatrix}, \quad (12)$$

$$E_2 = \begin{bmatrix} \alpha M_{s0} \end{bmatrix}.$$

And $\delta_M(t)$ is an unknown real time-varying matrix satisfying

$$\delta_M^T(t)\delta_M(t) \leq I. \quad (13)$$

We suppose the state feedback control law is

$$u(t) = Kx(t). \quad (14)$$

By applying the control law (14), the open-loop system (9) is transformed into the following closed-loop system:

$$\begin{cases} \dot{x}(t) = (A_c + H\delta_M(t)E_c)x(t) + B_1 w(t), \\ z_2(t) = C_{2c}x(t), \\ z_\infty(t) = C_{\infty c}x(t), \end{cases} \quad (15)$$

where

$$\begin{aligned} A_c &= A + B_2 K, \\ E_c &= E_1 + E_2 K, \\ C_{2c} &= C_2 + D_2 K, \\ C_{\infty c} &= C_\infty + D_\infty K. \end{aligned} \quad (16)$$

Let

$$\widetilde{A}_c = A_c + H\delta_M(t)E_c. \tag{17}$$

The closed loop system (15) can be reduced as

$$\begin{cases} \dot{x}(t) = \widetilde{A}_c x(t) + B_1 w(t), \\ z_2(t) = C_{2c} x(t), \\ z_\infty(t) = C_{\infty c} x(t). \end{cases} \tag{18}$$

Remark 1. We note that the parameter uncertainties of the active suspension system can be described by the bounded method. It is reasonable to make this compromise in most cases; the reason is due to this bound that can be determined in advance through experiments or estimations [5, 9, 14–19]. If the method cannot be used, parameter uncertainties of active suspension can be dealt with advanced technology such as adaptive strategy and other techniques [9, 14–19],whereas making this characterization can greatly simplify controller design.

3. Robust Mixed Controller Design

The H_∞ control method has good robust stability, but it is conservative. If all the performance indicators of IWMD-EV are considered as H_∞ performance indicators, the BA of vehicle may not reach the ideal effect. The H_2 control method can obtain superior dynamic performance but with poor robustness and stability. Therefore, we combine the advantages of the two control methods to design the mixed H_2/H_∞ guaranteed cost controller so that the active suspension system of IWMD-EV not only has greater robust stability but also meets better robust performance requirements.

The mixed H_2/H_∞ guaranteed cost control is to design a state feedback control law (14) for the closed-loop system (18) such that the following design criteria are satisfied as follows:

 (i) The closed-loop control system (18) is asymptotically stable.

 (ii) The closed-loop transfer function $G_{z_\infty \omega}(s)$ from $\omega(t)$ to $z_\infty(t)$ satisfies

$$\left\| G_{z_\infty \omega}(s) \right\|_\infty < \gamma_\infty, \tag{19}$$

 where

$$G_{z_\infty \omega}(s) = (C_1 + D_{12}K)(sI - (A + B_2K))^{-1}B_1 + D_{11},$$

$$\left\| G_{z_\infty \omega}(s) \right\|_\infty = \sup_\omega \sigma_{\max} \{ G_{z_\infty \omega}(j\omega) \}, \tag{20}$$

 where $\sigma_{\max}\{\cdot\}$ denotes the largest singular value, and γ_∞ is a prespecified positive scalar.

 (iii) The closed-loop transfer function $G_{z_2 \omega}(s)$ from $\omega(t)$ to $z_2(t)$ satisfies

$$\left\| G_{z_2 \omega}(s) \right\|_2 \le \gamma_2. \tag{21}$$

If $\widetilde{A}_c$ is asymptotically stable, then $G_{z_2 \omega}(s)_2$ can be expressed as

$$\left\| G_{z_2 \omega}(s) \right\|_2 = \sup_{\delta_M(t)} tr\{ B_1^T \widetilde{P} B_1 \}, \tag{22}$$

where $\widetilde{P} = \widetilde{P}^T \ge 0$ is obtained from the following Lyapunov equation:

$$\widetilde{P}\widetilde{A}_c + \widetilde{A}_c^T \widetilde{P} + C_{2c}^T C_{2c} = 0, \tag{23}$$

where γ_2 represents the upper bound of H_2 performance index.

To design a controller that meets the above three conditions, we introduce the following two lemmas:

Lemma 1 (See [20]). *Given the appropriate dimensions matrices $Y = Y^T$, D, and E, there is*

$$Y + DF\ E + E^T F^T D^T < 0, \tag{24}$$

for F satisfies $F^T F < I$, if and only if there exists a positive scalar ε such that

$$Y + \varepsilon DD^T + \varepsilon^{-1} E^T E < 0. \tag{25}$$

Lemma 2 (See [21]). *For any matrices X and Y with appropriate dimensions, there is*

$$X^T Y + Y^T X \le \beta X^T X + \beta^{-1} Y^T Y, \tag{26}$$

for any $\beta > 0$.

To design the mixed H_2/H_∞ robust guaranteed cost control of active suspension, we present the main design process of this controller via the following theorem.

Theorem 1. *For system (18) and a given scalar $\gamma_\infty > 0$, $\widetilde{A}_c$ is asymptotically stable, and $G_{z_\infty \omega}(s)_\infty < \gamma_\infty$ if and only if there exist two positive scalars ε and β such that the following inequality,*

$$A_c^T P + PA_c + P(\varepsilon HH^T P + \beta \gamma_\infty^{-2} B_1 B_1^T)P$$
$$+ \varepsilon^{-1} E_c^T E_c + \beta^{-1} C_{\infty c}^T C_{\infty c} + C_{2c}^T C_{2c} < 0, \tag{27}$$

has a symmetric positive definite solution P. Furthermore, for the allowable parameter uncertainty,

$$P \ge \widetilde{P} \ge 0, \tag{28}$$

where $\widetilde{P}$ is obtained from (23).

Proof. According to the strict bounded real lemma, if and only if there exists a symmetric positive definite matrix Q satisfying

$$\tilde{A}_c^T Q + Q\tilde{A}_c + \gamma_\infty^{-2} Q B_1 B_1^T Q + C_{\infty c}^T C_{\infty c} < 0, \qquad (29)$$

then $\tilde{A}_c$ is asymptotically stable and $G_{z_\infty \omega}(s)_\infty < \gamma_\infty$.

And if there is a positive scalar β, (32) can be equivalent to

$$\tilde{A}_c^T Q + Q\tilde{A}_c + \gamma_\infty^{-2} Q B_1 B_1^T Q + C_{\infty c}^T C_{\infty c} + \beta C_{2c}^T C_{2c} < 0. \qquad (30)$$

By substituting (8) and letting $P = \beta^{-1} Q$, inequality (29) can be rewritten as

$$\begin{aligned} A_c^T P &+ E_c^T \delta_M^T H^T P + P A_c + P H \delta_M E_c \\ &+ \beta \gamma_\infty^{-2} P B_1 B_1^T P + \beta^{-1} C_{\infty c}^T C_{\infty c} + C_{2c}^T C_{2c} < 0. \end{aligned} \qquad (31)$$

In the light of Lemma 1, the matrix inequality (31) holds for all unknown real matrices δ_M satisfying $\delta_M^T \delta_M < I$ if and only if there exists $\varepsilon > 0$ such that

$$\begin{aligned} A_c^T P &+ P A_c + \beta \gamma_\infty^{-2} P B_1 B_1^T P + \beta^{-1} C_{\infty c}^T C_{\infty c} \\ &+ C_{2c}^T C_{2c} + \varepsilon P H H^T P + \varepsilon^{-1} E_c^T E_c < 0. \end{aligned} \qquad (32)$$

Obviously, (32) is equivalent to (27).

Furthermore, let

$$J = \varepsilon P H H^T P + \varepsilon^{-1} E_c^T E_c - P H \delta_M E_c - E_c^T \delta_M^T H^T P. \qquad (33)$$

According to Lemma 2 and inequality (13) such that

$$\begin{aligned} P H \delta_M E_c + E_c^T \delta_M^T H^T P &\le \varepsilon^{-1} E_c^T E_c + \varepsilon P H \delta_M \delta_M^T H^T P \\ &\le \varepsilon^{-1} E_c^T E_c + \varepsilon P H H^T P. \end{aligned} \qquad (34)$$

Therefore, $J \ge 0$.

Then, by subtracting (23) from (32), we obtain

$$\begin{aligned} \tilde{A}_c^T (P - \tilde{P}) &+ (P - \tilde{P})\tilde{A}_c + \beta \gamma_\infty^{-2} P B_1 B_1^T P \\ &+ \beta^{-1} C_{\infty c}^T C_{\infty c} + C_{2c}^T C_{2c} + J < 0. \end{aligned} \qquad (35)$$

Since $\tilde{A}_c$ is asymptotically stable, and

$$J + \beta \gamma_\infty^{-2} P B_1 B_1^T P + \beta^{-1} C_{\infty c}^T C_{\infty c} \ge 0. \qquad (36)$$

We can get $P^\sim \le P$ directly from Lyapunov stability theory. Hence, Theorem 1 has been proved.

Furthermore, the solution P guarantees the worst-case H_2 performance index satisfying

$$\left\| G_{z_2 \omega}(s) \right\|_2 \le \gamma_2, \qquad (37)$$

where

$$\gamma_2 = tr\left(B_1^T P B_1\right). \qquad (38)$$

$\square$

Theorem 2. *For system (18) and a given scalar $\gamma_\infty > 0$, there exists a feedback control law $u(t) = Kx(t)$ such that the design criteria (i) and (ii) are satisfied if and only if there exists two positive scalars ε and β. A symmetric positive definite matrix X and a matrix Y such that*

$$\begin{bmatrix} W & * & * & * \\ N_1 & -\varepsilon I & * & * \\ N_2 & 0 & -\beta I & * \\ N_3 & 0 & 0 & -I \end{bmatrix} < 0, \qquad (39)$$

where

$$\begin{aligned} W &= \left(AX + B_2 Y\right)^T + AX + B_2 Y + \varepsilon H H^T + \beta \gamma^{-2} B_1 B_1^T, \\ N_1 &= E_1 X + E_2 Y, \\ N_2 &= C_\infty X + D_\infty Y, \\ N_3 &= C_2 X + D_2 Y. \end{aligned} \qquad (40)$$

Furthermore, if (32) has a feasible solution $(\varepsilon, \beta, X, Y)$, then the control law $K = YX^{-1}$.

Proof. According to Theorem 1, there exists a feedback control law (14) that satisfies the design criteria (i) and (ii) if and only if there exists two scalars ε and β, and a symmetric positive definite matrix is P such that the matrix inequality (27) holds

By multiplying both sides of (21) by P^{-1}, we obtain

$$\begin{aligned} P^{-1} A_c^T &+ A_c P^{-1} + \varepsilon H H^T P + \beta \gamma_\infty^{-2} B_1 B_1^T + \varepsilon^{-1} P^{-1} E_c^T E_c P^{-1} \\ &+ \beta^{-1} P^{-1} C_{\infty c}^T C_{\infty c} P^{-1} + P^{-1} C_{2c}^T C_{2c} P^{-1} < 0. \end{aligned} \qquad (41)$$

Using the Schur complement [22], we yield

$$\begin{bmatrix} \overline{W} & * & * & * \\ \overline{N}_1 & -\varepsilon I & * & * \\ \overline{N}_2 & 0 & -\beta I & * \\ \overline{N}_3 & 0 & 0 & -I \end{bmatrix} < 0, \qquad (42)$$

where

$$\begin{aligned} \overline{W} &= P^{-1}\left(A + B_2 K\right)^T + (A + B_2 K)P^{-1} + \varepsilon H H^T + \beta \gamma^{-2} B_1 B_1^T, \\ \overline{N}_1 &= (E_1 + E_2 K)P^{-1}, \\ \overline{N}_2 &= (C_\infty + D_\infty K)P^{-1}, \\ \overline{N}_3 &= (C_2 + D_2 K)P^{-1}. \end{aligned} \qquad (43)$$

Defining $X = P^{-1}$ and $Y = KP^{-1}$, the matrix inequality (42) can be easily reduced to (39). This proves Theorem 2. $\square$

Theorem 2. *provides the characterization of all controllers that guarantee the realization of design criteria (i) and (ii), while (39) provides a H_2/H_∞ guaranteed cost up bound $tr\left(B_1^T P B_1\right)$. Therefore, we can use this representation to design the desired mixed H_2/H_∞ guaranteed cost controller.*

Theorem 3. *We consider system (8) and a given scalar $\gamma_\infty > 0$, if following linear convex optimization problem*

$$\min_{\varepsilon, \beta, X, Y, N} tr(N)$$

s.t.

$$(a). \ (32), \tag{44}$$

$$(b). \begin{bmatrix} -N & B_1^T \\ B_1 & -X \end{bmatrix} < 0,$$

has a set of possible solutions $(\varepsilon, \beta, X, Y, N)$, then $u(t) = YX^{-1}x(t)$ is the mixed H_2/H_∞ guaranteed cost control law of the active suspension system, and the upper bound of H_2 performance index is $\gamma_2 = tr(N)$.

Proof. According to Theorem 2, the control law constructed from any feasible solution of problem (39) satisfies the design criteria (i) and (ii).

In the light of Schur complement lemma, the constraint condition (b) of convex optimization problem (44) is equivalent to

$$B_1^T X^{-1} B_1 < N. \tag{45}$$

So, minimizing $tr(N)$ is equal to minimizing the upper bound of H_2 performance index γ_2. Due to the convexity of the objective function and constraints, the optimization problem (44) can achieve global optimality. Thus, the proof is completed.

Through Theorem 2 and Theorem 3, the design of mixed H_2/H_∞ guaranteed cost control law is realized, which not only ensures the asymptotic stability of the closed-loop system (18) but also satisfies $G_{z_\infty \omega}(s)_\infty < \gamma_\infty$ when the

disturbance attenuation level γ_∞ is given; that is, the SWS constraint, DTD constraint, and active control force have certain safety constraints under external disturbance; moreover, γ_2 is minimized; that is, the BA is minimized under external disturbance. □

Remark 2. We note that perhaps this combination of the H_2 method is not proposed for the first time, while this mixed H_2/H_∞ guaranteed cost control method is particularly designed for active suspension of in-wheel-drive electric vehicles. Also, the proposed method can be extended to other vehicle dynamics control systems when multicontrol objectives in VDC systems are oriented by applying this mixed H_2/H_∞ guaranteed cost control strategy and framework.

4. Simulation and Analysis

The nominal values of parameters for the active suspension system in IWMD-EV are shown in Table 1. The sprung mass m_s is an uncertain parameter with a range of [40 kg, 60 kg], i.e., the perturbation value $\alpha = 0.16$.

We use LMI toolbox of MATLAB to solve the mixed H_2/H_∞ guaranteed cost state feedback control law for the active suspension system. Figure 2 shows the relationship between the disturbance attenuation level γ_∞ and the H_2 guaranteed performance index γ_2 of the closed-loop suspension system.

As can be seen from Figure 2, γ_2 increases gradually with the decrease of γ_∞, and when γ_∞ approaches the minimum value, γ_2 increases rapidly. Combining the two performance indexes, when we take $\gamma_\infty = 15$, the corresponding γ_2 and controller are as follows:

$$\begin{aligned} \gamma_2 &= 8.6743, \\ K &= 10^4 \times [\,1.6538 \ -0.0158 \ -0.1448 \ -0.1399 \ -0.0001 \ -0.0000\,], \\ K &= 10^4 \times [\,1.6538 \ -0.0158 \ -0.1448 \ -0.1399 \ -0.0001 \ -0.0000\,]. \end{aligned} \tag{46}$$

For comparison, optimizing all outputs as H_∞ performance indexes, we design a constrained H_∞ controller as

$$K_{con} = 10^4 \times [\,1.1293 \ -0.1084 \ 9.6321 \ 0.0748 \ -0.6461 \ -0.1400\,]. \tag{47}$$

Here, we note that the constrained H_∞ control for the active suspension of IWMD-EV is only used to compare the performance of the proposed controller, and the detailed design process is omitted for brevity. Interested readers can refer to related papers such as Refs [17–19] for H_∞ design of the suspension system. Besides, the solution time of proposed mixed H_2/H_∞ guaranteed cost controller can be executed offline, so the total computational load can be

tolerated for vehicle engineering application equipped with advanced hardware and processor.

4.1. Power Spectral Density Analysis. To obtain the frequency performance of the active suspension, power spectral density (PSD) analysis is performed based on the data obtained from random road simulation. The results are shown in

TABLE 1: Nominal value of active suspension parameters.

Parameter	Value	Parameter	Value
m_s	320 Kg	m_u	40 Kg
k_s	18000 N/m	m_h	20 Kg
k_t	220000 N/m	C_h	1000 $N \cdot s/m$
C_s	1400 $N \cdot s/m$	k_h	15000 N/m
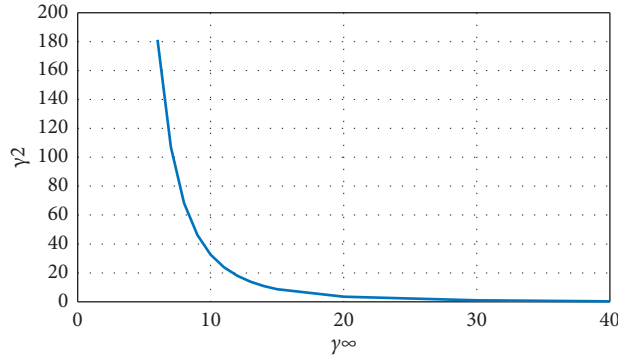
FIGURE 2: $\gamma_2 - \gamma_\infty$, the relationship between γ_2 and γ_∞.

--- Passive
— Mixed H_2/H_∞
-·-· Constrained H_∞
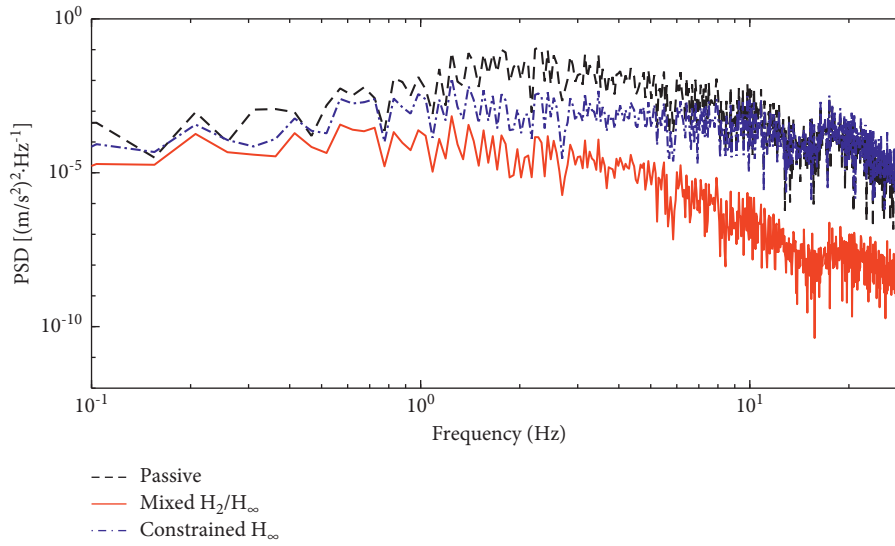
FIGURE 3: Power spectral density analysis of body acceleration.

Figures 3–5. As can be seen from these figures, the BA power spectral density of the mixed robust H_2/H_∞ guaranteed cost controller for active suspension is the minimum at the full frequency, which indicates that the corresponding controller has a good performance of suppressing vertical vibration. In the low frequency range of 0.1–5 Hz, the DTD power spectral density of the active suspension with mixed robust H_2/H_∞ guaranteed cost is also better than that of passive suspension and constrained H_∞ with active suspension. In terms of the SWS, although the two active suspension systems are slightly higher than the passive suspension in the low frequency range of 0.1–2 Hz, they are basically the same as the passive suspension in the high frequency. The power spectral density analysis reveals that the designed mixed robust H_2/H_∞

guaranteed cost controller possesses better passenger comfort and road holding ability.

4.2. Random Road Response. Firstly, the C-level road is selected as the system input, that is,

$$\dot{Z}_r(t) = -2\pi n_0 Z_r(t) + 2\pi n_0 \sqrt{G_{Z_r}(n_0)u} \cdot \omega(t), \quad (48)$$

where $n_c = 0.01 m^{-1}$ is the lower cut-off space frequency; $\omega(t)$ is the Gaussian white noise with an average of 0; Z_r is the vertical displacement of road surface; $u = 20 m/s$ denotes the velocity of vehicle; $G_{z_r}(n_0) = 64 \times 10^{-6} m^3$ is the coefficient of road roughness.
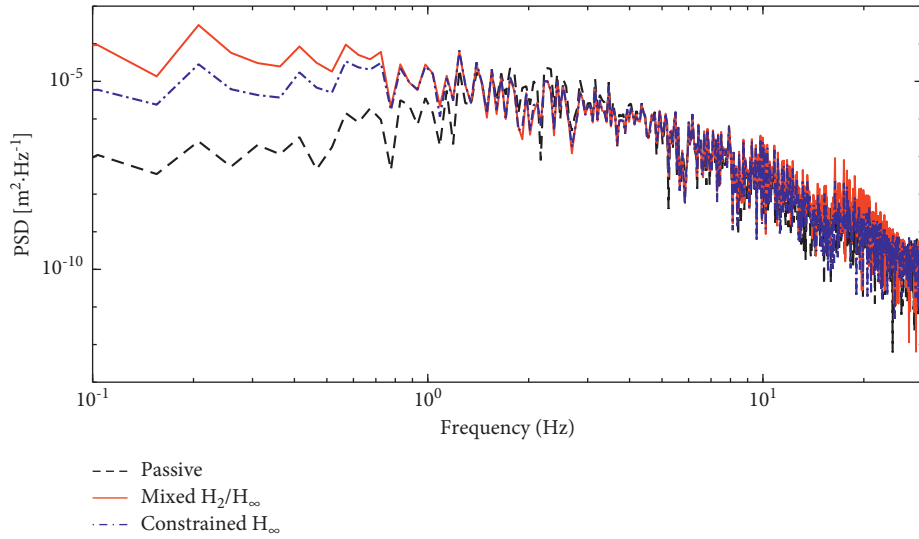
Figure 4: Power spectral density analysis of suspension working space.
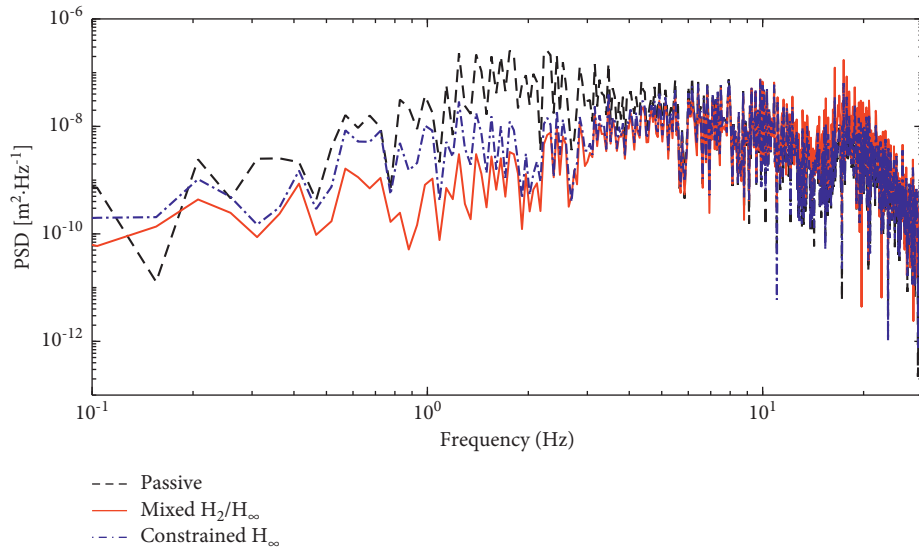
Figure 5: Power spectral density analysis of dynamic tire displacement.
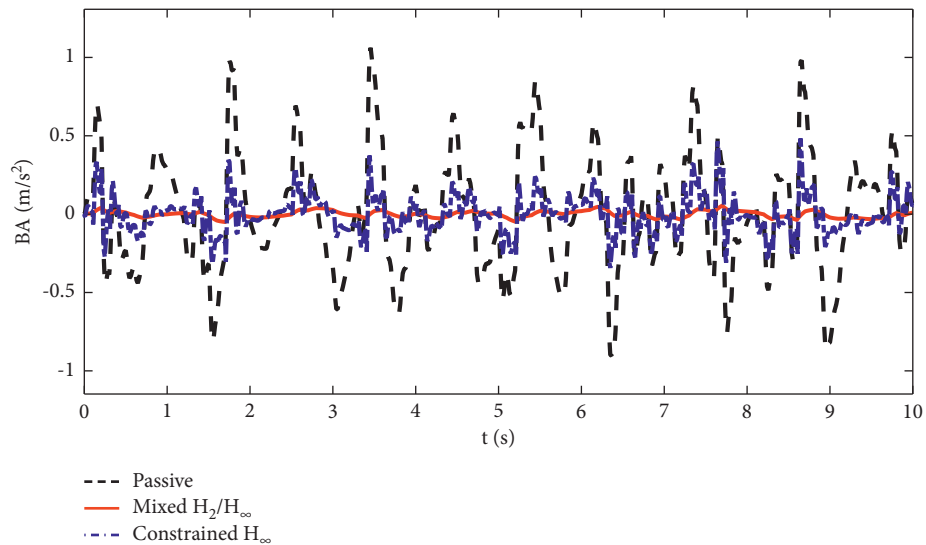
Figure 6: Random road body acceleration responses of nominal suspension.
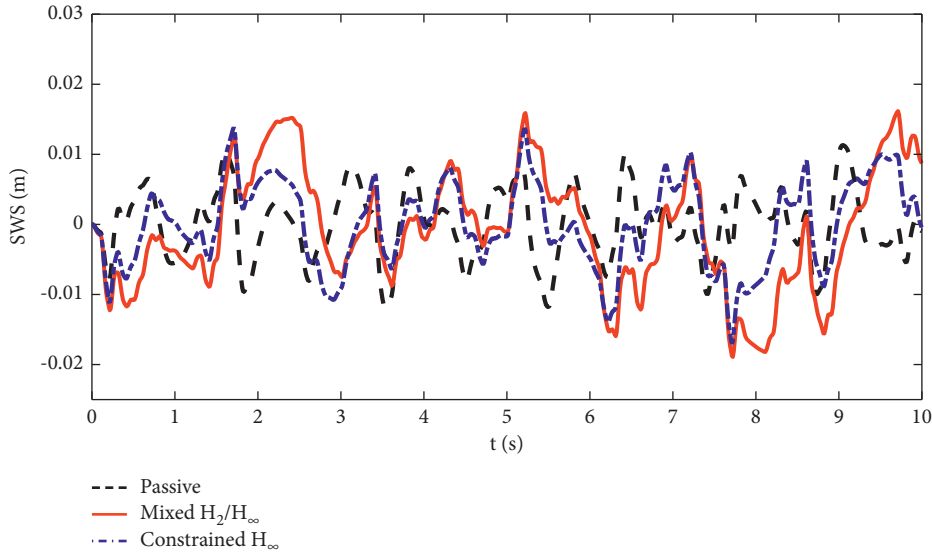
FIGURE 7: Random road working space responses of nominal suspension.
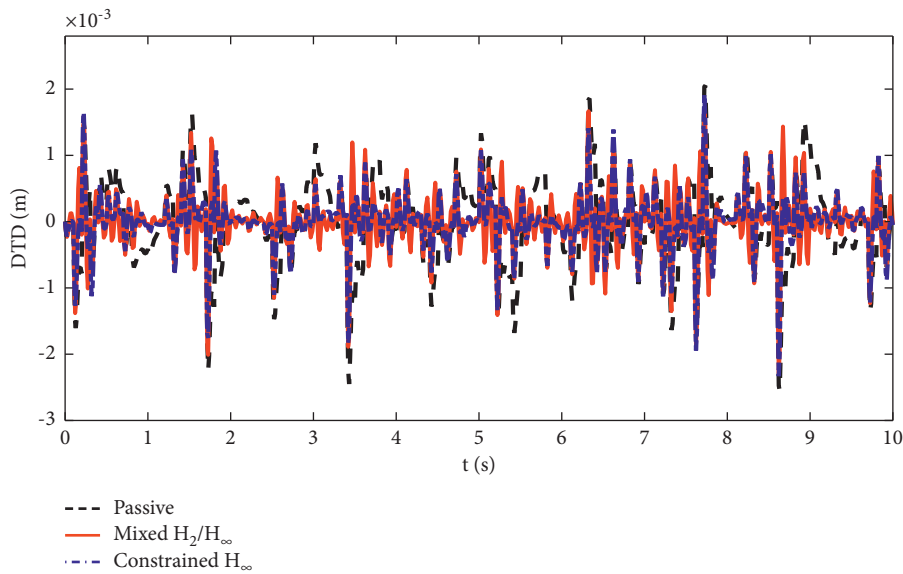
FIGURE 8: Random road dynamic tire displacement responses of nominal suspension.

Three random road responses of nominal suspension systems are illustrated in Figures 6–11. As shown in these figures, both active suspensions achieve better body acceleration performance, and the mixed robust H_2/H_∞ guaranteed cost controller is better than the constrained H_∞ controller. Compared with the passive suspension, the suspension working space of the two active suspensions is slightly worse but still within the acceptable range. This is because the SWS and the BA are a pair of contradictory performance. The dynamic tire displacement performance of the two active suspension is similar, which is smaller than that of the passive suspension.

4.3. Bump Road Response. The bump road excitation is selected as the second input road; it can be described as

$$Z_r(t) = \frac{h}{2}\left(1 - \cos\left(\frac{2\pi u}{L}t\right)\right), \tag{49}$$

where v is the vehicle velocity; L and h are the length and height of the bump, respectively. Here, we take $v = 45 km/h$, $L = 5m$, and $h = 0.1m$.

Figures 12–14 are the simulation results of the three performance indicators of the nominal suspension and Figures 15–17 are the simulation results of the perturbation suspension with 40 kg variation of the sprung mass. As can
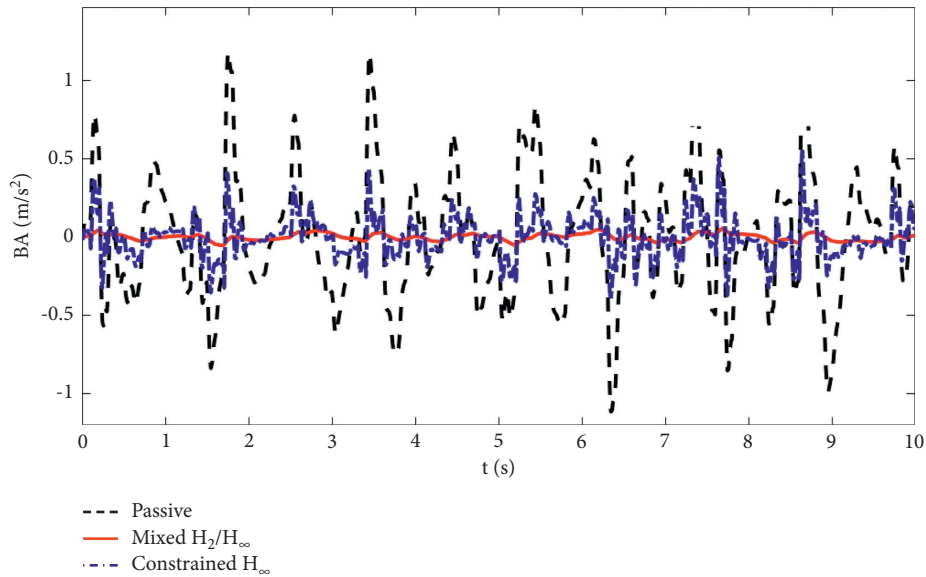
FIGURE 9: Random road body acceleration responses of suspension with parameter variation.
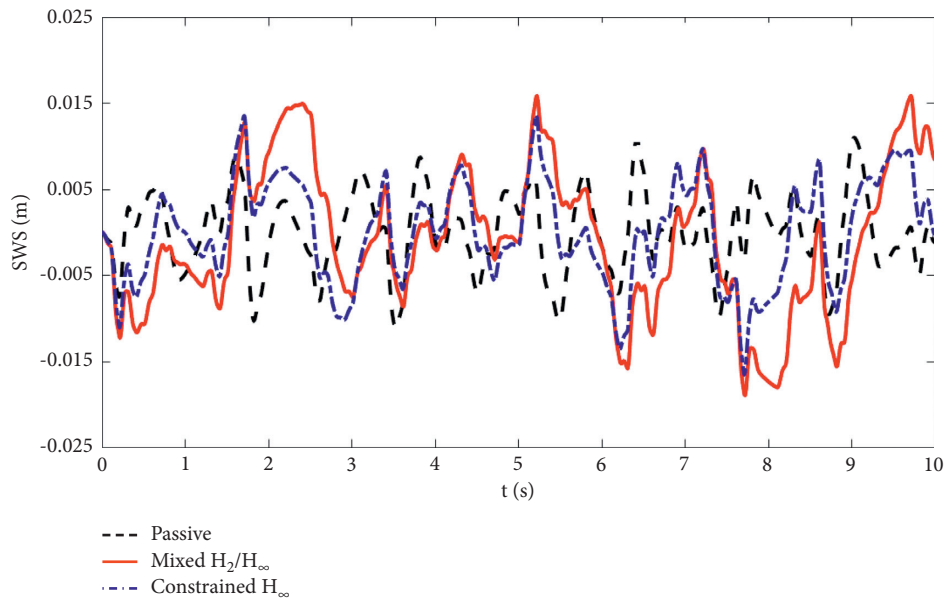
FIGURE 10: Random road working space responses of suspension with parameter variation.

be seen from these figures, the BA and the DTD performances of two active suspensions are much better than the passive suspension, and the mixed robust H_2/H_∞ guaranteed cost control suspension has the best performance. Although the SWS performance of two active suspensions is deteriorated, it remained within the constraint range (less than $\pm 0.1\,m$). In addition, the response of the perturbation model shows that the mixed robust H_2/H_∞ guaranteed cost controller has good robustness compared with alone H_∞ controller.
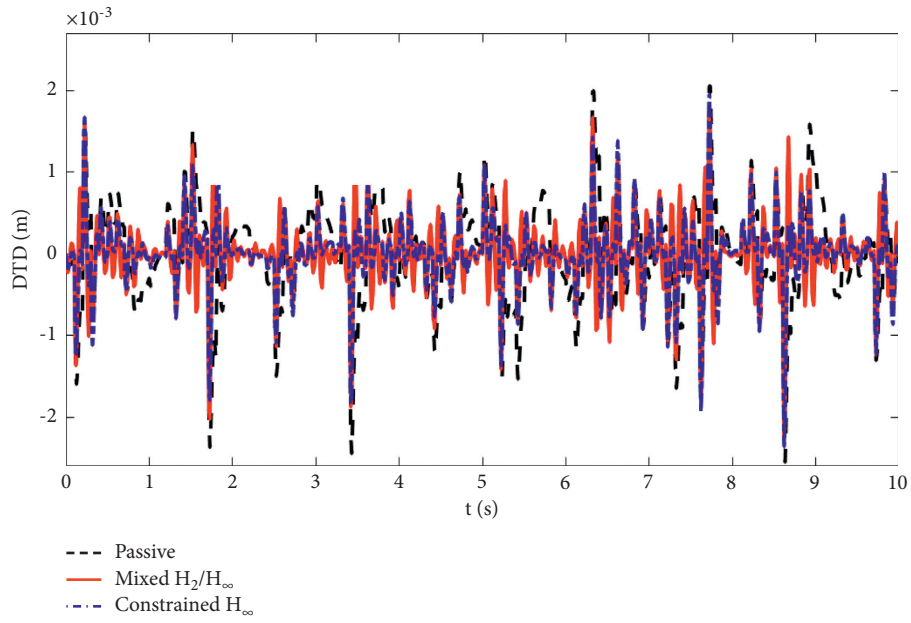
FIGURE 11: Random road dynamic tire displacement responses of suspension with parameter variation.
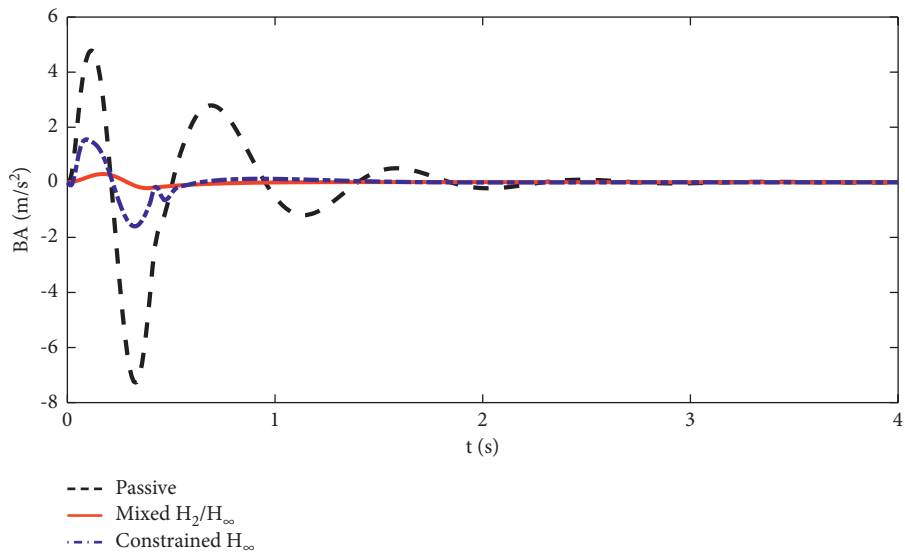
FIGURE 12: Bump body acceleration responses of nominal suspension.
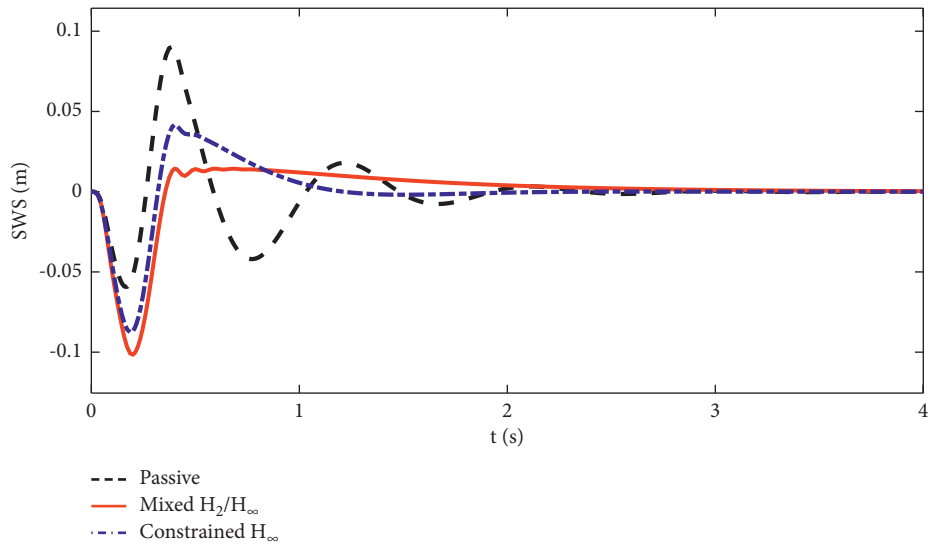
FIGURE 13: Bump working space responses of nominal suspension.
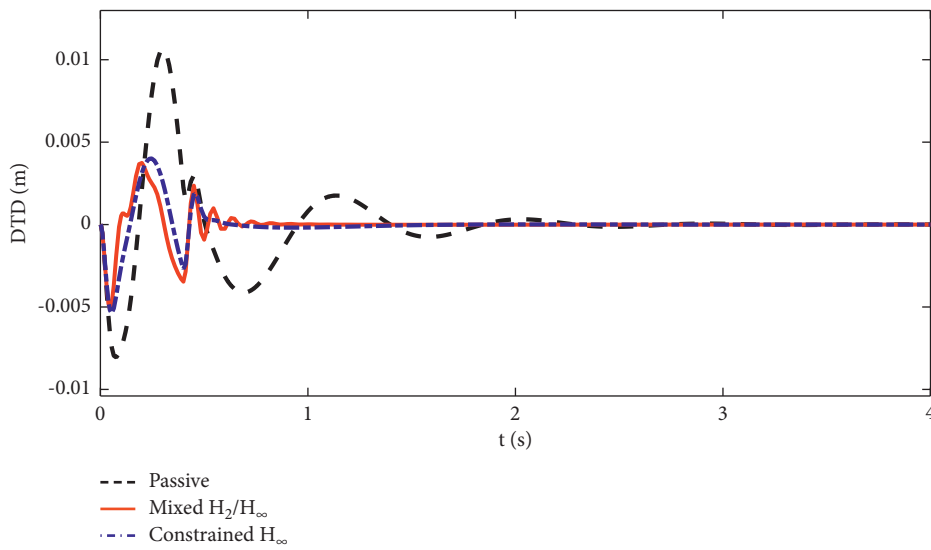
FIGURE 14: Bump dynamic tire displacement responses of nominal suspension.
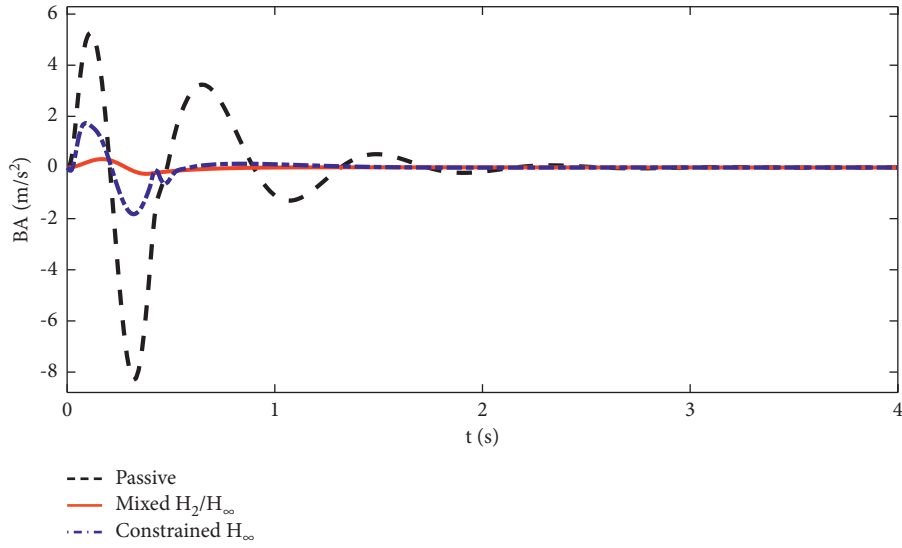
FIGURE 15: Bump body acceleration responses of suspension with parameter variation.
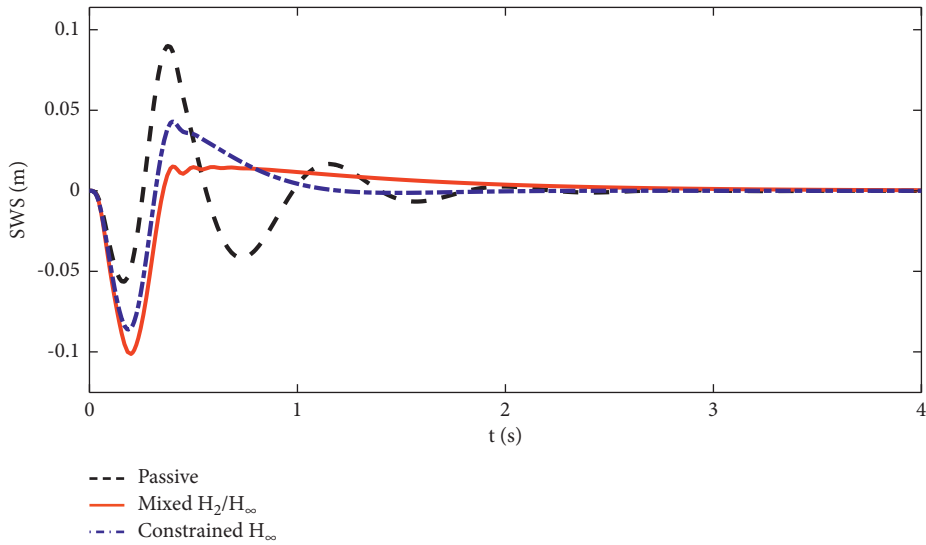
FIGURE 16: Bump working space responses of suspension with parameter variation.
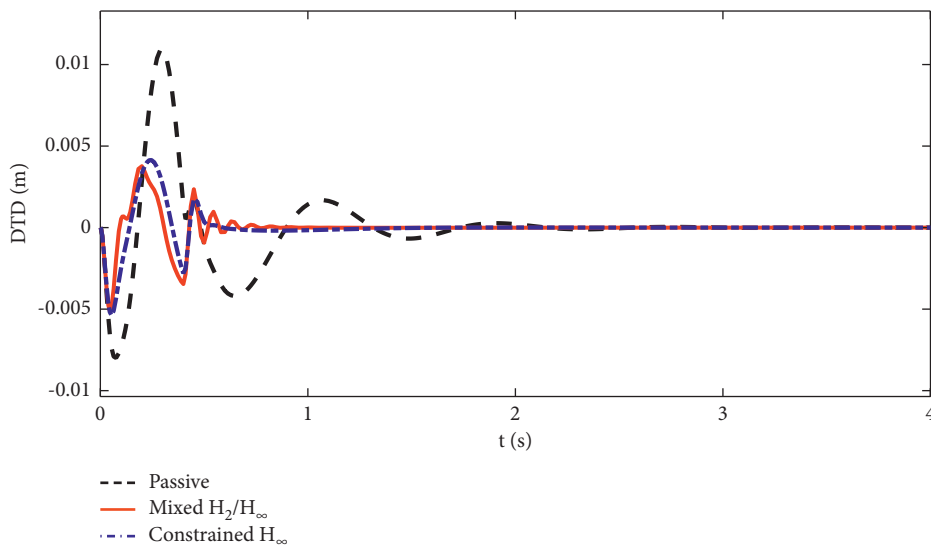
FIGURE 17: Bump dynamic tire displacement responses of suspension with parameter variation.

5. Conclusions

In this paper, a mixed H_2/H_∞-based robust guaranteed cost controller for the IWMD-EV active suspension system considering performance requirements and parameter variations is proposed. In the design process, the uncertain quarter-vehicle active suspension model is established; we regard the vertical body acceleration as the H_2 performance index and set other requirements output as the H_∞ performance index. Then, the proposed controller is designed using with Lyapunov stability theory. The proposed controller is simulated and compared with the constrained robust H_∞ controller. The results show that the proposed controller has good ride comfort and handling stability performance. In the future, we will further research and compare the effects of different advanced control methods for the active suspension system of IWMD-EV. In addition, we will expand the application of the proposed control method in other vehicle control fields, such as vehicle lateral dynamics and the active steering system.

Data Availability

The data used to support the findings of this study are included within the paper.

Conflicts of Interest

The authors declare that there are no conflicts of interest regarding the publication of this paper.

Acknowledgments

References

[1] X. Jin, Z. Yu, G. Yin, and J. Wang, "Improving vehicle handling stability based on combined AFS and DYC system via robust Takagi-Sugeno fuzzy control," *IEEE Transactions on Intelligent Transportation Systems*, vol. 19, no. 8, pp. 2696–2707, 2017.

[2] A. Goodarzi and E. Esmailzadeh, "Design of a VDC system for all-wheel independent drive vehicles," *IEEE*, vol. 12, no. 6, pp. 632–639, 2007.

[3] Y. Y. Luo and D. D. Tan, "Study on the dynamics of the in-wheel motor system," *IEEE Transactions on Vehicular Technology*, vol. 61, no. 8, pp. 3510–3518, 2012.

[4] Y. Chen, J. K. Hedrick, and K. Guo, "A novel direct yaw moment controller for in-wheel motor electric vehicles," *Vehicle System Dynamics*, vol. 51, no. 6, pp. 925–942, 2013.

[5] X. Jin, G. Yin, J. Chen, and N. Chen, "Robust guaranteed cost state-delayed control of yaw stability for four-wheel-independent-drive electric vehicles with active front steering system," *International Journal of Vehicle Design*, vol. 69, no. 1-4, pp. 304–323, 2015.

[6] B. Zheng and S. Anwar, "Yaw stability control of a steer-by-wire equipped vehicle via active front wheel steering," *Mechatronics*, vol. 19, no. 6, pp. 799–804, 2009.

[7] C. Poussot-Vassal, O. Sename, L. Dugard, and S. M. Savaresi, "Vehicle dynamic stability improvements through gain-scheduled steering and braking control," *Vehicle System Dynamics*, vol. 49, no. 10, pp. 1597–1621, 2011.

[8] V. Ivanov, D. Savitski, and B. Shyrokau, "A survey of traction control and antilock braking systems of full electric vehicles with individually controlled electric motors," *IEEE Transactions on Vehicular Technology*, vol. 64, no. 9, pp. 3878–3896, 2014.

[9] X. Jin, G. Yin, X. Zeng, and J. Chen, "Robust gain-scheduled output feedback yaw stability control for in-wheel-motor-driven electric vehicles with external yaw-moment," *Journal of the Franklin Institute*, vol. 355, no. 18, pp. 9271–9297, 2018.

[10] "C. Bridgestone, *Bridgestone Dynamic-Damping In-Wheel Motor Drive System*, http://enginuitysystems.com/files/In-Wheel_Motor.pdf, 2017.

[11] A. Kulkarni, S. A. Ranjha, and A. Kapoor, "A quarter-car suspension model for dynamic evaluations of an in-wheel electric vehicle," *Proceedings of the Institution of Mechanical Engineers - Part D: Journal of Automobile Engineering*, vol. 232, no. 9, pp. 1139–1148, 2018.

[12] F. Yang, L. Zhao, Y. Yu, and C. Zhou, "Analytical description of ride comfort and optimal damping of cushion-suspension for wheel-drive electric vehicles," *International Journal of Automotive Technology*, vol. 18, no. 6, pp. 1121–1129, 2017.

[13] W. Wang, M. Niu, and Y. Song, "Integrated vibration control of in-wheel motor-suspensions coupling system via dynamics parameter optimization," *Shock and Vibration*, vol. 2019, Article ID 3702919, 14 pages, 2019.

[14] Y.-J. Liu and H. Chen, "Adaptive sliding mode control for uncertain active suspension systems with prescribed performance," *IEEE Transactions on Systems, Man, and Cybernetics: Systems*, vol. 51, no. 10, pp. 6414–6422, 2021.

[15] J. Na, Y. Huang, X. Wu, S. Su, and G. Li, "Adaptive finite-time fuzzy control of nonlinear active suspension systems with input delay," *IEEE Transactions on Cybernetics*, vol. 50, no. 6, pp. 2639–2650, 2019.

[16] H. Li, J. Yu, C. Hilton, and H. Liu, "Adaptive sliding-mode control for nonlinear active suspension vehicle systems using T–S fuzzy approach," *IEEE Transactions on Industrial Electronics*, vol. 60, no. 8, pp. 3328–3338, 2012.

[17] H. D. Choi, C. K. Ahn, M. T. Lim, and M. K. Song, "Dynamic output-feedback H∞ control for active half-vehicle suspension systems with time-varying input delay," *International Journal of Control, Automation and Systems*, vol. 14, no. 1, pp. 59–68, 2016.

[18] S.-B. Choi and S.-S. Han, "H∞ control of electrorheological suspension system subjected to parameter uncertainties," *Mechatronics*, vol. 13, no. 7, pp. 639–657, 2003.

[19] P. Li, J. Lam, and K. C. Cheung, "Multi-objective control for active vehicle suspension with wheelbase preview," *Journal of Sound and Vibration*, vol. 333, no. 21, pp. 5269–5282, 2014.

[20] P. P. Khargonakar, I. R. Petersen, and K. Zhou, "Robust stabilization of uncertain linear systems: quadratic stability and H∞ control theory," *IEEE Transactions on Automatic Control*, vol. 35, no. 5, pp. 356–361, 1990.

[21] I. R. Petersen, B. D. O. Anderson, and E. A. Jonckheere, "A first principles solution to the non-singularH∞ control problem," *International Journal of Robust and Nonlinear Control*, vol. 1, no. 3, pp. 171–185, 1991.

[22] K. Jbilou, A. Messaoudi, and K. Tabaâ, "Some Schur complement identities and applications to matrix extrapolation methods," *Linear Algebra and Its Applications*, vol. 392, pp. 195–210, 2014.

[23] H. Liang, G. Liu, H. Zhang, and T. Huang, "Neural-network-based event-triggered adaptive control of nonaffine nonlinear multiagent systems with dynamic uncertainties," *IEEE Transactions on Neural Networks and Learning Systems*, vol. 32, no. 5, pp. 2239–2250, 2021.

[24] L. Liu, Y. Liu, A. Chen, S. Tong, and C. P. Chen, "Integral barrier Lyapunov function-based adaptive control for switched nonlinear systems," *Science China Information Sciences*, vol. 63, no. 3, pp. 1–14, 2020.

[25] H. Liang, X. Guo, Y. Pan, and T. Huang, "Event-triggered fuzzy bipartite tracking control for network systems based on distributed reduced-order observers," *IEEE Transactions on Fuzzy Systems*, vol. 29, no. 6, pp. 1601–1614, 2021.

[26] I. Ahmad, X. Ge, and Q.-L. Han, "Decentralized dynamic event-triggered communication and active suspension control of in-wheel motor driven electric vehicles with dynamic damping," *IEEE/CAA Journal of Automatica Sinica*, vol. 8, no. 5, pp. 971–986, 2021.

[27] X. Ge, I. Ahmad, Q.-L. Han, J. Wang, and X.-M. Zhang, "Dynamic event-triggered scheduling and control for vehicle active suspension over controller area network," *Mechanical Systems and Signal Processing*, vol. 152, Article ID 107481, 2021.

[28] X. Jin, J. Wang, Z. Yan, L. Xu, G. Yin, and N. Chen, "Robust vibration control for active suspension system of in-wheel-motor-driven electric vehicle via μ-synthesis methodology," *ASME Transactions Journal of Dynamic Systems, Measurement, and Control*, 2021.

[29] X. Jin, J. Wang, S. Sun, S. Li, J. Yang, and Z. Yan, "Design of constrained robust controller for active suspension of in-wheel-drive electric vehicles," *Mathematics*, vol. 9, no. 3, 2021.

Research Article

A Novel Rollover Warning Approach for Commercial Vehicles Using Unscented Kalman Filter

Junjian Hou,[1] Haizhu Lei,[1] Zhijun Fu ![ORCID],[1] Peixin Yuan,[1] Yuming Yin ![ORCID],[2] Heyang Feng,[1] Zihao Li,[1] Mingxu Zhang,[1] Minghui Cui,[1] and Yuqing Xu[1]

[1]*Henan Provincial Key Laboratory of Intelligent Manufacturing of Mechanical Equipment, Zhengzhou University of Light Industry, Zhengzhou, China*
[2]*College of Mechanical Engineering, Zhejiang University of Technology, Hangzhou, China*

Correspondence should be addressed to Zhijun Fu; fuzhijun2008@163.com

Roll responses of the semitrailer and the tractor provide higher lead time and characterise the roll instability of the commercial vehicles subjected to directional manoeuvres at highway speeds. This paper proposes a novel rollover index based on the synthesized roll angles of the tractor and trailer. Owing to the poor measurability, the unscented Kalman filter (UKF) algorithm is used to estimate the roll angle of the track and trailer, respectively. Meanwhile, different weight coefficients are considered in the rollover index to eliminate the influence of mutual coupling between the tractor and the trailer and improve the accuracy of the warning. For the practical implementation of the algorithm, a two-stage rollover warning method triggered by the video and audio is finally proposed to reduce the possibilities of false warnings. Co-simulation is presented to prove the validity of the proposed rollover warning approach.

1. Introduction

In heavy-duty semitrailer vehicles, owing to their heavy load, long vehicle body length, and high mass center (CG), the stability is worse compared with other vehicles. Rollover accident is a kind of traffic accident with high casualty rate, especially for semitrailer. The research on the rollover warning system firstly needs to construct a rollover index and then judge whether the rollover index reaches the threshold according to the real-time driving state of the vehicle [1–5].

The semitrailer rollover index can be roughly divided into two categories: static rollover index and dynamic rollover index. The static index mainly refers to the static stability coefficient (SSF) [6], which is defined as the ratio between the width of the half-track and the height of the center of gravity. Although the measurement and calculation are relatively simple, it does not perform well in the dynamic process. Dynamic rollover index is derived by considering the roll responses of different units of an articulated vehicle under dynamic manoeuvre and has been proved to be more reliable compared with the static index. Roll response amplification tendency (RAT) [7] is defined as the ratio of the peak lateral acceleration response of the trailer to the tractor, and its sensitivity to the parameter makes it impossible to reliably predict the rollover. The inherent defect of differential wheel slip (DWS) method [8], which is derived from the measurement of slip difference between left and right wheels, directly leads to poor warning reliability. In [9], the load transfer ratio (LTR) is used to evaluate the limit of dynamic roll stability of heavy vehicles based on lateral load transfer between the outer and inner tires. However, its practical application is too complex and rollovers' threshold is difficult to determine. Rakheja et al. [10] extend the LTR method by designing an improved online prediction algorithm called roll safety factor (RSF), which is defined as the ratio of load transfer of all axles except for the first axis with less contribution to the net restoring moment. The normalised roll response of semitrailer sprung mass (NRSSM) index [11], which incorporates the rearward amplification

tendency of the combination between the tractor and the trailer, has been proposed as an extension to RSF. The NRSSM index, based on roll responses of the semitrailer sprung mass and the tractor front and rear axles, is thus considered to be a more reliable rollover metric that may also yield reasonably good performance with respect to the sensitivity, reliability, and lead time. However, the roll angle is not easy to measure in practical application. In order to enhance the poor measurability of the dynamic rollover index, many estimation methods such as neural networks [12], Kalman filtering [13–16], and least square [17] are used to estimate the relevant key state variables in the rollover index online.

This study proposes a novel online rollover index based on the composite roll angles of the tractor and the trailer of semitrailer commercial vehicles. The unscented Kalman filter (UKF) algorithm is used to estimate the roll angle of the track and trailer, respectively. With combination of the rollover index and the semitrailer roll response, a two-stage early warning method triggered by video and audio is finally proposed for the actual algorithm implementation. The effectiveness of the proposed estimation method is illustrated under different directional manoeuvres using the TruckSim and simulation platform. The notable contributions of the study include (i) the synthesis of an rollover index based on the roll angles of the tractor and trailer to achieve higher accuracy and reliability, (ii) an UKF algorithm is used to estimate the roll angles of the tractor and trailer to enhance the measurability, and (iii) design of the two-stage warning method that relies only on roll response of the commercial vehicles and triggered by video and audio, which generally reduce the possibilities of false warnings.

The remainder of this paper is organized as follows. In Section 2, the seven-degree-of-freedom model of the semitrailer is given. A new rollover index is introduced in Section 3. Section 4 presents the unscented Kalman filter algorithm for estimating the roll angle of the semitrailer vehicle. The simulation results are shown in Section 5, and the conclusions for the whole paper are drawn in Section 6.

2. Vehicle Dynamics Model

In the actual driving process, the dynamic characteristics of the semitrailer are very complex. In this paper, we choose the commonly used five-axle tractor-semitrailer vehicle [18, 19] as the baseline commercial vehicle. In order to facilitate analysis, the three rear axles of the trailer are equivalent to one axle and make the following assumptions:

(1) The vehicle tire model is assumed to be linear

(2) The influence of suspension deformation and body roll on wheel steering and tire characteristics is not considered

(3) The longitudinal speed of the vehicle is constant, and the influence of aerodynamics and road slope is ignored

(4) The steering wheel angle is directly taken as the input of the vehicle model, and the left and right wheel angles are assumed to be approximately equal

(5) Taking the vehicle reference coordinate system as the reference, the model considers the vehicle lateral, yaw, roll, and hinged motion in four directions and ignores the vertical motion along the Z-axis and the pitch motion along the Y-axis

(6) Ignore the roll motion of the nonsuspension mass and its influence on the wheel

Based on the above assumptions, a single-track seven-degree-of-freedom (7-DOF) vehicle dynamics model is established as shown in Figure 1. The DOFS are yaw motion of the tractor, lateral motion of the tractor, roll motion of the tractor, yaw motion of the trailer, lateral motion of the trailer, roll motion of the trailer, and articulated motion of the tractor and the trailer.

Next, the detailed mathematical modeling process of the 7-DOF model is presented. The lateral force equation of the tractor is

$$\sum F_{Y1} = m_1 a_{y1} - m_{1s} a_y, \tag{1}$$

where a_y represents the centrifugal acceleration of the sprung mass of tractor and can be expressed as $a_y = (h_1 \cdot \dot{\phi}_1)' = h_1 \cdot \ddot{\phi}_1$; the corresponding lateral acceleration component is expressed as $a_{y1} = \dot{v}_1 + u_1 \omega_{r1}$.

Side slip angle of the tractor can be described as $\beta_1 = v_1/u_1$. With the assumption that the vehicle's longitudinal speed remains constant, i.e., $\dot{u}_1 = 0$, we obviously have $\dot{\beta}_1 = (v_1/u_1)' = \dot{v}_1/u_1$, $\dot{v}_1 = \dot{\beta}_1 \cdot u_1$. Then, (1) can be further rewritten as

$$\sum F_{Y1} = m_1 u_1 (\dot{\beta}_1 + \omega_{r1}) - m_{1s} h_1 \ddot{\phi}_1. \tag{2}$$

The moment of inertia of the tractor on the Z-axis can be described as

$$\sum M_{Z1} = I_{1zz} \dot{\omega}_{r1} - I_{1xz} \ddot{\phi}_1. \tag{3}$$

The moment of inertia of the tractor on the X-axis can be defined as

$$\sum M_{X1} = I_{1xx} \ddot{\phi}_1 + m_{1s} a_y h_1 - I_{1xz} \dot{\omega}_{r1}. \tag{4}$$

By substituting $a_y = (h_1 \cdot \dot{\phi}_1)' = h_1 \cdot \ddot{\phi}_1$ into equation (4), we have

$$\sum M_{X1} = (I_{1xx} + m_{1s} h_1^2) \ddot{\phi}_1 - I_{1xz} \dot{\omega}_{r1}. \tag{5}$$

The dynamic equations of the tractor can be obtained by synthesizing equations (2), (3), and (5), such that

$$\begin{cases} \sum F_{Y1} = m_1 u_1 (\dot{\beta}_1 + \omega_{r1}) - m_{1s} h_1 \ddot{\phi}_1 \\ \sum M_{Z1} = I_{1zz} \dot{\omega}_{r1} - I_{1xz} \ddot{\phi}_1 \\ \sum M_{X1} = (I_{1xx} + m_{1s} h_1^2) \ddot{\phi}_1 - I_{1xz} \dot{\omega}_{r1} \end{cases} \tag{6}$$

Similarly, the dynamic equations of the trailer can be derived as
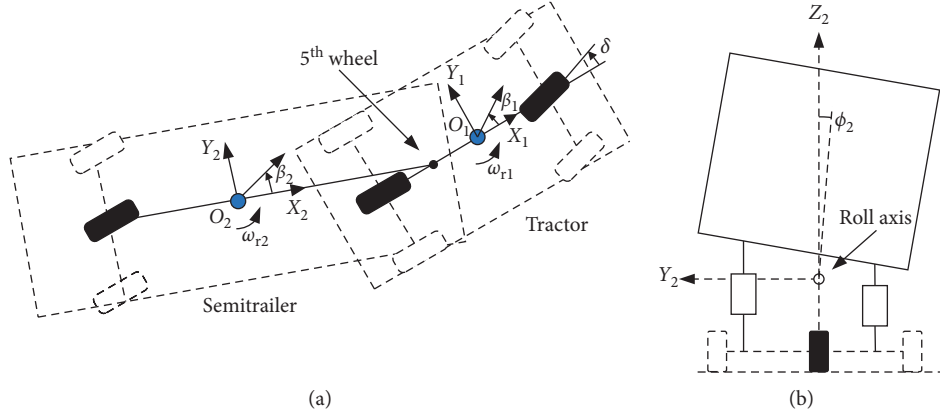
FIGURE 1: Semitrailer vehicle system: (a) top view of tractor semitrailer; (b) rear view of semitrailer.

$$\begin{cases} \sum F_{Y2} = m_2 u_2 (\dot{\beta}_2 + \omega_{r2}) - m_{2s} h_2 \ddot{\phi}_2 \\ \sum M_{Z2} = I_{2zz} \dot{\omega}_{r2} - I_{2xz} \ddot{\phi}_2 \\ \sum M_{X2} = (I_{2xx} + m_{2s} h_2^2)) \ddot{\phi}_2 - I_{2xz} \dot{\omega}_{r2} \end{cases} \tag{7}$$

Assuming that the front wheel angle and roll angle are small, the external force of the tractor can be expressed as

$$\begin{cases} \sum F_{Y1} = F_{y1} + F_{y2} + F_{y4} \\ \sum M_{Z1} = F_{y1} a - F_{y2} b - F_{y4} c \\ \sum M_{X1} = m_{1s} g h_1 \phi_1 + m_{1s} a_{yy1} h_1 - k_{r1} \phi_1 - c_1 \dot{\phi}_1 + k_{12} (\phi_2 - \phi_1) - F_{y4} h_{1c} \end{cases} \tag{8}$$

Furthermore, consider the case when the articulation angle is small; the resultant external force of the trailer can be described as

$$\begin{cases} \sum F_{Y2} = F_{y3} - F_{y4} \\ \sum M_{Z2} = -F_{y3} d - F_{y4} e \\ \sum M_{X2} = m_{2s} g h_2 \phi_2 + m_{1s} a_{yy2} h_2 - k_{r2} \phi_2 - c_2 \dot{\phi}_2 - k_{12} (\phi_2 - \phi_1) + F_{y4} h_{1c} \end{cases} \tag{9}$$

where a_{yy1} and a_{yy2} represent the sprung mass lateral acceleration of the tractor and semitrailer, respectively; $a_{yy1} = u_1 (\dot{\beta}_1 + \omega_{r1}) - h_1 \ddot{\phi}_1$.

In this paper, the linear tire model is adopted to analyse the force of each tire. The lateral force on each axis and the cornering force on each tire are assumed to be equal; the tire's cornering force can thus be depicted as

$$\begin{cases} F_{y1} = k_1 \alpha_1 \\ F_{y2} = k_2 \alpha_2 \\ F_{y3} = k_3 \alpha_3 \end{cases} \tag{10}$$

Using δ to represent the front wheel angle, then the tire slip angle is defined as

$$\begin{cases} \alpha_1 = \dfrac{v_1 + \omega_{r1} a}{u_1} - \delta = \beta_1 + \dfrac{a \omega_{r1}}{u_1} - \delta \\ \\ \alpha_2 = \dfrac{v_1 - \omega_{r1} b}{u_1} = \beta_1 - \dfrac{b \omega_{r1}}{u_1} \\ \\ \alpha_3 = \dfrac{v_2 - \omega_{r2} d}{u_2} = \beta_2 - \dfrac{d \omega_{r2}}{u_2} \end{cases} \tag{11}$$

In case that there is no speed difference between the tractor and the trailer, i.e., $u_1 = u_2 = u$, then the cornering force of each tire can be expressed as

$$\begin{cases} F_{y1} = k_1\left(\beta_1 + \dfrac{a\omega_{r1}}{u} - \delta\right) \\[2mm] F_{y2} = k_2\left(\beta_1 - \dfrac{b\omega_{r1}}{u}\right) \\[2mm] F_{y3} = k_3\left(\beta_2 - \dfrac{d\omega_{r2}}{u}\right) \end{cases} \tag{12}$$

Combining with the above analysis, the full vehicle dynamics equation of the semitrailer shown in Figure 1 is shown as follows:

$$\begin{cases} m_1 u\left(\dot{\beta}_1 + \omega_{r1}\right) - m_{1s}h_1\ddot{\phi}_1 = k_1\left(\beta_1 + \dfrac{a\omega_{r1}}{u} - \delta\right) + k_2\left(\beta_1 - \dfrac{b\omega_{r1}}{u}\right) + F_{y4} \\[3mm] I_{1zz}\dot{\omega}_{r1} - I_{1xz}\ddot{\phi}_1 = ak_1\left(\beta_1 + \dfrac{a\omega_{r1}}{u} - \delta\right) - bk_2\left(\beta_1 - \dfrac{b\omega_{r1}}{u}\right) - cF_{y4} \\[3mm] \left(I_{1xx} + m_{1s}h_1^2\right)\ddot{\phi}_1 - I_{1xz}\dot{\omega}_{r1} = m_{1s}gh_1\phi_1 + m_{1s}h_1\left[u\left(\dot{\beta}_1 + \omega_{r1}\right) - h_1\ddot{\phi}\right]_1 - k_{r1}\phi_1 - c_1\dot{\phi}_1 + k_{12}\left(\phi_2 - \phi_1\right) - F_{y4}h_{1c} \\[3mm] m_2 u\left(\dot{\beta}_2 + \omega_{r2}\right) - m_{2s}h_2\ddot{\phi}_2 = k_3\left(\beta_2 - \dfrac{d\omega_{r2}}{u}\right) - F_{y4} \\[3mm] I_{2zz}\dot{\omega}_{r2} - I_{2xz}\ddot{\phi}_2 = -dk_3\left(\beta_2 - \dfrac{d\omega_{r2}}{u}\right) - eF_{y4} \\[3mm] \left(I_{2xx} + m_{2s}h_2^2\right)\ddot{\phi}_2 - I_{2xz}\dot{\omega}_{r2} = m_{2s}gh_2\phi_2 + m_{2s}h_2\left[u\left(\dot{\beta}_2 + \omega_{r2}\right) - h_2\ddot{\phi}_2\right] - k_{r2}\phi_2 - c_2\dot{\phi}_2 - k_{12}\left(\phi_2 - \phi_1\right) + F_{y4}h_{2c} \\[3mm] \dot{\beta}_1 - \dot{\beta}_2 - \dfrac{h_{1c}}{u}\ddot{\phi}_1 + \dfrac{h_{2c}}{u}\ddot{\phi}_2 - \dfrac{c}{u}\dot{\omega}_{r1} - \dfrac{e}{u}\dot{\omega}_{r2} + \omega_{r1} - \omega_{r2} = 0 \end{cases} \tag{13}$$

3. Rollover Index Design

Rollover index is a real-time dynamic factor indicating the likelihood of a rollover and is used to trigger the controller to prevent rollover. It is well known that the most basic indicator of rover index is the lateral load transfer ratio (LTR), which is defined as the normal load between the left and right tires caused by the rolling motion of the vehicle, such that

$$LTR = \frac{F_L - F_R}{F_L + F_R}, \tag{14}$$

where R denotes the rollover index.

Clearly, from equation (14), we know that rollover index R varies in the interval $[-1, 1]$. When it is either left side or right side of the wheel lift-off, the extreme value is reached, and for a perfectly symmetric commercial vehicle with the straight manoeuvres, it is 0. For semitrailers, since the first

axle (the front axle of the tractor) does not contribute much to the net restoring torque [11], the first axle is thus omitted from the LTR, so the roll safety factor (RSF) is defined as follows:

$$RSF = \left| \frac{\sum_{j=1}^{m}\left(FL_j - FR_j\right)}{\sum_{j=1}^{m}\left(FL_j + FR_j\right)} \right|, \tag{15}$$

where m represents the number of axles remaining after removing the first axle.

However, equation (15) cannot be applied directly in practice due to the fact that the vertical force cannot be obtained by actual measurement. Therefore, it is necessary to propose a rollover index with simple measurement, low cost, and accurate warning, and equation (15) can be used as theoretical reference value to compare and evaluate the proposed rollover index. In [11], the performance characteristics of various potential measures related to onset of a manoeuvre-induced rollover are investigated in terms of

their reliability, measurability, and lead time, where the results suggest that roll angle is directly related to the relative rollover condition and may thus be considered as the most reliable measure, irrespective of the vehicle configuration and design and operating variables. In view of this fact, this paper proposes a new roll index RI as follows:

$$RI = x \times RI_1 + y \times RI_2, \tag{16}$$

with

$$
\begin{aligned}
RI_1 &= \frac{2h_1}{gl_{w1}}a_{y1} + \frac{2h_1}{l_{w1}}\phi_1, \\
RI_2 &= \frac{2h_2}{gl_{w2}}a_{y2} + \frac{2h_2}{l_{w2}}\phi_2,
\end{aligned} \tag{17}
$$

where l_{w1} and l_{w2} represent the wheelbase of the tractor and the trailer, a_{y1} and a_{y2} denote the lateral acceleration of the tractor and the trailer, respectively, and x and y represent different weight coefficients of the tractor and the trailer contributing to the total rollover index.

Remark 1. Note from (17) that the rollover index mainly depends on the state variables as $a_{y1}, a_{y2}, \phi_1, \phi_2, h_1$, and h_2. Lateral accelerations a_{y1} and a_{y2} can be obtained via a sensor measurement. Center of gravity height h is usually assumed to be a prior constant [20, 21] or can be estimated online [22]. However, there is no effective method available to measure roll angles ϕ_1 and ϕ_2. The commonly used way is to measure the roll angular velocity via the gyroscope, and then, the roll angular velocity is integrated to finally obtain the roll angle, but this method could enlarge the gain error of the sensor and lead to inaccurate results. Therefore, in order to obtain the roll angle of the tractor and trailer, this paper will use UKF algorithm to estimate the roll angle of the

tractor and trailer online in real time, respectively. The detailed analytical results will be given in Section 4.

4. Unscented Kalman Filter Estimate Algorithm

Kalman filter is one of the most important and common estimation algorithms. Extend Kalman filter (EKF), in which state distribution is propagated analytically by first-order linearization of nonlinear systems, has been developed as an extension to the Kalman filter. However, the posterior mean and covariance may be corrupted in EKF. The UKF [23], which is a derivative-free alternative to EKF, overcomes this problem by using a deterministic sampling approach. The state distribution is represented using a minimal set of carefully chosen sample points called sigma points. UKF has been proved to be a more effective way to deal with the nonlinear state estimation problem. Details of the estimation of roll angle based on UKF are described below.

Firstly, the estimation model is established according to equation (13). Select the vectors in terms with the vehicle states and observed measurement as $x = [\phi_1, \dot{\phi}_1, \ddot{\phi}_1, \phi_2, \dot{\phi}_2, \ddot{\phi}_2]^T$ and $y = [\dot{\phi}_1, \ddot{\phi}_1, \dot{\phi}_2, \ddot{\phi}_2]^T$, respectively. The parameters for simulation are set as follows: process noise covariance matrix $Q = 1e8 \times I_4$, measurement noise covariance matrix $R = 1 \times I_3$, initial state of the system $x_0 = [0, 0, 0, 0, 0, 0]^T$, and initial covariance matrix $P_0 = I_6$, where I represents the unit matrix.

Then, the state space equation of the system is derived as follows:

$$
\begin{aligned}
x_k &= f_k(x_{k-1}, u_{k-1}) + w_k, \\
y_k &= Hx_{k-1} + v_k,
\end{aligned} \tag{18}
$$

with

$$
f_k(x_{k-1}, u_{k-1}) =
\begin{bmatrix}
\left(I_{1xx}x(3) - m_1 a_{y1} h_1 + CR_1(x(2) + t\Delta nTq \times hx(3))\right)/(m_1 gh_1 - KR_1) \\
x(2) + \Delta T \times x(3) \\
x(3) \\
\left(I_{2xx}x(6) - m_2 a_{y2} h_2 + CR_2(x(5) + t\Delta nTq \times hx(6))\right)/(m_2 gh_2 - KR_2) \\
x(5) + \Delta T \times x(6) \\
x(6)
\end{bmatrix}, \tag{19}
$$

$$
H =
\begin{bmatrix}
0 & 1 & 0 & 0 & 0 & 0 \\
0 & 0 & 1 & 0 & 0 & 0 \\
0 & 0 & 0 & 0 & 1 & 0 \\
0 & 0 & 0 & 0 & 0 & 1
\end{bmatrix}, \tag{20}
$$

where $f(x, u)$ is the state transition equation, H is the coefficient matrix of the observation equation, and w_k and v_k denote process noise and observation noise, respectively, which are assumed to be Gaussian white noise. The basic flowchart of the UKF algorithm is shown in Figure 2.

The statistical characteristics of y are calculated by unscented transform (UT) when state mean $\overline{x}$ and variance P are known. The sigma point is selected using a symmetrical distribution sampling strategy.

Calculate $2n + 1$ sigma sampling points, such that

$$X^{(0)} = \overline{X}, i = 0,$$

$$X^{(i)} = \overline{X} + (\sqrt{(n+\lambda)P})_i, i = 1 \sim n, \qquad (21)$$

$$X^{(i)} = \overline{X} - (\sqrt{(n+\lambda)P})_i, i = n + 1 \sim 2n,$$

where $(\sqrt{P})_i$ represents the ith column of the square root of a matrix.

Calculate the corresponding weight of the sampling point as

$$\omega_m^{(0)} = \frac{\lambda}{n+\lambda},$$

$$\omega_c^{(0)} = \frac{\lambda}{n+\lambda} + (1 - \alpha^2 + \beta), \qquad (22)$$

$$\omega_m^{(i)} = \omega_c^{(i)} = \frac{\lambda}{2(n+\lambda)}, \quad 5i = 1 \sim 2n,$$

where m represents the mean, c represents the covariance, and i represents the number of sampling points. Parameter $\lambda = \alpha^2(n+\kappa) - n$ is the scaling factor, which can reduce the total prediction error. The small positive number α controls

the distribution of sampling points and is selected as 0.01. Parameter κ is usually taken as 0, β is the nonnegative weighting coefficient, and the value of 2 is the best in Gaussian distribution.

On the premise of the above unscented transformation, the process of UKF is summarized as follows:

Step 1: obtain sigma points and corresponding weights by unscented transformation:

$$X^{(i)}(k|k) = [\widehat{X}(k|k)\widehat{X}(k|k)$$
$$+ \sqrt{(n+\lambda)P(k|k)}\,\widehat{X}(k|k) - \sqrt{(n+\lambda)P(k|k)}].$$
$$(23)$$

Step 2: one-step prediction for sigma points:

$$X^{(i)}(k+1|k) = f[k, X^{(i)}(k|k)]. \qquad (24)$$

Step 3: perform a weighted summation on the one-step prediction of the sigma point to obtain the one-step prediction of the system state quantity and the covariance matrix:

$$\widehat{X}(k+1|k) = \sum_{i=0}^{2n} \omega^{(i)} X^i(k+1|k),$$

$$P(k+1|k) = \sum_{i=0}^{2n} \omega^{(i)} \left[\widehat{X}(k+1|k) - X^{(i)}(k+1|k)\right]\left[\widehat{X}(k+1|k) - X^{(i)}(k+1|k)\right]^T + Q. \qquad (25)$$

Step 4: according to the one-step predicted value, use the unscented transformation again to generate a new sigma point set:

$$X^{(i)}(k+1|k) = \begin{bmatrix} \widehat{X}(k+1|k) \\ \widehat{X}(k+1|k) + \sqrt{(n+\lambda)P(k+1|k)} \\ \widehat{X}(k+1|k) - \sqrt{(n+\lambda)P(k+1|k)} \end{bmatrix}. \qquad (26)$$

Step 5: substitute the newly obtained sigma point set into the observation function to obtain the predicted value of the sigma point set:

$$Z^{(i)}(k+1|k) = h[X^{(i)}(k+1|k)]. \qquad (27)$$

Step 6: perform a weighted summation of the predicted values of the observation values of the sigma point set obtained in the fifth step to obtain the mean and covariance of the system prediction, such that

$$\overline{Z}(k+1|k) = \sum_{i=0}^{2n} \omega^{(i)} Z^{(i)}(k+1|k),$$

$$P_{z_k z_k} = \sum_{i=0}^{2n} \omega^i \left[Z^{(i)}(k+1|k) - \overline{Z}(k+1|k)\right]\left[Z^{(i)}(k+1|k) - \overline{Z}(k+1|k)\right]^T + R, \qquad (28)$$

$$P_{x_k z_k} = \sum_{i=0}^{2n} \omega^i \left[X^{(i)}(k+1|k) - \overline{Z}(k+1|k)\right]\left[Z^{(i)}(k+1|k) - \overline{Z}(k+1|k)\right]^T.$$
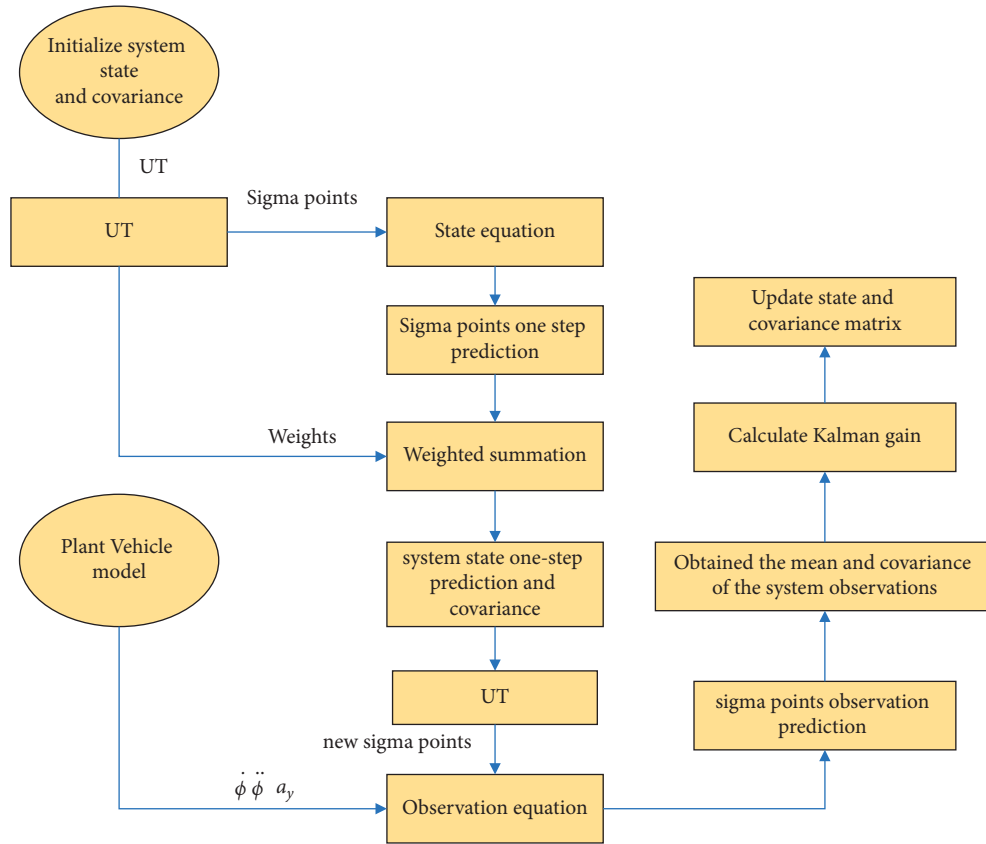
FIGURE 2: UKF algorithm flowchart.

Step7: calculate Kalman gain:

$$K(k + 1) = P_{x_k z_k} P_{z_k z_k}^{-1}. \tag{29}$$

Step8: update the state and covariance matrix of the system:

$$\hat{X}(k + 1|k + 1) = \hat{X}(k + 1|k) + K(k + 1)[Z(k + 1) - \hat{Z}(k + 1|k)].$$

$$P(k + 1|k + 1) = P(k + 1|k) + K(k + 1)P_{z_k z_k} K^T(k + 1), \tag{30}$$

5. Simulation and Implementation Discussion

5.1. Simulation. The proposed rollover warning approach for commercial vehicles using unscented Kalman filter estimation algorithm is implemented in the TruckSim software together with Matlab/Simulink, where the co-simulation diagram is shown in Figure 3. The numbers①-④indicate the selected vehicle type and the different driving condition of the vehicle and represent the relevant information of the tractor and trailer, respectively, these four parts constitute the semitrailer model in TruckSim, which is then sent to Simulink through ⑤ and conduct a co-simulation between ⑥ and ⑦; the final simulation results are shown in⑧. A semitrailer model with the parameters listed in Table 1 is built from TruckSim library.

Two different manoeuvres with two different steering inputs corresponding two different constant forward speeds

are performed in this paper to validate the proposed approach. Detailed simulation analysis is carried out as follows.

In the first manoeuvre, the semitrailer is simulated with a steering input, as shown in Figure 4, at the initial longitudinal velocity (70 *km/h*). Roll angle estimation results are illustrated in Figure 5. The above simulation results show that when the unscented Kalman filter algorithm is used to estimate the roll angle of tractor and trailer simultaneously, the estimation result of trailer is more accurate, but the estimation error of tractor is smaller. This may be due to the coupling effect between the trailer and the tractor. Fortunately, this will not have much impact on the result of rollover warning because the rollover of semitrailer is mainly caused by the rollover angle of the trailer, which can be eliminated by setting the different weight of tractor and trailer rollover angle in the total rollover index reasonably. Therefore, by
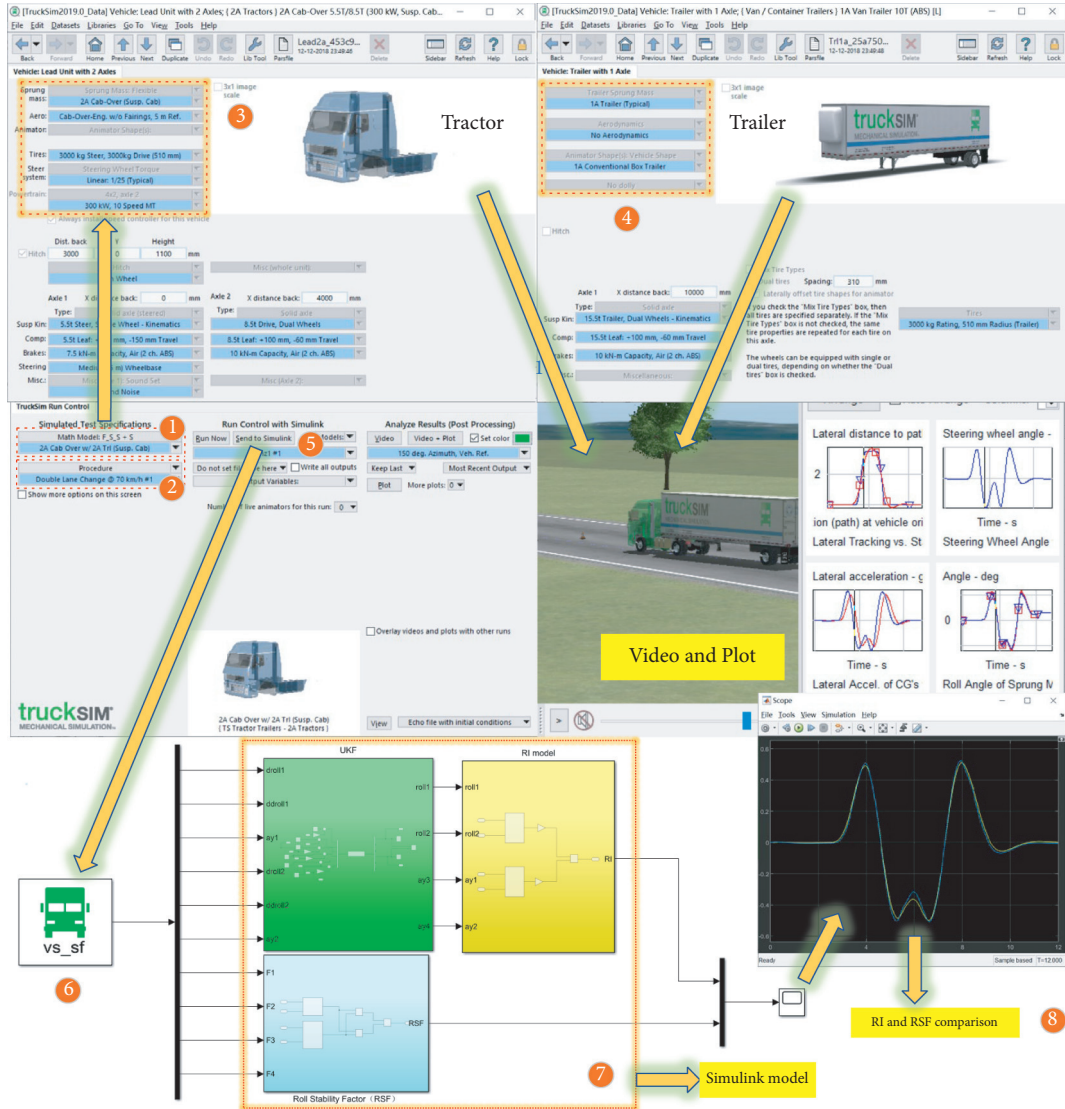
Figure 3: Matlab/TruckSim co-simulation diagram.

Table 1: Semitrailer vehicle parameters used in simulation.

Parameter	Value/unite
Tractor sprung mass (m_s), trailer unsprung mass (m_u), tractor roll moment of sprung mass(I_{1xx}), trailer roll moment of sprung mass(I_{2xx}), tractor CG height (h_1), trailer CG height (h_2), tractor wheelbase (l_{s1}), trailer wheelbase (l_{s3}), and suspension damper (b_s)	4455 kg, 6000 kg, 2283.9 kg*m^2, 10140 kg*m^2, 1.175 m, 1.935 m, 2.03 m, 1.863 m, and 1000N*s/m

appropriately selecting the weights of tractors and trailers, respective, then the roll index RI can be obtained as follows:

$$RI = 0 \cdot 3 \times RI_1 + 0 \cdot 7 \times RI_2. \tag{31}$$

Substitute the previously estimated roll angle results into the rollover index (31), and compare with the rollover index obtained from the TruckSim using equation (15). It can be seen from the comparison results in Figure 6 that the proposed rollover warning index can well track the given

reference value, which indicates the effectiveness of the proposed method.

In the second manoeuvre, the semitrailer is simulated with a steering input, as shown in Figure 7, at the initial longitudinal velocity (50 km/h). The simulation results are shown in Figures 8 and 9.

Note that the proposed rollover index still demonstrates good performance when encountering time-varying longitudinal speed and different steering inputs. The above simulation results show the effectiveness of the proposed
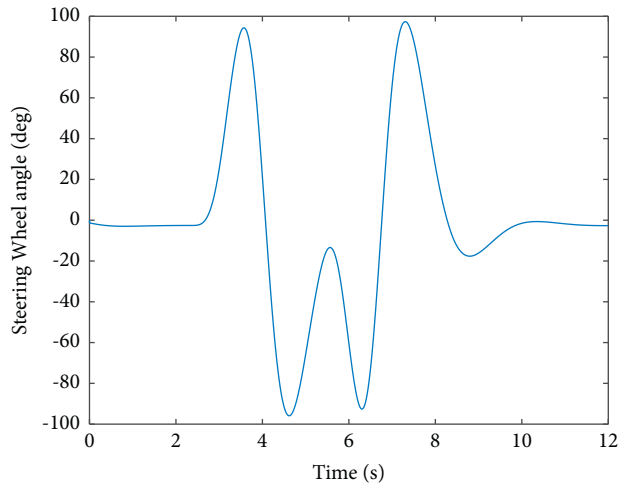
FIGURE 4: Steering input.

(a)

(b)
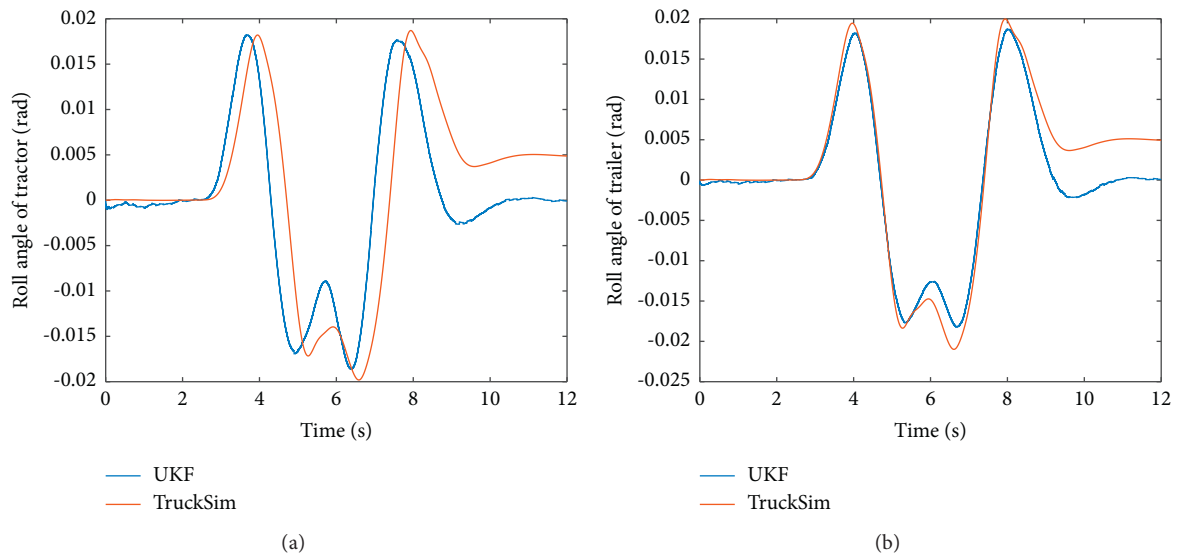
FIGURE 5: Roll angle estimation results. (a) Tractor roll angle estimation result. (b) Trailer roll angle estimation result.
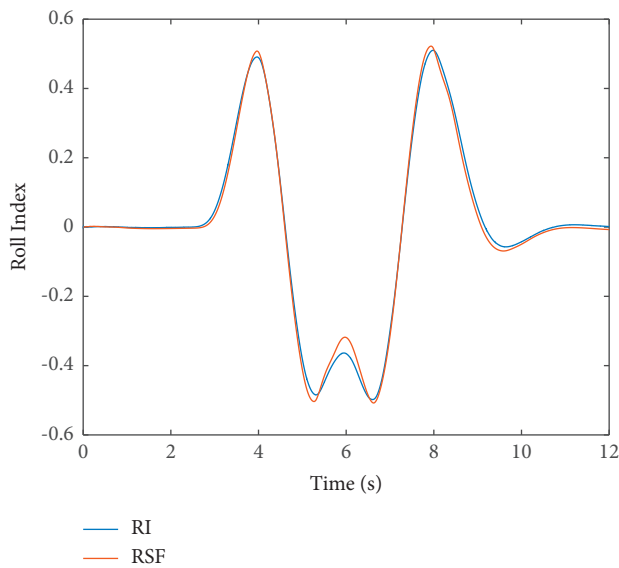
FIGURE 6: Comparison results of proposed RI and RSF.
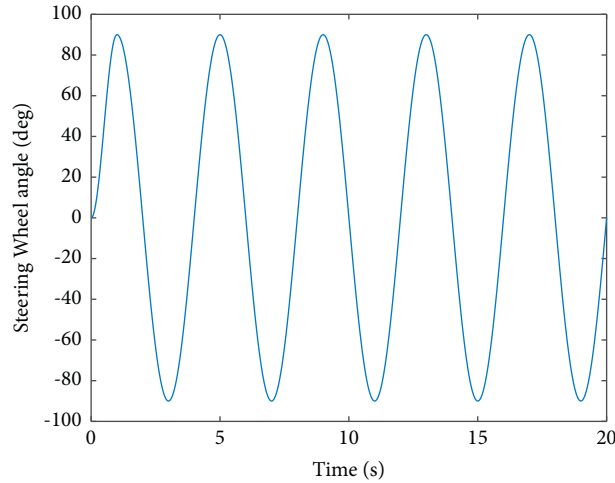
FIGURE 7: Steering input.

(a)

(b)
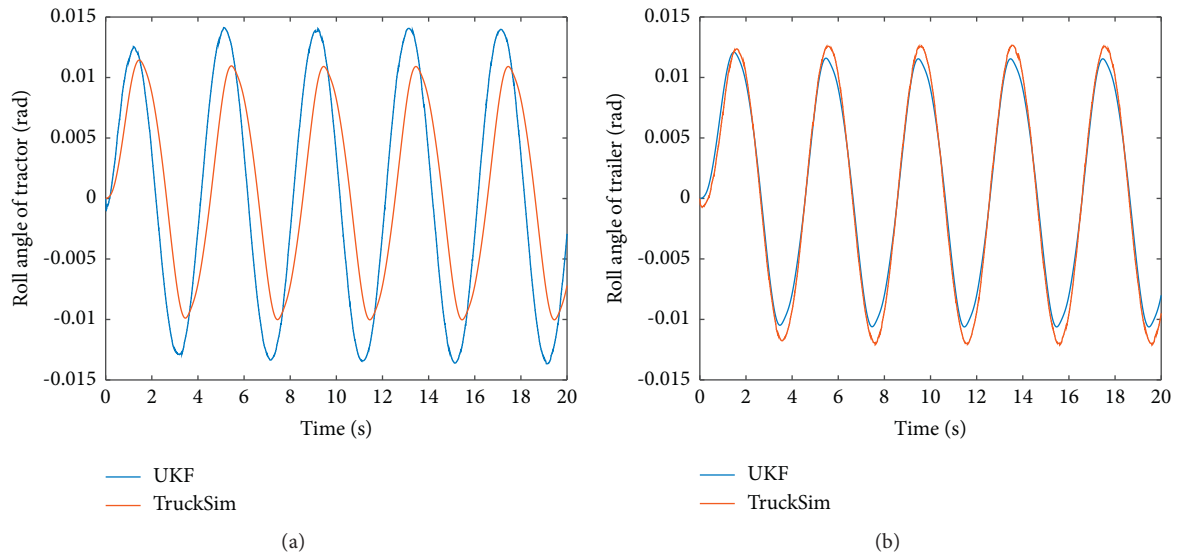
FIGURE 8: Roll angle estimation results. (a) Tractor roll angle estimation result. (b) Trailer roll angle estimation result.

rollover index, which will lay a prerequisite foundation for the future antiroll control design.

5.2. Implementation Discussion. The implementation of the proposed rollover warning approach for commercial vehicles mainly includes the following three aspects:

Step 1: calculation onset of potential rollover through online monitoring of the designed rollover index

Step 2: compare with the set threshold and trigger the warning signal to the driver

Step 3: a corrective action to be acted by the driver

Since the proposed rollover index ignores the contribution of the front axle of the tractor to the restoring torque, there may be some errors in the prediction of an impending rollover. In view of this fact, a two-stage rollover warning

approach based on online monitoring of the proposed rollover index and the roll angle of the trailer is adopted, as shown in Figure 10.

In Figure 10, ϕ_2 represents the roll angle of the trailer. The reason why roll angle ϕ_2 is used as the second evaluation index here is that roll angle ϕ_2 plays a dominant role in the roll of the semitrailer. If the roll angle ϕ_2 exceeds the threshold, the probability of the semitrailer rolling is very high. The minimum and mean values of the rollover thresholds M1, N1, M2, and N2 can be obtained corresponding to the design and operating parameters of related commercial vehicle. Minimum values can be implemented to trigger the visual warning, which would be followed by audio warning when the mean threshold values are reached.

The first state warning is triggered only if both measurements exceed their respective initial threshold limits, which will reduce the possibility of early false warnings.
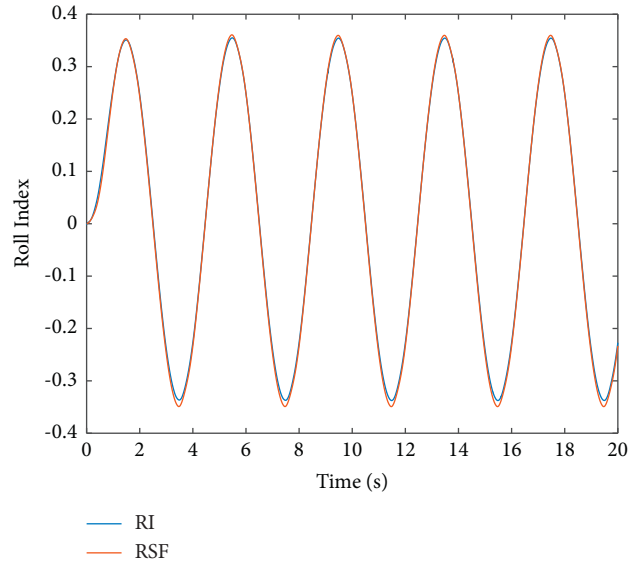
FIGURE 9: Comparison results of proposed RI and RSF.
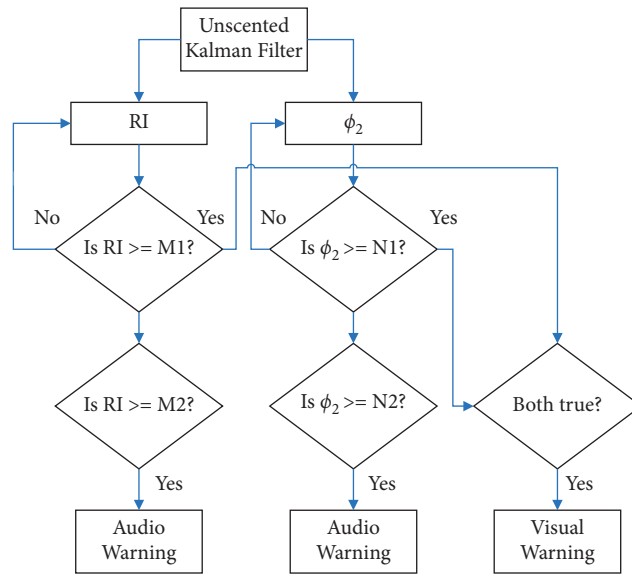
FIGURE 10: A two-stage rollover warning approach.

When either of the two measurements exceeds the final threshold limit, a second-stage warning is generated regardless of the other measurements. This would enhance the timeliness and reliability of warning.

6. Conclusion

The roll responses of a commercial vehicles form the essential basis for developing a strategy for predicting impending roll instability. This study reported a novel rollover index based on the roll angle of the tractor and the trailer of a semitrailer. To overcome the poor measurability and sensitivity to variations in vehicle design and operating parameters, unscented Kalman filter is used to estimate the roll angles in the rollover index online. In addition, different weights in terms of roll angles of the tractor and the trailer are considered to overcome the influence of coupling between the tractor and the trailer. Finally, a two-stage rollover warning method is present. Co-simulation results verify the effectiveness of the proposed rollover warning approach. Based on the rollover warning results, a more effective rollover prevention system for heavy commercial vehicles will be developed in the future research.

Nomenclature

m_1:   Tractor mass (kg)
m_2:   Trailer mass (kg)
m_{1s}:   Tractor sprung masses (kg)
m_{2s}:   Trailer sprung masses (kg)

u: Longitudinal speed of the vehicle (m/s)

β_1:   Tractor side slip angle (rad)

β_2:   Trailer side slip angle (rad)

ω_{r1}:   Tractor yaw rate (rad/s)

ω_{r2}:   Trailer yaw rate (rad/s)

h_1:   The distance from the center of mass of the tractor to its roll axis (m)

h_2:   The distance from the center of mass of the trailer to its roll axis (m)

h_{1c}:   The distance from the articulation point to the tractor roll axis (m)

h_{2c}:   The distance from the articulation point to the trailer roll axis (m)

ϕ_1:   Tractor roll angle (rad)

ϕ_2:   Trailer roll angle (rad)

k_1:   Tractor front axle cornering stiffness (N/rad)

k_2:   Tractor rear axle cornering stiffness (N/rad)

k_3:   Trailer axle cornering stiffness (N/rad)

k_{r1}:   Tractor roll stiffness (N $*$ m/rad)

k_{r2}:   Trailer roll stiffness (N $*$ m/rad)

k_{12}:   The fifth axle roll stiffness (N $*$ m/rad)

c_1:   Tractor roll damping (N $*$ m $*$ s/rad)

c_2:   Trailer roll damping (N $*$ m $*$ s/rad)

a: The distance from the front axle to the center of mass of the tractor (m)

b: The distance from the rear axle to the center of mass of the tractor (m)

c: The distance from the articulated point to the center of mass of the tractor (m)

d: The distance from the rear axle to the center of mass of the trailer (m)

e: The distance from the articulated point to the center of mass of the trailer (m)

I_{1xx}:   The moment of inertia of the tractor around the X-axis (kg $*$ m^2)

I_{2xx}:   The moment of inertia of the trailer around the X-axis (kg $*$ m^2)

I_{1zz}:   The moment of inertia of the tractor around the Z-axis (kg $*$ m^2)

I_{2zz}:   The moment of inertia of the trailer around the Z-axis (kg $*$ m^2)

I_{1xz}:   The yaw product of inertia of the tractor around the center of mass (kg $*$ m^2)

I_{2xz}:   The yaw product of inertia of the trailer around the center of mass (kg $*$ m^2).

Data Availability

The underlying data supporting the results of the study can be obtained from the corresponding author upon request.

Conflicts of Interest

The authors declare that there are no conflicts of interest regarding the publication of this article.

References

[1] Y. He, X. Yang, and X. Lu, "A review of anti-rollover prediction and control technologies for heavy-duty vehicles," *Journal of Transport Information and Safety*, vol. 37, no. 4, pp. 1–9, 2019.

[2] Z. Ye, W. Xie, Y. Yin, and Z. Fu, "Dynamic rollover prediction of heavy vehicles considering critical frequency," *Automotive Innovation*, vol. 3, no. 3, pp. 158–168, 2020.

[3] K. Shao, J. Zheng, B. Deng, K. Huang, and H. Zhao, "Active steering control for vehicle rollover risk reduction based on slip angle estimation," *IET Cyber-systems and Robotics*, vol. 2, no. 3, pp. 132–139, 2020.

[4] S. Zhang, S. Bei, B. Li, Y. Zhang, and X. Zhang, "Simulation analysis of vehicle rollover model based on energy method," *International Core Journal of Engineering*, vol. 5, no. 12, pp. 191–200, 2019.

[5] K. Shao, J. Zheng, and K. Huang, "Robust active steering control for vehicle rollover prevention," *International Journal of Modelling, Identification and Control*, vol. 32, no. 1, 2019.

[6] R. Rajamani, *Vehicle Dynamics and Control*, Springer, Berlin, Germany, 2012.

[7] E. Gindy, "An overview of performance measures for heavy commercial vehicles in north America," *Int. J. of Vehicle Design*, vol. 16, no. 4–5, pp. 441–463, 1995.

[8] L. Palcovics, A. Semsey, and E. Gerum, "Rollover prevention system for commercial vehicles-additional sensorless function of electronic braking system," *Intl. Symp. on Advanced Vehicle Control-AVEC*, vol. 98, pp. 311–316, 1998.

[9] Z. Jin, J. Li, and Y. Huang, "Study on rollover index and stability for a triaxle bus," *Chinese Journal of Mechanical Engineering*, vol. 32, no. 1, pp. 1–15, 2019.

[10] S. Rakheja, A. Ahmed, and P. Liu, "Detection of dynamic roll instability of heavy vehicles for open loop rollover control," *Heavy Vehicle and Highway Dynamics, SAE SP-*, vol. 1308, pp. 105–112, 1997.

[11] S. Kar, S. Rakheja, and A. K. W. Ahmed, "A normalised measure of relative roll instability for open-loop rollover warning," *International Journal of Heavy Vehicle Systems*, vol. 13, no. 1-2, pp. 74–97, 2006.

[12] L. P. González, S. S. Sánchez, J. G. Guzman, and M. J. Boada, "Simultaneous estimation of vehicle roll and sideslip angles through a deep learning approach," *Sensors*, vol. 20, no. 13, 2020.

[13] V. M. Leandro, B. Beatriz, B. María, G. Antonio, and D. Vicente, "A sensor fusion method based on an integrated neural network and kalman filter for vehicle roll angle estimation," *Sensors*, vol. 16, no. 9, 2016.

[14] L. Zhao, Z. Liu, and B. Shen, "Vehicle velocity and roll angle estimation with road and friction adaptation for four-wheel

independent drive electric vehicle," *Mathematical Problems in Engineering*, vol. 2014, Article ID 801628, 11 pages, 2014.

[15] M. Mazhar, M. Khan, A. Bhatti, and N. Naseer, "A novel roll and pitch estimation approach for a ground vehicle stability improvement using a low cost IMU," *Sensors*, vol. 20, no. 2, pp. 1–30, 2020.

[16] L. Xiong, X. Xia, Y. Lu et al., "IMU-based automated vehicle body sideslip angle and attitude estimation aided by GNSS using parallel adaptive kalman filters," *IEEE Transactions on Vehicular Technology*, vol. 69, no. 10, Article ID 10668, 2020.

[17] C. Cheng and D. Cebon, "Parameter and state estimation for articulated heavy vehicles," *Vehicle System Dynamics*, vol. 49, no. 1-2, pp. 399–418, 2011.

[18] V. T. Vu, O. Sename, L. Dugard, and P. Gaspar, "H ∞/LPV controller design for an active anti-roll bar system of heavy vehicles using parameter dependent weighting functions," *Heliyon*, vol. 5, no. 6, Article ID e01827, 2019.

[19] Z. Jin, C. Wang, and L. Zhang, "Rollover prevention for a heavy vehicle using optimised slide mode steering control," *International Journal of Heavy Vehicle Systems*, vol. 26, pp. 3-4, 2019.

[20] F. Yakub and R. Mori, "Heavy vehicle stability and rollover prevention via switching model predictive control," *Int. J. Innovative Computing, Information and Control*, vol. 11, no. 5, pp. 1751–1764, 2015.

[21] R. Kamnik, F. Boettiger, and K. Hunt, "Roll dynamics and lateral load transfer estimation in articulated heavy freight vehicles," *Proceedings of the Institution of Mechanical Engineers - Part D: Journal of Automobile Engineering*, vol. 217, no. 11, pp. 985–997, 2003.

[22] X. Huang and J. Wang, "Longitudinal motion based light-weight vehicle payload parameter real-time estimations," *Trans. ASME, J. Dyn. Syst. Meas. Control*, vol. 135, no. 1, pp. 1–10, 2013.

[23] Y. Zhang, J. Ma, X. Zhao, X. Liu, K. Zhang, and X. Shao, "A modified unscented kalman filter combined with ant lion optimization for vehicle state estimation," *Mathematical Problems in Engineering*, vol. 2021, Article ID 8847075, 21 pages, 2021.

Research Article

A Cooperative Positioning Method of Connected and Automated Vehicles with Direction-of-Arrival and Relative Distance Fusion

Faan Wang,[1] Liwei Xu,[1] Xianjian Jin,[1,2] Guodong Yin [ID],[1] and Ying Liu[1,3]

[1]*School of Mechanical Engineering, Southeast University, Nanjing 211189, China*
[2]*School of Mechanical Engineering and Automation, Shanghai University, Shanghai 200444, China*
[3]*School of Cyber Science and Engineering, Southeast University, Nanjing 211189, China*

Correspondence should be addressed to Guodong Yin; ygd@seu.edu.cn

The rapid development of science and technology has created favorable conditions for Connected and Automated Vehicles (CAVs). Accurate localization is one of the fundamental functions of CAV to realize some advanced operations such as vehicle platooning. However, complicated urban traffic environments, such as the flyover, significantly influence vehicular positioning accuracy. The inability of CAV to accurately perceive self-localization information has become an urgent issue to be addressed. This paper proposed a novel cooperative localization method by introducing the relative Direction-of-Arrival (DOA) and Relative Distance (RD) into CAV to improve the localization accuracy of CAV in the multivehicle environment. First, the three-dimensional positioning error model of the host vehicle concerning adjacent vehicles in azimuth angle and pitch angle and intervehicle distances under the vehicle-to-vehicle communication was established. Second, two least-squares estimation algorithms, linear and nonlinear, are established to decrease the position errors by combining relative DOA and RD measurement information. To verify the proposed algorithm's effect, the PreScan-Simulink joint simulation is carried out. The results show that the host vehicle's localization accuracy by the proposed method can be improved by 25% compared with direct linearization. Besides, by combining relative DOA and relative RD measurement, the locating capability of the least-square-based nonlinear optimization method can be enhanced by 22%.

1. Introduction

Connected and automated vehicles (CAV) are promising methods worldwide to improve traffic safety, enhance driving comfort, and reduce energy consumption [1–3]. As an essential CAV function, accurate localization technology is all-important for CAV to realize high-grade performances such as vehicle platooning [4] and cooperative merging on highway ramps [5, 6] and has been widely studied. The most common localization technique used in CAV is realized by the global navigation satellite system (GNSS). However, the urban forest in downtowns, such as dense buildings, usually weakens the signal quality of GNSS and reduces the positioning precision of vehicles [7–9]. Besides, when cars drive as a group, the small intervehicle distance demands that the

vehicular positioning accuracy is centimeter-level [10], which is much higher than the current GNSS road-positioning accuracy level.

Various techniques have been proposed to improve vehicular positioning accuracy further to meet multivehicle cooperative control requirements [11–15]. Differential GNSS is proposed in [16] to achieve higher positioning accuracy by eliminating the common biases through a network of fixed reference stations. The real-time kinematic (RTK) technique is employed based on carrier phase measurements in [17] to realize centimeter-level accuracy. Moreover, higher vehicle positioning accuracy is achieved using the inertial navigation system (INS) in [18, 19]. Nonetheless, the methods mentioned above depend on the expensive infrastructures or onboard devices. Some scholars

recently studied cooperative localization-based multi-UAVs' technical possibility to simultaneously reduce costs and achieve lane-level positioning accuracy [20–22].

The cooperative localization usually requires two additional pieces of information to enhance the positioning accuracy, i.e., Direction-of-Arrival (DOA) and Relative Distance (RD) between vehicles. Tomic et al. [23] developed a suboptimal estimator to calculate the location of multiple targets in a three-dimensional wireless sensor network by using DOA measurement, whose model is linearized. Wang et al. presented a DOA estimation method based on sparse Bayesian learning (SBL) to improve vehicle localization accuracy [24]. Another study proposed by Yin et al. measured the RD between the base station and target vehicle by combining Time Difference of Arrival (TDOA) and Angle of Arrival (AOA) [25]. Localization errors are reduced by solving the mean square error matrix.

Also, some researchers attempt to combine the DOA and RD information by several fusion algorithms to improve the positioning accuracy. Rohani et al. [26] adopt the particle-filter probability-statistics method to conduct information fusion for the distance between the front and rear vehicles to increase relative position precision. Song et al. [27] develop a cooperative localization method based on the Bayesian framework, which uses GPS, distances, and azimuth between vehicles. The effects of vehicle speed, acceleration, and variable spacing on vehicle localization accuracy are analyzed. Naseri et al. [28] propose a Message Passing Hybrid Localization (MPHL) algorithm, a distributed algorithm based on information propagation and Markov chain Monte Carlo sampling. Joint estimation of DOA and RD is conducted to solve the cooperative distributed localization problem. Additionally, Yin et al. [29] propose a cooperative multisensor Edge Cloud Cooperative Localization (ECCL) method, which has relative distance and relative angle observations from neighbor nodes and absolute coordinate positioning systems (such as GPS) to obtain relevant information. A centralized cooperative fusion unit is built in the cloud to fuse the multiple localization information.

Although the information of DOA, RD, or DOA-RD is fused by filter algorithms in [23–29], the filter algorithms may not meet real-time localization performance because of the computational complexity. This paper investigates the fusion of DOA-RD information without filter algorithms to achieve the cooperative localization of CAVs in the flyover environment. The localization framework based on least-squares DOA-RD information fusion is also established. The main contributions of this article are threefold. First, host vehicles' three-dimensional positioning error model concerning adjacent vehicles in azimuth angle and pitch angle and intervehicle distances was established. Second, to eliminate the position errors, a least-square-based linear localization method is designed by combining relative DOA and RD measurement information. Then, in light of the positioning results obtained by the linear localization method, a nonlinear calculation method fusing DOA- and RD-related communication between vehicles is proposed to optimize cars' positioning accuracy further. The presented cooperative localization method based on connected and automated vehicles on the localization accuracy is finally analyzed.

The remainder of this paper is organized as follows: Section 2 introduces the system model and the framework of cooperative localization. In Section 3, the calculation process of the cooperative localization optimization algorithm is presented. Section 4 gives the simulation and results. Section 5 concludes this paper.

2. System Model and Cooperative Localization

This paper will focus on the cooperative localization of multiple vehicles by using the DOA and RD information. This section will introduce the modeling of cooperative localization and its fundamental principle.

2.1. System Model. The localization in the multistack interchange is challenging due to the intricate positions of the vehicles. This paper will focus on this scenario. Figure 1 shows a typical multistack interaction, where the cars drive on different levels.

Figure 2 is the simplified model of the cooperative localization for n vehicles. The position of the target vehicle is $\mathbf{V}_t = [v_{x_t}, v_{y_t}, v_{z_t}]^T$, and the position of the assistance vehicle is $\mathbf{V}_i = [v_{x_i}, v_{y_i}, v_{z_i}]^T$. Note that only the vehicle with onboard sensors to measure the DOA and RD could be the assistance vehicle. Each car could obtain the basic localization information using the GNSS. The relative DOA between vehicles are azimuth angles $\alpha_1, \alpha_2, \alpha_3, \ldots, \alpha_i$ and pitch angles $\beta_1, \beta_2, \beta_3, \ldots, \beta_i$, while the relative RD between vehicles is $D_{12}, D_{13}, D_{23}, \ldots, D_{ij}$.

There are n CAVs communicating with the target vehicle to measure the DOA and RD. The DOA and RD between target and assistance vehicles are

$$
\begin{cases}
\alpha_i = \arctan \dfrac{v_{y_t} - v_{y_i}}{v_{x_t} - v_{x_i}}, \\[3mm]
\beta_i = \arctan \dfrac{v_{z_t} - v_{z_i}}{\sqrt{\left(v_{x_t} - v_{x_i}\right)^2 + \left(v_{y_t} - v_{y_i}\right)^2}}, \\[3mm]
D_{ij} = \sqrt{\left(v_{x_i} - v_{x_j}\right)^2 + \left(v_{y_i} - v_{y_j}\right)^2 + \left(v_{z_i} - v_{z_j}\right)^2}, \\[3mm]
(i, j = 1, 2, \ldots; i \neq j),
\end{cases}
\tag{1}
$$

where α_i, β_i, and D_{ij} are the azimuth, pitch, and intervehicle distance between the target and assistance vehicles. Besides, the azimuth angle, pitch angle, and distance between vehicles can be expressed as $\mathbf{W} = [\alpha_i, \beta_i, D_{ij}]^T$. Since sensor noise exists, the system model is depicted as

$$
\begin{bmatrix} \widehat{\alpha}_i \\ \widehat{\beta}_i \\ \widehat{D}_{ij} \end{bmatrix} = \begin{bmatrix} \alpha_i \\ \beta_i \\ D_{ij} \end{bmatrix} + \begin{bmatrix} \varepsilon_{\alpha_i} \\ \varepsilon_{\beta_i} \\ \varepsilon_{D_{ij}} \end{bmatrix}, \quad (i, j = 1, 2, \ldots, n; i \neq j), \tag{2}
$$
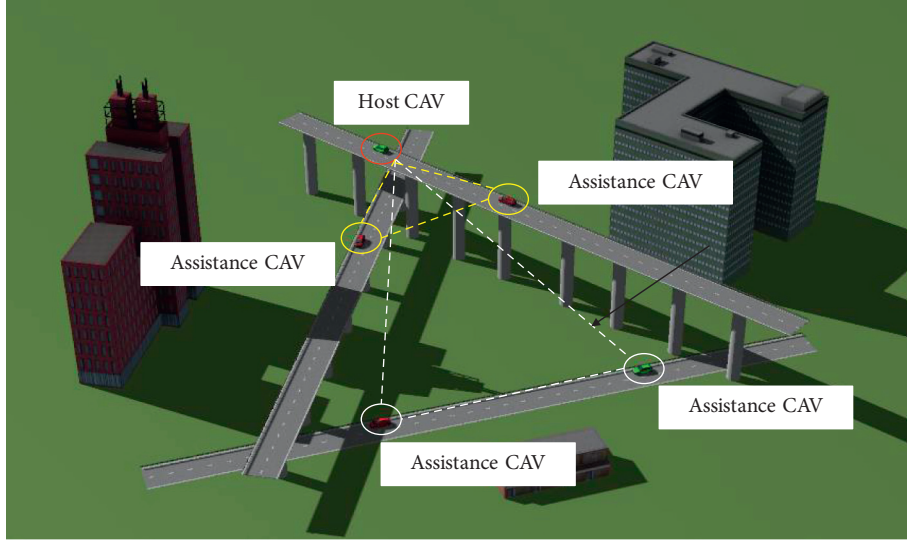
Figure 1: CAV driving on the road scene of a flyover.
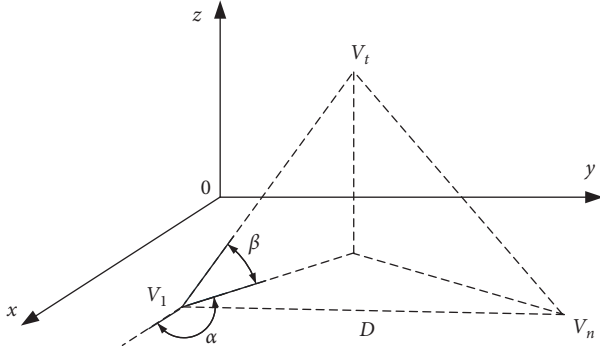
Figure 2: Simplified diagram of multiple vehicles.

where $\widehat{W} = [\widehat{\alpha}_i, \widehat{\beta}_i, \widehat{D}_{ij}]^T$ is the measurement value of sensors with noise and $\varepsilon_{\alpha_i} \sim (0, \sigma_{\alpha_i}^2)$, $\varepsilon_{\beta_i} \sim (0, \sigma_{\beta_i}^2)$, and $\varepsilon_{D_{ij}} \sim (0, \sigma_{D_{ij}}^2)$ are the measurement noise of azimuth angle, pitch angle, and intervehicle distance, respectively. They are Gaussian white noises and uncorrelated.

2.2. Cooperative Localization Principle. The main idea of cooperative localization is using the measured azimuth, pitch angle, and distances between vehicles to improve the positioning accuracy of all cars in the multivehicle system. Assuming that the DOA and RD errors are zero, we will derive the following vehicle positions. Since there exist errors by using GNSS for each vehicle, the position can be expressed as

$$\begin{cases} \widehat{v}_{x_i} = v_{x_i} + \varepsilon_{v_{x_i}}, \\ \widehat{v}_{y_i} = v_{y_i} + \varepsilon_{v_{y_i}}, \\ \widehat{v}_{z_i} = v_{z_i} + \varepsilon_{v_{z_i}}, \end{cases} \tag{3}$$

where $\varepsilon_{v_{x_i}}$, $\varepsilon_{v_{y_i}}$, and $\varepsilon_{v_{z_i}}$ represent the localization noise of GNSS, which are Gaussian white noises.

According to the distance between the CAVs, the location of the assistance vehicle i can be calculated by the target vehicle t, i.e.,

$$\begin{cases} v_{x_i} = v_{x_t} + \Delta x_i, \\ v_{y_i} = v_{y_t} + \Delta y_i, \\ v_{z_i} = v_{z_t} + \Delta z_i, \end{cases} \tag{4}$$

where Δx_i, Δy_i, and Δz_i are the distances in three directions. Since the measured values are independent of each other, the measured location of vehicle i is

$$\begin{cases} \widehat{v}_{x_i} = v_{x_t} + \Delta x_i + \varepsilon_{v_{x_i}}, \\ \widehat{v}_{y_i} = v_{y_t} + \Delta y_i + \varepsilon_{v_{y_i}}, \\ \widehat{v}_{z_i} = v_{z_t} + \Delta z_i + \varepsilon_{v_{z_i}}. \end{cases} \tag{5}$$

If the locations are measured by n times, the position of the target CAV can be obtained as

$$\begin{cases} v_{x_t} = \dfrac{1}{n} \sum_{i=1}^{n} \left(\widehat{v}_{x_i} - \Delta x_i - \varepsilon_{v_{x_i}} \right), \\ v_{y_t} = \dfrac{1}{n} \sum_{i=1}^{n} \left(\widehat{v}_{y_i} - \Delta y_i - \varepsilon_{v_{y_i}} \right), \\ v_{z_t} = \dfrac{1}{n} \sum_{i=1}^{n} \left(\widehat{v}_{z_i} - \Delta z_i - \varepsilon_{v_{z_i}} \right). \end{cases} \tag{6}$$

At the same time, the variances of the least-squares method are

$$\begin{cases} \mathrm{Var}\left[\widehat{v}_{x_t} \right] = \dfrac{\mathrm{Var}\left[\widehat{v}_{x_i} - \Delta x_i - \varepsilon_{v_{x_i}} \right]}{n} = \dfrac{\sigma_x^2}{n}, \\ \mathrm{Var}\left[\widehat{v}_{y_t} \right] = \dfrac{\mathrm{Var}\left[\widehat{v}_{y_i} - \Delta y_i - \varepsilon_{v_{y_i}} \right]}{n} = \dfrac{\sigma_y^2}{n}, \\ \mathrm{Var}\left[\widehat{v}_{z_t} \right] = \dfrac{\mathrm{Var}\left[\widehat{v}_{z_i} - \Delta z_i - \varepsilon_{v_{z_i}} \right]}{n} = \dfrac{\sigma_z^2}{n}. \end{cases} \tag{7}$$

The positioning accuracy of the target vehicle is improved with the increase in the cooperation vehicle number.

3. Cooperative Localization Algorithm Design

This section will introduce the linear and nonlinear least-squares optimization methods to improve the positioning accuracy by fusing the DOA and RD information between vehicles.

$$
\begin{cases}
v_{x_{t0}} = \dfrac{v_{x_{i0}} \tan \alpha_i - v_{x_{j0}} \tan \alpha_j - v_{y_{i0}} + v_{y_{j0}}}{\tan \alpha_i - \tan \alpha_j}, \\[4mm]
v_{y_{t0}} = \dfrac{\tan \alpha_i \tan \alpha_j \left(v_{x_{i0}} - v_{x_{j0}} \right) - v_{y_{i0}} \tan \alpha_j + v_{y_{j0}} \tan \alpha_i}{\tan \alpha_i - \tan \alpha_j}, \\[4mm]
v_{z_{t0}} = \dfrac{1}{2}\left[v_{z_i} + v_{z_j} - \tan \beta_i \sqrt{\left(v_{x_{t0}} - v_{x_i}\right)^2 + \left(v_{x_{t0}} - v_{x_i}\right)^2} - \tan \beta_i \sqrt{\left(v_{x_{t0}} - v_{x_i}\right)^2 + \left(v_{x_{t0}} - v_{x_i}\right)^2} \right].
\end{cases}
\tag{8}
$$

Therefore, the positions of all vehicles are

$$
\mathbf{V}_0 = \left[v_{x_{10}}, v_{y_{10}}, v_{z_{10}}, \ldots, v_{x_{n0}}, v_{y_{n0}}, v_{z_{n0}}, v_{x_{t0}}, v_{y_{t0}}, v_{z_{t0}} \right]^T. \tag{9}
$$

3.2. Linear Least-Squares Optimization.

Assuming that there are n CAVs in a flyover scene, the corresponding coordinate positions in three directions can be set as $\vec{x}$, $\vec{y}$, and $\vec{z}$, which can be represented as

$$
\begin{bmatrix} \hat{x} \\ \hat{y} \\ \hat{z} \end{bmatrix} = \begin{bmatrix} \vec{x} \\ \vec{y} \\ \vec{z} \end{bmatrix} + \begin{bmatrix} \varepsilon_{\vec{x}} \\ \varepsilon_{\vec{y}} \\ \varepsilon_{\vec{z}} \end{bmatrix}. \tag{10}
$$

The mean values of $\varepsilon_{\vec{x}} \sim (0, \sigma^2_{\vec{x}})$, $\varepsilon_{\vec{y}} \sim (0, \sigma^2_{\vec{y}})$, and $\varepsilon_{\vec{z}} \sim (0, \sigma^2_{\vec{z}})$ in the three-dimensional coordinates are zero while satisfying the uncorrelated white Gaussian noise.

According to equations (2) and (10), we can define linearized solution observation value $\omega = [\alpha_i, \beta_i, D_{ij}, \vec{x}, \vec{y}, \vec{z}]^T$; then,

$$
\hat{\boldsymbol{\omega}} = \begin{bmatrix} \hat{\alpha}_i \\ \hat{\beta}_i \\ \hat{D}_{ij} \\ \hat{x} \\ \hat{y} \\ \hat{z} \end{bmatrix} = \begin{bmatrix} \alpha_i \\ \beta_i \\ D_{ij} \\ \vec{x} \\ \vec{y} \\ \vec{z} \end{bmatrix} + \begin{bmatrix} \varepsilon_{\alpha_i} \\ \varepsilon_{\beta_i} \\ \varepsilon_{R_{ij}} \\ \varepsilon_{\vec{x}} \\ \varepsilon_{\vec{y}} \\ \varepsilon_{\vec{z}} \end{bmatrix}, \quad (i, j = 1, 2, \ldots, n; i \neq j),
\tag{11}
$$

where $\hat{\omega} = [\hat{\alpha}_i, \hat{\beta}_i, \hat{D}_{ij}, \hat{x}, \hat{y}, \hat{z}]^T$ represents the actual measured value with noise.

3.1. Vehicle Initial Position.

The initial position of assistance vehicle is provided by the GNSS, i.e., $\mathbf{V}_{n0} = [v_{x_{10}}, v_{y_{10}}, v_{z_{10}}, \ldots, v_{x_{n0}}, v_{y_{n0}}, v_{z_{n0}}]^T$. According to the three-point positioning principle, the position of the target CAV, $\mathbf{v}_{t0} = [v_{x_{t0}}, v_{y_{t0}}, v_{z_{t0}}]^T$, can be calculated by using the positions of two known CAVs and the DOA information between them. Then, if two assistance vehicles are selected, the position of the target CAV is calculated by

According to system model (1), it is necessary to perform a first-order Taylor expansion at the initial vehicle value $\mathbf{V}_0$ (the error of the second order and above is small and can be ignored). The linearization solution is as follows.

Azimuth linearization is

$$
\alpha_i \approx \phi_{1i} v_{x_i} + \phi_{2i} v_{y_i} + \phi_{3i} v_{x_t} + \phi_{4i} v_{y_t} + \phi_{5i}, \tag{12}
$$

where

$$
\begin{cases}
\phi_{1i} = \dfrac{1}{\gamma}\left(v_{y_{t0}} - v_{y_{i0}}\right), \\[4mm]
\phi_{2i} = -\dfrac{1}{\gamma}\left(v_{x_{t0}} - v_{x_{i0}}\right), \\[4mm]
\phi_{3i} = -\dfrac{1}{\gamma}\left(v_{y_{t0}} - v_{y_{i0}}\right), \\[4mm]
\phi_{4i} = -\dfrac{1}{\gamma}\left(v_{x_{t0}} - v_{x_{i0}}\right), \\[4mm]
\phi_{5i} = \arctan \dfrac{v_{y_{t0}} - v_{y_{i0}}}{v_{x_{t0}} - v_{x_{i0}}}, \\[4mm]
\gamma = \left(v_{x_{t0}} - v_{x_{i0}}\right)^2 + \left(v_{y_{t0}} - v_{y_{i0}}\right)^2.
\end{cases}
\tag{13}
$$

Linearization of the pitch angle is

$$
\beta_i \approx \Psi_{1i} v_{x_i} + \Psi_{2i} v_{y_i} + \Psi_{3i} v_{z_i} + \Psi_{4i} l_{x_t} + \Psi_{5i} l_{y_t} + \Psi_{6i} l_{z_t} + \Psi_{7i}, \tag{14}
$$

where

$$
\begin{cases}
\Psi_{1i} = \dfrac{1}{\lambda}\left(v_{x_t} - v_{x_j}\right)\left(v_{z_{i0}} - v_{z_{j0}}\right), \\[2mm]
\Psi_{2i} = \dfrac{1}{\lambda}\left(v_{y_{t0}} - v_{y_{j0}}\right)\left(v_{z_{i0}} - v_{z_{j0}}\right), \\[2mm]
\Psi_{3i} = -\dfrac{1}{\lambda}\left(v_{x_t} - v_{x_j}\right)^2 + \left(l_{y_t} - v_{y_j}\right)^2, \\[2mm]
\Psi_{4i} = -\dfrac{1}{\lambda}\left(v_{x_t} - v_{x_j}\right)\left(v_{z_{i0}} - v_{z_{j0}}\right), \\[2mm]
\Psi_{5i} = -\dfrac{1}{\lambda}\left(v_{y_{t0}} - v_{y_{j0}}\right)\left(v_{z_{i0}} - v_{z_{j0}}\right), \\[2mm]
\Psi_{6i} = \dfrac{1}{\lambda}\left(v_{x_t} - v_{x_j}\right)^2 + \left(v_{y_t} - v_{y_j}\right)^2, \\[2mm]
\Psi_{7i} = \arctan \dfrac{v_{z_{i0}} - v_{z_{j0}}}{\sqrt{\left(v_{x_{t0}} - v_{x_{j0}}\right)^2 + \left(v_{y_{t0}} - v_{y_{j0}}\right)^2}}, \\[2mm]
A = \left(v_{x_{t0}} - v_{x_{j0}}\right)^2 + \left(v_{y_{t0}} - v_{y_{j0}}\right)^2 + \left(v_{z_{i0}} - v_{z_{j0}}\right)^2, \\[2mm]
B = \sqrt{\left(v_{x_t} - v_{x_j}\right)^2 + \left(v_{y_t} - v_{y_j}\right)^2}, \\[2mm]
\lambda = A * B.
\end{cases}
\tag{15}
$$

Linearization of vehicle distance can be written as

$$
D_{ij} \approx \mu_{1i} v_{x_i} + \mu_{2i} v_{y_i} + \mu_{3i} v_{z_i} + \mu_{4i} v_{x_t} + \mu_{5i} v_{y_t} + \mu_{6i} v_{z_i}. \tag{16}
$$

The positions of vehicles can be solved as

$$
\mathbf{V} = \left[v_{x_1}, v_{y_1}, v_{z_1}, \ldots, v_{x_n}, v_{y_n}, v_{z_n}, v_{x_t}, v_{y_t}, v_{z_t} \right]^T. \tag{17}
$$

The relationship of the observation equation $\widehat{\omega} = [\widehat{\alpha}_i, \widehat{\beta}_i, \widehat{D}_{ij}, \widehat{x}, \widehat{y}, \widehat{z}]^T$ is

$$
\widehat{\omega} = \boldsymbol{\eta}\mathbf{V} + \boldsymbol{\psi}, \tag{18}
$$

where

$$
\boldsymbol{\eta} = \begin{bmatrix} \mathscr{R} & \cdots & \mathscr{O} \\ \cdots & \ddots & \cdots \\ \mathscr{F} & \cdots & \mathscr{H} \end{bmatrix},
$$

$$
\mathscr{R} = \begin{bmatrix} \phi_{11} & \phi_{12} & 0 & 0 & \cdots \\ \cdots & \phi_{1i} & \phi_{2i} & \phi_{3i} & \vdots \\ \cdots & \Psi_{1i} & \Psi_{1i} & \Psi_{1i} & \vdots \\ \cdots & \mu_{1i} & \mu_{2i} & \mu_{3i} & \vdots \end{bmatrix},
$$

$$
\mathscr{O} = \begin{bmatrix} 0 & 0 & 0 & \phi_{31} & \phi_{41} & 0 \\ 0 & 0 & 0 & \phi_{3i} & \phi_{4i} & 0 \\ 0 & 0 & 0 & \Psi_{1i} & \Psi_{5i} & \Psi_{6i} \\ \mu_{4i} & \mu_{5i} & \mu_{6i} & \cdots & 0 & 0 \end{bmatrix},
$$

$$
\mathscr{F} = \begin{bmatrix} \cdots & 0 & \mu_{1i} & \mu_{2i} & \mu_{3i} \\ \dfrac{1}{n} & 0 & 0 & \dfrac{1}{n} & \cdots \\ 0 & \dfrac{1}{n} & 0 & 0 & \dfrac{1}{n} \\ 0 & 0 & \dfrac{1}{n} & 0 & 0 \end{bmatrix},
$$

$$
\mathscr{H} = \begin{bmatrix} \mu_{4i} & \mu_{5i} & \mu_{6i} & 0 & 0 & 0 \\ \dfrac{1}{n} & 0 & 0 & 0 & 0 & 0 \\ \cdots & \dfrac{1}{n} & 0 & 0 & 0 & 0 \\ \dfrac{1}{n} & \cdots & \dfrac{1}{n} & 0 & 0 & 0 \end{bmatrix},
$$

$$
\boldsymbol{\psi} = \left[\phi_{51}, \Psi_{71}, 0, \ldots, 0, \phi_{5i}, \Psi_{7i}, 0\right]^{\mathbf{T}}. \tag{19}
$$

According to Taylor expansion coefficients and constant terms, least-squares equation (18) is solved as

$$
\mathbf{V} = \left(\boldsymbol{\eta}^T \boldsymbol{\eta}\right)^{-1} \boldsymbol{\eta}^T \widehat{\omega} - \boldsymbol{\psi}. \tag{20}
$$

The high-precision position coordinates of CAVs can be solved as

$$
\mathbf{V} = \left[v_{x_1}, v_{y_1}, v_{z_1}, \ldots, v_{x_n}, v_{y_n}, v_{z_n}, v_{x_t}, v_{y_t}, v_{z_t} \right]^T. \tag{21}
$$

The position of the target CAV can be solved by $\mathbf{V}_t = [v_{x_t}, v_{y_t}, v_{z_t}]^T$.

3.3. Nonlinear Least-Squares Optimization.

The nonlinear optimization algorithm mainly adopts the minimum residual sum of squares (RSS). Let $h(\mathbf{V_t})$ be the functional relationship from the position $\mathbf{V_t}$ to the observation $\mathbf{W}$. We can obtain the following equation:

$$
\widehat{W} = h(\mathbf{V_t}) + \boldsymbol{\delta}, \tag{22}
$$

where $\widehat{W}$ is the measured value with noise and $\boldsymbol{\delta} = [\varepsilon_{\alpha_i}, \varepsilon_{\beta_i}, \varepsilon_{D_{ij}}]^T$ $(i, j = 1, 2, \ldots, n)$ is Gaussian white noise. Assuming that the measurement error of each sensor is zero mean and Gaussian white noise is not correlated with each other, the positioning error formula is

$$
\boldsymbol{\delta} = \mathbf{H} \cdot d\mathbf{v}_t, \tag{23}
$$

where $d\mathbf{v}_t = [dv_{x_t}, dv_{y_t}, dv_{z_t}]^T$ and $\mathbf{H} = \partial h / \partial v_t$ is the Jacobian matrix as follows:

$$\mathbf{H} = \begin{bmatrix} \dfrac{v_{x_t} - v_{x_1}}{D_{t1}} & \dfrac{v_{y_t} - v_{y_1}}{D_{t1}} & \dfrac{v_{z_t} - v_{z_1}}{D_{t1}} \\[3mm] \dfrac{v_{y_1} - v_{y_t}}{d_1^2} & \dfrac{v_{x_t} - v_{x_1}}{d_1^2} & 0 \\[3mm] A & B & \dfrac{d_1}{D_{t1}^2} \end{bmatrix}. \tag{24}$$

Also,

$$A = \frac{-\left(v_{x_t} - v_{x_1}\right) * \left(v_{z_t} - v_{z_1}\right)}{D_{t1}^2 * d_1},$$

$$B = \frac{-\left(v_{y_t} - v_{y_1}\right) * \left(v_{z_t} - v_{z_1}\right)}{D_{t1}^2 * d_1}, \tag{25}$$

$$d_1 = \left(v_{x_t} - v_{x_1}\right)^2 + \left(v_{y_t} - v_{y_1}\right)^2.$$

Among them, according to $\widehat{W} = h\mathbf{v}_{x_t} + \delta$, when the value of $\widehat{W} - h\mathbf{v}_{x_t}$ tends to 0, the residual δ reaches a minimum. When $\widehat{W} - h v_{x_t}^2$ achieves the minimum value, the optimal state quantity is obtained, which can be calculated by using the Gauss–Newton iteration method:

$$\widehat{W} = \mathbf{H}_j \left(\Delta v_{\mathbf{x}_t}\right)_j + \left(\mathbf{h} v_{\mathbf{x}_t}\right)_j,$$

$$\left(\Delta v_{\mathbf{x}_t}\right)_j = \left(\mathbf{H}_j^T \mathbf{H}_j\right)^{-1} \mathbf{H}_j^T \left(\widehat{W} - \mathbf{h}\left(v_{\mathbf{x}_t}\right)_j\right), \tag{26}$$

$$\left(v_{\mathbf{x}_{t+1}}\right)_j = \left(v_{\mathbf{x}_t}\right)_j + \left(\Delta v_{\mathbf{x}_t}\right)_j,$$

where j is the number of iterations.

According to the estimation of the least-squares method, the root mean square error (RMSE) matrix is obtained:

$$\mathbf{E}\left[dv_{\mathbf{x}_t} dv_{\mathbf{x}_t}^T\right] = \left(\mathbf{H}^T \mathbf{H}\right)^{-1} \mathbf{H}^T \mathbf{Q} \mathbf{H} \left(\mathbf{H}^T \mathbf{H}\right)^{-1}, \tag{27}$$

where $\mathbf{E}[d\mathbf{v}_{\mathbf{x}_t} d v_{\mathbf{x}_t}^{\mathbf{T}}]$, $\mathbf{Q}$ is the variance error matrix, and $\mathbf{Q} = \text{diag}\,[\sigma\varepsilon_{\alpha_i}^2, \sigma\varepsilon_{\beta_i}^2, \sigma\varepsilon_{D_{ij}}^2]$ $(i, j = 1, 2, \ldots, n)$, where $\sigma\varepsilon_{\alpha_i}$, $\sigma\varepsilon_{\beta_i}$, and $\sigma\varepsilon_{D_{ij}}$ are the standard deviation of the error for the azimuth angle, pitch angle, and distance between vehicles. The azimuth angle obtains the initial value of the target CAV $\mathbf{V}_0 = [v_{x_{10}}, v_{y_{10}}, v_{z_{10}}]^T$, which is treated as the starting point of the least-squares iteration. By the Newton–Raphson method, $\Delta\mathbf{v}_{x_t}$ is continuously iterated until $\|\widehat{W} - h\mathbf{V}_{x_t}\|^2$ reaches the minimum value. The target localization can be obtained as the optimal solution.

4. Simulation Results and Discussion

4.1. Simulation Method.
We use PreScan-Simulink joint simulation software to perform Monte Carlo simulations on the flyover driving scene and analyze the localization

accuracy according to the RMSE. The localization accuracy in the $x - y - z$ direction is defined as follows:

$$\begin{cases} \text{RMSE}_x = \sqrt{\dfrac{1}{M}\sum_{i=1}^{M}\dfrac{1}{N}\sum_{j=1}^{N}\left(v_{x_{it}} - v_{x_{it\_true}}\right)^2}, \\[4mm] \text{RMSE}_y = \sqrt{\dfrac{1}{M}\sum_{i=1}^{M}\dfrac{1}{N}\sum_{j=1}^{N}\left(v_{y_{it}} - v_{y_{it\_true}}\right)^2}, \\[4mm] \text{RMSE}_z = \sqrt{\dfrac{1}{M}\sum_{i=1}^{M}\dfrac{1}{N}\sum_{j=1}^{N}\left(v_{z_{it}} - v_{z_{it\_true}}\right)^2}. \end{cases} \tag{28}$$

4.2. Simulation Conditions.
We set up a flyover scenario to conduct the simulation analysis. The initial positions, directions, and speeds of multi-CAVs have been given. The accuracy of the onboard sensors is shown in Table 1.

4.3. Simulation Results.
We can only solve the target CAV's localization when using the relative direction information to obtain the RMSE of the target vehicle. The simulation results show that the single relative direction information cannot improve each connected vehicle's localization accuracy. The RMSE result of the target CAV is shown in Figure 3, and the RMSE statistics of the target CAV are shown in Table 2.

In single relative direction information, the RMSE after linearization is solved by the least-squares method. The RMSE obtained by the linear optimization solution method is shown in Figure 4, and the RMSE statistics are shown in Table 3.

When the target CAV's initial position is obtained by single relative direction information, the RMSE of the target CAV is obtained as shown in Figure 5 through combining the least-squares method with the nonlinear optimization method, and the RMSE statistics are shown in Table 4.

When the target CAV's initial position is obtained by relative-direction finding and ranging, the nonlinear optimization algorithm solves the RMSE of the target CAV. The simulation results are shown in Figure 6, and the RMSE statistics are shown in Table 5.

4.4. Analysis of Factors Affecting Localization Accuracy.
Vehicle speed is one of the most important factors for road safety. Therefore, the reasonable target speeds of CAVs and the distance between the assistance CAVs are necessary to guarantee the flyover scenario's driving safety. The localization accuracies of the target CAV under different conditions are simulated and analyzed by using the linear least-squares fusion algorithm. The simulation results are shown in Figures 7–9. In Figure 7, two assistance CAVs are assumed driving on the road with constant speeds of 30 km/h and the distance between them is 100 m. The

TABLE 1: Sensor measurement accuracy.

Type	Azimuth accuracy (°)	Ranging accuracy (m)	Self-localization accuracy (m)
	0.15	0.5	10
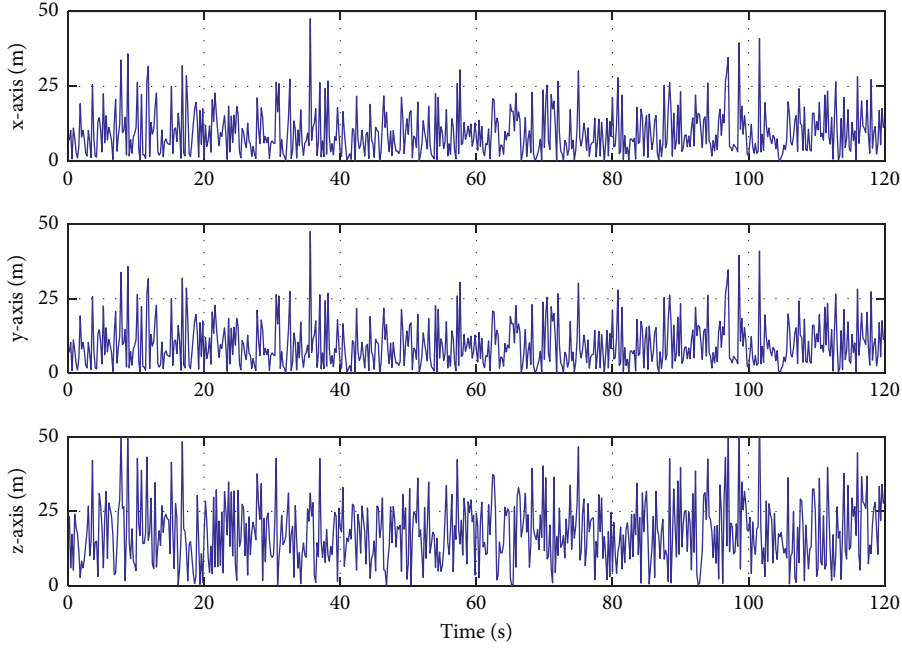
FIGURE 3: RMSE of the relative DOA solution for the target CAV.

TABLE 2: RMSE statistics of direction-finding solution for target CAV.

	x-label (m)	y-label (m)	z-label (m)
RMSE	8.0960	8.1532	9.7026
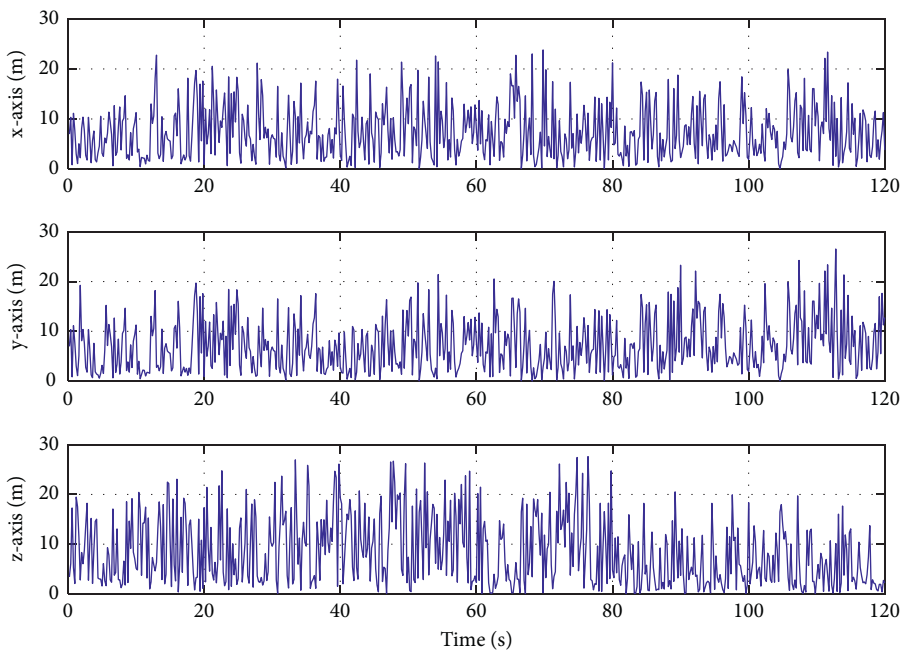
FIGURE 4: RMSE of linear optimization solution.

TABLE 3: RMSE statistics for linear optimization to solve the target CAV.

	x-label (m)	y-label (m)	z-label (m)
RMSE	6.361	7.0571	7.3956
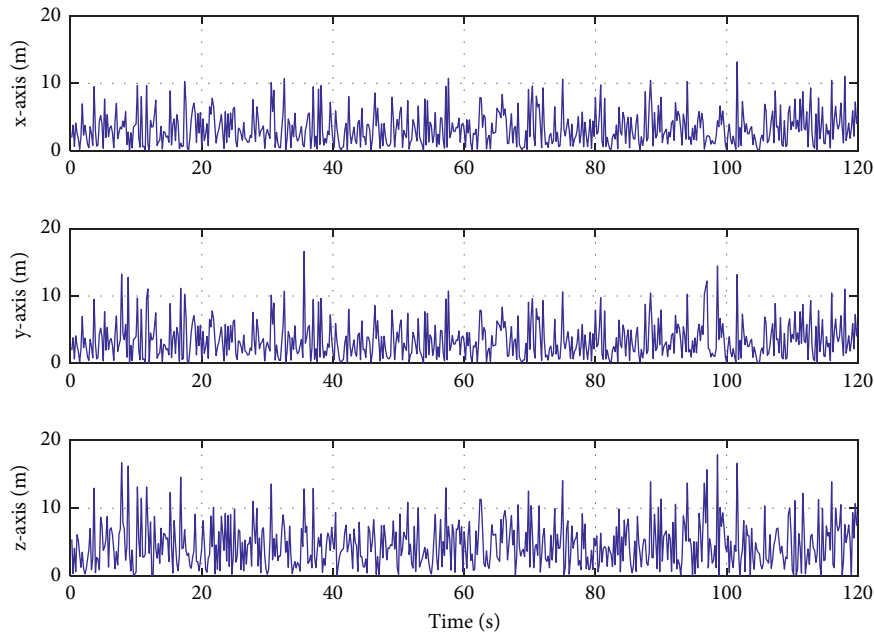
FIGURE 5: The RMSE of the downward nonlinear optimization solution.

TABLE 4: RMSE statistics of the target CAV measuring downward nonlinear solution.

	x-label (m)	y-label (m)	z-label (m)
RMSE	4.5475	4.6351	4.9571
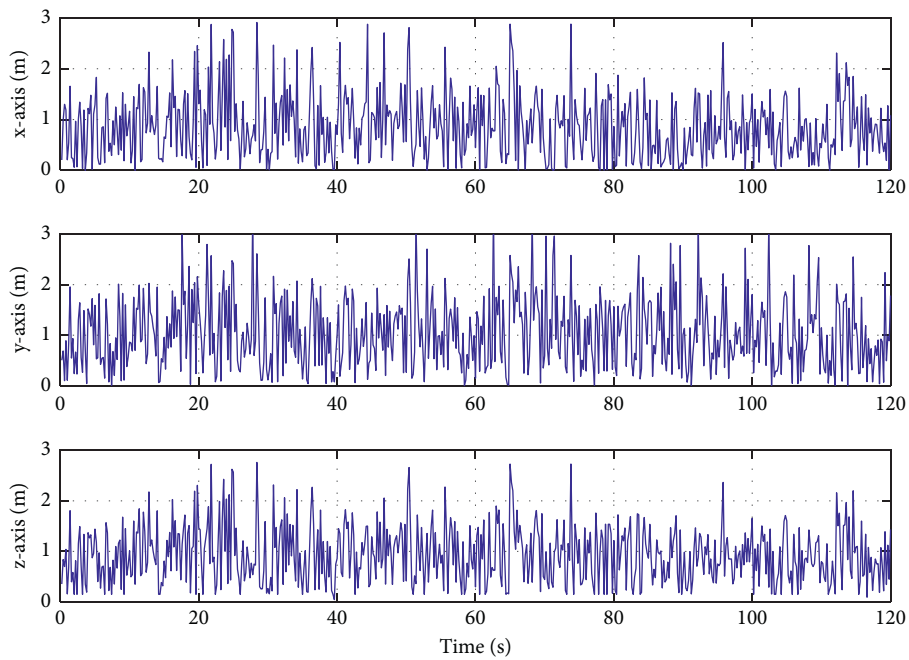
FIGURE 6: RMSE of nonlinear optimization solution under direction finding and ranging.

Table 5: RMSE statistics of nonlinear optimization solution under direction finding and ranging.

	x-label (m)	y-label (m)	z-label (m)
RMSE	0.6174	0.6935	0.8287
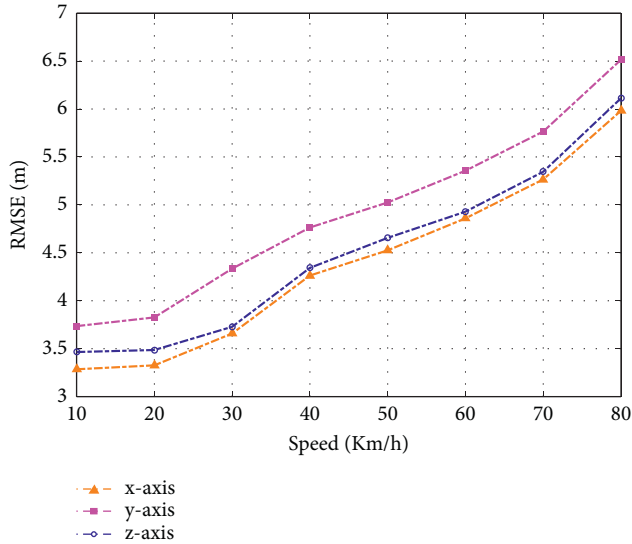
Figure 7: RMSE of speed change to the target CAV.
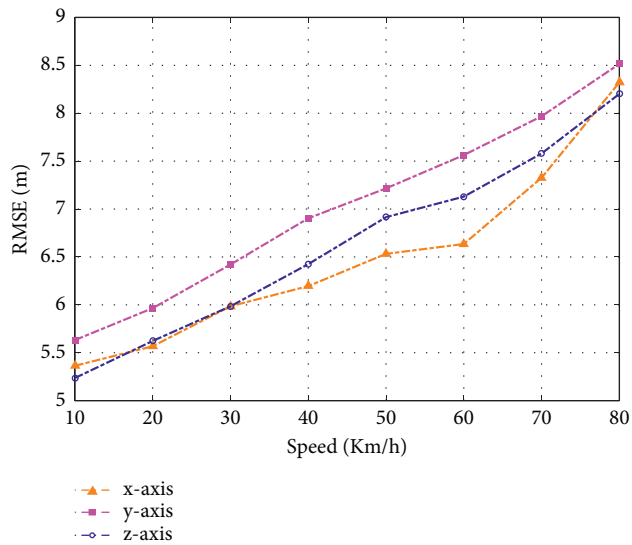
Figure 8: RMSE of the speed change of the multivehicles to the target CAV.

velocity of target CAV is changed between 10 and 80 km/h. In Figure 8, the target CAV and the assistance CAVs are hypothesized to run along different roads and the relative speeds of assistance vehicles vary from 10 km/h to 80 km/h. The previous figure changes the distance between the assistance CAVs from 20 m to 200 m. Note that the cooperative positioning method proposed in this paper is based on the azimuth and the distance between the assistance CAVs. Therefore, similar to the spatial three-point positioning principle, at least two assistance CAVs are needed to
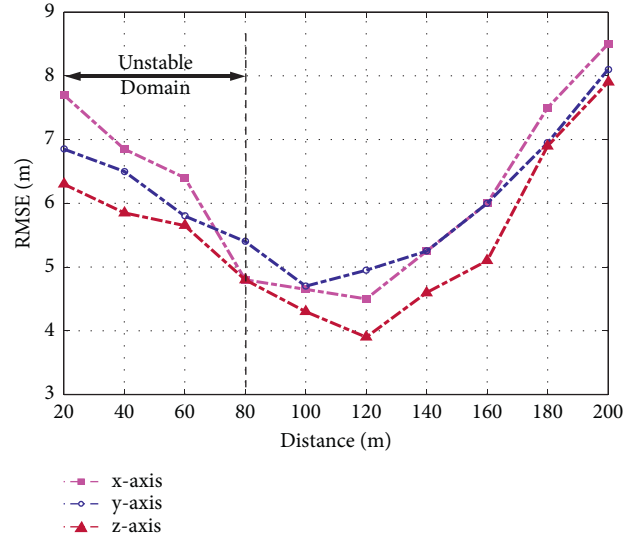
Figure 9: Effect of assistance CAV distance on target CAV localization accuracy.

complete the cooperative positioning of the host vehicle in the application.

From Figures 7 and 8, we can see that both the host vehicle speed and the relative speeds of assistance vehicles can affect the position accuracy of the host vehicle and the location accuracy is weakened with augments of these two factors. By observing Figure 9, one can get that the positioning error of the host vehicle decreases first and then increases and reaches the lowest point between 80 km/h and 120 km/h. When the distance between two assistance CAVs is 20 m, a significant positioning error occurs because the GNSS system works. However, with the functioning of the cooperative location method, the positioning error is gradually reduced and the positioning error is less than 5 m at between 80 km/h and 120 km/h. As the distance between the two cars grows, the localization accuracy of the target CAV decreases, possibly due to the phenomena of communication delay and data dropout in vehicle-to-vehicle wireless communication networks. Therefore, the changing trend of target vehicle positioning RMSE is finally shown in Figure 9.

4.5. Result Analysis. By Figures 3–6, the average value of vehicle localization errors is calculated and a method to reduce the error percentage is proposed. When the self-localization accuracy of CAVs given by the simulation is 10 m, the result shows the following:

(1) When only relative DOA is employed to obtain the localization of the target CAV, the low-accuracy position values of CAVs are directly used for calculation. Due to the low accuracy of the comparative DOA method, the positioning error of the target CAV is about 9–12 m, unable to improve the localization accuracy of the CAVs.

(2) The least-squares method linearization optimization for solving the localization of the target CAV can be

concluded that the target CAV's localization error is about 5–7 m, which improves the target's localization accuracy of CAV.

(3) Using the least-squares linearization optimization solution method combining relative DOA and relative RD measurement, the target CAV's localization value is about 4–5 m. Compared with direct linearization, the accuracy is improved by 25%.

(4) Using the nonlinear optimization solution method of the least-squares method combining relative DOA and relative RD measurement, the target CAV's localization value is about 3–4 m. Compared with the linear optimization solution method, the improvement of the least-squares method nonlinear optimization solution method is about 22%.

(5) The localization accuracy of the target CAV among the multi-CAVs decreases and increases as the distance of the assistance multi-CAVs increases. When the assistance CAV space is 100–120 m, the localization error reaches the minimum.

5. Conclusion

This paper studies the localization accuracy of the CAV in the flyover scenario when the accurate localization information of the vehicle is hard to obtain. The fusion algorithm that assists the relative DOA and relative RD measurement of multi-CAVs for cooperative localization is also researched. Using nonlinear optimization estimation and linearized least-squares estimation algorithm, the simulation results show that the proposed method improves the localization accuracy of the target CAV in road scenes such as flyover without increasing infrastructure costs. It can also conclude that reducing the CAV speed in the multivehicle cooperative of the CAV can increase the localization accuracy of the vehicle and enable driving. Reducing the distance between the assistance CAVs can increase the localization accuracy of the target CAV. This method is used for the cooperative localization of multi-vehicles in the flyover road scene. It can also be used for multi-aircraft combined attacks or target tracking in aerospace.

Data Availability

No data were used to support this study.

Conflicts of Interest

The authors declare that there are no conflicts of interest regarding the publication of this paper.

Acknowledgments

References

[1] L. Xu, W. Zhuang, G. Yin, C. Bian, and H. Wu, "Modeling and robust control of heterogeneous vehicle platoons on curved roads subject to disturbances and delays," *IEEE Transactions on Vehicular Technology*, vol. 68, no. 12, pp. 11551–11564, 2019.

[2] F. A. Wang, L. Xu, W. Zhuang et al., "Geometry-based cooperative localization for connected vehicle subject to temporary loss of GNSS signals," *IEEE Sensors Journal*, vol. 21, no. 20, pp. 23527–23536, 2021.

[3] F. Wang, W. Zhuang, G. Yin, S. Liu, Y. Liu, and H. Dong, "Robust inter-vehicle distance measurement using cooperative vehicle localization," *Sensors*, vol. 21, no. 6, 2021.

[4] R. F. Brena, J. P. García-Vázquez, C. E. Galván-Tejada, and D. Muñoz-Rodriguez, "Evolution of indoor positioning technologies: a survey," *Journal of Sensors*, vol. 2017, 2017.

[5] L. Xu, W. Zhuang, G. Yin, and C. Bian, "Energy-oriented cruising strategy design of vehicle platoon considering communication delay and disturbance," *Transportation Research Part C: Emerging Technologies*, vol. 107, pp. 34–53, 2019.

[6] N. Sun, M. G. Yan, and J. Ni, "A study on multi-vehicle cooperative positioning based on GRI," *Automotive Engineering*, vol. 40, no. 4, pp. 117–122+128, 2018.

[7] C. Xu, X. Wang, S. Duan, and J. Wan, "Spatial-temporal constrained particle filter for cooperative target tracking," *Journal of Network and Computer Applications*, vol. 176, 2021.

[8] S. Wang and X. Jiang, "Three-dimensional cooperative positioning in vehicular ad-hoc networks," *IEEE Transactions on Intelligent Transportation Systems*, vol. 22, no. 2, pp. 937–950, 2021.

[9] Y. Yuan, F. Shen, and X. Li, "GPS multipath and NLOS mitigation for relative positioning in urban environments," *Aerospace Science and Technology*, vol. 107, 2020.

[10] S. B. Cruz and A. Aguiar, "MagLand: magnetic landmarks for road vehicle localization," *IEEE Transactions on Vehicular Technology*, vol. 69, no. 4, pp. 3654–3667, 2020.

[11] A. Liu, L. Lian, V. Lau, G. Liu, and M. J. Zhao, "Cloud-assisted cooperative localization for vehicle platoons: a turbo approach," *IEEE Transactions on Signal Processing*, vol. 68, pp. 605–620, 2020.

[12] J. Kim, "Non-line-of-sight error mitigating algorithms for transmitter localization based on hybrid TOA/RSSI measurements," *Wireless Networks*, vol. 26, no. 5, pp. 3629–3635, 2020.

[13] L. Dou, C. Song, X. Wang, L. Liu, and F. Gang, "Target localization and enclosing control for networked mobile agents with bearing measurements," *Automatica*, vol. 118, 2020.

[14] L. Dong, D. Sun, G. Han, X. Li, Q. Hu, and L. Shu, "Velocity-free localization of autonomous driverless vehicles in underground intelligent mines," *IEEE Transactions on Vehicular Technology*, vol. 69, no. 9, pp. 9292–9303, 2020.

[15] S. Cui, Y. Wang, S. Wang, R. Wang, W. Wang, and M. Tan, "Real-time perception and positioning for creature picking of an underwater vehicle," *IEEE Transactions on Vehicular Technology*, vol. 69, no. 4, pp. 3783–3792, 2020.

[16] V. Kubelka, P. Dandurand, and P. Babin, "Radio propagation models for differential GNSS based on dense point clouds," *Journal of Field Robotics*, vol. 37, no. 1, 2020.

[17] X. He, X. Zhang, L. Tang, and W Liu, "Instantaneous real-time kinematic decimeter-level positioning with BeiDou triple-

frequency signals over medium baselines," *Sensors*, vol. 16, no. 1, 2015.

[18] F. Shen, J. W. Cheong, and A. G. Dempster, "A DSRC Doppler/IMU/GNSS tightly-coupled cooperative positioning method for relative positioning in VANETs," *Journal of Navigation*, vol. 70, no. 1, pp. 120–136, 2016.

[19] B. Nan, T. Yuan, L. Ye, Z. Yuan, Z. Xiao, and J. Zhou, "A high-precision and low-cost IMU-based indoor pedestrian positioning technique," *IEEE Sensors Journal*, vol. 20, no. 12, pp. 6716–6726, 2020.

[20] Y. H. Qu, F. Zhang, R. N. Gu, and D. Yuan, "Target cooperative location method of multi-UAV based on pseudo range measurement," *Journal of Northwestern Polytechnical University*, vol. 37, no. 02, pp. 63–69, 2019.

[21] K. X. Guo, X. X. Li, and L. H. Xie, "Ultra-Wideband and Odometry-Based Cooperative Relative Localization with Application to Multi-Uav Formation Control," *IEEE Transactions Cybernetics*, vol. 50, no. 6, pp. 2590–2603, 2019.

[22] S. Goel, A. Kealy, and B. Lohani, "Posterior cramér rao bounds for cooperative localization in low-cost UAV swarms," *Journal of the Indian Society of Remote Sensing*, vol. 47, no. 1, pp. 671–684, 2018.

[23] S. Tomic, M. Beko, and M. Tuba, "A linear estimator for network localization using integrated RSS and AOA measurements," *IEEE Signal Processing Letters*, vol. 26, no. 3, pp. 405–409, 2019.

[24] H. Wang, L. Wan, M. Dong, K. Ota, and X. Wang, "Assistant vehicle localization based on three collaborative base stations via SBL-based robust DOA estimation," *IEEE Internet of Things Journal*, vol. 6, no. 3, pp. 5766–5777, 2019.

[25] S. Xu, "Optimal sensor placement for target localization using hybrid RSS, AOA and TOA measurements," *IEEE Communications Letters*, vol. 24, no. 9, pp. 1966–1970, 2020.

[26] M. Rohani, D. Gingras, V. Vigneron, and D. Gruyer, "A new decentralized bayesian approach for cooperative vehicle localization based on fusion of GPS and VANET based inter-vehicle distance measurement," *IEEE Intelligent Transportation Systems Magazine*, vol. 7, no. 2, pp. 85–95, 2015.

[27] X. Song, Y. Ling, H. Cao, and Z. Huang, "Cooperative vehicle localisation method based on the fusion of GPS, inter-vehicle distance, and bearing angle measurements," *IET Intelligent Transport Systems*, vol. 13, no. 4, pp. 644–653, 2019.

[28] H. Naseri and V. Koivunen, "A bayesian algorithm for distributed network localization using distance and direction data," *IEEE Transactions on Signal and Information Processing over Networks*, vol. 5, no. 2, pp. 290–304, 2019.

[29] L. Yin, Q. Ni, and Z. Deng, "Intelligent Multisensor Cooperative Localization under Cooperative Redundancy Validation," *IEEE Transactions on Cybernetics*, vol. 51, no. 4, pp. 2188–2200, 2019.

Research Article

Optimal Design of the Six-Wheel Steering System with Multiple Steering Modes

Haixiang Bu (ID),[1] **Aijuan Li** (ID),[1,2] **Xin Huang** (ID),[3] **Wei Li** (ID),[1] and **Jian Wang** (ID)[1]

[1]*School of Automotive Engineering, Shan Dong Jiaotong University, Jinan 250357, China*
[2]*Zhejiang Samsung Electromechanical Co. Ltd., Wenzhou 325000, China*
[3]*School of Information Science and Electrical Engineering, Shan Dong Jiaotong University, Jinan 250357, China*

Correspondence should be addressed to Aijuan Li; 65826990@qq.com and Xin Huang; huangxin@sdjtu.edu.cn

Vehicles will face different working conditions during the use, and different working conditions have different requirements for vehicle functions, which results in many subdivided models. An off-road vehicle is a subdivision model produced to adapt to complex road conditions. In order to adapt to complex road conditions, vehicles should have a good passing ability, small size, and good flexibility. The six-wheeled vehicle has both good passing ability and small volume, which is the best choice for off-road vehicles. The design of the steering system becomes the key step to improve the flexibility of the six-wheeled vehicle. This paper mainly designs an independent steering system for a six-wheel electric vehicle with higher flexibility. The system is designed for six-wheel electric vehicles driven by six in-wheel motors. It mainly includes mechanical steering system and electronic control steering system. Both mechanical steering systems and electronic control steering system have multiple steering modes. Firstly, this paper introduces the various steering modes of the mechanical steering system and the electronic control steering system. Secondly, a CAD model is established by using the software Solidworks, and the system structure is introduced in detail combined with the CAD model. Finally, a kinematics model is established and calculated. The calculation results showed that the steering system can significantly improve the flexibility of the vehicle, so that the vehicle can complete the steering stably and quickly on complex road sections.

1. Introduction

With the rapid development of the automobile industry, automobile technology has made comprehensive progress. Among them, electric vehicles have developed rapidly with their excellent environmental performance, and the development of electric vehicles has alleviated the energy problem. In an electric vehicle, the steering system is one of the important subsystems, and the steering system has a great influence on the maneuverability and flexibility of the vehicle. Although the traditional steering system can achieve steering, in some cases, the vehicle cannot achieve steering easily. For example, the vehicle needs a small turning radius to pass through a narrow space or requires zero-radius steering to pass through a curve with a large turn angle. With the rapid development of the automobile industry, automobile

practitioners have proposed several new types of steering systems, which improve the flexibility of vehicles. Relevant documents introduced a new type of electric vehicle steering system, including four-wheel steering system [1–4], in-wheel motor drive system [5], control of steering system [6–10], kinematics model, and calculation of four-wheel steering [11–13]. The above system is applied to the four-wheel steering system to improve the handling and flexibility of the four-wheel steering vehicle. The four-wheel steering system includes a four-wheel independent steering system and a four-wheel linkage steering system. The four-wheel independent steering system generally uses the steering motor to drive the wheels to steer independently, so that the steering angle of each wheel can be controlled separately, which improves the flexibility of the vehicle, but the stability is relatively poor. The four-wheel linkage steering system is

generally mechanical linkage steering. In this way, the four-wheel linkage steering has better stability but less steering modes that can be achieved, and the vehicle's flexibility is relatively poor. Therefore, a steering system that combines mechanical steering and electronic control steering is needed to achieve the combination of stability and flexibility.

However, four-wheeled vehicles have a poor passing ability when passing through potholes. In order to improve the passing ability of the vehicle on the complex roads, it is necessary to increase the number of axles. And the length of the four-axle and the eight-wheeled vehicle is too large, which is not conducive to passing through narrow sections during off-road conditions. The three-axle six-wheel vehicle not only has a strong passing ability when passing potholes but also can ensure that its vehicle length is short enough to pass through narrow sections. It is the best choice of axle number for off-road vehicles. Based on the above reasons, this paper proposes a new type of steering system. This steering system is a steering system designed for a three-axle six-wheel in-wheel motor-driven vehicle, which realizes the combination of mechanical steering and electronic control steering. The vehicles driven by in-wheel motors can achieve greater steering angles, and the vehicles can achieve more steering modes. Due to the adoption of a new steering structure, this system has the following advantages:

(1) It can realize multiple steering modes such as the front two-wheel steering mode, the six-wheel in-phase steering mode, the six-wheel reverse-phase steering mode, lateral parking mode, and the zero-radius steering mode. The multiple steering modes make the steering system more flexible.

(2) The electronic control six-wheel steering system has high flexibility, and the mechanical six-wheel steering system has high stability. This steering system realizes the combination of the electronically controlled six-wheel steering system and the mechanical six-wheel steering system so that the system has both the advantages of the electronic control six-wheel steering system and the advantages of the mechanical six-wheel steering system, which makes the steering system have high flexibility and high stability.

(3) The mechanical steering system and the electronic control steering system can work independently. Without the electronic control steering system, the mechanical steering system can realize the three steering modes of the front two-wheel steering, six-wheel in-phase steering, and six-wheel reverse-phase steering. The mechanical steering system can ensure the stable operation of the steering system. The electronic control steering system can also work independently without the use of a mechanical steering system. The electronic control steering system can realize five steering modes to improve the flexibility of the vehicle.

(4) The electronic control steering system can execute the steering command issued by the automatic driving module to realize the steering of automatic driving. Thanks to the multiple steering modes of the system, the driver or the automatic driving module can select the steering mode to control the vehicle, so that the vehicle can adapt to different road conditions with a more appropriate steering mode, and improve the flexibility and passing ability of the vehicle.

The first section of this paper introduces the steering modes of the system [14, 15] and introduces the application scenarios of each steering mode. In the second section, the six-wheel steering system structure is described, and its main components are introduced briefly. The third section combines the CAD model to introduce the working principle of the steering system components in detail and explains the switching principle of the mechanical steering mode of the system. The fourth section mainly introduces the electronic control steering system including system hardware and control methods. The fifth section calculates the steering system, which verifies the performance of the system and provides the necessary data for the electronic control system.

2. Steering Mode and Its Application

This system is a steering system of a six-wheel electric vehicle driven by six in-wheel motors independently. Due to the use of the in-wheel motor drive, the vehicle can achieve large-angle steering easily, which can also achieve more steering modes. Moreover, this steering system adopts a combination of mechanical steering and electronic control steering. Both the mechanical steering system and the electronic control steering system have multiple steering modes.

Figure 1 is a schematic diagram of the steering mode, where Figure 1(a) indicates the vehicle is not steering, Figure 1(b) indicates the front two-wheel steering mode, Figure 1(c) indicates the six-wheel reverse-phase steering mode, Figure 1(d) indicates the six-wheel in-phase steering mode, Figure 1(e) indicates the zero-radius steering mode, and Figure 1(f) indicates the lateral parking mode. Figure 2 is a schematic diagram of the application scenario of the steering mode, where Figure 2(a) represents the application of the six-wheel reverse-phase steering mode, Figure 2(b) represents the application of the six-wheel in-phase steering mode, Figure 2(c) represents the application of the zero-radius steering mode, and Figure 2(d) represents the application of the lateral parking mode, because the application of the front two-wheel steering mode is relatively simple, so it is not marked in Figure 2. The steering mode is introduced in combination with Figure 1, and the application of steering mode is introduced in combination with Figure 2.

(a)   (b)   (c)

(d)   (e)   (f)
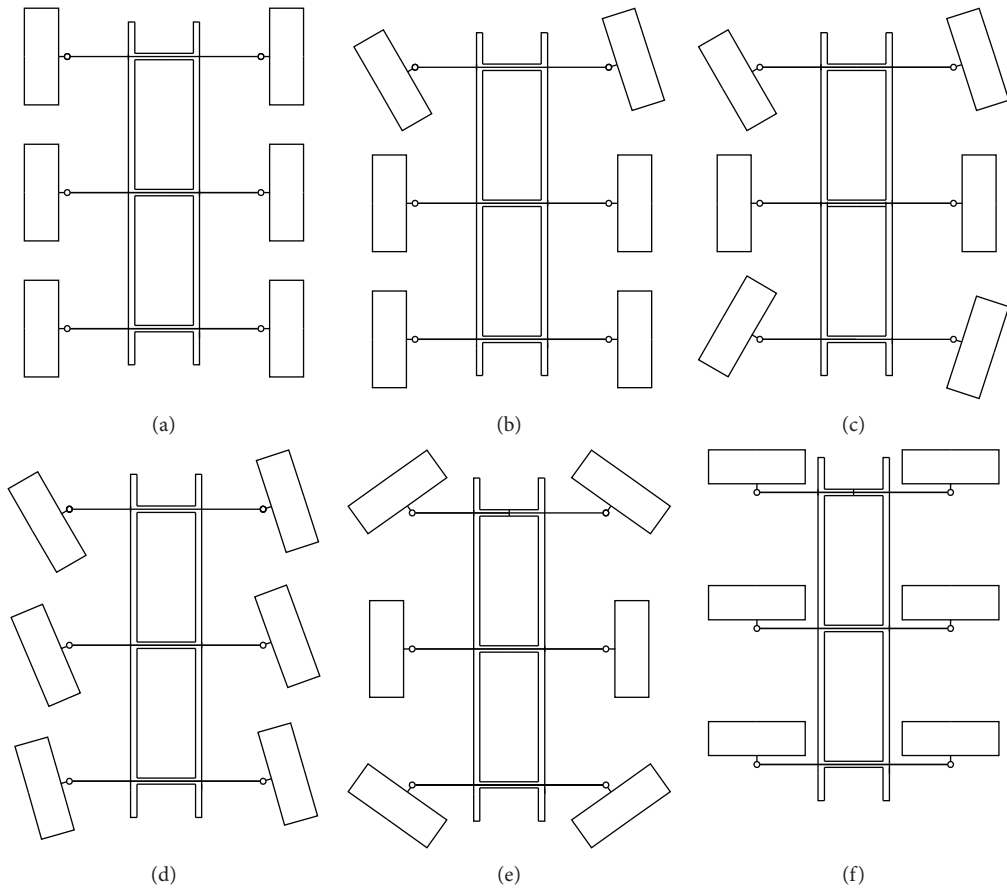
FIGURE 1: Schematic diagram of steering mode.

(a)   (b)

(c)   (d)
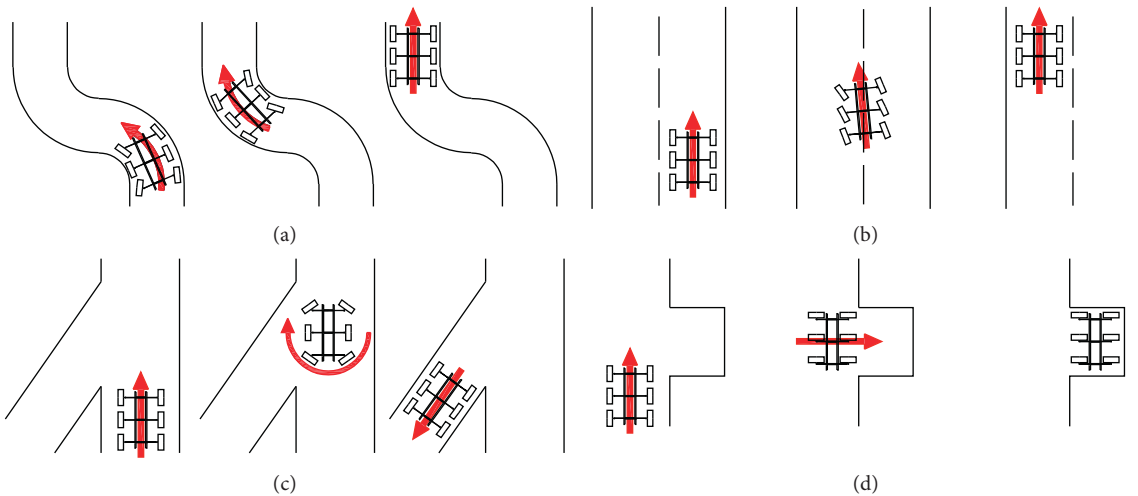
FIGURE 2: Schematic diagram of the application scenario of the steering mode.

2.1. Front Two-Wheel Steering. When the steering system is in the mechanical front two-wheel steering mode, the mechanical steering mechanism of the rear four wheels is locked. Only the front-wheel steering mechanism is linked with the steering wheel, and the steering operation is relatively light at this time, which can reduce the labor intensity of the driver. When the front two wheels are steered electronically, only the steering motors of the front two wheels need to be controlled independently, and the control strategy is relatively simple. The vehicle can adopt front two-wheel steering mode when driving at medium or low speeds on a generally straight road.

2.2. Six-Wheel Reverse-Phase Steering. When the steering system is in the mechanical six-wheel reverse-phase steering mode, the steering wheel is linked with the steering mechanism of the first and third axle. At this time, the mechanical steering mechanism of the intermediate axle is locked, and the steering gears of the first and third axles are linked reversely. When in the electric control six-wheel reverse-phase steering mode, the four steering motors of the first axle and the third axle drive the four wheels to steer independently. The six-wheel reverse-phase steering mode has a smaller steering radius and better flexibility. As shown in Figure 2(a), the six-wheel reverse-phase steering is suitable for working conditions when steering in a narrow space such as an S-shaped curve. Even in a narrower and more tortuous S-shaped curve, the vehicle can pass quickly.

2.3. Six-Wheel In-Phase Steering. When the steering system is in the six-wheel in-phase steering mode, all six wheels steer in the same direction, which can ensure that the tires receive less lateral force when the vehicle is steering, and increase the steering stability of the vehicle. When the steering system is in the mechanical six-wheel in-phase steering mode, the steering wheel and the three axles are linked. When the steering system is in the electronic control six-wheel in-phase steering mode, the steering controller controls the six steering motors independently, and the motors drive the six wheels to steer independently. This mode is suitable for high-speed vehicle operating conditions. As shown in Figure 2(b), when the vehicle changes lanes at high speed, the six wheels steer at the same time, which makes the vehicle more stable and has better maneuverability.

2.4. Zero-Radius Steering. The mechanical steering system of this steering system cannot realize the function of zero-radius steering, and the zero-radius steering mode can only be realized by an electronic control steering system. In the zero-radius steering mode, the steering center of the vehicle is located at the center of the second axle, and the wheels of the second axle do not steer when the vehicle is steering. The steering controller controls the four steering motors of the first and third axles to drive the wheels to steer independently. The zero-radius steering mode is mainly used to realize a zero-radius U-turn of the vehicle and is suitable for steering the vehicle in a narrow space. As shown in Figure 2(c), when a vehicle passes a Y-shaped intersection in a narrow space, it can turn directly to the target direction by zero-radius steering mode, so that the vehicle can pass the intersection quickly.

2.5. Lateral Parking. The mechanical steering system of this steering system cannot realize the function of lateral parking, and the lateral parking mode can only be realized by the electronic control steering system. When moving laterally, the steering controller controls the six motors to drive the six wheels to rotate 90° independently. At this time, the wheels are parallel to the *Y* direction of the vehicle coordinate

system, and the vehicle can move laterally easily. The main design purpose of lateral parking is to facilitate parking on the side of the city. As shown in Figure 2(d), the lateral parking space is only slightly larger than the vehicle. If it is a car equipped with a traditional steering mechanism, it cannot park in the parking space. However, the steering mode of lateral movement allows the vehicle to move laterally into the parking space directly, making the parking of the vehicle more convenient.

3. System Structure

The advantage of traditional mechanical steering technology is to maintain kinematic constraints through the mechanical connecting rods of the front wheels. The traditional vehicle steering system has good stability, which can ensure the safety of vehicle driving. However, in order to achieve zero-radius steering and lateral parking, each wheel needs to steer independently, and each wheel is equipped with an independent steering motor, which can realize the independent steering of the wheel. The independent steering system of the wheels has better functionality, but its control is more difficult. Although each wheel can achieve the kinematic constraint in a steady state independently, it can not guarantee the kinematic constraint in a transient state. Based on the problems of the traditional vehicle steering system and independent steering system, a new steering system is proposed in this paper. The system is composed of a mechanical steering system and electric control steering system. The system combines the advantages of a mechanical steering system and electric control steering system and has good stability and function. Both the mechanical steering system and electric steering system have many steering modes, which can choose more appropriate steering mode in different scenarios.

The mechanical steering system of this system is pure mechanical steering in essence. The mechanical steering system mainly includes the steering wheel, the transmission device of the steering wheel and the steering mechanism, the steering mechanism on the three axles, and the longitudinal linkage rack. The driver controls the steering system through the steering wheel, and the transmission device of the steering wheel and the steering mechanism can transmit the steering wheel angle to the steering mechanism of the first axle. The steering mechanism of the first axles is linked with the steering mechanism of the other two axles through the longitudinal transmission rack to realize the three-axle linkage steering. The longitudinal movement of the longitudinal transmission rack can realize the linkage of three steering mechanisms, and the lateral movement of the longitudinal transmission rack can switch the steering mode.

The electronic control steering system and the mechanical steering system can work independently, but they are not two completely independent systems in the design scheme, and some parts are shared. The electronic control steering system also drives the wheels to steer through the tie rod, and the steering motor is installed on the sliding base. When the steering motor drives the tie rod to achieve steering, the sliding base is fixed, and each sliding base is

equipped with two steering motors, and the steering motor drives the corresponding wheels to steer independently. And when the motor drives the tie rod to move, the screw transmission mechanism is adopted, which makes it produce a self-locking effect. In this way, the steering motor can drive the tie rod to move, but the tie rod cannot drive the steering motor to move, which improves the accuracy of motor control.

4. CAD Modeling

The structure of the steering system is relatively complicated. In order to analyze the steering system comprehensively, this paper uses the software Solidworks to establish a three-dimensional CAD model. Figure 3 is the overall model of the steering system. From the figure, the overall structure of the steering system can be seen. The following is a detailed introduction of this structure combined with a three-dimensional CAD model.

4.1. Steering Mechanism. The steering system has three steering mechanisms; each axle has a steering mechanism. The structures of the steering mechanism on the three axles are roughly the same. However, in order to realize different functions of the steering mechanism on each axle, the parts on the steering mechanism are different to a certain extent. The sliding sleeve of the steering mechanism of the first axle is connected with the transmission shaft, the steering mechanism of the second axle needs to have a locking device, and the steering mechanism of the third axle needs to have a gear locking device and a reverse steering function. The following takes the steering mechanism of the second axles as an example to introduce. As shown in Figures 4 and 5, it includes a sliding base, a fixed base, a sliding sleeve, a gear set, and a steering rack.

The composition of the sliding base is shown in Figures 6 and 7. Two steering motors are fixed on the sliding base, and the steering motor drives the driving gear and the driven gear to rotate. There is a threaded hole in the center of the driven gear, the D-type screw is matched with the threaded hole of the driven gear. The axial displacement of the driven gear is fixed and can only be rotated. Then, the D-type screw and the driven gear form a spiral transmission mechanism. In this way, the rotation of the motor can be converted into the lateral movement of the D-type screw to drive the wheels to steer, and the screw transmission mechanism can be self-locking, so the D-type screw cannot drive the motor in reverse, which reduces the difficulty of controlling the motor, and also improves control precision. In the electronic control steering mode, the sliding base is in the initial position and locked. At this time, the sliding base cannot slide. The two steering motors drive the D-type screw to move independently, thereby driving the tie rod to achieve steering. In mechanical steering mode, since the screw mechanism can be self-locked, the D-type screw will not move relative to the sliding base when the steering motor is not working, so the D-type screw and the sliding base are relatively fixed, and the movement of the sliding base can directly drive the tie rod to realize steering.

4.2. Linkage Mode of Steering Mechanism. This system can realize six-wheel steering, and six-wheel steering needs to realize the linkage of the steering mechanism on the three axles. The steering mechanism linkage diagram is shown in Figure 8. The longitudinal linkage rack realizes the linkage of the steering mechanism on the three axles. The longitudinal linkage rack has longitudinal and lateral movement relative to the fixed base. The longitudinal movement of the longitudinal linkage rack will drive the steering mechanism to linked steering, and the lateral movement can switch the steering mode. The installation of the longitudinal linkage rack and the sliding sleeve is shown in Figure 9. This paper uses the sliding sleeve to connect the longitudinal linkage rack and the fixed base. The sliding sleeve can slide left and right within a certain range on the fixed base, and the longitudinal linkage rack can move longitudinally relative to the sliding sleeve. There is a linkage gear set on the fixed base, and the linkage gear set has a driving gear, which drives the steering rack to move when the driving gear rotates. The steering rack drives the sliding base to move left and right, which drives the wheels to steer. The longitudinal linkage rack meshes with the driving gear on the three steering gears to realize the linkage of the steering gear, and the meshing situation varies according to the steering mode.

4.3. Switching the Steering Mode. This system has two steering modes: the mechanical steering mode and the electronic control steering mode. The conversion of electronic control steering mode can be realized in the control strategy. The switch of mechanical steering mode will be introduced first. For the stability of mechanical steering mode switching, there is an initial state of the mechanical steering system. The initial state of mechanical steering is that all wheels are not steering. The steering system needs to be in the initial state when switching the steering mode.

The meshing conditions of the longitudinal linkage rack and the driving gears on the three steering mechanisms are different under different steering modes. The longitudinal linkage rack changes the meshing with the driving gear through lateral movement and realizes the conversion of the steering mode. The switching of the steering mode is shown in Figure 10. Figure 10(a) is the front two-wheel steering mode. In this mode, only the steering gear of the first axle meshes with the longitudinal linkage rack. Figure 10(b) is a six-wheel reverse-phase steering mode. In this mode, the steering gear of the first axle and the reverse-phase steering gear of the third axle mesh with the longitudinal linkage rack. Figure 10(c) is the six-wheel in-phase steering mode. In this mode, the steering gear of the first axle, the steering gear of the second axle, and the in-phase steering gear of the third axle mesh with the longitudinal linkage rack. When the gear and the rack are disengaged, there is a corresponding mechanism to lock it, so that the next time it is engaged, it can be engaged in the correct position. The mode switching joystick drives the sliding base to move by pulling the wire, thereby driving the longitudinal linkage rack to move horizontally. The parts in Figure 10 are only schematic diagrams and do not reflect the size of the parts.
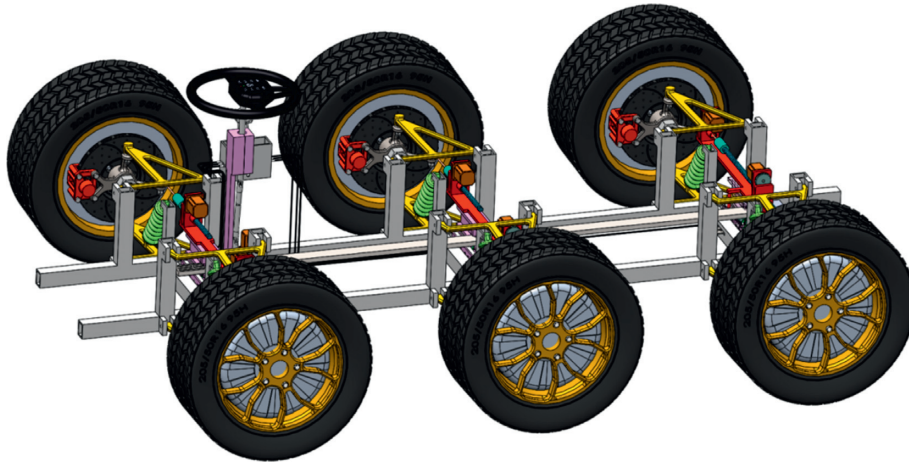
FIGURE 3: General diagram of the steering system.
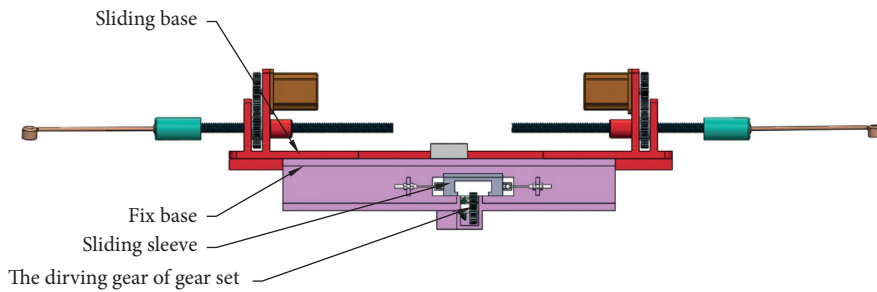
FIGURE 4: First view of the steering gear.
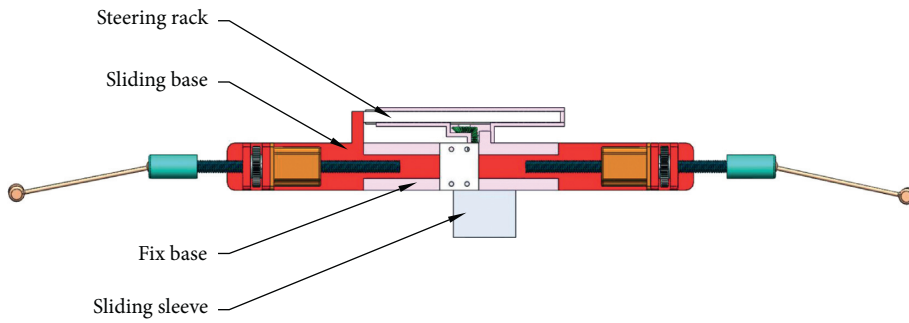
FIGURE 5: Second view of the steering gear.
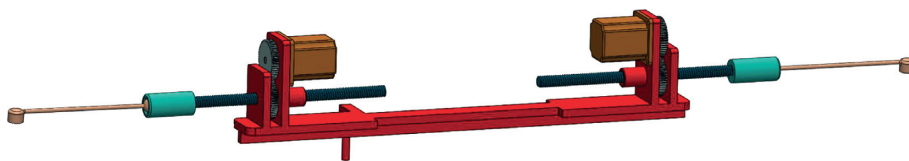
FIGURE 6: General composition of the sliding base.

4.4. Transmission of Steering Wheel and Longitudinal Linkage Rack. The steering wheel drives the longitudinal movement of the longitudinal linkage rack to drive the corresponding sliding base to move to achieve steering. The schematic diagram of the steering wheel and longitudinal linkage rack transmission is shown in Figure 11. The steering wheel drives

the steering column, the universal joint, the transmission shaft, the gear set on the sliding sleeve, and finally the pinion of the gear set to rotate. The pinion meshes in the longitudinal groove of the longitudinal linkage rack. The gear set on the sliding sleeve is fixed on the sliding sleeve of the first axle, and the sliding sleeve can only slide laterally, so when the pinion
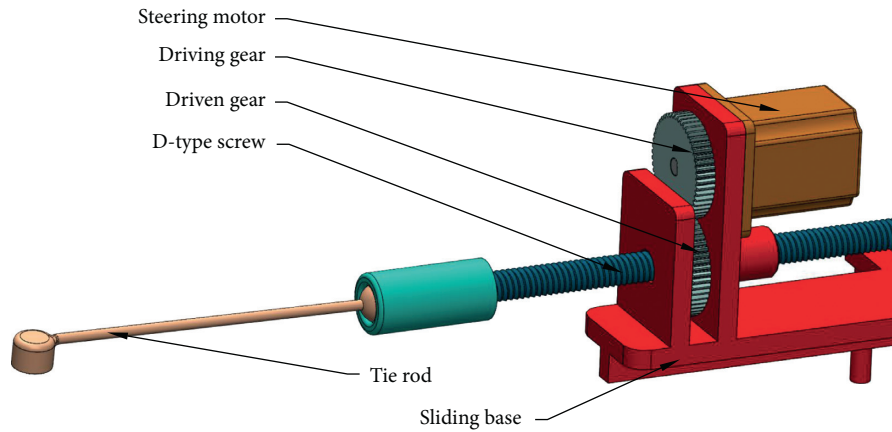
FIGURE 7: Enlarged view of sliding base.
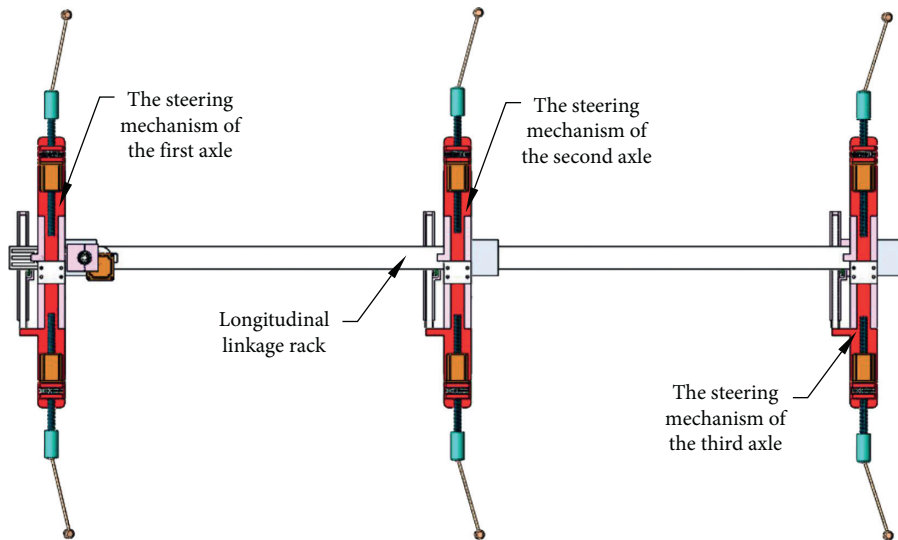
FIGURE 8: Steering mechanism linkage diagram.

rotates, it drives the longitudinal linkage rack to move longitudinally and will not cause lateral movement of the sliding sleeve. The power-assisted motor in Figure 11 plays the role of assisting the driver when steering and restoring the initial state of mechanical steering when the electronic control mode is activated.

5. Control of the Electronic Steering System

5.1. Operation of Electronic Steering. The operation of the electronic control steering system can be controlled directly by the driver, and it can also be controlled by the automatic driving module. The automatic driving module does not need to operate the panel, and the driver needs to have an operation panel when operating, and the operation panel of the steering system is integrated into the steering wheel. The steering wheel control panel is shown in Figure 12.

The power button is used to activate and deactivate the electronic control steering system. In Figure 12, the five buttons 2FWS, 6WRS, 6WIS, LP, and ZRS are the selection buttons for the five steering modes of the front two-wheel

steering mode, six-wheel reverse-phase steering mode, six-wheel in-phase steering mode, lateral shift parking mode, and zero-radius steering mode. The two buttons of the left and right arrows are used to control the steering direction, and the reset button is used to reset the electronic control steering system.

The driver presses the power button for 3 seconds to enter the electronic control mode. After the green light flashes, press the corresponding steering mode button to select the steering mode. After the green light is always on, it enters the corresponding steering mode. At this time, pressing the two buttons of the left and right arrows will turn the steering system in the corresponding direction and release the button to stop the steering system.

5.2. Realization of Control. In order to realize the functions of this system, the hardware of the electrical system needs to cooperate to realize cooperative work. Figure 13 is the hardware diagram of this system. The system hardware needs a corresponding control method to realize the control
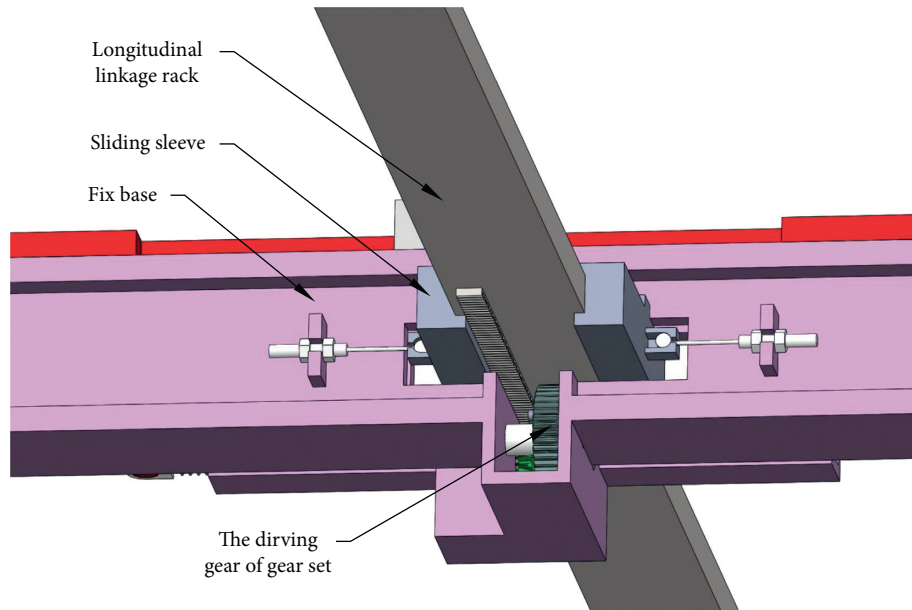
FIGURE 9: Installation diagram of the sliding sleeve of longitudinal linkage rack.

(a)   (b)   (c)
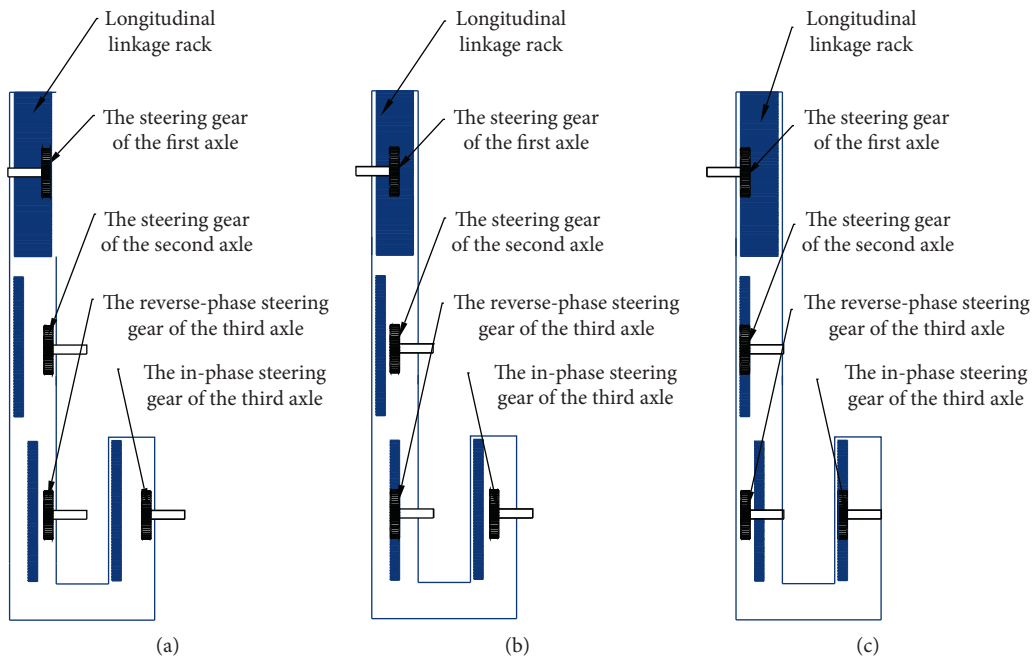
FIGURE 10: Schematic diagram of steering mode.

of the system. The control method of this system will be introduced combined with the system hardware.

In the default state, the electronic control steering system is not started. When entering the electronic control steering mode, the electronic control steering system should be started first. Firstly, when starting the electronic control steering system, the steering controller will receive the signal of starting the electronic control steering system from the control button or the automatic driving module. After receiving this signal, the wheel angle sensor will detect whether the wheel is in the initial steering state. If it is in the initial

steering state, the mechanical steering locking motor will lock the mechanical steering system. If it is not in the initial steering state, the red light on the control panel will flash, and then the power-assisted motor will restore the steering system to the initial steering state. The red light no longer flashes after returning to the initial state. At this time, the locking motor of the mechanical steering will lock the mechanical steering system, and the green light will flash after the mechanical steering system is locked. Then, the corresponding steering mode is selected according to the steering mode signal input by the automatic driving module
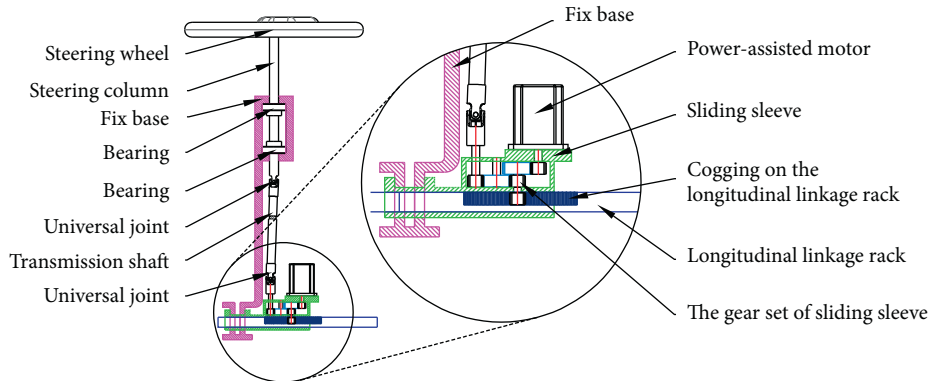
FIGURE 11: Schematic diagram of the steering wheel and longitudinal linkage rack transmission.

or the driver. After confirming the steering mode, the green light is always on, and the steering system enters the electronic control steering state.

The control input of the system has two input modes: the input of the automatic driving module and the input of the driver. When the automatic driving module inputs the control signal, the automatic driving controller analyzes the data collected by the automatic driving sensor and then calculates the steering angle of the front inner wheel and then inputs the steering angle signal of the front inner wheel to the steering controller. When the driver inputs the control signal, the driver inputs the front inner wheel angle signal to the steering controller by pressing the button. After the steering controller receives the input signal of the front inner wheel angle, it compares the steering angles of the remaining five wheels in the database according to the steering mode and then controls the steering motor separately according to the steering angle of each wheel. After the steering motor generates the steering angle, the wheel angle sensor detects the wheel angle, corrects the error of the angle in time, and realizes the closed-loop control of the steering angle. The steering controller individually controls the steering angle of each steering motor to realize the independent steer of the wheels by a certain angle. In order to satisfy Ackerman's theorem [16, 17] under different steering modes, the steering angle of each wheel is different. In the steering kinematics model, the relationship between the wheel steering angles in various modes is calculated.

6. Modeling and Analysis

When a vehicle is steering, it will be affected by the tire slip angle, and the tire slip angle affects the vehicle's steering center. Since there are many factors that affect the tire slip angle, and it is difficult to accurately determine, the following is to analyze the steering problem of the vehicle under the influence of ignoring the slip angle. Since the vehicle has different steering modes, this section will analyze the different steering modes and compare the steering states under different steering modes.

6.1. Kinematics Analysis of Different Steering Modes. The steering system has five steering modes, including the front

two-wheel steering mode, six-wheel reverse-phase steering mode, six-wheel in-phase steering mode, and zero-radius steering mode, which are all steering around a steering center. This paper mainly analyzes the kinematics of these four steering modes. In the lateral parking mode, the vehicle moves horizontally, and the kinematics model is relatively simple, so the kinematics analysis is not needed.

(1) Front two-wheel steering mode: for the general steering system, the axes of all wheels should intersect at the instantaneous steering center. The system has three axles, and the wheels of the rear two axles do not steer in this mode. In this mode, not all the axes of the wheels intersect at the instantaneous steering center, and the instantaneous steering center is located in the middle of the rear two axles.

As shown in Figure 14, the inner wheel steering angle of the first axle is α_1, the outer wheel steering angle of the first axle is β_1, the wheelbase $L_1 = 1350$ mm, and the kingpin distance $K = 1225$ mm. Usually, the maximum steering angle of the wheel is 35°; although the system can achieve a large steering angle, it cannot make the steering angle too large in this mode. The maximum wheel's steering angle of the system is controlled at 35°, and the minimum steering radius is calculated.

When the minimum turning radius is calculated, the outer wheel steering angle is required. And when the vehicle is steering, the inner wheel steering angle is greater than the outer wheel steering angle. Therefore, the steering angle of the inner wheel is limited by a maximum of 35°. In order to obtain the degree of outer wheel steering angle when the inner wheel steering angle is 35°, the relationship between the steering angle of the inner wheel and the steering angle of the outer wheel is required. The relationship between the inner wheel steering angle α and the outer wheel steering angle β is as follows:

$$\cot \beta - \cot \alpha = \frac{K}{L}. \tag{1}$$

According to formula (1), the calculation formula of β is obtained:
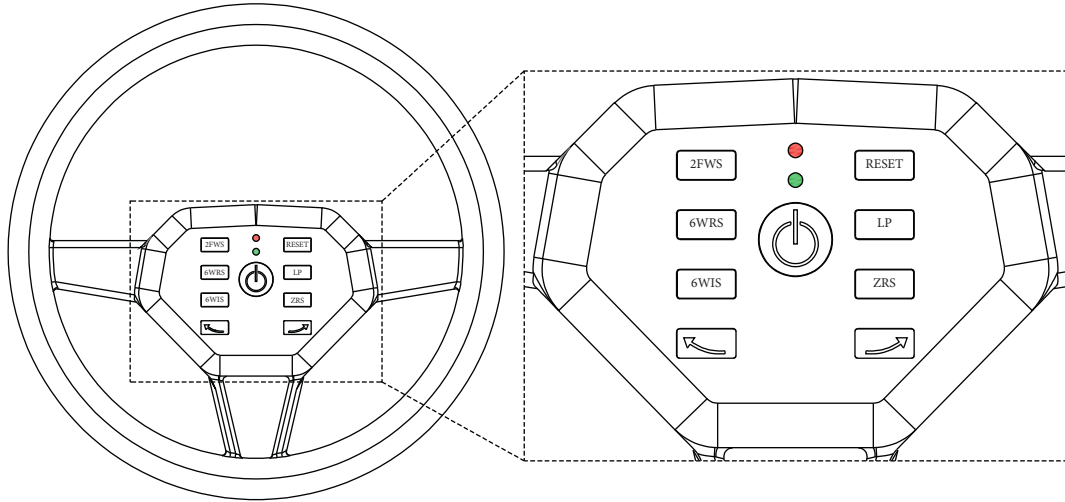
FIGURE 12: Steering wheel control panel.
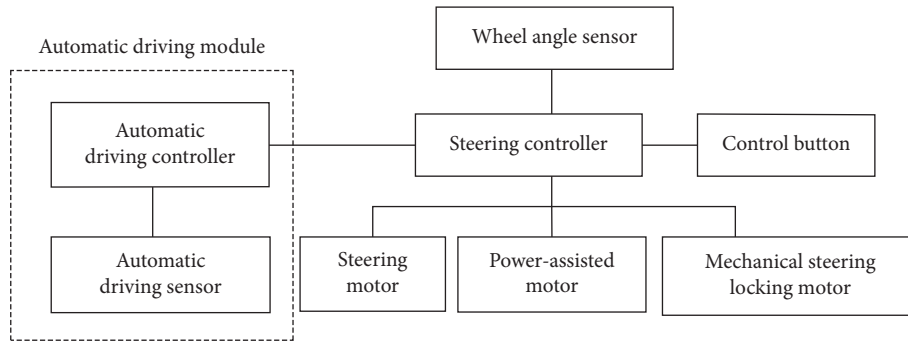
FIGURE 13: Hardware diagram of the electronic control steering system.

$$\beta = \arctan\left(\frac{1}{(K/L) + (1/\tan \alpha)}\right). \tag{2}$$

And, the steering radius of the vehicle can be calculated by

$$r = \frac{L}{\sin \beta} + r_S. \tag{3}$$

When formula (2) is brought into formula (3), we can get the relationship between r and L, K, α, and r_S which is shown in

$$r = \frac{L}{\sin\left(\arctan\left(1/((K/L) + (1/\tan \alpha))\right)\right)} + r_S. \tag{4}$$

From formula (1) to formula (4), r is the steering radius, β is the outer wheel steering angle, α is the inner wheel steering angle, K is the kingpin distance and $K = 1225$ mm, r_S is the kingpin offset distance, and $r_S = 165$ mm. For general vehicles, L is the wheelbase, but for multiaxle vehicles, L is the distance from the steering axle to the horizontal straight line where the steering center is located. So, in this system, L is different in different steering modes.

In the front two-wheel steering mode, the relationship between the inner wheel steering angle α_1 and outer wheel steering angle β_1 of the first axle can be calculated according to formula (2), and the result is shown in Figure 15. According to formula (4), the turning radius can be calculated. And in the front two-wheel steering mode, the distance from the steering axle to the horizontal straight line where the steering center is located is L_1, so in this mode, $L = L_1 = 1225$ mm. When the inner wheel steering angle is the maximum, the steering radius is the minimum, and the maximum inner wheel steering angle is 35°. Putting $L = 1350$ mm, $\alpha = 35°$, $K = 1225$ mm, and $r_S = 165$ mm into formula (4), we can calculate the minimum turning radius, and the minimum steering radius in front two-wheel steering mode is about 3595 mm calculated by formula (4).

(2) Six-wheel reverse-phase steering mode: in this mode, the steering center is on the extension line of the second axle, the wheels of the second axle do not steer in this mode, and the wheels of the first and third axles steer.

As shown in Figure 16, the inner wheel steering angle of the first axle is α_2, the outer wheel steering angle of
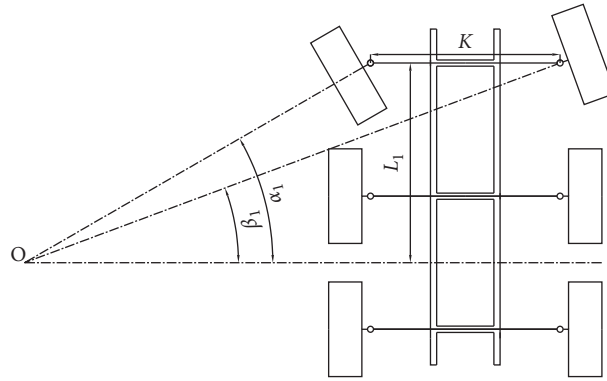
FIGURE 14: Schematic diagram of the steering angle of each wheel in the front two-wheel steering mode.
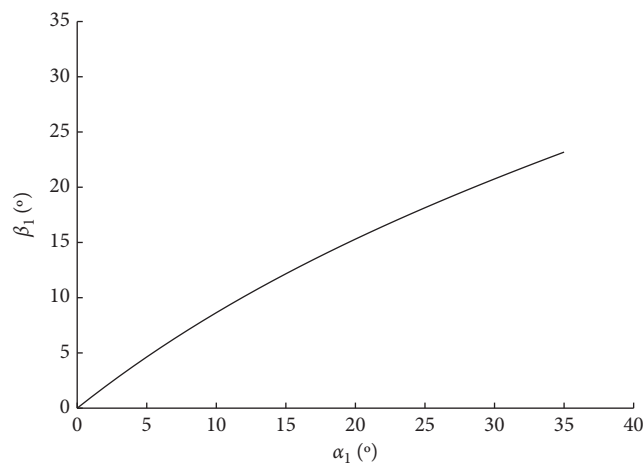
FIGURE 15: The relationship diagram of the first axle inner wheel angle for the outer wheel angle.

the first axle is β_2, the inner wheel steering angle of the third axle is α_3, the outer wheel steering angle of the third axle is β_3, the wheelbase between the first axle and the second axle is L_2, and the wheelbase between the second axle and third axle is L_3. In the six-wheel reverse-phase steering mode, the first axle and the third axle are steering axles, so the inner wheel steering angle is α_2 or α_3, and the outer wheel steering angle is β_2 or β_3. And $L_2 = L_3 = 900$ mm, $K = 1225$ mm, $\alpha_2 = \alpha_3$, and $\beta_2 = \beta_3$. According to formula (2), the relationship between the α_2 and β_2 is calculated, and the result is shown in Figure 17. Because of $\alpha_2 = \alpha_3$, $\beta_2 = \beta_3$, the relationship between α_3 and β_3 can also be represented by Figure 17.

In the six-wheel reverse-phase steering mode, the first and third axles are steering axles, and the steering center is on the extension line of the second axle. So, the distance from the steering axle to the horizontal straight line where the steering center is located is L_2 and L_3, and $L_2 = L_3 = 900$ mm, so in this mode, $L = L_2 = L_3 = 900$ mm. In this mode, α_2 and α_3 are both inner wheel steering angles and $\alpha_2 = \alpha_3$, so in this mode, $\alpha = \alpha_2 = \alpha_3 = 35°$. When the inner wheel steering angle α is the maximum, the steering radius

is the minimum, and the maximum of α is 35°. Taking $L = 900$ mm, $\alpha = 35°$, $K = 1225$ mm, and $r_S = 165$ mm into formula (4) can calculate the minimum turning radius, and the minimum steering radius in six-wheel reverse-phase steering mode is about 2832 mm calculated by formula (4).

It can be seen from the calculation results that when the maximum in-wheel steering angle is 35°, and the minimum turning radius in the six-wheel reverse-phase steering mode is approximately 763 mm smaller than that in the front two-wheel steering mode. The main reason is that in the front two-wheel steering mode, only the two wheels of the first axle are responsible for steering. In this mode, the steering center is located in the middle of the rear two axles. So the wheelbase L is bigger in this mode. In the six-wheel reverse-phase steering mode, two wheels of the first axle and two wheels of the third axle are responsible for steering. The steering center is located on the extension line of the second axle, and the wheelbase L is small in this mode. When the wheelbase L of the vehicle is larger, the turning radius of the vehicle is larger. When the wheelbase L of the vehicle is smaller, the turning radius of the

vehicle is smaller. Therefore, the minimum turning radius in the front two-wheel steering mode is bigger than that in the six-wheel reverse-phase steering mode. The flexibility of the six-wheel reverse-phase steering mode has been improved significantly.

(3) Six-wheel in-phase steering mode: in this mode, the wheels on all three axles are steered, and the steering center is located behind the third axle.

As shown in Figure 18, the steering angle of the inner wheel of the first axle is α_4, the outer steering angle of the first axle is β_4, the steering angle of the inner wheel of the second axle is α_5, the outer steering angle of the second axle is β_5, the steering angle of the inner wheel of the third axle is α_6, the outer steering angle of the third axle is β_6, the lateral distance from steering center to kingpin joint is X, the longitudinal distance from the first axle to the steering center is L_4, the longitudinal distance from the second axle to the steering center is L_5, and the longitudinal distance from the third axle to the steering center is L_6. We calculate the relationship between the first, second, and third axle inner wheel steering angles by formula (6). Then, we calculate the steering angle of the outer wheels of each shaft according to formula (2), and the corresponding steering angle relationship is shown in Figure 19. In Figure 18 $L_4 = 3600\,\text{mm}$, $L_5 = 2700\,\text{mm}$, $L_6 = 1800\,\text{mm}$, and $K = 1225\,\text{mm}$.

The following can be drawn from Figure 18:

$$\tan \alpha_4 = \frac{L_4}{X},$$

$$\tan \alpha_5 = \frac{L_5}{X}, \qquad (5)$$

$$\tan \alpha_6 = \frac{L_6}{X}.$$

Then, there is

$$\alpha_5 = \arctan\left(\frac{3}{4}\tan \alpha_4\right),$$
$$\qquad (6)$$
$$\alpha_6 = \arctan\left(\frac{1}{2}\tan \alpha_4\right).$$

As can be seen from Figure 19, the relationship between the inner wheels steering angle of the three axles is fixed, with the change of the steering angle, the proportion of the steering angle of each axle also changes, but it is always stable in a range. The steering ratio of the mechanical steering system is fixed, so it is necessary to choose a more appropriate transmission ratio. According to the angle relationship in Figure 19 and considering the design of the steering gear set, this paper selects the transmission ratio between the three axles as $1 : 0.75 : 0.50$ in the mechanical six-wheel in-

phase steering mode, which can ensure that the three axles steer at the appropriate angle ratio.

(4) Zero-radius steering mode: in this mode, the vehicle has the minimum steering radius, and the steering center of the vehicle is located in the center of the vehicle, that is, at the midpoint of the second axle of the vehicle. At this time, the wheels of the first axle and the third axle steer, and the wheels of the second axle do not steer. And the vehicle revolves around the steering center in the vehicle; only a small circular field is needed to realize the U-turn or steering.

As shown in Figure 20, the wheel diameter is D, the tire width is W, the radius of the circular space required for steering is R, the first axle left wheel steering angle is n_1, the third axle left wheel steering angle is n_2, the third axle right wheel steering angle is n_3, the first axle right wheel steering angle is n_4, the wheelbase between the first axles and the second axles is $L_7 = 900\,\text{mm}$, the wheelbase between the second axles and the third axles is $L_8 = 900\,\text{mm}$, and the distance between the kingpin joint of the first axle and the steering center is F. The distance between two kingpin joints is $M = 1225\,\text{mm}$. In this mode, $n_1 = n_2 = n_3 = n_4$. The tire specifications selected by this system are 205/50 R16 95H. According to formula (10), the space required for the vehicle's zero-radius steering can be calculated.

To calculate the space required for zero-radius steering, the tire diameter D should be calculated first.

$$D = \frac{2WV}{100} + d \times 25.4. \qquad (7)$$

Then, according to Figure 20, it is concluded that

$$F = \sqrt{L_7^2 + \left(\frac{M}{2}\right)^2}, \qquad (8)$$

$$R = \sqrt{\left(F + r_S + \frac{W}{2}\right)^2 + \left(\frac{D}{2}\right)^2}, \qquad (9)$$

$$R = \sqrt{\left(\sqrt{L_7^2 + \left(\frac{M}{2}\right)^2} + r_S + \frac{W}{2}\right)^2 + \left(\frac{D}{2}\right)^2}, \qquad (10)$$

$$n_1 = n_2 = n_3 = n_4 = \arctan \frac{2L_7}{M}, \qquad (11)$$

where tire aspect ratio $V = 50$ and the distance between two kingpin joints $r_s = 165\,\text{mm}$. We put $L_7 = 900\,\text{mm}$, $L_8 = 900\,\text{mm}$, $M = 1225\,\text{mm}$, $r_s = 165\,\text{mm}$, and $V = 50$ into formula (10) to calculate the required steering space in this mode. It is calculated that the steering radius required in this mode is about 1390 mm, and the wheel steering angle is $n_1 = n_2 = n_3 = n_4 = 55.76°$. Compared with the steering radius of 2834 mm in the six-wheel reverse-phase steering mode, it is reduced by 1444 mm, and the flexibility of the vehicle is significantly improved [18].
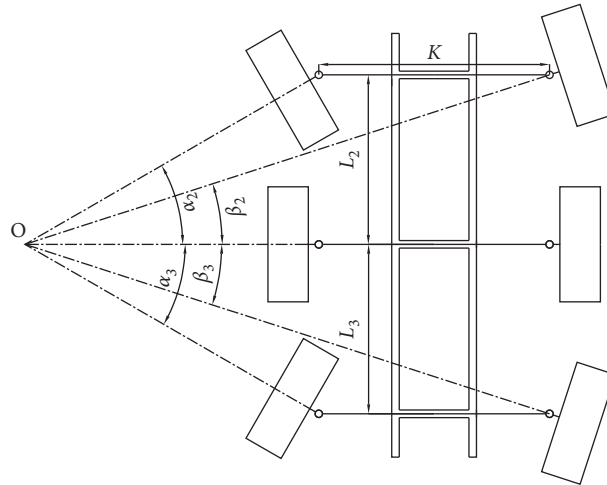
Figure 16: Schematic diagram of each wheel angle under the six-wheel reverse-phase steering mode.
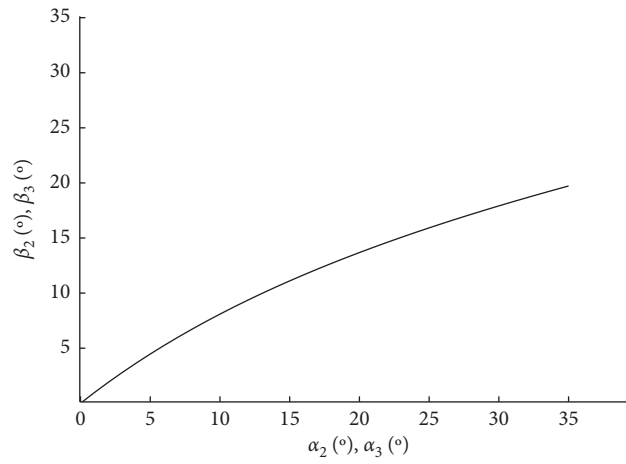
Figure 17: Relationship between $\alpha_2(\alpha_3)$ and $\beta_2(\beta_3)$.
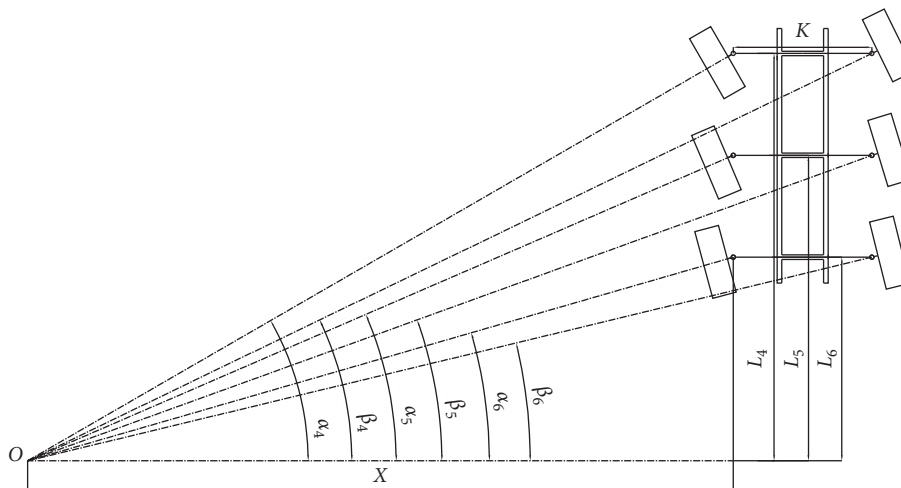
Figure 18: Schematic diagram of the steering angle of each wheel in the six-wheel in-phase steering mode.

6.2. Kinematics Analysis of the Steering Trapezoid. The vehicle matched with the steering system is an off-road vehicle, and the design of the steering system is more inclined to the off-road performance. The six-wheel reverse-phase steering is more suitable for off-road conditions. Therefore, the steering trapezoid is designed according to the theoretical Ackerman steering angle of six-wheel reverse-phase steering [19]. The suspension of the vehicle matched with this steering system adopts independent suspension, so a segmented steering trapezoid mechanism is needed. The kinematics model of steering trapezoid is shown in Figure 21.

According to experience and vehicle parameters, the parameters of the steering trapezoid of this system are selected [20], the software Solidworks is used for simulation, and the parameters are adjusted. The parameters of the steering trapezoid are finally determined as shown in Table 1.

The Ackerman ratio is the ratio of the actual angle difference between the inner and outer wheels and the theoretical angle difference between the inner and outer wheels. According to different situations, the steering Ackerman ratio will affect the tire wear and steering return performance, so it is necessary to calculate the steering Ackerman ratio. According to the actual outer wheel angle and formula (12), the steering trapezoid is verified, and the Ackerman ratio satisfaction of the steering system is shown in Table 2.

$$R_{AC} = \frac{\theta_i - \theta_{or}}{\theta_i - \theta_o} \times 100\%. \tag{12}$$

Here, R_{AC} is the Ackerman rate, θ_i is the inner wheel steer angle, θ_{or} is the actual outer wheel steer angle, and θ_o is the Ackerman theoretical outer wheel steer angle.

The Ackerman rate is 100% for standard Ackerman steering because the tire is a nonrigid body, the steering

performance of the vehicle in the standard Ackerman steering mode is not the best, and the tire wear is more serious. Generally speaking, when the inner wheel angle is less than 20°, the Ackerman rate is more appropriate in the range of 40–60. And when the inner wheel angle is 20° to 35°, the Ackerman rate is more appropriate in the range of 60–80. From the data in Table 2, it can be seen that the Ackerman rate of the mechanical steering system meets the requirements, and the performance of the steering trapezoid is better.

The steering controller controls the rotation angle of the steering motor. The steering motor drives the lateral movement of the D-type screw, and the lateral movement of the D-type screw drives the tie rod, which in turn drives the wheels to steer. In the transmission process, the distance between the motor rotation angle and the lateral movement of the D-type screw has a fixed transmission ratio. However, there is no fixed transmission ratio between the moving distance of the D-type screw and the wheel steer angle. It is necessary to calculate the relationship between the moving distance of the D-type screw and the wheel steer angle so that the motor can be controlled more quickly during the control process. Combining the parameters of the steering trapezoid, the relationship between the moving distance of the D-type screw and the wheel steer angle is analyzed. The kinematics model is shown in Figure 22.

The parameters of the steering trapezoid are shown in Table 1. According to the parameters of the steering trapezoid, the relationship between S and θ can be derived, and the relationship is shown in

$$\theta_3 = \theta_1 - \arctan \frac{t_1 + t_2 - t_3}{t_4 + \sqrt{t_5^2 - (t_2 - t_3)^2}}, \tag{13}$$

where

$$t_1 = 2\left[4h^2 + 4(b + c + s)^2\right]h, \tag{14}$$

$$t_2 = \sqrt{4\left[4h^2 + 4(b + c + s)^2\right]\left[\left(h^2 + (a + b + s)\right)^2 + l_2^2 - l_1^2 - 4(b + c + s)^2 l_2^2\right]}, \tag{15}$$

$$t_3 = 4h\left[h^2 + (a + b + S)^2 + l_2^2 - l_1^2\right], \tag{16}$$

$$t_4 = 2(b + c + s)\left[4h^2 + 4(b + c + s)^2\right], \tag{17}$$

$$t_5 = 2l_2\left[4h^2 + 4(b + c + s)^2\right], \tag{18}$$

where b and c are as follows:

$$b = \cos\theta_1, \tag{19}$$

$$c = \sqrt{l_2^2 - (l_1\sin\theta_3 - h)^2}. \tag{20}$$

As shown in Figure 22, taking the left half of the steering trapezoid as an example, the D-type screw moves to the left

to drive the wheels to turn right, and the D-type screw to move to the right drives the wheels to turn to the left. The left wheel can turn right up to 90°, the left turn can turn left up to 35°(the right wheel is the opposite), and the value range of θ_3 is −35° to 90°. In order to distinguish the moving direction of the D-type screw and the steering direction of the wheels, it is assumed that the left shift of the D-type screw is negative and the right shift is positive, and the left steer of the wheel is
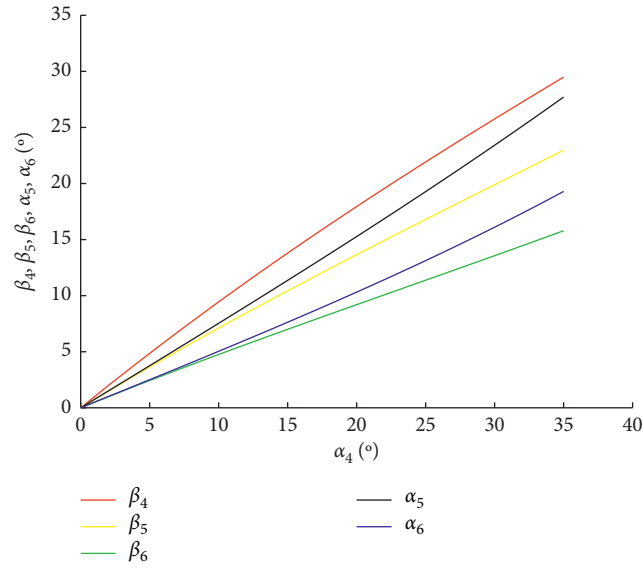
FIGURE 19: The relationship between the steering angle of each wheel and the internal rotation angle of the first axles in the six-wheel in-phase steering mode.
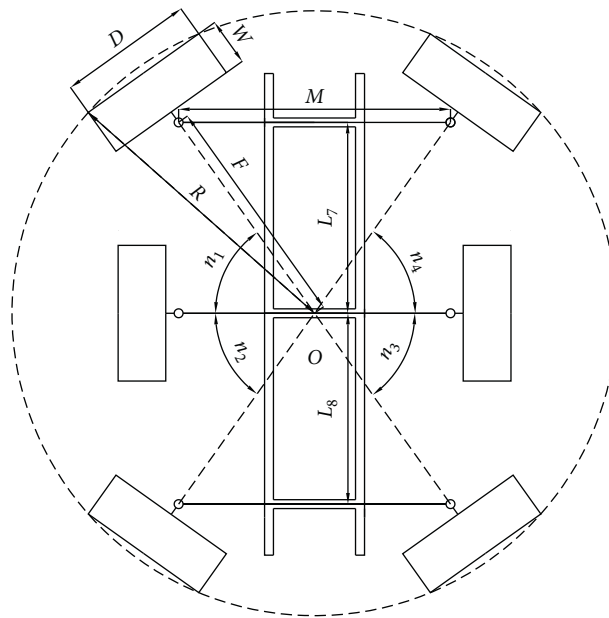
FIGURE 20: Schematic diagram of zero-radius steering.
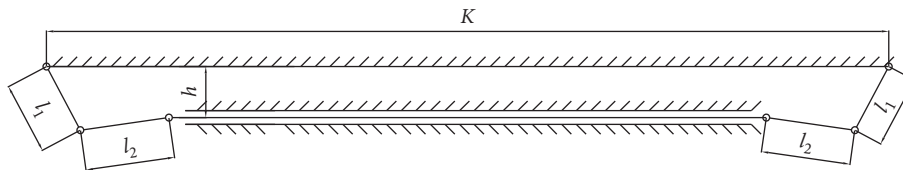
FIGURE 21: Steering trapezoid kinematics model.

negative and the right steer is positive. We put the value range of θ_3 into formula (13) to obtain the relationship between s and θ_3 as shown in Figure 23.

According to Figure 23, it can be seen that S and θ_3 are not proportional. When the steering motor drives the steering wheel to steer, the motor angle can be quickly

TABLE 1: Steering trapezoid parameters.

Parameter name	Numerical value (mm)
Distance between two kingpin joints (K)	1225.00
Length of steering arm (l_1)	105.00
Length of the tie rod (l_2)	130.00
Distance of steering mechanism and the first axle (h)	74.41
The universal joint of the steering mechanism (M)	869.00

TABLE 2: Check calculation of the Ackerman rate.

θ_i (°)	θ_o (°)	θ_{or} (°)	R_{AC}
1	0.98	0.99	50
5	4.47	4.77	43
10	8.09	9.09	48
15	11.11	12.96	52
20	13.68	16.36	58
25	15.92	19.24	63
30	17.92	21.54	70
35	19.72	23.20	77
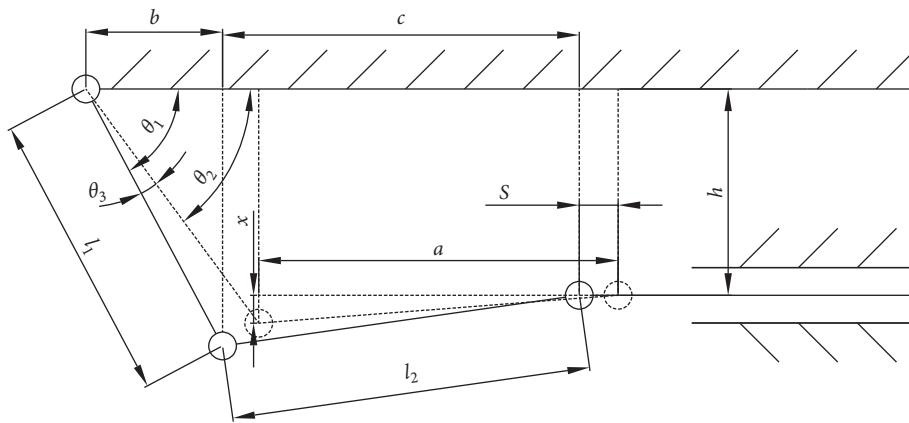
FIGURE 22: One-sided steering kinematics model.
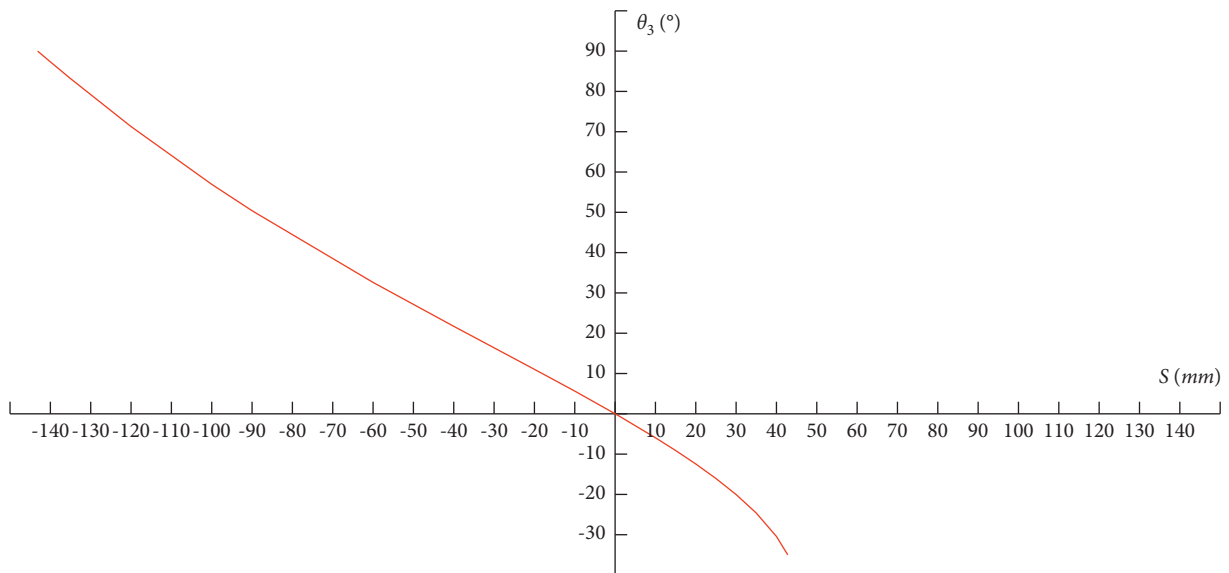
FIGURE 23: The relationship between S and θ_3.

controlled according to this diagram, and then, the angle of steer is corrected according to the angle signal fed back by the wheel angle sensor, so that the wheel angle can be controlled quickly and accurately.

7. Conclusions

The steering system is one of the key subsystems of the vehicle. A steering system with good performance is the guarantee for the safe operation of the vehicle. Six-wheeled off-road vehicles need to pass complex roads. A good performance steering system can improve the passing and flexibility of the vehicle. Therefore, this paper studies the steering system of three-axle six-wheeled vehicles. And the steering system of a three-axle six-wheeled vehicle is designed, modeled, and simulated. The main research contents and conclusions of this paper are as follows:

(1) Combining the design goals of the off-road vehicle, the steering mode and the application scenarios of the steering mode are established. Considering the application scenarios of off-road vehicles, the steering mode of the steering system is designed, and the specific application scenarios of the steering mode are introduced. Since the vehicle has five steering modes, the vehicle can adapt to more usage scenarios. For example, the application scenarios of lateral parking, zero-radius steering, and six-wheel reverse-phase steering can significantly improve the flexibility of the vehicle. It can be seen that the performance of the steering system is superior.

(2) The structure of the system and the working principle of each main component are analyzed combined with the CAD model. Among them, the longitudinal linkage rack is the key to the mechanical steering system, which can realize the linkage of the three steering mechanisms on three axles and the switching of the steering mode. The sliding base is the key part of the combination of mechanical steering and electronic control steering. Through the design of the structure, the ingenious combination of mechanical steering and electronic control steering is realized, and the performance of the steering system is improved.

(3) The hardware and control method of the electronic control system are combined to realize the control of the electronic control steering system. When controlling the wheel angle, the wheel angle controller determines the target angle of other wheels according to the input front inner wheel angle signal, and then, the wheel angle controller controls each steering motor according to the target angle of each wheel. Then, through the feedback of the angle sensor to correct the wheel angle to form a closed-loop control, this can control the wheel angle more quickly and accurately.

(4) The construction of the kinematics model and the calculation of related data were carried out. The calculation results showed that the six-wheel in-phase steering can significantly reduce the steering radius, and the zero-radius steering can also achieve U-turn steering in a narrow space. This will ensure the flexibility of the vehicle. Through the calculation of the steering trapezoid, it is found that the design of the steering trapezoid can better meet the Ackerman rate, and the steering trapezoid has good performance.

Data Availability

The data used to support the findings of this study are included within the article.

Conflicts of Interest

The authors declare that they have no conflicts of interest.

Authors' Contributions

Methodology and original draft preparation were done by Haixiang Bu; three-dimensional modeling and analysis were contributed by Aijuan Li and Wei Li; reviewing and editing were performed by Xin Huang and Jian Wang. All authors have read and agreed to the published version of the manuscript.

Acknowledgments

References

[1] Z. Zhang, X. Zhang, H. Pan et al., "A novel steering system for a space-saving 4WS4WD electric vehicle: design, modeling, and road tests," *IEEE Transactions on Intelligent Transportation Systems*, vol. 18, no. 1, pp. 114–127, 2017.

[2] Z. Yang, G. Li, H. He, and G. Li, "Study on road feeling simulation control algorithm for four-wheel independent drive and steering electric vehicle," in *Proceedings of the 2017 Chinese Automation Congress (CAC)*, pp. 4872–4875, Jinan, China, October 2017.

[3] H.-J. Yan, D.-B. Luo, and L.-F. Qi, "Research on the omni-directional steering system of patrol vehicles in urban utility tunnels," *Machine Design and Manufacture*, vol. 1, pp. 159–162, 2021.

[4] L. Wang, "Research on four-axis mechanical linkage steering mechanism based on single steering tie-rod," *Coal Mine Machinery*, vol. 41, no. 2, pp. 53–56, 2020.

[5] A. N. Kazak and D. M. Filippov, "Development of in-wheel motor for vehicles," in *Proceedings of the 2019 IEEE Conference of Russian Young Researchers in Electrical and Electronic Engineering (EIConRus)*, pp. 1406–1408, Moscow, Russia, January 2019.

[6] Y. Cao and M. Qiao, "Application of fuzzy control in four wheel steering control system," in *Proceedings of the 2017 International Conference on Advanced Mechatronic Systems (ICAMechS)*, pp. 62–66, Xiamen, China, December 2017.

[7] R. Prasad and Y. Ma, "Hierarchical control coordination strategy of six wheeled independent drive (6WID) skid steering vehicle," *IFAC-PapersOnLine*, vol. 52, no. 5, pp. 60–65, 2019.

[8] F. Du, Z. Guan, D. Su, and J. He, "Control strategy for four-wheel steering vehicle based on collaborative simulation," in *Proceedings of the 2017 9th International Conference on Modelling, Identification and Control (ICMIC)*, pp. 348–353, Kunming, China, July 2017.

[9] J. Wang, G. Tan, and C. Sun, "Research on vehicle four-wheel steering based on model-free adaptive control," in *Proceedings of the 2020 5th International Conference on Electromechanical Control Technology and Transportation (ICECTT)*, pp. 372–376, Nanchang, China, May 2020.

[10] Y. Ye, L. He, and Q. Zhang, "Steering control strategies for a four-wheel-independent-steering bin managing robot," *IFAC-PapersOnLine*, vol. 49, no. 16, pp. 39–44, 2016.

[11] G. S. G. Ravikanth and C. Sujatha, "Dynamic modeling and simulation of a three-wheeled hub motor vehicle," in *Proceedings of the 2017 IEEE Transportation Electrification Conference (ITEC-India)*, pp. 1–5, Pune, India, December 2017.

[12] Y. Zhao, G. Tao, J. Li, X. Zhang, and J. Gong, "Dynamic model and predictive control of electric driven eight-wheeled differential steering autonomous vehicle," in *Proceedings of the 2020 3rd International Conference on Unmanned Systems (ICUS)*, pp. 412–417, Harbin, China, November 2020.

[13] M. Muenster, M. Lehner, and D. Rixen, "Requirement derivation of vehicle steering using mechanical four-poles in the presence of nonlinearities," *Mechanical Systems and Signal Processing*, vol. 155, 2021.

[14] S. Yim, "Comparison among active front, front independent, 4-wheel and 4-wheel independent steering systems for vehicle stability control," *Electronics*, vol. 9, no. 5, 2020.

[15] F. Xu, X. Liu, W. Chen, and C. Zhou, "Dynamic switch control of steering modes for four wheel independent steering rescue vehicle," *IEEE Access*, vol. 7, pp. 135595–135605, 2019.

[16] Z. M. U. Din, W. Razzaq, U. Arif, W. Ahmad, and W. Muhammad, "Real time Ackerman steering angle control for self-driving car autonomous navigation," in *Proceedings of the 2019 4th International Conference on Emerging Trends in Engineering, Sciences and Technology (ICEEST)*, pp. 1–4, Karachi, Pakistan, December 2019.

[17] Q. Qiu, Z. Fan, Z. Meng et al., "Extended Ackerman steering principle for the coordinated movement control of a four wheel drive agricultural mobile robot," *Computers and Electronics in Agriculture*, vol. 152, pp. 40–50, 2018.

[18] S. S. Singh and G. Singh Mavi, "Optimization and mathematical calculation of turning radius for 4 wheel steering systems in maruti suzuki baleno," *International Journal of Innovative Technology and Exploring Engineering (IJITEE)*, vol. 8, no. 11, pp. 3961–3963, 2019.

[19] D. Wei, Y. Wang, T. Jiang, S. Zheng, W. Zhao, and Z. Pan, "Chaos vibration of pinion and rack steering trapezoidal mechanism containing two clearances," *Mechanical Systems and Signal Processing*, vol. 92, pp. 146–155, 2017.

[20] G. R. Kiranchand, T. Soni, and A. C. Mitra, "Experimental design, sensitivity analysis of steering geometry and suspension parameters," *Materials Today: Proceedings*, vol. 5, no. 2, pp. 5743–5756, 2018.

Research Article

Research on Torque Distribution of Four-Wheel Independent Drive Off-Road Vehicle Based on PRLS Road Slope Estimation

Hongwei Ling [1] and Bin Huang [1,2]

[1]*Hubei Key Laboratory of Advanced Technology for Automotive Components, Wuhan University of Technology,*
 Wuhan 430070, China
[2]*Hubei Collaborative Innovation Center for Automotive Components Technology, Wuhan University of Technology,*
 Wuhan 430070, China

Correspondence should be addressed to Bin Huang; huangbinbi@163.com

In view of the high difficulty in coupling of various electric vehicle parameters, intractable parameter estimation, and unreasonable distribution of vehicle driving torque, the four-wheel hub motor is applied to drive electric vehicles, which can instantly obtain the torque and speed of the hub motor and achieve precise control of the torque of each wheel. According to the vehicle longitudinal dynamics model, a progressive RLS (PRLS) algorithm for real-time estimation of vehicle mass and road gradient is proposed. Meanwhile, by means of taking the longitudinal acceleration of the vehicle and the road gradient obtained from the estimation algorithm as the parameter of the torque distribution at the front and rear axles, a dynamic compensation and distribution control strategy of the front and rear axle torques is designed. Moreover, based on hardware-in-the-loop real-time simulation and real-vehicle tests, the effectiveness of the proposed estimation algorithm and the rationality of the real-time distribution control strategy of driving torque are verified.

1. Introduction

With continuous progress of automobile industry, in addition to the gradually highlighted issues such as energy, environmental protection, and safety, the electric vehicle has also become the focus of attention, in which hub motor drive is an important direction for the future electric vehicle development [1]. By means of directly installing the drive motor into wheel hub to integrate the power system, transmission system, and braking system, the hub motor-driven vehicle not only greatly reduces mechanical transmission components but also simplifies the vehicle structure and lowers the entire vehicle mass. At the same time, hub motor creates a more flexible driving mode so that the four-wheel drive electric vehicle can easily switch between two-wheel and four-wheel drive modes, and the front and rear axle torque distribution ratio control is more precise and flexible. Besides, compared with the internal combustion engine, hub motor can further improve the vehicle efficiency, making electric drive vehicles advantaged in active safety and energy saving control. Moreover, based on real-time vehicle dynamic information feedback, accurate identification of more parameters and precise control of more variables can be achieved [2].

At present, the algorithms for vehicle parameter estimation, mainly include least squares method, least squares method with forgetting factor, Kalman filter, extended Kalman filter, and adaptive Kalman filter. In addition, sliding mode observers, fuzzy observers, the nonlinear observer derived from Lyapunov theory, and the neural network algorithm have also been applied to a certain extent [3]. Literature [4] is put forward to estimate vehicle state and adhesion coefficient while using dual extended Kalman filter. Literature [5] realized the identification of battery model parameters by the least square method and achieved and used more accurate estimate of battery SOC through the

genetic particle filter algorithm. The above parameter estimation or identification methods are the approaches commonly used in the domestic and foreign literature with better estimation effect. However, due to high complexity and many input variables, the above estimation algorithms generally have poor real-time calculation, choosing a parameter estimation algorithm that can meet the needs of vehicle control with high accuracy, low input variable requirements, and fast calculation speed which is quite significant.

The reasonable distribution of vehicle driving torque can comprehensively improve various performances such as vehicle power, maneuverability, steering, and safety [6–11]. According to the four-wheel drive vehicle driving torque distribution control strategy in literature [12], the driving condition is divided into straight driving and turning driving from the perspectives of improving vehicle dynamics and stability. In the straight driving condition, the vertical load transfer of vehicle front and rear axles is determined through longitudinal acceleration, and the vertical load ratio of front and rear axles is used as the driving torque distribution ratio so as to determine the amount of driving torque distributed to the rear wheels. In the turning driving condition, for the sake of ensuring good steering and stability of the whole vehicle, under the driving torque distribution control strategy with the given transmission system, the driving force is distributed from the front wheels to the rear wheels to reduce the tendency of understeer trend [13]. In high-speed operating conditions, the torque distribution control of four-wheel independent drive vehicles is prone to robust stability problems. Literature [14, 15] designed a gain-scheduled robust controller using the linear parameter varying (LPV) system, which can not only obtain strong robustness but also reduce the order of controller to address the vehicle handling stability control considering system uncertainties. Because the power system of the hub motor-driven vehicle has undergone fundamental changes, the traditional driving torque control strategy cannot be fully applied to the new hub motor vehicle. In this consideration, it is necessary to improve and optimize driving torque distribution control strategy by virtue of hub motor.

From the perspective of vehicle dynamics, vehicle mass, road adhesion coefficient, road gradient, and vehicle longitudinal acceleration are the key parameters involving the distribution of vehicle driving torque [16]. Due to the different weights of occupants and loaded goods each time when driving the vehicle, the vehicle mass is an indispensable factor in the driving torque distribution of the front and rear axles. Besides, on the premise of obtaining vehicle longitudinal acceleration, road gradient, and vehicle mass, the real-time distribution of the torque of four-wheel hub motors at the front and rear axles can be realized.

Considering that the RLS estimation algorithm requires few parameters and has good real-time performance, a progressive RLS estimation algorithm for the four-wheel hub motor vehicle is proposed in this paper. On the one hand, the algorithm can estimate the quality of the vehicle and the road slope with the least information from the on-board sensors, and on the other hand, it introduces a progressive algorithm

to further improve the accuracy and stability of the estimation algorithm which realizes the accurate estimation of vehicle mass and road gradient. On this basis, a four-wheel hub motor torque dynamic distribution control strategy is proposed by utilizing the estimated parameters and the vehicle longitudinal acceleration proposed. Based on the equal distribution of front and rear axle driving torques, vehicle longitudinal acceleration and road gradient are studied comprehensively, and the front and rear axle driving torques are redistributed as well as dynamically compensated to adapt to different driving conditions and fully exert the strengths of the hub motor-driven electric vehicle.

2. Design of Progressive RLS Parameter Estimation Algorithm

Compared with traditional vehicles, the proposed four-wheel hub motor electric vehicle, instead of using the engine and gearbox, adopts a wheel reducer at the reduction ratio of $i_0 = 5$.

The longitudinal dynamics model in the traditional vehicle is shown in the following formulas:

$$F_t = F_f + F_i + F_w + F_j, \tag{1}$$

$$\frac{T_{tq} i_g i_0 \eta_T}{r} = Gf \cos \alpha + G \sin \alpha + \frac{C_D A}{21.15} u_a^2 + \delta m \frac{du}{dt}. \tag{2}$$

As can be learned from the driving mode of the hub motor-driven vehicle, the longitudinal dynamics model of the proposed vehicle is shown in the following formula:

$$\frac{T_{tq} i_0 \eta_T}{r} = Gf \cos \alpha + G \sin \alpha + \frac{C_D A}{21.15} u_a^2 + m \frac{du}{dt}, \tag{3}$$

where i_0 is the reduction ratio of the wheel reducer and T_{tq} is the sum of the torques of four hub motors.

In the field of parameter real-time estimation and identification, the least square method has been well promoted and applied, of which RLS is a recursive form. For a single-input-single-output system (SISO), the adoption of algorithm can achieve small calculation, quick convergence speed, and fast convergence of parameter identification without needing any given condition so that the real-time and accuracy requirements in vehicle control system can be met.

The idea of the recursive identification algorithm can be summarized as follows:

New parameter estimate = old parameter estimate + correction term

That is, the new recursive parameter estimates are iterated based on the old recursive estimates.

For an AR (n) (n-order autoregressive) model [17],

$$y(t) = a_1 y(t-1) + \cdots + a_n y(t-n) + \varepsilon(t), \tag{4}$$

where $\varepsilon(t)$ is the zero mean, variance is white noise with $\sigma_\varepsilon^2 > 0$, $y(t)$ is the observation, and the order is known at n.

Its parameter estimation through the recursive least square method is expressed as follows:

$$\hat{\theta}(t+1) = \hat{\theta}(t) + K(t+1)\left[y(t+1) - \varphi^T(t+1)\hat{\theta}(t)\right],$$

$$K(t+1) = \frac{P(t)\varphi(t+1)}{1 + \varphi^T(t+1)P(t)\varphi(t+1)},$$

$$P(t+1) = P(t) - \frac{P(t)\varphi(t+1)\varphi^T(t+1)P(t)}{1 + \varphi^T(t+1)P(t)\varphi(t+1)}. \tag{5}$$

The vehicle mass is a parameter that does not change with time after the start of driving, but the road gradient is a time-varying parameter, so t general RLS and exponentially weighted RLS are applied to separately identify the vehicle mass and road gradient online. When identifying multiple parameters with the recursive least square method, the identification results are affected by different parameter identification sequences. Regarding the identification sequence, an initial value close to the true value can be selected as vehicle mass when initializing the algorithm while the road gradient at the start is unknown. In this consideration, this paper proposes a progressive RLS estimation algorithm that estimates the road gradient based on the initial value of vehicle mass and then returns the estimated road gradient to the mass estimation module to estimate the vehicle mass in real-time. The logic diagram of this estimation algorithm is shown in Figure 1.

The longitudinal dynamics model of the vehicle is transformed as follows:

$$\frac{T_{tq}i_0\eta_T}{r} - \frac{C_D A}{21.15}u_a^2 - \left(m\frac{du}{dt}\right) = m(gf\cos\alpha + g\sin\alpha). \tag{6}$$

Let $y = (T_{tq}i_0\eta_T/r) - (C_D A/21.15)u_a^2 - (m(du/dt))$, $\varphi = m$, and $\theta = gf\cos\alpha + g\sin\alpha$.

Then, the above formula becomes

$$Y = \varphi\theta, \tag{7}$$

where θ is the expression containing the road gradient variable.

Therefore, the RLS algorithm recursive expression for gradient estimation is shown in (8)–(10). The selection range of forgetting factor is [0, 1]. In view that the road gradient changes constantly and the old observation data have small influence on new parameters, the forgetting factor $\lambda = 0.9$ is selected in this paper:

$$K(k) = \frac{P(k-1)\varphi(k)}{\lambda + \varphi^T(k)P(k-1)\varphi(k)}, \tag{8}$$

$$\hat{\theta}(k) = \hat{\theta}(k-1) + K(k)\left[y(k) - \varphi^T(k)\hat{\theta}(k-1)\right], \tag{9}$$

$$P(k) = P(k-1) - \frac{P(k-1)\varphi(k)\varphi^T(k)P(k-1)}{1 + \varphi^T(k)P(k-1)\varphi(k)}$$

$$= \frac{\left(1 - K(k)\varphi^T(k)\right)P(k-1)}{\lambda}. \tag{10}$$

In the above expression, k represents the current sampling time and k-1 represents the previous sampling time. During the algorithm calculation, the least square gain is firstly calculated by formula (9), and then $\hat{\theta}(k)$ and $\mathbf{P}(k)$ are calculated. The corresponding estimated value of road gradient can be obtained from the following formula:

$$\alpha = \frac{\arccos\left\{(\theta/g) - \sqrt{1 + f^2 - \left(\theta^2/g^2\right)}\right\}}{1 + f^2}. \tag{11}$$

The gradient estimation value, after being obtained, is taken as the input variable of mass estimation module for estimating the whole vehicle mass.

By transforming the vehicle longitudinal dynamics expression,

$$\frac{T_{tq}i_0\eta_T}{r} - \frac{C_D A}{21.15}u_a^2 = m\left(gf\cos\alpha + g\sin\alpha + \frac{du}{dt}\right). \tag{12}$$

Let $y_1 = (T_{tq}i_0\eta_T/r) - (C_D A/21.15)u_a^2$, $\varphi_1 = (gf\cos\alpha + g\sin\alpha + (du/dt))$, and $\theta_1 = m$;

$$y_1 = \varphi_1\theta_1. \tag{13}$$

Then, expression of the recursive least squares method for vehicle mass estimation can be obtained as follows:

$$K(k) = \frac{P(k-1)\varphi_1(k)}{1 + \varphi_1^T(k)P(k-1)\varphi_1(k)}, \tag{14}$$

$$\hat{\theta}_1(k) = \hat{\theta}(k-1) + K(k)\left[y_1(k) - \varphi^T(k)\hat{\theta}_1(k-1)\right], \tag{15}$$

$$P(k) = \left(1 - K(k)\varphi_1^T(k)\right)P(k-1). \tag{16}$$

Formulas (14)–(16) help obtain the real-time estimation of vehicle mass, formula (15) is the update of the least square gain, and formula (16) is the update of the error covariance.

3. Design of Dynamic Self-Compensation Torque Distribution Control Strategy

The force analysis of the hub motor-driven vehicle is shown in Figure 2.

According to the vehicle theoretical dynamics formula [18], through taking the moment of each force acting on the vehicle to the contact center of the front and rear wheels and
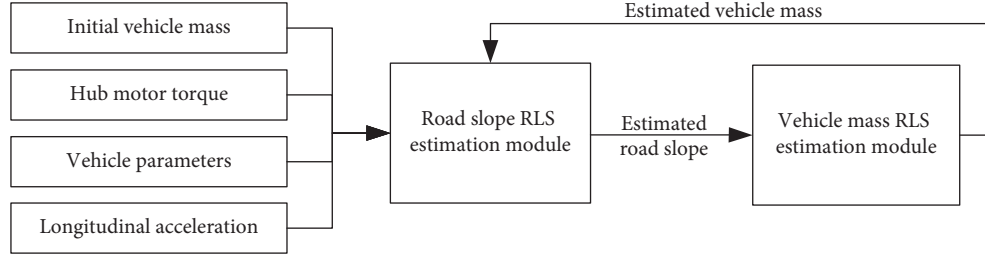
Figure 1: Logic diagram of the estimation algorithm.
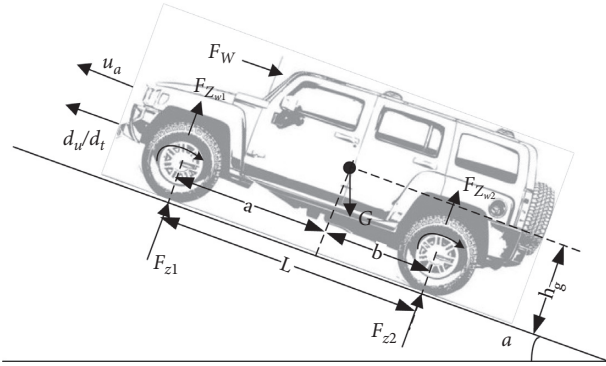
Figure 2: Vehicle climbing force analysis.

the road surface, the normal reaction force of the front and rear axles can be expressed as follows:

$$
\begin{aligned}
F_{Z1} &= G\left(\frac{b}{L}\cos\ \alpha - \frac{h_g}{L}\sin\ \alpha\right) - \left(\frac{G}{g}\frac{h_g}{L} - \frac{\sum I_w}{Lr}\right)\frac{\mathrm{d}u}{\mathrm{d}t} \\
&\quad - F_{Zw1} - G\frac{rf}{L}\cos\ \alpha, \\
F_{Z2} &= G\left(\frac{a}{L}\cos\ \alpha + \frac{h_g}{L}\sin\ \alpha\right) + \left(\frac{G}{g}\frac{h_g}{L} - \frac{\sum I_w}{Lr}\right)\frac{\mathrm{d}u}{\mathrm{d}t} \\
&\quad - F_{Zw2} + G\frac{rf}{L}\cos\ \alpha.
\end{aligned}
\tag{17}
$$

After analyzing the normal reaction force components of the proposed hub motor-driven vehicle, the rotating mass inertial resistance couple moment, rolling resistance couple moment, and air lift can be ignored under certain conditions, and the front, so that the dynamic ground normal reaction force of the front and rear axles is as follows:

$$
F_{Z1} = G\left(\frac{b}{L}\cos\ \alpha - \frac{h_g}{L}\right) - \left(m\frac{h_g}{L}\right)\frac{\mathrm{d}u}{\mathrm{d}t},
\tag{18}
$$

$$
F_{Z2} = G\left(\frac{a}{L}\cos\ \alpha + \frac{h_g}{L}\sin\ \alpha\right) + \left(m\frac{h_g}{L}\right)\frac{\mathrm{d}u}{\mathrm{d}t}.
\tag{19}
$$

Compared with the vehicle longitudinal acceleration, the road gradient changes slowly. Therefore, in the process of dynamic distribution of the front and rear axle driving torque, the change in the front and rear axle loads under road gradient change is used as a benchmark, and that

under the vehicle longitudinal acceleration is taken as real-time dynamic compensation. According to the estimated vehicle mass and road gradient value, different front and rear axle driving torque distribution benchmarks can be obtained. At the same time, the vehicle longitudinal acceleration is obtained through the longitudinal accelerometer, and the dynamic compensation of the front and rear axle driving torque is performed accordingly [7, 19].

In order to prevent the jump of driving torque of the front and rear axles under the conditions of small acceleration and gradient, the gradient threshold i_0 and acceleration threshold a_0 are designed. When the gradient reaches the threshold, the new front and rear axle driving torque distribution relationship is used for the secondary distribution of driving torque; on this basis, the vehicle longitudinal acceleration signal is further collected, and dynamic compensation of the driving torque of front and rear axles based on the longitudinal acceleration is performed when the acceleration reaches the set threshold. This torque distribution control strategy not only considers the changes in driving conditions but also ensures the smooth output of torque.

The gradient threshold point is determined according to the proportional relationship of the static normal reaction force of the front and rear axles under different road gradients [20]. According to the automobile normal mathematical model established by (18) and (19), when the road gradient is 16°, the static normal reaction force ratio of the front and rear axles is 46 : 54. In order to make the selected torque distribution ratio adapt to more road conditions, the front and rear axle driving torque distribution ratio is determined at 40 : 60 when the road gradient is ≥16°; the front and rear axle static normal reaction ratio is determined at 38 : 62 when the road gradient is 26°. Based on the same selection principle, the ratio of the front and rear axle driving torque distribution is determined at 30 : 70 when the road gradient is ≥26°.

The driving torque output control logic of the vehicle front and rear axles is shown in Figure 3.

4. Hardware-in-the-Loop Simulation and Actual Vehicle Test Verification

4.1. Hardware-in-the-Loop Real-Time Simulation Test. With the purpose to verify the effectiveness of the proposed mass and gradient estimation algorithm, as well as the feasibility of the dynamic self-compensation distribution
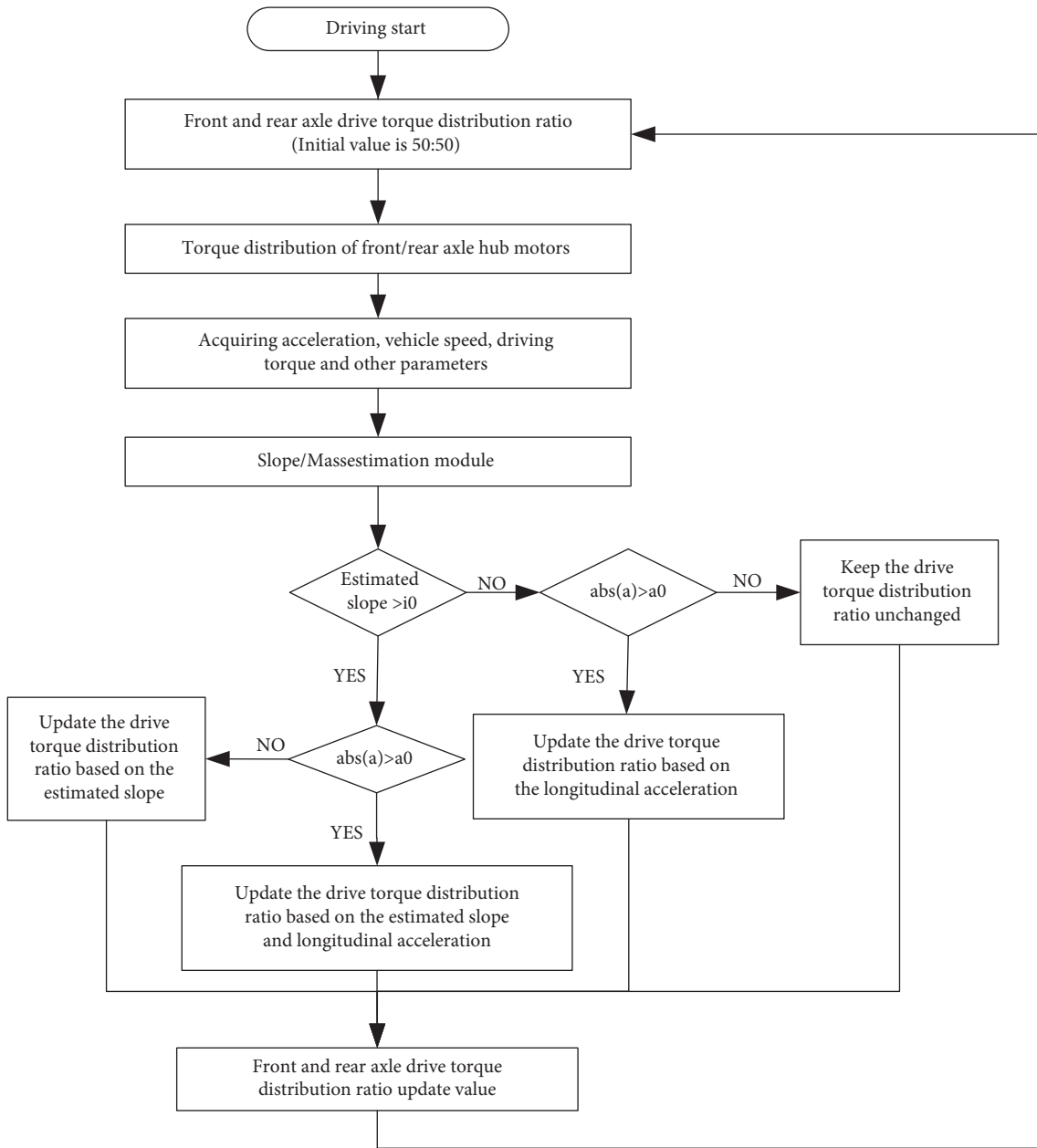
FIGURE 3: The driving torque output control logic.

control strategy of the front and rear axle driving torque, the vehicle control strategy model is established in Matlab/Simulink . Among them, the mass and slope estimation module uses S_Function to write the estimation algorithm program, which realizes the iterative process of the progressive RLS algorithm. Then, one-key automatic code generation is used to download the control strategy model to the actual vehicle control unit (VCU). In dSPACE-ASM, a vehicle dynamics model of four-wheel hub motor-driven full-size SUV is built, and it communicates with the VCU through the CAN bus. The hardware-in-the-loop simulation platform is shown in Figure 4.

The parameter estimation simulation results are under the condition of 50% of road gradient. At the same time, the impact of the torque dynamic self-compensation

distribution on the climbing performance of the vehicle is verified. The front and rear axle torques are equally distributed as a comparative experiment, and the simulation road adhesion coefficient is set to 0.8. The vehicle starts to accelerate by stepping on the accelerator pedal at 50% on a flat road and keeps the accelerator pedal fully open after touching the slope in the 4.2 s. The simulation results of vehicle mass and road slope estimation are shown in Figure 5.

The proposed progressive least square method can achieve real-time estimation of road gradient and vehicle mass. As can be observed from the results of joint simulation, the actual vehicle mass is 2530 kg, and the estimated mass quickly converges near the true value; the actual value of road gradient is 25°–28°; the estimated gradient quickly
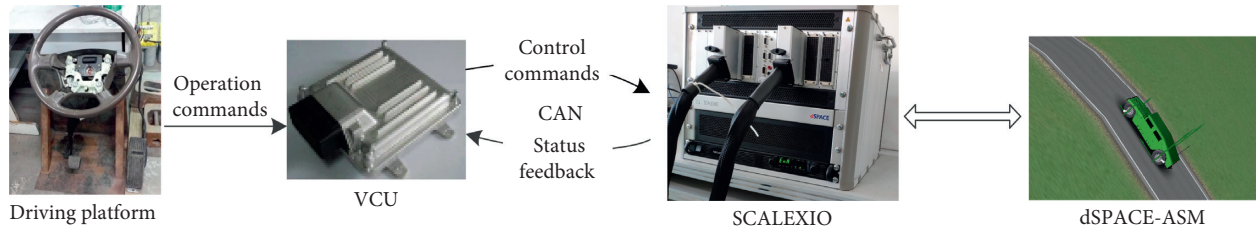
FIGURE 4: Hardware-in-the-loop real-time simulation platform.
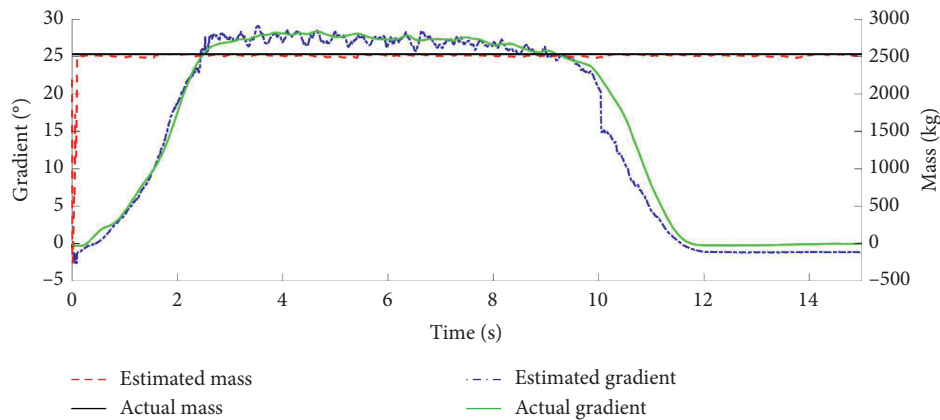
FIGURE 5: Estimation results of vehicle mass and road slope.

converges to the actual value and maintains the same trend as the actual value. The error of gradient estimation is within 2°, and the mass estimation error is within 10 kg. The algorithm has high estimation accuracy, fast convergence speed, and good stability.

The torque dynamic self-compensation distribution result is shown in Figure 6.

Figures 6(a) and 6(b) show that, at 4.2 s, the driver recognized the climb and stepped on the pedal at full throttle. The VCU sends a command to switch the motor controller to peak torque operation mode, and the motor output torque increases rapidly. Figures 6(c) and 6(d) show that when the car is running on a slope, the front and rear axle loads are shifted due to the slope of the road surface. The normal load of the front axle is greatly reduced. When the torque of each axle is evenly distributed, the maximum wheel can use the road grip which is less than the expected value of the wheel torque, the wheels slip, the motor output torque is reduced, and the vehicle traction is insufficient. Therefore, the vehicle is decelerating on the slope, and the final speed drops to zero. However, the dynamic allocation control algorithm proposed in this paper can effectively suppress the front wheel slip. Figure 6(e) shows the front axle torque distribution factors during the even distribution and dynamic distribution control, respectively. It can be seen in the figure that as the front axle load decreases, the target torque allocated to the front axle also decreases. Figure 6(f) shows that the test vehicle using the dynamic distribution torque control algorithm can smoothly climb a steep slope of 50%, while the test vehicle that does not use the algorithm fails to climb.

4.2. Actual Vehicle Test. Based on the test platform of the four-wheel hub motor-driven off-road vehicle, the real-vehicle tests of mass and gradient estimation algorithms and front and rear axle dynamic compensation torque distribution control strategy are carried out.

The vehicle related parameters are shown in Table 1.

The parameters related to hub motor are shown in Table 2.

The physical photo of the in-wheel motor assembly system is shown in Figure 7.

In order to test the key state data of the vehicle, the sensor configuration of the vehicle is shown in Figure 8.

A 50% of the gradient climbing test is performed in the standard test site, and the standard test ramp is shown in Figure 9.

A longitudinal accelerometer is installed at the center of vehicle mass to instantly measure the vehicle longitudinal acceleration. Meanwhile, the parameter estimation algorithm is loaded into the vehicle controller for real-time operation, which is taken as an input parameter for parameter estimation and torque dynamic distribution control [20]. The test results are shown in Figures 10–12.

Results of 50% of the gradient climbing test are as follows. According to the test results, when the designed progressive RLS estimation algorithm operates on a real vehicle, it can accurately estimate the vehicle mass and road gradient in a real-time. As can be seen from real-time torque curve of each wheel of the front and rear axles, at 2.3 s, the estimation algorithm accurately estimates that the road gradient is greater than 16°, and the front and rear axle driving force distribution coefficient is switched to 40 : 60
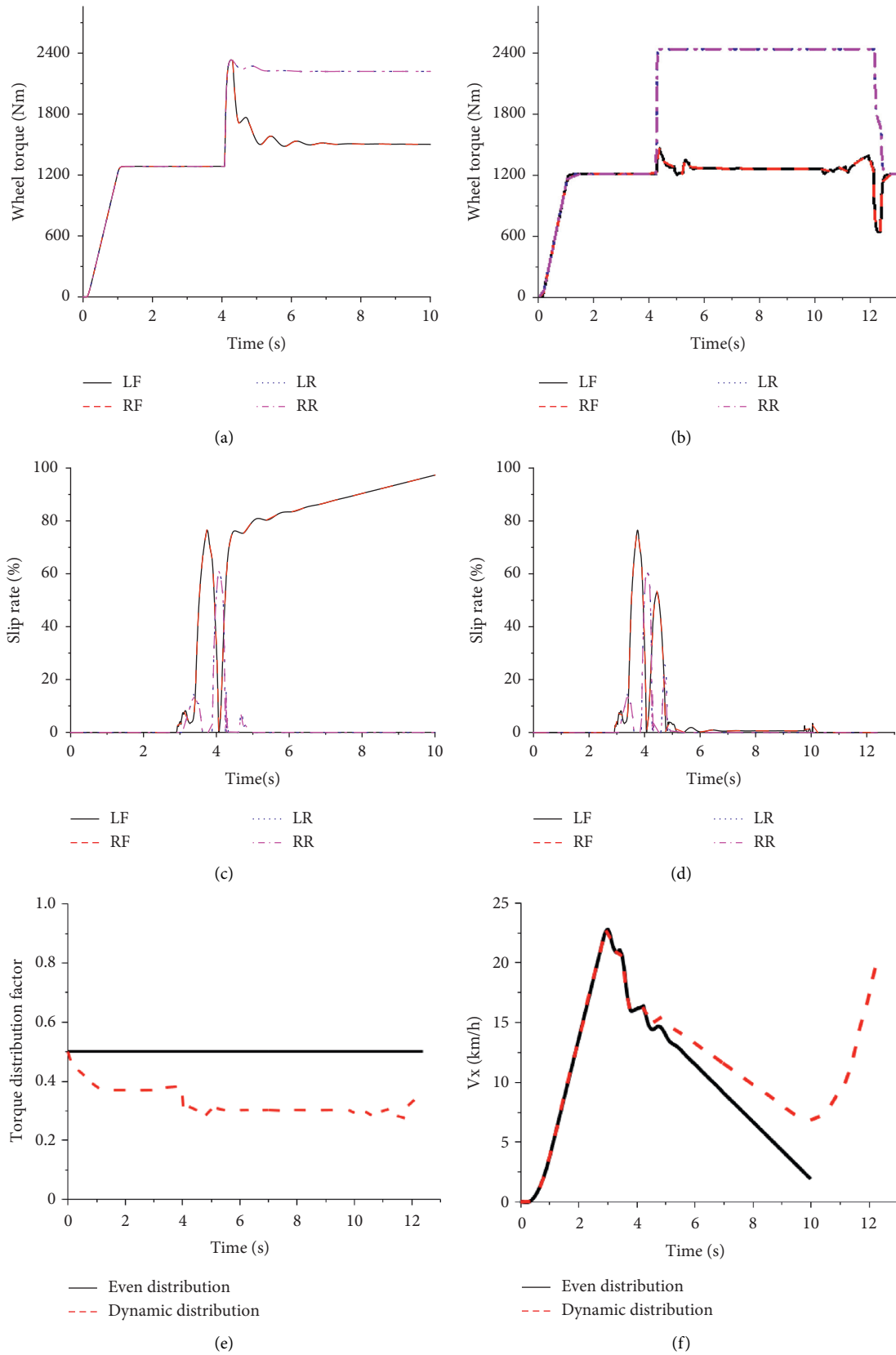
FIGURE 6: 50% slope driving simulation. (a) Even distribution-wheel torque. (b) Dynamic distribution-wheel torque. (c) Even distribution-slip rate. (d) Dynamic distribution-slip rate. (e) Front axle torque distribution factor. (f) Longitudinal speed comparison.

TABLE 1: Vehicle parameters.

Vehicle parameters	Value
Curb weight (kg)	2500
Gross vehicle weight (kg)	3500
Wheelbase (mm)	2946
Center of mass height (mm)	781
Distance from center of mass to front axle (m)	1.33
Distance from center of mass to rear axle (m)	1.616
Frontal area (m^2)	2.4
Reduction ratio	5

TABLE 2: Motor parameters.

Motor parameters	Value
Rated/peak power (kW)	35/70
Rated/peak speed (RPM)	1670/3500
Rated/peak torque (N·m)	200/500

FIGURE 7: In-wheel motor assembly system.
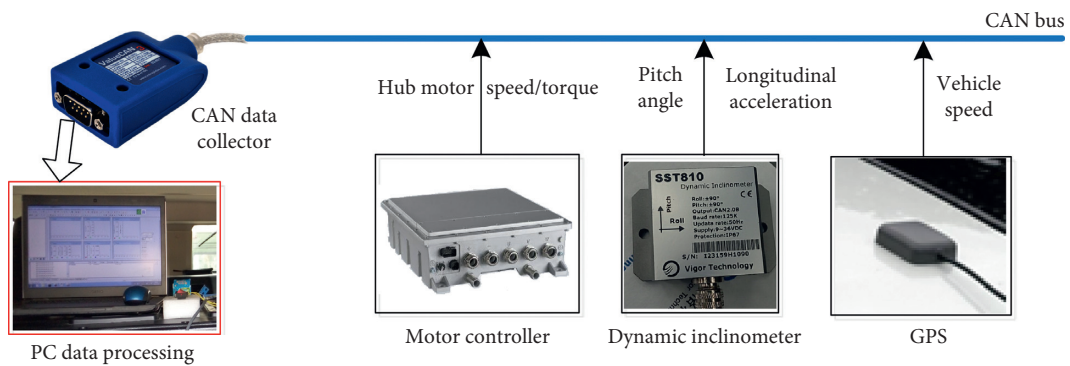
FIGURE 8: The sensor configuration.

accordingly; at 4.6 s, the road gradient is estimated greater than 26° so that the front and rear axle driving torque distribution coefficient is switched to 30 : 70. At the same time, the vehicle driving torque distribution coefficient takes into account the changes in vehicle longitudinal acceleration to timely compensate the torque distribution

coefficients of the front and rear axles. Therefore, the dynamic self-compensation torque distribution strategy of the front and rear axles not only realizes the real-time control of the front and rear axle torque but also greatly enhances the power performance and trafficability of the whole vehicle.

Figure 9: Standard test ramp.
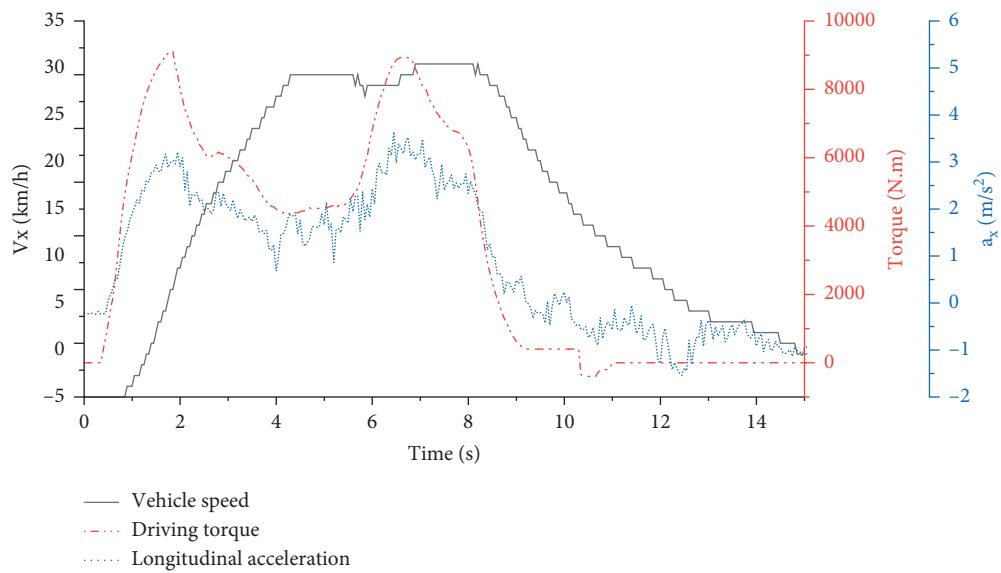
Figure 10: Vehicle speed, longitudinal acceleration, and driving torque.
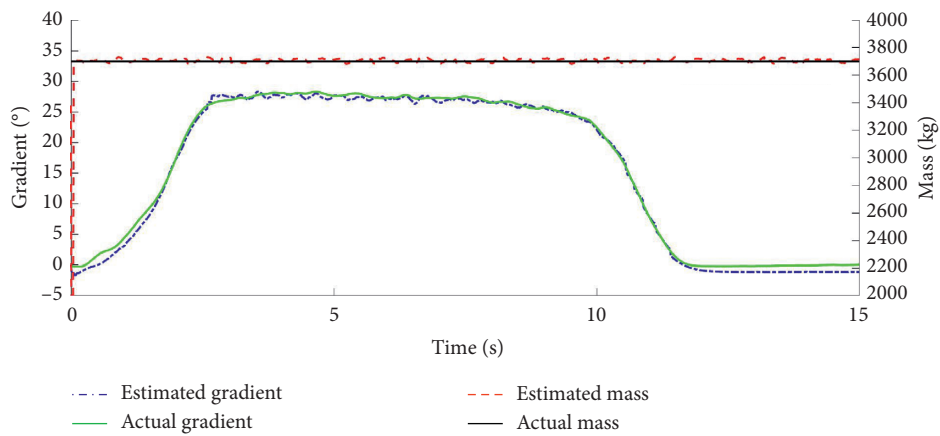
Figure 11: Estimation results of vehicle quality and road slope.
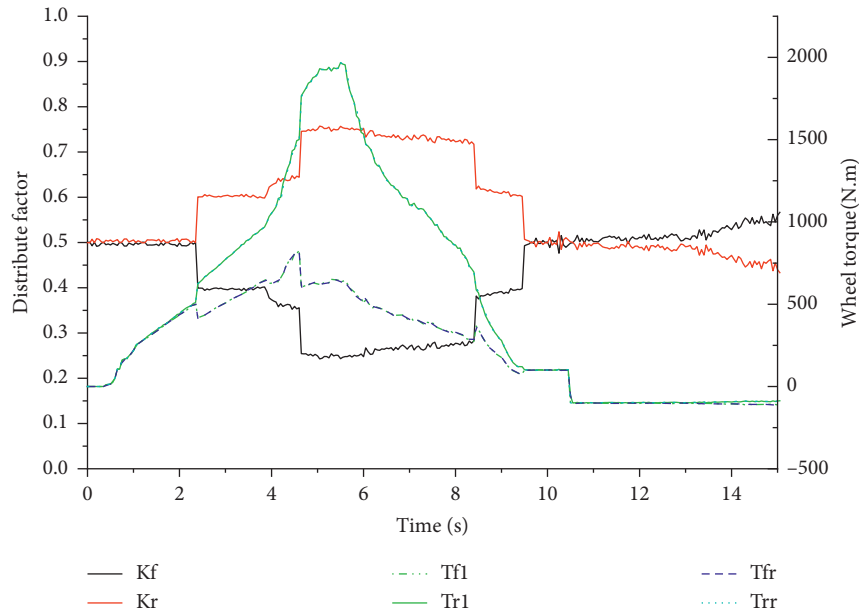
FIGURE 12: Torque distribution factor of front and rear axles and torque of each wheel.

5. Conclusions

In this paper, by means of focusing on a certain type of the four-wheel hub motor-driven off-road vehicle and making full use of the hub motor vehicle, a progressive RLS estimation algorithm is designed based on the vehicle longitudinal dynamics model, which can accurately estimate the vehicle mass as well as road gradient. Also, a dynamic self-compensation torque distribution control strategy is proposed, which, through using estimated parameters and the vehicle longitudinal acceleration, realizes the dynamic distribution of the driving torque of vehicle front and rear axles and improves the vehicle trafficability and power performance. Besides, the CarSim and Matlab/Simulink joint simulation shows that the proposed progressive RLS estimation is more accurate in vehicle and road gradient estimation, and the estimated value can be taken as a reference for vehicle torque dynamic distribution. In the real-vehicle test, the results are consistent with the simulation, verifying the effectiveness of the proposed estimation algorithm and control strategy.

However, there is still some room for optimizing the designed control strategy. Specifically, in terms of driving torque distribution, vehicle longitudinal acceleration, road gradient, real-time vehicle dynamic parameters including yaw rate and roll angle, and road conditions such as road adhesion coefficient are all the parameters that need to be considered in the real-time control of the whole vehicle. In view of this, the future learning and research look into the changing law of each dynamic parameter and its application in the control of the whole vehicle.

Data Availability

The data used to support the findings of this study are available from the corresponding author upon request.

Conflicts of Interest

The authors declare that there are no conflicts of interest.

Acknowledgments

References

[1] G. Li and C. Zong, "Review on electric vehicle with four-wheel independent drive in-wheel motors," *Journal of Liaoning University of Technology (Natural Science Edition)*, vol. 35, no. 1, pp. 47–52, 2014.

[2] M. Izhar Ishak, H. Ogino, and Y. Yamamoto, "Numerical simulation analysis of an oversteer in-wheel small electric vehicle integrated with four-wheel drive and independent steering," *International Journal of Vehicular Technology*, vol. 2016, Article ID 7235471, 12 pages, 2016.

[3] X. Jin, G. Yin, X. Zeng, and J. Chen, "Robust gain-scheduled output feedback yaw stability control for in-wheel-motor-driven electric vehicles with external yaw-moment," *Journal of the Franklin Institute*, vol. 355, no. 18, pp. 9271–9297, 2018.

[4] Y.-H. Liu, T. Li, Y.-Y. Yang, X.-W. Ji, and J. Wu, "Estimation of tire-road friction coefficient based on combined APF-IEKF and iteration algorithm," *Mechanical Systems and Signal Processing*, vol. 88, pp. 25–35, 2017.

[5] R. Wang, H. Jing, C. Hu, F. Yan, and N. Chen, "Robust $H\infty$ path following control for autonomous ground vehicles with delay and data dropout," *IEEE Transactions on Intelligent Transportation Systems*, vol. 17, no. 7, pp. 2042–2050, 2016.

[6] D. Savitski, D. Schleinin, V. Ivanov et al., "Improvement of traction performance and off-road mobility for a vehicle with four individual electric motors: driving over icy road," *Journal of Terramechanics*, vol. 69, pp. 33–43, 2017.

[7] B. Li, A. Goodarzi, A. Khajepour, S. K. Chen, and B. Litkouhi, "An optimal torque distribution control strategy for four-independent wheel drive electric vehicles," *Vehicle System Dynamics*, vol. 53, no. 8, pp. 1172–1189, 2017.

[8] D. Tan, Q. Wang, and Y. Wu, "Modal analysis of in-wheel motor-driven electric vehicle based on bond graph theory," *Shock and Vibration*, vol. 2017, Article ID 6459154, 9 pages, 2017.

[9] Z. Shuai, H. Zhang, J. Wang, J. Li, and M. Ouyang, "Lateral motion control for four-wheel-independent-drive electric vehicles using optimal torque allocation and dynamic message priority scheduling," *Control Engineering Practice*, vol. 24, no. 1, pp. 55–66, 2014.

[10] X. Jin, J. Yang, Y. Li, B. Zhu, J. Wang, and G. Yin, "Online estimation of inertial parameter for lightweight electric vehicle using dual unscented Kalman filter approach," *IET Intelligent Transport Systems*, vol. 14, no. 5, pp. 412–422, 2020.

[11] B. Huang, S. Wu, S. Huang, and X. Fu, "Lateral stability control of four-wheel independent drive electric vehicles based on model predictive control," *Mathematical Problems in Engineering*, vol. 2018, Article ID 6080763, 15 pages, 2018.

[12] L. Chen, T. Chen, X. Xu, Y. Cai, H. Jiang, and X. Sun, "Multi-objective coordination control strategy of distributed drive electric vehicle by orientated tire force distribution method," *IEEE Access*, vol. 6, pp. 69559–69574, 2018.

[13] X. Jin, Z. Yan, G. Yin, S. Li, and C. Wei, "An adaptive motion planning technique for on-road autonomous driving," *IEEE Access*, vol. 9, pp. 2655–2664, 2021.

[14] X. Xia, L. Xiong, and Y.-Y. Hou, "Vehicle stability control based on driver's emergency alignment intention recognition," *International Journal of Automotive Technology*, vol. 18, no. 6, pp. 993–1006, 2017.

[15] P. Hang, X. Xia, and X. Chen, "Handling stability advancement with 4WS and DYC coordinated control: a gain-scheduled robust control approach," *IEEE Transactions on Vehicular Technology*, vol. 70, no. 4, pp. 3164–3174, 2021.

[16] Z. Li, L. Zheng, W. Gao, and Z. Zhan, "Electromechanical coupling mechanism and control strategy for in-wheel-motor-driven electric vehicles," *IEEE Transactions on Industrial Electronics*, vol. 66, no. 6, pp. 4524–4533, 2019.

[17] Z. Yu, Y. Feng, and L. Xiong, "Review on vehicle dynamics control of distributed drive electric vehicle," *Journal of Mechanical Engineering*, vol. 49, no. 8, pp. 105–114, 2013.

[18] B. Ren, H. Chen, H. Zhao, and L. Yuan, "MPC-based yaw stability control in in-wheel-motored EV via active front steering and motor torque distribution," *Mechatronics*, vol. 38, pp. 103–114, 2016.

[19] Z. Wang, Y. Wang, L. Zhang, and M. Liu, "Vehicle stability enhancement through hierarchical control for a four-wheel-independently-actuated electric vehicle," *Energies*, vol. 10, no. 7, p. 947, 2017.

[20] M.-D. Gong, H.-H. Wang, and X. Wang, "Active suspension control based on estimated road class for off-road vehicle," *Mathematical Problems in Engineering*, vol. 2019, Article ID 3483710, 17 pages, 2019.

Research Article

Research on Global Dynamic Path Planning Method Based on Improved A^* Algorithm

Chuanhu Niu [1], **Aijuan Li** [1,2] **Xin Huang** [3] **Wei Li** [1], **and Chuanyan Xu** [1]

[1] *School of Automotive Engineering, Shandong Jiaotong University, Jinan 250357, China*
[2] *Energy and Power Engineering College, Nanjing University of Aeronautics & Astronautics, Nanjing 210016, China*
[3] *School of Information Science and Electrical Engineering, Shandong Jiaotong University, Jinan 250357, China*

Correspondence should be addressed to Aijuan Li; 65826990@qq.com and Xin Huang; huangxin@sdjtu.edu.cn

Aiming at the optimal path and planning efficiency of global path planning for intelligent driving, this paper proposes a global dynamic path planning method based on improved A^* algorithm. First, this method improves the heuristic function of the traditional A^* algorithm to improve the efficiency of global path planning. Second, this method uses a path optimization strategy to make the global path smoother. Third, this method is combined with the dynamic window method to improve the real-time performance of the dynamic obstacle avoidance of the intelligent vehicle. Finally, the global dynamic path planning method of the proposed improved A^* algorithm is verified through simulation experiments and real vehicle tests. In the simulation analysis, compared with the modified A^* algorithm and the traditional A^* algorithm, the method in this paper shortens the path distance by 2.5%~3.0%, increases the efficiency by 10.3%~13.6% and generates a smoother path. In the actual vehicle test, the vehicle can avoid dynamic obstacles in real time. Therefore, the method proposed in this paper can be applied on the intelligent vehicle platform. The path planning efficiency is high, and the dynamic obstacle avoidance is good in real time.

1. Introduction

As one of the development directions of future automobiles, intelligent driving is receiving more and more attention [1]. In particular, path planning is an important part of intelligent driving. Path planning is an obstacle-free path from the starting point to the target point that the intelligent vehicle plans out based on environmental information [2]. Especially in the dynamic environment, in order to ensure the real-time obstacle avoidance and the efficiency of path planning, it is necessary to improve the path planning algorithm.

In recent years, the most representative and common path planning algorithms in the field are mainly divided into neural network algorithm [3], artificial potential field algorithm [4], rapidly expanding random tree algorithm [5], ant colony algorithm [6], and A^* algorithm [7, 8]. In particular, the A^* algorithm is a heuristic search algorithm; because of its strong global search ability, high search efficiency, and shortest path, it is widely used. Ziang Zhang et al. [9] proposed an improved

hybrid path planning method for a spherical mobile robot based on a pendulum, which improves the efficiency of path search, but it is aimed at a spherical mobile robot. Bijun Tang et al. [10] proposed an algorithm that uses an artificial potential field method to optimize the path of the hybrid A^* algorithm. The generated path not only is smooth but also maintains a safe distance from obstacles. However, the real-time obstacle avoidance is not good in a dynamic environment. Oleiwi et al. [11] proposed a path planning method for multiobjective mobile robots based on the ant colony algorithm and genetic algorithm which can efficiently select the optimal path for multiobjectives in a static environment, but it is not suitable for dynamic environments. Jikai Wang et al. [12] proposed a global path planning framework based on hybrid mapping, which improved the efficiency of path planning in complex environments, but it cannot guarantee the optimal path. Xiaoru Song et al. [13] proposed a dynamic global path planning method suitable for mobile robots, which can plan a smooth path in a dynamic environment, but the efficiency of path

planning still needs to be improved. The A^* algorithm based on a grid map is suitable for global path planning. This algorithm has the advantages such as a simple structure and small calculation amount [14]. However, the path planned by the traditional A^* algorithm has many folding points, which is not conducive to the driving of the intelligent vehicle. Moreover, if the space of the environment increases, A^* algorithm needs large storage space and it has low efficiency and poor real-time performance. The dynamic window method has good obstacle avoidance ability in a dynamic environment, but it is not suitable for global path planning [15].

Aiming at the optimal path and planning efficiency of global path planning for intelligent driving, this paper proposes a global dynamic path planning method based on improved A^* algorithm and dynamic window method. The improved path planning method has many advantages. First, the heuristic function of the traditional A^* algorithm is improved to make the A^* path search more biased. The time of the path planning is reduced, and the efficiency is increased. Then, the optimization strategy is used to reduce the redundant turning points and nodes of the path planning. The distance of the path is optimized, and the smoothness of the path is improved. Finally, the A^* algorithm global search capability is combined with the dynamic window method local planning capability so that the intelligent vehicle can perform global dynamic path planning, and the real-time performance of dynamic obstacle avoidance is good. The remainder of the paper is organized as follows: Section 2 discusses the improved A^* algorithm; Section 3 discusses the dynamic window method; Section 4 discusses the simulation and experimental results; Section 5 discusses the real vehicle test; and Section 6 discusses the conclusions of this research.

2. The Improved $A*$ Algorithm

The traditional A^* algorithm is a heuristic search algorithm, which constantly expands the nodes and calculates the value of each node. Finally, we can find a path with the least value. The use of heuristic function can greatly improve the search efficiency. The formula of traditional A^* algorithm is shown as follows:

$$f(n) = g(n) + h(n), \tag{1}$$

where $f(n)$ is the estimated value from the initial node to the target node, $g(n)$ is the actual value from the initial node to the node of state n, and $h(n)$ is the estimated value from the node of state n to the target node.

The selection of $h(n)$ directly affects the performance of the algorithm. Only when the value of $h(n)$ is closer to the actual cost value from the node of state n to the target node, the optimal path can be guaranteed and the efficiency of the algorithm can be improved. Therefore, the following improvements have been made.

2.1. Improved Heuristic Function $h(n)$.
Assume that $d(n)$ is the actual value from the node of state n to the target node. When the heuristic function $h(n)$ is selected differently, the following three conditions will occur:

(1) When $h(n) > d(n)$, the search range of A^* algorithm is small and the extended nodes are relatively few. Therefore, the algorithm has high efficiency, but the result is not the optimal path.

(2) When $h(n) < d(n)$, A^* algorithm has a large search range and a relatively large number of extended nodes. Therefore, the algorithm has low efficiency, but the result can get the optimal path.

(3) When $h(n) = d(n)$, this is the most ideal choice, so the A^* algorithm will search strictly according to the shortest path. Therefore, the A^* algorithm has the highest search efficiency.

In the traditional A^* algorithm, the heuristic function $h(n)$ usually used Euclidean distance [16] $h_1(n)$, Manhattan distance [17] $h_2(n)$, or Chebyshev distance $h_3(n)$:

$$h_1(n) = D * \sqrt{\left(M_x - G_x\right)^2 + \left(M_y - G_y\right)^2}, \tag{2}$$

$$h_2(n) = D * \left(\left|M_x - G_x\right| + \left|M_y - G_y\right|\right), \tag{3}$$

$$h_3(n) = D * \max\left(\left|M_x - G_x\right|, \left|M_y - G_y\right|\right), \tag{4}$$

where (M_x, M_y) represents the coordinate value of the current node, (G_x, G_y) represents the coordinate value of the target node, and D is the actual cost value of the intelligent vehicle moving one grid.

In order to make the heuristic function $h(n)$ closer to the actual value $d(n)$, a new heuristic function is designed using Manhattan distance and Chebyshev distance. The heuristic function is then dynamically weighted:

$$h(n) = D * \left(\left|M_x - G_x\right| + \left|M_y - G_y\right| - 2 \right.$$
$$* \min\left(\left|M_x - G_x\right|, \left|M_y - G_y\right|\right)\right)$$
$$+ \sqrt{2} * \min\left(\left|M_x - G_x\right|, \left|M_y - G_y\right|\right),$$
$$\tag{5}$$
$$f(n) = g(n) + (1 + k(n))h(n),$$

$$k(n) = \begin{cases} 1 - \dfrac{m(n)}{R}, & \dfrac{m(n)}{R} > K, \\[2mm] 1 - K, & \dfrac{m(n)}{R} \le K, \end{cases}$$

where $m(n)$ is the depth of search, R is the expected path length, and K is constant. Other parameters are the same as formulas (2)–(4).

2.2. Path Optimization Strategy.
The traditional A^* algorithm expands nodes based on the grid, which contains more turning points and redundant nodes [18]. They are not good for driving intelligent vehicles. In order to solve these problems, this paper proposes a path optimization strategy.

(1) Find redundant nodes and remove them. Assume that the path planned by the A^* algorithm is $\{M_k \mid k = 1, 2, 3, \ldots, n\}$. First, start from the second node M_2 of the path plan and judge whether the child node M_3 of M_2 and its parent node M_1 are in the same straight line. If it is on the same straight line, M_2 is a redundant node. Delete and update the path list. Then, check whether the child node of the next node and its parent node are on the same line. Delete redundant nodes and update the path list. Finally, all nodes are traversed to get a set of points including the starting point, turning point, and target point.

(2) Look for redundant turning points and delete them. Assume that the path planned by the A^* algorithm is $\{M_k \mid k = 1, 2, 3, \ldots, n\}$. After the optimization of strategy (1), except the starting point M_1 and the target point M_n, the other nodes are turning points. First, connect the node M_1M_3. If the straight line M_1M_3 does not pass through the obstacle and the distance from the nearest obstacle is greater than the set safe distance, M_2 is the redundant turning point and M_2 is deleted. Then connect M_1M_k ($k = 4, 5, 6, \ldots, n$) and repeat the above inspection steps. If M_1M_k passes through an obstacle or the distance from the nearest obstacle is less than the safe distance, the node M_{k-2} is deleted and the node M_1M_{k-1} is connected. Update the path list and connect node M_2M_k ($k = 4, 5, 6, \ldots, n$). Finally, repeat the above checking steps until all the nodes are traversed.

3. Dynamic Window Method

The dynamic window method can make an intelligent vehicle have a good obstacle avoidance ability in a dynamic environment. The dynamic window method is mainly used to sample multiple groups of velocities in the velocity space (linear velocity v and angular velocity w) and simulate the trajectory of intelligent vehicle in the next time interval. After obtaining multiple sets of trajectories, the multiple sets of trajectories are evaluated according to the evaluation function [19] and the intelligent vehicle will select the speed corresponding to the optimal trajectory for the next step of driving [20].

3.1. The Vehicle Kinematics Model.
According to the dynamic window method, it can continuously simulate the trajectory of the intelligent vehicle in a period of time. Therefore, it is necessary to know the kinematics model of the intelligent vehicle [21, 22]. The trajectory is represented by $(\dot{x}_t, \dot{y}_t)$. The kinematic model is shown in Figure 1.

Using the fundamental law of dynamics, we can get the dynamic formula:
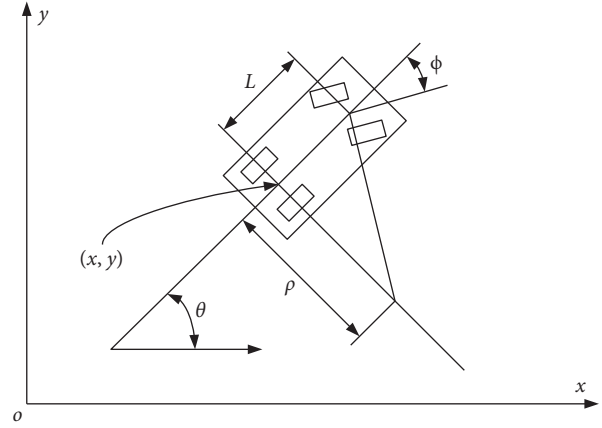
Figure 1: The vehicle kinematics model.

$$\begin{cases} \dot{x}_t = v * \cos(\theta_t), \\ \\ \dot{y}_t = v * \sin(\theta_t), \\ \\ \dot{\theta}_t = v * \dfrac{\tan \phi_t}{L}, \end{cases} \tag{6}$$

where $(\dot{x}_t, \dot{y}_t)$ is the projection speed of the intelligent vehicle on the coordinate axis at time t, v is the speed of the intelligent vehicle, θ_t is the attitude angle at time t, $\dot{\theta}_t$ is the angular velocity of attitude at time t, L is the wheelbase of the intelligent vehicle, ϕ_t is the front wheel angle at time t, and ρ is the turning radius.

In practical application, considering the omnidirectional motion of the intelligent vehicle and the transformation of the world coordinate system, the new kinematics formula is obtained:

$$\begin{aligned} x_t &= x_{t-1} + v_x\Delta t \cos(\theta_t) - v_y\Delta t \sin(\theta_t), \\ y_t &= y_{t-1} + v_y\Delta t \sin(\theta_t) + v_y\Delta t \cos(\theta_t), \\ \theta_t &= \theta_{t-1} + \omega\Delta t. \end{aligned} \tag{7}$$

3.2. Design of Speed Sampling.
After establishing the kinematics model of the intelligent vehicle, the trajectory can be calculated according to its speed (linear velocity v and angular velocity w). However, there are infinite groups of speed in the speed space. In order to control the speed sampling better, the speed group must be limited in a certain control range according to the limitations of the intelligent vehicle and the environment space.

(1) The linear speed of the intelligent vehicle and its angular speed limit range formula are shown as follows:

$$V_t = \{v_t \in [v_{\min}, v_{\max}], w_t = [w_{\min}, w_{\max}]\}. \tag{8}$$

(2) In practical application, the motor must go through a certain time interval to make the intelligent vehicle reach the corresponding speed and the speed is within a dynamic range under the influence of the motor torque. Therefore, the formula is shown as follows:

$$V_{t1} = \left\{ (v_t, \omega_t) \left| \begin{array}{l} v_t \in [v_d - \dot{v}_e \Delta t, v_d + \dot{v}_c \Delta t] \cap \\ \omega_t \in [\omega_d - \dot{\omega}_e \Delta t, \omega_d + \dot{\omega}_c \Delta t] \end{array} \right. \right\}, \quad (9)$$

where v_d and ω_d are the current front linear speed and angular speed of the intelligent vehicle, $\dot{v}_c$ and $\dot{v}_e$

are the maximum acceleration and deceleration of linear velocity, respectively, and $\dot{\omega}_c$ and $\dot{\omega}_e$ are the maximum acceleration and deceleration of angular velocity, respectively.

(3) During the operation of the intelligent vehicle, when an obstacle is detected within a safe distance, the intelligent vehicle needs to slow down or even stop. Therefore, it is necessary to further limit the velocity (linear velocity and angular velocity):

$$V_{t2} = \left\{ (v_t, \omega_t) | v_t \leq \sqrt{2 \cdot \text{dist}(v_t, \omega_t) \cdot \dot{v}_e} \cap \omega_t \leq \sqrt{2 \cdot \text{distance}(v_t, \omega_t) \cdot \dot{\omega}_e} \right\}, \quad (10)$$

where $\text{dist}(v_t, \omega_t)$ is the distance between the current position of the intelligent vehicle and the nearest obstacle.

3.3. Design of Dynamic Window Evaluation Function.
According to the dynamic window method, we need an appropriate evaluation function to select the optimal

trajectory from the final planned multiple trajectories. The priority criterion of the evaluation function is to make the intelligent vehicle avoid obstacles and move toward the target with the shortest track. The formulas are shown as follows:

$$G(v, w) = \sigma(\alpha \cdot s\_\text{head}(v, w) + \beta \cdot s\_\text{dist}(v, w) + \gamma \cdot s\_\text{velocity}(v, w)),$$

$$s\_\text{head}(v_t, \omega_t) = \frac{\text{head}(v_t, \omega_t)}{\sum_{i=1}^{n} \text{head}(v_t, \omega_t)},$$

$$s\_\text{dist}(v_t, \omega_t) = \frac{\text{dist}(v_t, \omega_t)}{\sum_{i=1}^{n} \text{dist}(v_t, \omega_t)}, \quad (11)$$

$$s\_\text{velocity}(v_t, \omega_t) = \frac{\text{velocity}(v_t, \omega_t)}{\sum_{i=1}^{n} \text{velocity}(v_t, \omega_t)},$$

where $\text{head}(v_t, \omega_t)$ is the sampling speed of the robot at time t, $\text{dist}(v_t, \omega_t)$ is the distance between the robot's trajectory and the nearest obstacle at time t, and $\text{velocity}(v_t, \omega_t)$ is the velocity of the robot at time t.

3.4. Flowchart of the Algorithm.
The flowchart of the algorithm is shown in Figure 2.

Step 1: the map is initialized and the improved A^* algorithm is used for global path planning

Step 2: strategy optimization of the planned path

Step 3: the kinematics model is established, and the velocity group is sampled

Step 4: according to the planned global path and the multiple trajectories simulated by the speed at the next moment, the optimal trajectory is selected by using the evaluation function

Step 5: establishing the optimal path

4. Simulation Experiment and Analysis

In order to verify the effectiveness of the fusion algorithm designed in this paper, MATLAB 2019b is used for simulation experiments to build a grid map scene (20 m × 20 m, grid spacing 1 m) and simultaneously place seven static obstacles of different shapes and sizes and two dynamic obstacles. In the grid map built by the simulation experiment, the starting point coordinates are (1.5 m, 1.5 m) and the target point coordinates are (19.5 m, 19.5 m).

4.1. Simulation Experiment of Improved Heuristic Function.
The traditional A^* algorithm has many redundant nodes and large search range, which reduces the efficiency of the algorithm. In this paper, the A^* algorithm is improved to reduce the scope of search and improve the efficiency of the
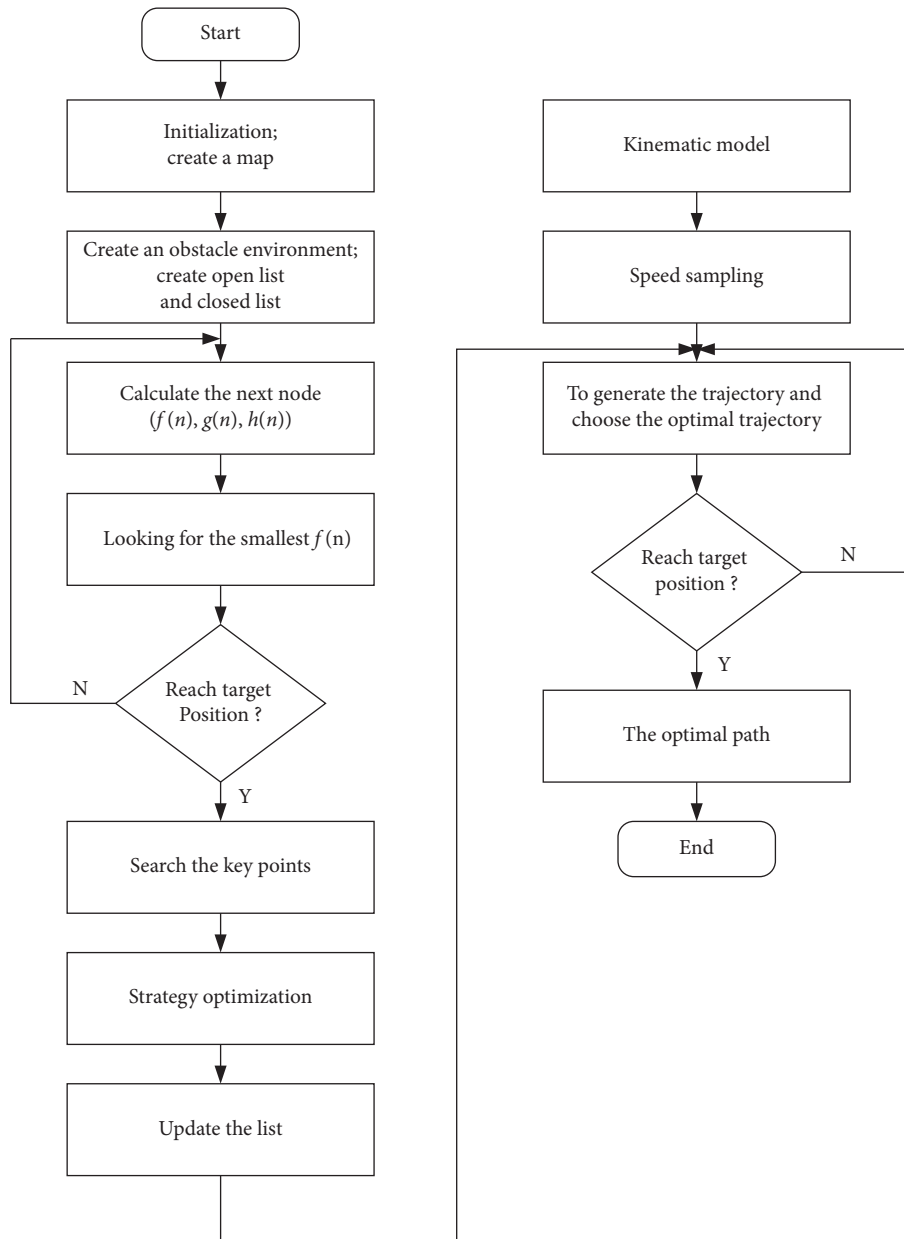
FIGURE 2: Flowchart of the algorithm.

algorithm. Black is the initial position, green is the target position, red is the optimal path, and yellow is the search area except the optimal path. The experimental results are shown in Figure 3.

The experimental image of the improved A^* algorithm used in this paper is shown in Figure 3(a). The search area is $128\,\mathrm{m}^2$, the path length is $28.38\,\mathrm{m}$, and the time is $0.040\,\mathrm{s}$.

The experimental image of traditional A^* algorithm is shown in Figure 3(b). The search area is $180\,\mathrm{m}^2$, the path length is $28.38\,\mathrm{m}$, and the time is $0.050\,\mathrm{s}$.

The experimental image of the improved A^* algorithm using Manhattan distance and Euclidean distance is shown in Figure 3(c). To distinguish, it is named the modified A^* algorithm. The search area is $166\,\mathrm{m}^2$, the path length is $28.38\,\mathrm{m}$, and the time is $0.045\,\mathrm{s}$.

The detailed data are shown in Table 1.

From the above data, compared with the traditional A^* algorithm, the improved A^* algorithm in this paper can reduce the search area by 28.9% and increase the efficiency by 20.0%. Compared with the modified A^* algorithm, the improved A^* algorithm in this paper can reduce the search area by 22.9% and increase the efficiency by 11.1%.

4.2. Static Global Path Planning. In a static simulation environment, the simulation experiments results based on different algorithms will be compared in this section. The simulation experiments in this paper are in the same environment, the maximum speed and acceleration of the intelligent vehicle are the same, and the red line is the actual trajectory of the intelligent vehicle.

(a)

(b)

(c)
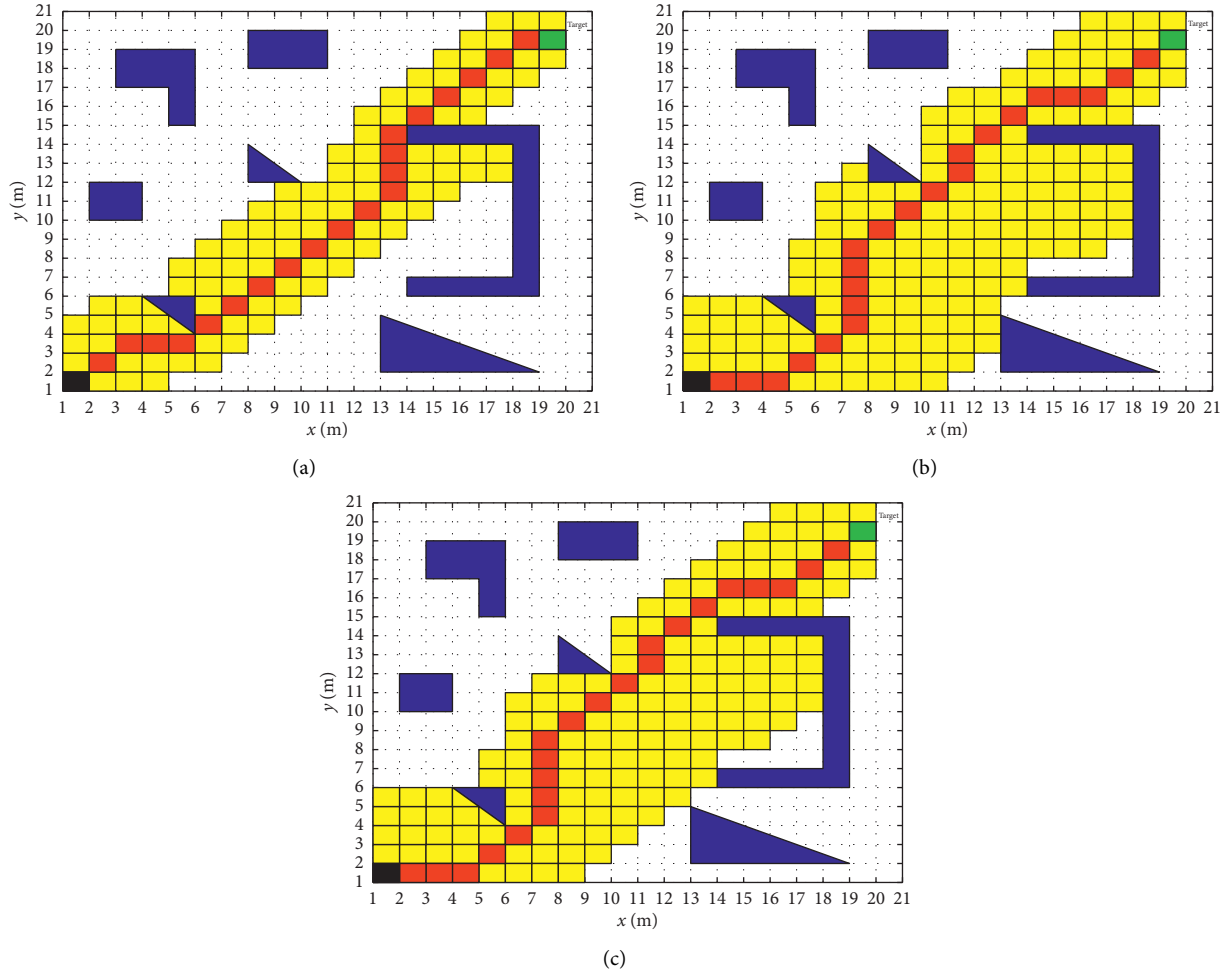
FIGURE 3: Path planning results of various algorithms. (a) The improved A^* algorithm. (b) Traditional A^* algorithm. (c) Modified A^* algorithm.

TABLE 1: Statistics 1.

Name	The improved A^* algorithm	Traditional A^* algorithm	Modified A^* algorithm
Search area (m²)	128	180	166
Path length (m)	28.38	28.38	28.38
Average time (s)	0.040	0.050	0.045

Working condition 1: the experimental image of the traditional A^* algorithm is shown in Figure 4(a). Each circle in the figure represents a node, and various polygons are obstacle environments. According to the results of simulation experiments, this algorithm has many redundant nodes and turning points, the number of optimal path nodes is 24, the number of turning points is 7, and a total of 180 nodes are expanded. The search path length is 28.38 m, and the time is 0.050 s.

Working condition 2: the experimental image of the modified A^* algorithm is shown in the blue line in Figure 4(b). Each circle in the figure represents a node, and various polygons are obstacle environments. According to the results of simulation experiments, the number of optimal path nodes in this algorithm is 4, the number of turning points is 2, and a total of 166 nodes

are expanded. The length of the search path is 27.50 m, and the time is 0.045 s.

Working condition 3: the experimental images of the modified A^* algorithm and the dynamic window method are shown in the red line in Figure 4(b). Each circle in the figure represents a node, and various polygons are obstacle environments. According to the results of the simulation experiment, the trajectory planned by this algorithm is smooth, the optimal path length is 28.56 m, and the time is 51.31 s.

Working condition 4: the experimental image of the improved A^* algorithm in this paper is shown in the blue line in Figure 4(c). Each circle in the figure represents a node, and various polygons are obstacle environments. According to the results of the simulation experiment, the number of optimal path nodes of this

(a)

(b)

(c)
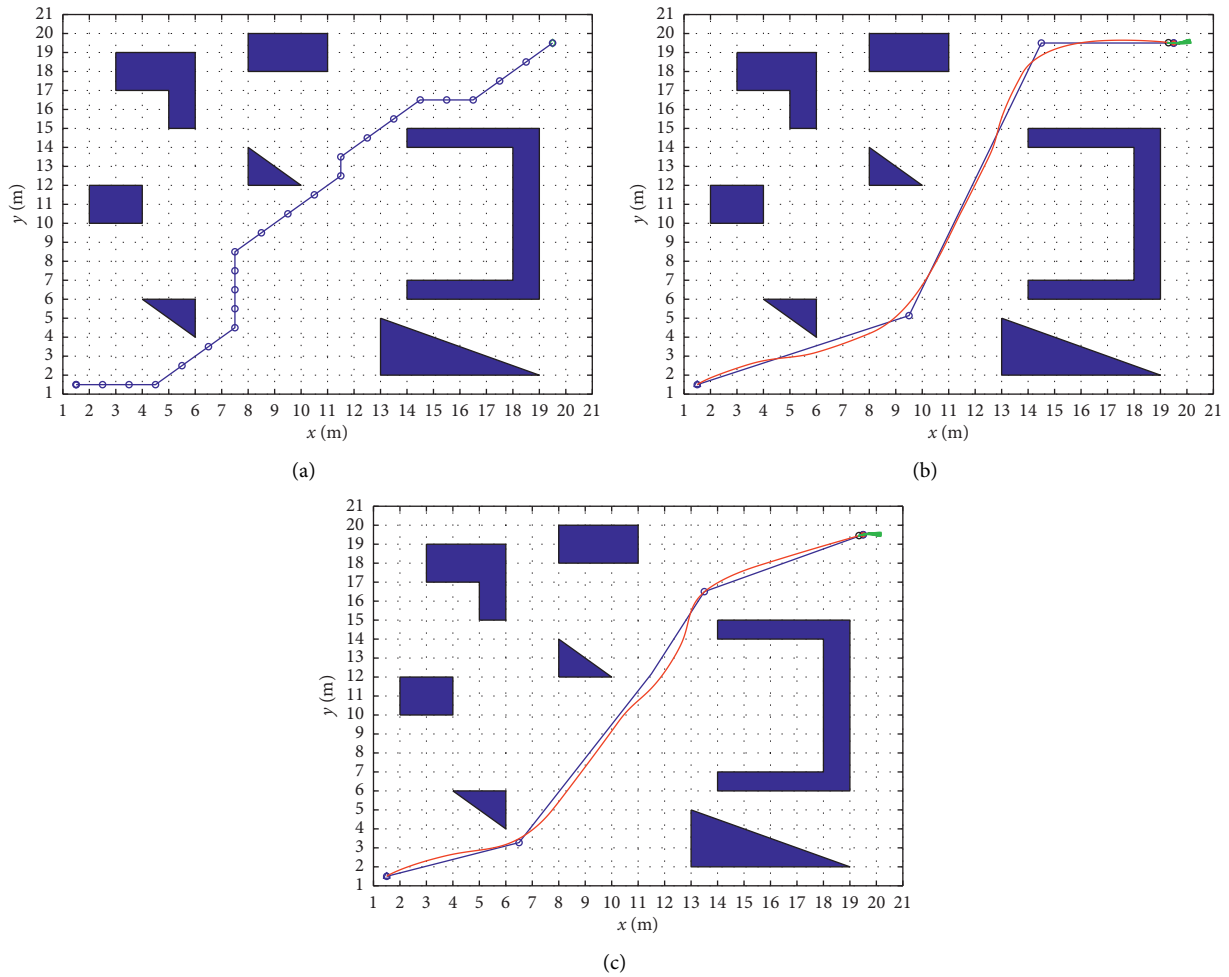
Figure 4: Path planning results of three algorithms. (a) Traditional A^* algorithm. (b) Modified A^* algorithm. (c) Improved A^* algorithm.

algorithm is 4, the number of turning points is 2, and a total of 128 nodes are expanded. The optimal path length of this algorithm is 26.99 m, and the time is 0.04 s.

Working condition 5: the experimental images of the improved A^* algorithm and dynamic window method in this paper are shown in the red line in Figure 4(c). Each circle in the figure represents a node, and various polygons are obstacle environments. According to the results of the simulation experiment, the path planned by this algorithm is smooth, the optimal path length is 27.13 m, and the time is 46.69 s.

Detailed statistics are shown in Tables 2 and 3.

4.3. Dynamic Global Path Planning. In the dynamic simulation environment, this section will compare simulation experiments based on different algorithms. The simulation experiment in this paper is in the same environment, the maximum speed and acceleration of the intelligent vehicle are the same, and the red line is the actual trajectory of the intelligent vehicle.

Working condition 1: the experimental images of the traditional A^* algorithm and dynamic window method are shown in Figure 5. The figure shows the dynamic obstacle avoidance situation at different moments. Various polygons are the obstacle environment. According to the results of simulation experiments, the optimal path length of this algorithm is 29.63 m and the total time is 54.77 s.

Working condition 2: the experimental images of the modified A^* algorithm and dynamic window method are shown in Figure 6. The figure shows the dynamic obstacle avoidance situation at different moments. Various polygons are the obstacle environment. According to the results of simulation experiments, the optimal path length of this algorithm is 29.48 m and the total time is 52.75 s.

Working condition 3: the experimental images using the improved A^* algorithm and dynamic window method in this article are shown in Figure 7. The figure shows the dynamic obstacle avoidance situation at different moments. Various polygons are the obstacle environment. According to the results of simulation

TABLE 2: Simulation data statistics 2.

Name	Number of nodes (piece)	Number of break points (piece)	Search node (piece)	Path length (m)	Average time (s)
Working condition 1 (static)	24	7	180	28.38	0.050
Working condition 2 (static)	4	2	166	27.50	0.045
Working condition 4 (static)	4	2	128	26.99	0.040

TABLE 3: Simulation data statistics 3.

Name	Working condition 3 (static)	Working condition 5 (static)	Working condition 1 (dynamic)	Working condition 2 (dynamic)	Working condition 3 (dynamic)
Path length (m)	28.56	27.13	29.63	29.48	28.74
Average time (s)	51.31	46.69	54.77	52.75	47.30

(a)

(b)

(c)

(d)
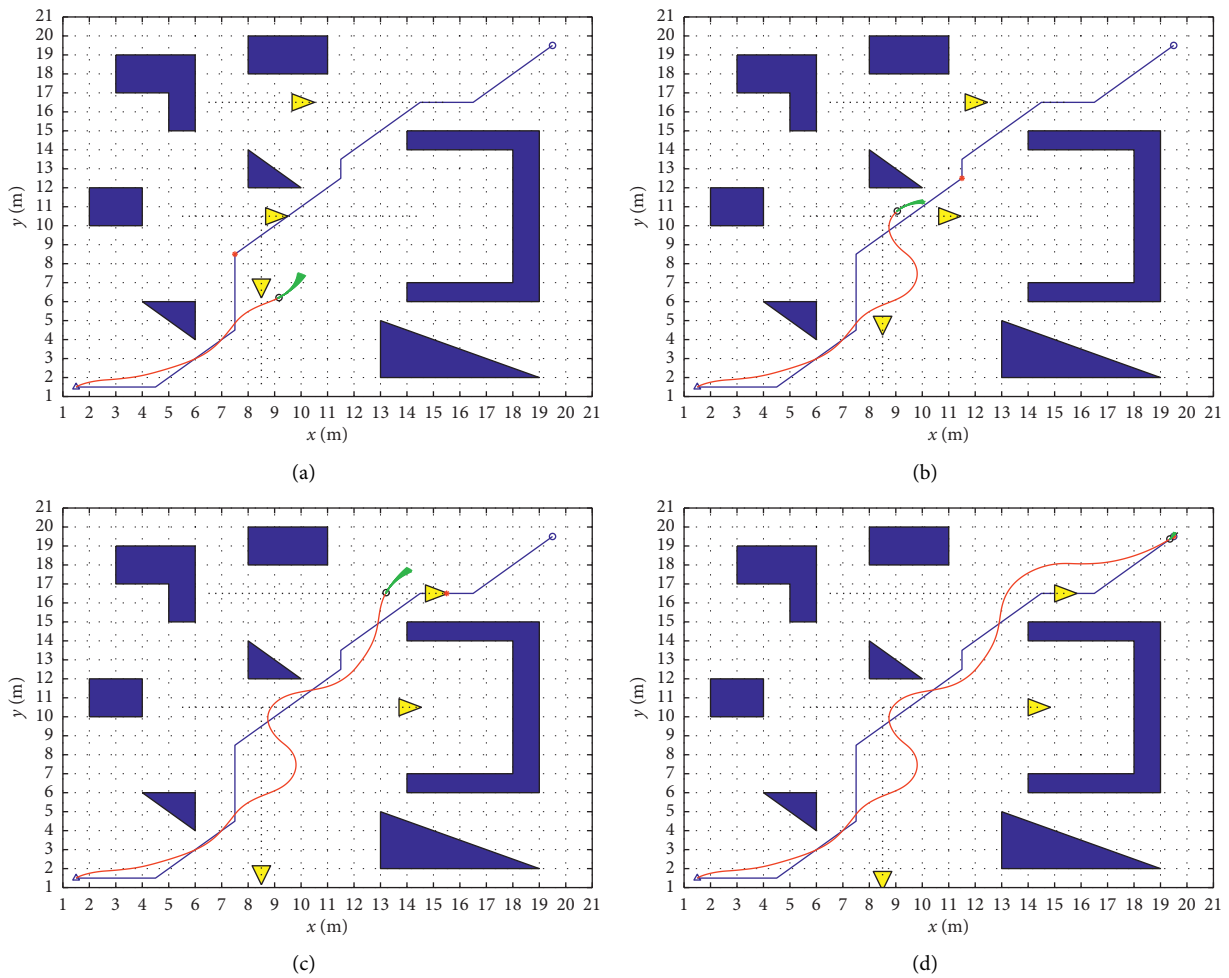
FIGURE 5: Trajectory of the traditional A^* algorithm. (a) Traditional A^* algorithm 1. (b) Traditional A^* algorithm 2. (c) Traditional A^* algorithm 3. (d) Traditional A^* algorithm 4.
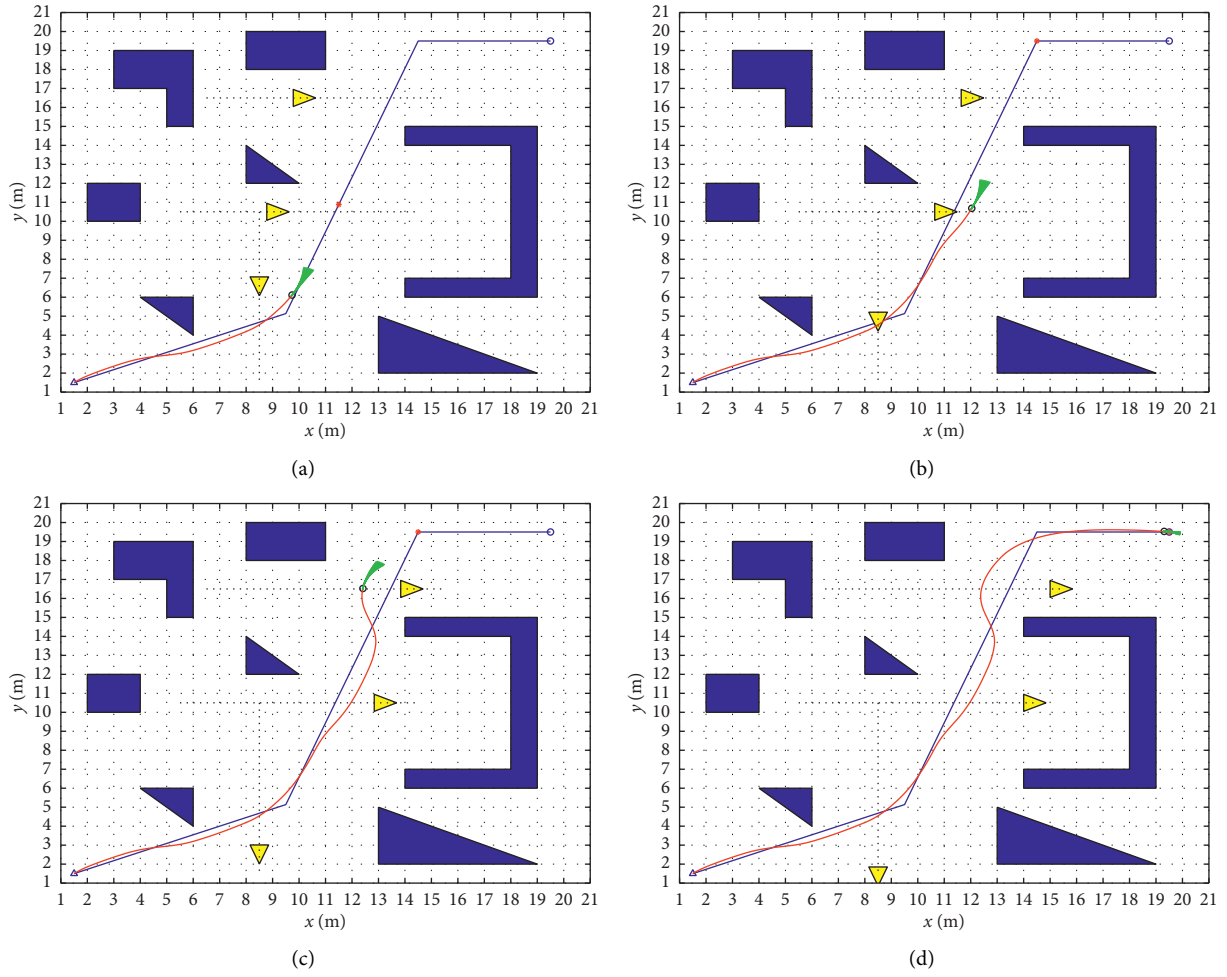
Figure 6: Trajectory of the modified A^* algorithm. (a) Modified A^* algorithm 1. (b) Modified A^* algorithm 2. (c) Modified A^* algorithm 3. (d) Modified A^* algorithm 4.
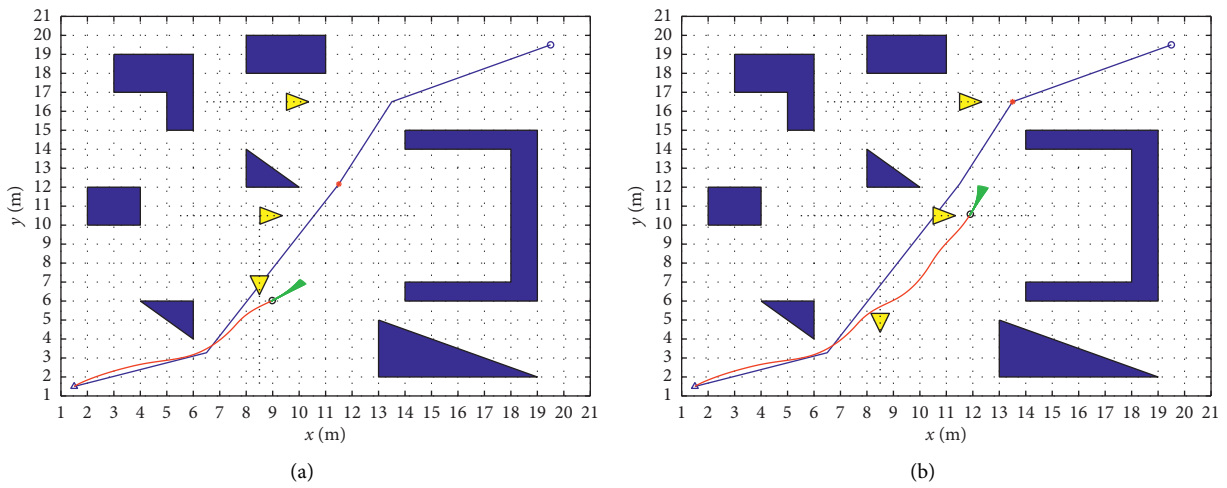
Figure 7: Continued.

(c)

(d)
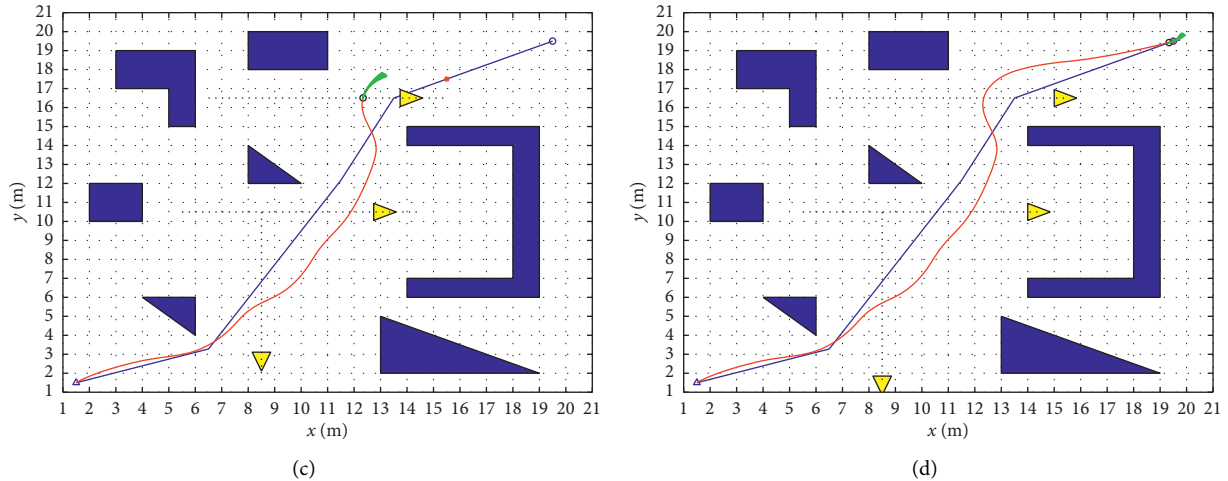
FIGURE 7: Trajectory of the improved A^* algorithm. (a) Improved A^* algorithm 1. (b) Improved A^* algorithm 2. (c) Improved A^* algorithm 3. (d) Improved A^* algorithm 4.

experiments, the optimal path length of this algorithm is 28.74 m and the total time is 47.30 s.

Detailed statistics are shown in Table 3.

4.4. Simulation Experiment Results and Analysis. In the static obstacle environment, compared with the modified A^* algorithm and the dynamic window algorithm, the improved A^* algorithm and the dynamic window algorithm in this paper reduce the path distance by 5.0% and the time by 9.0%.

In the dynamic obstacle environment, compared with the modified A^* algorithm and dynamic window algorithm, the improved A^* algorithm and dynamic window algorithm in this paper reduce the path distance by 2.5% and the time by 10.3%. Compared with the traditional A^* algorithm and dynamic window algorithm, the path distance of the algorithm proposed in this paper is reduced by 3.0% and the time is reduced by 13.6%

Therefore, the algorithm proposed in this paper is more efficient. The planned path is shorter and smoother, which is conducive to the driving of intelligent vehicle.

5. Real Vehicle Test

This paper uses an unmanned dual-head driving test vehicle based on the Linux system to verify the improved A^* path planning algorithm. The platform supports complete independent development, equipped with 16-line laser radar, millimeter wave radar, binocular vision module, GPS positioning module, and other equipment, with high-precision positioning, automatic navigation, and tracking functions. The actual vehicle is shown in Figure 8. The static obstacle is a cardboard box, and the dynamic obstacle is a tester. To ensure safety, the test vehicle is equipped with a driver responsible for emergency situations, and the maximum speed is set to 30 km/h.

FIGURE 8: Intelligent driving platform.

Figure 9 is an image displayed by binocular vision, which shows an obstacle environment. Figure 10 is a lidar image, including the location of obstacles. Figure 11 shows the static obstacle avoidance trajectory. The red trajectory is the trajectory of global path planning and local path planning, the yellow is the obstacle, and the blue is the actual trajectory of the experimental vehicle. The static obstacles are cartons with a large width, so the obstacle avoidance range is large. Figures 12 and 13 are dynamic obstacle avoidance trajectories. The red trajectory is the trajectory of global path planning and local path planning, the yellow is the obstacle, the blue is the actual trajectory of the experimental vehicle, and the dynamic obstacle is the experimental personnel. Figures 14–17 are the obstacle avoidance pictures taken during the real vehicle test at high speed.

The real vehicle test shows that the vehicle can avoid dynamic obstacles in real time. The trajectory is smooth. Therefore, the algorithm proposed in this paper can be applied to the practical application of intelligent electric vehicle platform and has practical value of engineering application.

FIGURE 9: Binocular vision image.
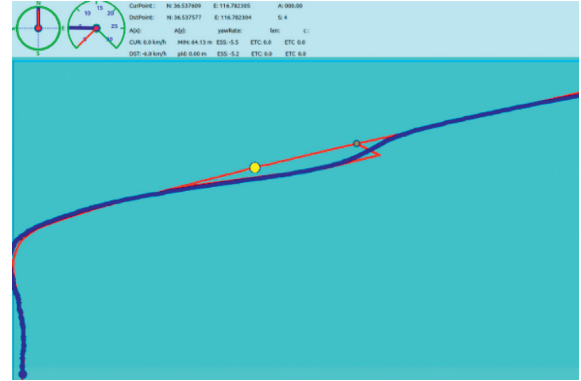
FIGURE 13: Dynamic obstacle avoidance trajectory 2.
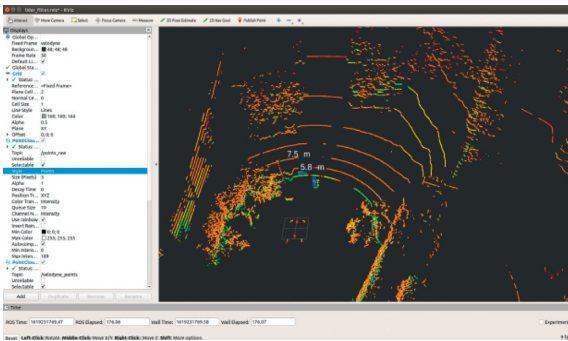
FIGURE 10: Lidar image.

FIGURE 14: Static obstacle avoidance diagram.

FIGURE 11: Static obstacle avoidance trajectory diagram.

FIGURE 15: Dynamic obstacle avoidance 1.
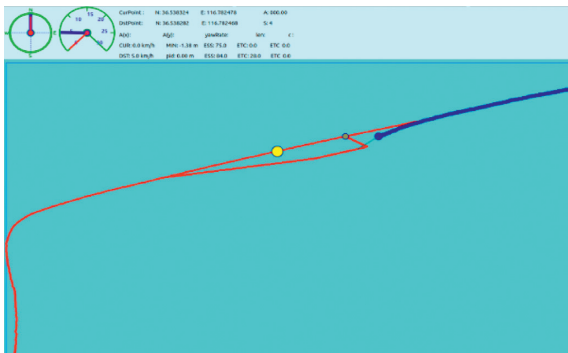
FIGURE 12: Dynamic obstacle avoidance trajectory 1.

FIGURE 16: Dynamic obstacle avoidance 2.

Figure 17: Dynamic obstacle avoidance 3.

6. Conclusions

In this paper, a global dynamic path planning method based on the improved A^* algorithm is proposed to deal with the optimal path and planning efficiency of global path planning for intelligent driving. This method has high efficiency and smoother path planning, and the real-time performance of dynamic obstacle avoidance is good. The specific contents of this article are summarized as follows:

(1) The heuristic function $h(n)$ of traditional A^* algorithm is improved, and the dynamic weighting method is used to make $h(n)$ closer to the actual distance $d(n)$. This method reduces the search area in the A^* path search, reduces the planning time, and improves the efficiency of the algorithm.

(2) Use optimization strategies to optimize the optimal path, reduce redundant nodes and turning points of the optimal path, and make the path smoother, which is conducive to the driving of intelligent vehicle. The improved A^* algorithm is combined with the dynamic window method for dynamic obstacle avoidance. This not only ensures that the improved A^* algorithm can efficiently plans the optimal path but also improves the local optimal problem of dynamic window method so that the intelligent vehicle has global dynamic path planning capabilities.

(3) In the simulation analysis, the method in this paper shortens the path distance by 2.5%~3.0%, increases the efficiency by 10.3%~13.6%, and generates a smoother path. Through the actual vehicle test, the results show that the algorithm proposed in this paper has good real-time performance and good stability for dynamic obstacle avoidance. The improved A^* method can be applied in practice on the intelligent electric vehicle platform, and it has a practical value in engineering application.

Data Availability

The data used to support the findings of this study are included within the article.

Conflicts of Interest

The authors declare that there are no conflicts of interest regarding the publication of this article.

Authors' Contributions

Chuanhu Niu was responsible for methodology and prepared the original draft; Aijuan Li and Chuanyan Xu were responsible for software and validated the data; Xin Huang and Wei Li reviewed and edited the manuscript. All authors have read and agreed to the published version of the manuscript.

Acknowledgments

References

[1] X. Jin, Z. Yan, G. Yin et al., "An adaptive motion planning technique for on-road autonomous driving," *IEEE Access*, vol. 14, pp. 2169–3536, 2020.

[2] B. Pradhan, A. Nandi, N. B. Hui, D. S. Roy, and J. J. P. C. Rodrigues, "A novel hybrid neural network-based multirobot path planning with motion coordination," *IEEE Transactions on Vehicular Technology*, vol. 69, no. 2, pp. 1319–1327, 2020.

[3] M. Chen and D. Zhu, "Optimal time-consuming path planning for autonomous underwater vehicles based on a dynamic neural network model in ocean current environments," *IEEE Transactions on Vehicular Technology*, vol. 69, no. 12, pp. 14401–14412, 2020.

[4] S.-O. Park, M. C. Lee, and J. Kim, "Trajectory planning with collision avoidance for redundant robots using jacobian and artificial potential field-based real-time inverse kinematics," *International Journal of Control, Automation and Systems*, vol. 18, no. 8, pp. 2095–2107, 2020.

[5] B. Hu, Z. Cao, and M. Zhou, "An Efficient rrt-based framework for planning short and smooth wheeled robot motion under kinodynamic constraints," *IEEE Transactions on Industrial Electronics*, vol. 68, no. 4, pp. 3292–3302, 2021.

[6] C. Wu, S. Zhou, and L. Xiao, "Dynamic path planning based on improved ant colony algorithm in traffic congestion," *IEEE Access*, vol. 8, pp. 180773–180783, 2020.

[7] C. Liu, Q. Mao, X. Chu et al., "An improved A-Star algorithm considering water current, traffic separation and berthing for vessel path planning," *Applied Sciences*, vol. 9, no. 6, pp. 1–17, 2019.

[8] S. Erke, D. Bin, N. Yiming et al., "An improved A-star based path planning algorithm for autonomous land vehicles,"

International Journal of Advanced Robotic Systems, vol. 17, no. 5, pp. 1–13, 2020.

[9] Z. Zhang, Y. Wan, Y. Wang et al., "Improved hybrid A * path planning method for spherical mobile robot based on pendulum," *International Journal of Advanced Robotic Systems*, vol. 18, no. 1, pp. 1–14, 2021.

[10] B. Tang, K. Hirota, K. Hirota, X. Wu, Y. Dai, and Z. Jia, "Path planning based on improved hybrid A * algorithm," *Journal of Advanced Computational Intelligence and Intelligent Informatics*, vol. 25, no. 1, pp. 64–72, 2021.

[11] B. K. Oleiwi, H. Roth, and B. I. Kazem, "A hybrid approach based on ACO and GA for multi objective mobile robot path planning," *Applied Mechanics and Materials*, vol. 527, pp. 203–212, 2014.

[12] J. Wang and Z. Chen, "A novel hybrid map based global path planning method," in *Proceedings of the 2018 3rd Asia-Pacific Conference on Intelligent Robot Systems (ACIRS)*, pp. 66–70, Singapore, July 2018.

[13] X. Song, S. Gao, C. B. Chen, K. Cao, and J. Huang, "A new hybrid method in global dynamic path planning of mobile robot," *International Journal of Computers Communications & Control*, vol. 13, no. 6, pp. 1032–1046, 2018.

[14] A. V. Le, V. Prabakaran, V. Sivanantham, and R. E. Mohan, "Modified A-star algorithm for efficient coverage path planning in tetris inspired self-reconfigurable robot with integrated laser sensor," *Sensors*, vol. 18, no. 8, pp. 1–27, 2018.

[15] T. J. Chen, Y. Sun, W. Dai, W. Tao, and S. Liu, "On the shortest and conflict-free path planning of Multi-AGV system based on dijkstra algorithm and the dynamic time-window method," *Advanced Materials Research*, vol. 645, pp. 267–271, 2013.

[16] C. Juan, E. Leal, E. F. P. González et al., "The exact euclidean distance transform: a new algorithm for universal path planning," *International Journal of Advanced Robotic Systems*, vol. 10, no. 6, pp. 1–10, 2013.

[17] W. Liu and W. Zhang, "A quantum protocol for secure manhattan distance computation," *IEEE Access*, vol. 8, pp. 16456–16461, 2020.

[18] H. Ren, S. Chen, L. Yang, and Y. Zhao, "Optimal path planning and speed control integration strategy for UGVs in static and dynamic environments," *IEEE Transactions on Vehicular Technology*, vol. 69, no. 10, pp. 10619–10629, 2020.

[19] L. Chang, L. Shan, C. Jiang, and Y. Dai, "Reinforcement based mobile robot path planning with improved dynamic window approach in unknown environment," *Autonomous Robots*, vol. 45, no. 1, pp. 51–76, 2020.

[20] X. Jin, J. Yang, Y. Li, B. Zhu, and G. Yin, "Online estimation of inertial parameter for lightweight electric vehicle using dual unscented kalman filter approach," *IET Intelligent Transport Systems*, vol. 14, no. 5, 2020.

[21] L. Jiang, H. Huang, and Z. Ding, "Path planning for intelligent robots based on deep Q-learning with experience replay and heuristic knowledge," *IEEE/CAA Journal of Automatica Sinica*, vol. 7, no. 4, pp. 1179–1189, 2020.

[22] X. Jin, J. Wang, S. Sun, S. Li, J. Yang, and Z. Yan, "Design of constrained robust controller for active suspension of in-wheel-drive electric vehicles," *Mathematics*, vol. 9, no. 3, pp. 2227–7390, 2021, https://www.mdpi.com/.

Research Article

Response Time Analysis for Nonperiodic CAN Message Based on GI/G/1 Queue Model

Fei Meng [ID],[1] Ying Zhu,[1] and Zhenzhong Chu [ID][2]

[1]*Department of System Science, University of Shanghai for Science and Technology, Shanghai 200093, China*
[2]*Logistics Engineering College, Shanghai Maritime University, Shanghai 201306, China*

Correspondence should be addressed to Zhenzhong Chu; chu_zhenzhong@163.com

Controller area network (CAN) has wide applications in modern industrial control systems. Automobile manufacturers use this communication protocol for vehicle control, which is subject to real-time and high-reliability performance. However, with the increasing actuators gathered in the vehicle, time delay will lead to a serious problem for the vehicle safety and performance control. Thus, the information transmission stability of the CAN message needs to be investigated. In order to find out the delay response time of nonperiodic CAN message in the vehicle bus area, the response of the message transmitted in the CAN bus is modeled based on the GI/G/1 queue theory. The test platform is developed to verify the methodology. In the experimental test, some conditions with different IDs, load ratios, and priorities are investigated. Experimental results are compared with the theoretical results, and the simulation results show that the method is valid and verify the real response delay time of nonperiodic CAN message.

1. Introduction

With the rapid development of the vehicle technology, vehicles are developed as a transportation facility and become more convenient for people. More and more functions are developed for comfort, accessibility, and practicality compared with the past. In order to meet the comfortable and reliability demands of passengers, modern technology has integrated entertainment equipment, personal communication electronic device, wireless connection, and other functions into one car. All these components connected to the network system achieve their function through the electronic control units (ECUs); with the increasing demand for cars, the number of ECUs is growing. There may be more than 100 ECUs to provide all the electronic functions in high-end vehicles [1–3]. Since the information is exchanged through those ECUs with the interconnected data buses, it is

necessary to optimize the communication network to reduce the cost and improve the performance.

Controller area network [4–6] is designed as a microcontroller in the automotive industry and has become a global standard. Now CAN has been well extensively used in other areas due to its high real-time properties and low cost, such as industrial automation, aircraft industry, industrial control, safety protection, and other fields. No matter in which field, the real-time analysis of CAN bus is still the research; see [7–9] and the references therein. In [2], Sato and Fukumoto analyzed the response time of CAN with randomly occurring messages based on M/G/1 queuing theory. Lim et al. [10] investigated the signal distortion in a controller area network with flexible data rate, and the presented model-based analysis can closely approximate the size and time response of ringing and the extent of bit time distortion. Mubeen et al. [11] analyzed periodic, sporadic,

and mixed transmission of messages in CAN with implementation of priority queues and FIFO queues.

However, for the general CAN bus network communication, due to the message triggered randomly, the real-time property is also related to the random sending messages. In this paper, the nonperiodic CAN bus communication is investigated. Based on the queue theory GI/G/1 and the bit-stuffing mechanism, the delay time can be read clearly at different ratios.

The rest of this paper is organized as follows. Section 2 mainly describes the basics of CAN bus and mathematical queue GI/G/1 model. Section 3 presents the delay model of nonperiodic CAN message which is composed of queue theory about the waiting time and bit-stuffing mechanism about the transmission time. The experimental platform is set up in Section 4. In Section 5, the analysis work about the data compared with the experimental theory is developed. Finally, Section 6 concludes the paper.

2. Theoretical Analysis

CAN is a multimaster serial communication bus, and it is designed not only with high bit rate and high anti-electromagnetic interference but also detecting any occurring error. The CAN communication protocol mainly described the ways of information communication between different devices. With the CAN layer and the definition of the open systems interconnection (OSI), all devices can communicate with the same layer. Real communication can be implemented on every equipment between two layers, and information was only interconnected by physical media. Usually, the specification of CAN defines the bottom transmission via two layers: the data link layer and physical layer. CAN communication could use a variety of physical media, such as twisted-pair cable and optical fiber. The most commonly used is twisted-pair wiring. Signals using a differential voltage and two signal lines are referred to as CAN_H and CAN_L, the static voltage is about 2.5 V, the state is expressed as logic 1, which can also be called a Recessive, and CAN_H is higher than CAN_L, which can be presented as logic 0, known as the "dominant"; thus, CAN_H equals 3.5 V and CAN_L becomes 1.5 V.

The delay of CAN communication can be divided into four parts: generation delay, queuing delay, transmission delay, and delivery delay [12]. The generation delay refers to the time from receiving the request of sending message from the sending node processor to writing the message data into the cache queue; queuing delay refers to the time from message frame entering the sending buffer queue to the time when the message frame occupies the bus; the transmission delay refers to the time from the message occupying the bus to leaving the bus; delivery delay refers to the time when a message departs from the bus to the receiving node receiving data and providing it to the target processor. Generally, the generation delay and the delivery delay are generally related to the characteristics of the hardware electrical equipment, and the delay time is small. Therefore, once considering the CAN communication delay, the queuing delay and the

transmission delay are considered. This paper mainly discusses these two parts of the CAN delay.

2.1. Transmission Mechanism of CAN Bus.
Data in CAN bus is divided into two types: one is the standard frame, and the other is extended frames. The main difference between these is the length of identifier ID. The schematic diagram of the standard frames is shown in Figure 1.

The main difference of two CAN types between standard frame and extended frame is the length of message. The standard frame has an 11-bit identifier and the extended one has 29-bit identifier. The identifier must be unique, which means that the message derived from different sources must have different identifiers.

Once the bus is at least 6 recessive bits, it is called idle, and all nodes join in the bus with pending messages ready to transmit from the identifier field. According to the arbitration mechanism, a node will not transmit a message if it sent a recessive bit, and the bus level is dominant. Only when the node level is the same as the bus level through whole ID field will the node be allowed to transmit messages. That means the message ID is used for the arbitration mechanism: the smaller the ID, the higher the priority. Thus, the identifier has two purposes: (1) the priority of the frame and (2) making the receivers able to filter frames. It should be noted that the data transmit in the bus will only have 0~8 bytes and each byte of message occupies 8 bits in data field, and the data field has 0~64 bits. For more details about other fields in the frame, the reader is referred to [2, 9].

CAN uses NRZ (non-return-to-zero) encoding mode for bit synchronization. In CAN bus, it will be seen as an error flag when the bus has 6 consecutive same polarity bits (000000 or 111111). To avoid those special bit patterns, once a send node has successively transmitted 5 same polarity bits (00000 or 11111), it will additionally add one opposite polarity bit (as a stuff bit). When the receive node has detected 5 same polarity bits, it will remove the stuff bit. This process is called bit-stuffing mechanism.

2.2. Queue Mode Modeling.
Queuing is a normal phenomenon in daily life; for example, people queue to register in the hospital and line up in the store and cars on the highway queue to toll station. The queue system [13–15] consists of two parts: one needs to be served and the other provides the services. Those people or things that need to be served are called customers and service for customers is called service counter. The queuing service system can be seen as the customers and the service counter. The GI/G/1 queue [16, 17] model is usually described as follows: the customers arrived at time $T_1, T_2, T_3 \ldots$; arrival time interval sequence $\tau_n = T_n - T_{n-1}$, where $(n = 1, 2, \ldots, \tau_0 = 0)$ are independent from each other and follow the same distribution function $A(t); t \geq 0$, and $0 < (1/\lambda) = \int_0^\infty t \, dA(t)$; here $\lambda > 0$ is a constant. The service time sequence $\chi\_i, i > 1$ of customers needed is independent and follows the general distribution $B(t)$, and $0 < (1/\mu) = \int_0^\infty t \, dB(t)$ is taken as the average service time. The system follows the FIFO (first-in-first-out) mechanism and only has one service counter.
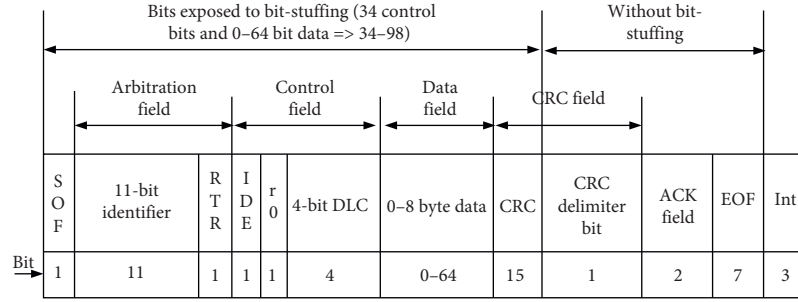
Figure 1: Standard format of CAN data frame.

In GI/G/1 queue system, C_n can be seen as the n_{th} customer arriving in the system at time T_n, and w_n can be seen as the waiting time of customer C_n. Customer C_{n+1} arriving in the system will meet two statuses: one is that the service counter is busy and the other is that the service counter is idle. The two statuses are shown in Figures 2(a) and 2(b). The process can be formulated as

$$\tau_{n+1} + w_{n+1} = w_n + \chi_n. \tag{1}$$

Here, $w_{n+1} = w_n + \chi_n - \tau_{n+1}$ is the $(n+1)_{th}$ customer's waiting time when it arrives in the system, and thereby w_{n+1} could be greater than 0 or equal to 0. w_{n+1} could be shown as

$$w_{n+1} = \begin{cases} w_n + \chi_n - \tau_{n+1}, & w_n + \chi_n - \tau_{n+1} > 0, \\ 0, & w_n + \chi_n - \tau_{n+1} \le 0. \end{cases} \tag{2}$$

Let $U_n = \chi_n - \tau_{n+1}$, and equation (2) can be described as

$$w_{n+1} = \max\{0, w_n + \chi_n - \tau_{n+1}\} = \max\{0, w_n + U_n\}. \tag{3}$$

According to equation (3), we can know that

$$\begin{aligned} w_1 &= \max\{0, w_0 + U_0\}, \\ w_2 &= \max\{0, w_1 + U_1\} = \max[0, U_1 + \max\{0, w_0 + U_0\}], \\ w_n &= \max\{0, w_{n-1} + U_{n-1}\} \\ &= \max[0, U_{n-1}, U_{n-1} + U_{n-2}, \ldots, +U_0 + w_0]. \end{aligned} \tag{4}$$

According to [18], the upper boundary of the average waiting time for the mean waiting time of the GI/G/1 system is adopted. In this paper, when $\rho < 1$, there will be

$$E[W_q] \le \lambda \frac{D[\chi_i] + D[\tau_i]}{2(1 - \rho)}. \tag{5}$$

Here, $D[\chi_i]$ is the variance of service time, $D[\tau_i]$ is the variance of arrive interval time, and $\rho = \lambda/\mu$ indicates the load level or intensity of the system. Thereby, the inequation can be deduced into two parts.

$$E[W_q] \le \rho E[W_q] + \lambda \frac{D[\chi_i] + D[\tau_i]}{2}. \tag{6}$$

In equation (6), the first part on the right can be seen as the waiting time of customers in the queue when a new message arrived, and the second part is the average service time of the current customer served by service counter when

a new message arrived. That means if $E[W_{rs}]$ denotes the current customer-rest service time when a new customer arrives, we can get

$$E[W_{rs}] = \lambda \frac{D[\chi_i] + D[\tau_i]}{2}. \tag{7}$$

The average staying time of a message can be obtained by the total time of the average service time and average waiting time, and the expression is

$$E[W] = \frac{1}{\mu} + \lambda \frac{D[\chi_i] + D[\tau_i]}{2(1 - \rho)}. \tag{8}$$

3. Delay Analysis for Nonperiodic CAN Message

Based on the knowledge of queue theory, if messages occupy the bus and transmitted data was considered as service, then the nodes in the CAN bus need to occupy the bus in the messages transmission process which can be regarded as customer, and the CAN bus provides the physical media to transmit the messages by arbitration and managing the message transmission; the bus can be called service counter.

Generally, the messages in the CAN bus system are sent continuously; the total number of customers is infinite, and let the arrival interval time of customer follow general independent distribution. The CAN bus employs the Carrier Sense Multiple Access (CSMA) protocol to arbitrate the messages. This means that if the low-priority message is sent, the higher-priority message needs to wait to be sent until the low-priority messages are sent completely, and if the higher-priority messages are sent, the priority message cannot be sent. This process accords with the service protocol of nonpreemptive discrimination of priorities. The status of transmission finish for a message in CAN bus is only when all the bits were sent completely. Thus, we could consider the transmission time as the service time. Due to the fact that the CAN bus transmission time followed a probability distribution according to the difference of stuffing bit, the service time followed the general probability distribution. There are many nodes in a CAN bus but only one node can send message transmitted on the bus at a moment, which means that there is only one service counter. On the basis of these features of the CAN bus transmission mechanism, we adopt the GI/G/1 queue theory [12, 19, 20] to model the delay of nonperiodic CAN messages.
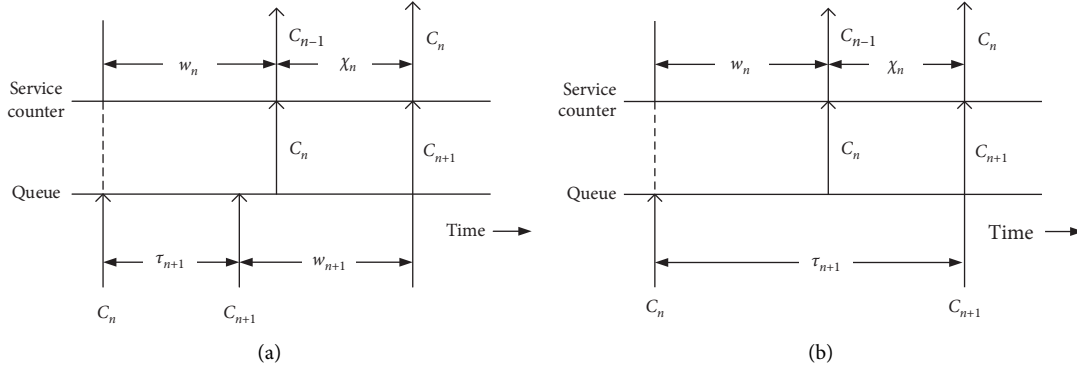
FIGURE 2: Message arriving in different service states. (a) When C_{n+1} arrives in the system, the service is busy. (b) When C_{n+1} arrives in the system, the service is idle.

3.1. Queue Theory and the Waiting Time.

The model of CAN bus queue and service is shown in Figure 3. The following can be summarized based on the figure:

(1) N nodes in CAN bus represent n customer's arrival interval time sequence, and they share one bus.

(2) The customers have priority; the range of the priority from high to low was 1, 2, ..., n, respectively. Service mechanism employs the nonpreemptive discrimination of priorities.

(3) The speeds of arrivals are $\lambda_1, \lambda_2, \ldots, \lambda_n$.

(4) The customer's service time followed the general distribution, and, in different levels, the average service time is $1/\mu_1, 1/\mu_2, \ldots, 1/\mu_n$.

On the basis of the message priority from high to low, the first high-priority message is called class 1, the higher-priority message is class 2, and the lowest-priority message is class n. For the class 1 message, its average waiting time $E[W_{q1}]$ is expressed as below. When a class 1 message arrives, the remaining transmission time (the average rest service time) of the messages that are transmitting through the bus is $E[W_{rs}]$, and the average waiting time is supposed to be

$$E[W_{q1}] \leq E[W_{rs}]. \tag{9}$$

From equation (7), the average rest service time is supposed to be

$$E[W_{rs}] = \sum_{i=1}^{n} \lambda_i \frac{D[\chi_i] + D[\tau_i]}{2}. \tag{10}$$

Here, n represents the n kinds of messages, λ_i represents the speed of class i message arrivals, $D[\chi_i]$ is the variance of transmission time, and $D[\tau_i]$ is the variance of arrive interval time. For the class 2 message, its average waiting time $E[W_{q2}]$ is expressed as follows:

(1) $E[W_{rs}]$ is the remaining transmission time (the average rest service time) of the messages that are transmitting through the bus.
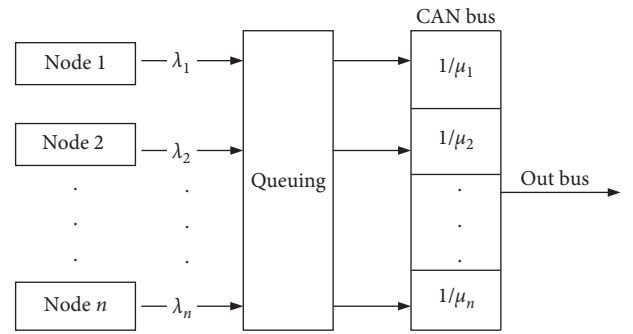
FIGURE 3: The model of CAN bus queue and service.

(2) When class 2 message arrives, the total transmission time of remaining class 1 message in the queue $E[W_2^{rt}]$ is supposed to be

$$E[W_2^{rt}] = \frac{\lambda_1 E[W_1]}{\mu_1} = \rho_1 E[W_{q1}]. \tag{11}$$

(3) When class 2 message arrives and during its waiting period, a new class 1 message arrives, and the total transmission time of new higher-priority (class 1) message is supposed to be

$$E[W_2^{nrt}] = \frac{\lambda_1 E[W_{q2}]}{\mu_1} = \rho_1 E[W_{q2}]. \tag{12}$$

According to equations (9), (11), and (12), the average waiting time of class 2 message can be deduced:

$$E[W_{q2}] \leq \frac{E[W_{q1}](1 + \rho_1)}{(1 - \rho_1)}. \tag{13}$$

For the class i message, its average waiting time $E[W_{qi}]$ is expressed as follows:

(1) $E[W_{rs}]$ is the remaining transmission time (the average rest service time) of the messages that are transmitting through the bus.

(2) When class i message arrives, the total transmission time of remaining higher priority than i messages in the queue $E[W_i^{rt}]$ is supposed to be

$$E\left[W_i^{rt}\right] = \sum_{j=1}^{i-1} \frac{\lambda_j E\left[W_{qj}\right]}{\mu_j} = \sum_{j=1}^{i-1} \rho_j E\left[W_{qj}\right]. \qquad (14)$$

(3) When class i message arrives and during its waiting period, a new higher-priority message arrives, and the total transmission time of new higher-priority messages is supposed to be

$$E\left[W_i^{nrt}\right] = \sum_{j=1}^{i-1} \frac{\lambda_j E\left[W_{qi}\right]}{\mu_j} = \sum_{j=1}^{i-1} \rho_j E\left[W_{qi}\right]. \qquad (15)$$

According to equations (14) and (15), the message average waiting time of class i can be deduced:

$$E\left[W_i\right] = \frac{1}{\mu_i} + E\left[W_{qi}\right] \le \frac{E\left[W_{q(i-1)}\right]\left(1 - \sum_{j=1}^{i-2}\rho_j + \rho_{i-1}\right)}{1 - \sum_{j=1}^{i-1}\rho_j}. \qquad (16)$$

3.2. Bit-Stuffing Mechanism and the Transmission Time. The transmission time is regarded as service time, so we need to figure out the transmission time. As mentioned above for the bit-stuffing mechanism, it will make the real transmitted message bits be greater than original bits.

According to the CAN standard, before the bit-stuffing mechanism, the total number of bits in a CAN frame is

$$N = 8L_i + g + 13. \qquad (17)$$

Here, L_i is the number of bits of the data in messages, $0 \le L_i \le 8$; g is the number of control bits in CAN frame, and, for standard frame, $g = 34$; and, for extended frame, $g = 54$. The total number of bits exposed to bit-stuffing is $8L_i + g$; the remainder including Cyclic Redundancy Check (CRC) delimiter bit, ACK field, EOF, and Int, all 13 bits, are without bit-stuffing.

After bit-stuffing, the total number of bits of a message is

$$N = 8L_i + g + 13 + T, \qquad (18)$$

where T is the total number of stuffed bits.

In the worst situation, an opposite polarity bit every 4 bits will be inserted, as shown in Figure 4. Due to exposure to bit-stuffing only having $8L_i + g$ bits, the maximum of T is

$$T_{\max} = \left\lfloor \frac{8L_i + g - 1}{4} \right\rfloor. \qquad (19)$$

The transmission time of a message in the worst situation will be

$$C_{iwcrt} = \left(8L_i + g + 13 + \left\lfloor \frac{8L_i + g - 1}{4} \right\rfloor\right)\tau_{\text{bit}}, \qquad (20)$$

where τ_{bit} represents the time taken to transmit a bit on bus.

In fact, the message's stuffing bits are always less than the worst-case scenario; the value of T is less than the maximum

After bit-stuffing ⟶ 11111000001111000001111100000⋯
Stuffed bits
Original data ⟶ 11111 0000 1111 0000 1111 0000 ⋯
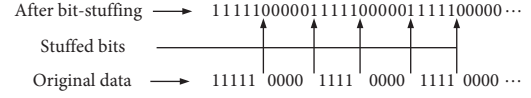
FIGURE 4: The worst-case scenario bit-stuffing.

$T_{\max}$, and the real transmission time is less than the value as shown in equation (20); the relationship between transmission time C_i and stuffing bits T satisfies the equation

$$C_i = \left(8L_i + g + 13 + T\right)\tau_{\text{bit}}. \qquad (21)$$

Due to the bits having different arrangements, the transmission time changes randomly. In [9], after bit-stuffing, the real probabilities of having a certain frame length can be calculated. If we transmit a message with 7 bytes, before bit-stuffing, the length of a frame can be at most 103 bits and among them 90 bits are exposed to bit-stuffing. In this 90-bit probabilities model, the following will be assumed: (1) equal probability of bit values 0 and 1 and (2) no dependency among bits. According to the bit-stuffing probability distribution, the mean and variance of transmission time can be calculated by using equation (21). The mean and variance of transmission time for standard format messages with 7 bytes are 106.48104 τ_{bit} t and 2.0078405 τ_{bit}^2, respectively.

As mentioned above, according to the waiting time and the transmission time, the online delay of nonperiodic CAN message can be derived from equations (8), (16), and (21).

$$E\left[W_i\right] = \frac{1}{\mu_i} + E\left[W_{qi}\right], \qquad (22)$$

where $1/\mu_i = C_i = (8L_i + g + 13 + T)\tau_{\text{bit}}$ represents the average service time and $E[W_{qi}] \le E[W_{q(i-1)}](1 - \sum_{j=1}^{i-2}\rho_j + \rho_{i-1}/1 - \sum_{j=1}^{i-1}\rho_j)$ represents the average waiting time.

4. Experimental Test

Actually, the nonperiodic CAN messages transmission is a triggering process. In real condition, the CAN nodes get a send request which is random and then the message is sent. Therefore, we use the random sequence as the messages arrival interval time in this experiment through the random interval sequence to send CAN messages in send nodes and use the oscilloscope to detect the received messages in the receiving node and save the datum.

The experimental platform includes two parts: the hardware network nodes system and the data collecting system. The hardware devices adopt the Freescale MC9S12X series single chip which is built-in CAN module. This nodes system totally has five nodes, which are consistent with three built-in CAN modules and two CAN analyzer device named CANalyst as four send nodes and one receive node. In more detail, one built-in CAN module acts as a receiving node, the other built-in module acts as the sending node, and the test built-in CAN module and two CAN analyzer act as the interrupt nodes to change the bus load ratio and compete the bus with the sending node. The test and save system was the

digital oscilloscope; it could give intuitive level changes and could save the delay datum about the sending and receiving moment. The whole platform is shown in Figure 5. Numbers 1, 2, and 5 are the CAN module embedded in the Freescale 16-bit MC9S12X series single chip. Number 1 is the sending node in CAN bus, number 2 is the interrupting node in CAN bus, and number 5 is a receiving node in CAN bus; numbers 3 and 4 are the CAN analyzers as two interrupting nodes in the CAN bus; number 6 is a high-accuracy digital oscilloscope, as the delay time data save system; number 7 is the computer, mainly for the CANalyst sent data through a software interface on the computer.

In the experimental platform, the delay of nonperiodic CAN messages with different bus load ratios at different IDs and different priorities is tested and saved in an actual CAN communication process.

4.1. Nonperiodic CAN Test Results. The experiment is implemented and the data are handled, respectively, in ID1, ID2, ID3, and ID4 with ratios of 9.84%, 12.208%, 15.168%, and 18.974%. In each test, 50 time intervals are set, 51 messages are sent at one time, and 10 times data are saved for the data of every ID with every bus load ratio. Then, the time difference between receiving and sending is adopted to be the response time, and the value obtained is the average of 10 test data. The following are the detailed data for the nonperiodic CAN messages' response time.

In the first experiment, ID1 is set as the send node, and the nonperiodic CAN messages transmitted from the send node to receive node are tested. Then, deal with the datum to get the difference between receiving moment and sending moment and the other operations. In the second experiment, ID1 is set as the send node and, like the first experiment, the third and fourth experiments are similar to the above; the response times of nonperiodic CAN messages are obtained in Table 1.

5. Comparative Analysis

As discussed above, we can calculate the theory value of the upper boundary of response time with different ratios and different priorities as shown in Table 2. According to the experiment, the ratios of 9.84%, 12.208%, 15.168%, and 18.974% are chosen. Due to the fact that the bus baud rate is 250 kb/s, the value of τ_{bit} is $4\,\mu$s. It is worth mentioning that the ID also means the priority, and the lowest ID has the highest priority which is already mentioned in Section 3.

Table 2 shows the response time trend with different priorities in ratios of 9.84%, 12.208%, 15.168%, and 18.974%, respectively. Figure 6(a) shows the priority increase in a certain bus load ratio, and the upper boundary of response time is increased. Figure 6(b) shows the bus load ratio increase in a certain priority; the upper boundary of response time is increased, and when the priority is the lowest, the trend of response time increases more quickly than the others, and the highest one is stable.
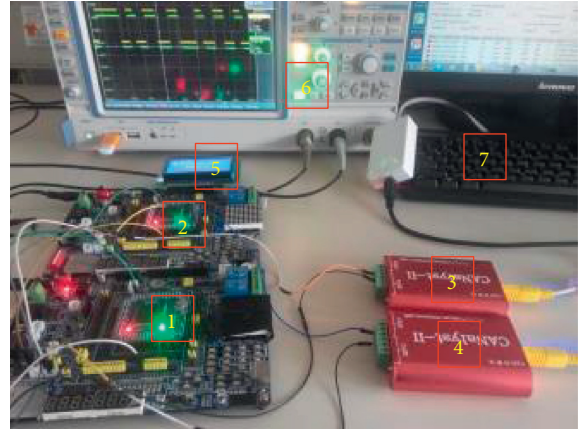
Figure 5: The experimental platform for testing the delay of CAN messages.

Table 1: The response time in four load ratios.

Ratio (%)	9.84	12.208	15.168	18.974
ID1 (s)	0.001051541	0.001070196	0.001045752	0.00108549
ID2 (s)	0.00104549	0.001096296	0.001122004	0.001081569
ID3 (s)	0.001486275	0.00150549	0.001521569	0.001535294
ID4 (s)	0.001510675	0.001512745	0.001541569	0.001555991

Table 2: Upper boundary response time of CAN message.

Ratio (%)	ID1	ID2	ID3	ID4
9.84	0.002754	0.002836	0.002989	0.003084
12.208	0.002850	0.002890	0.003048	0.003211
15.168	0.002914	0.002961	0.003126	0.003386
18.974	0.002972	0.003056	0.00323	0.003632

The experimental data are processed in the same ways as in the theory part. From Table 2, the trend about the response time with different priorities in ratios of 9.84%, 12.208%, 15.168%, and 18.974% is obtained and it is shown in Figures 7(a) and 7(b).

From Figure 7(a), we can draw the conclusion that, with the priority decrease in a certain bus load ratio, the upper boundary of response time is increasing; and, from Figure 7(b), it is shown that, with the bus load ratio increase in a certain priority, the upper boundary of response time is increasing and when the priority is lower, the response time is higher than the higher priority.

Comparing the test and theory data, Figures 8(a)~8(d) represent the relationship between the test delay time of nonperiodic CAN messages and the theory in different bus load ratios; the results show that the theory analysis about the experimental data of the nonperiodic CAN message delay time is under the upper boundary of theory response time in GI/G/1queue system; and the trend of experimental change curve is similar to the theory.
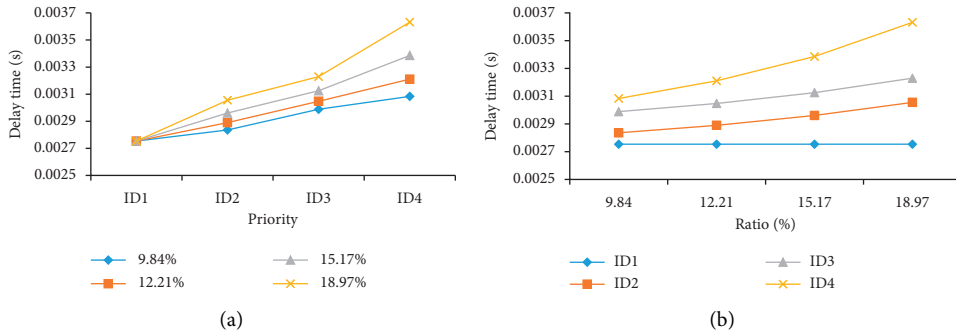
Figure 6: Theory response time in a certain ratio with different priorities and ratios.
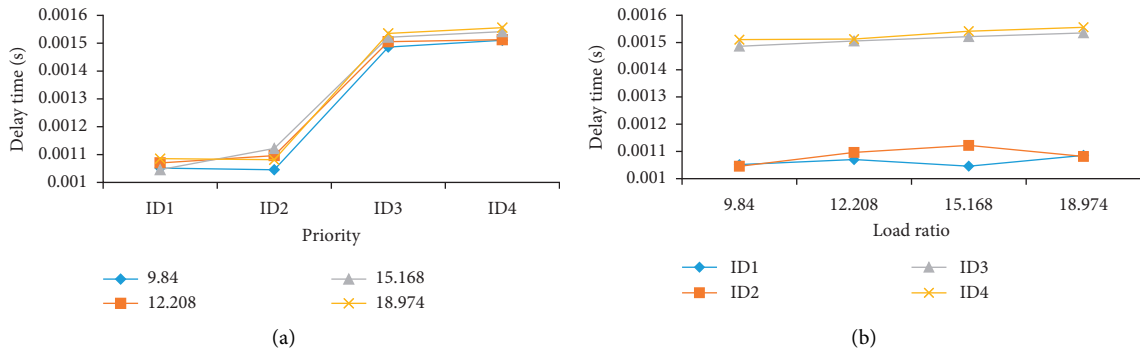
Figure 7: Experimental response time in a certain ratio, respectively, with different priorities and ratios.
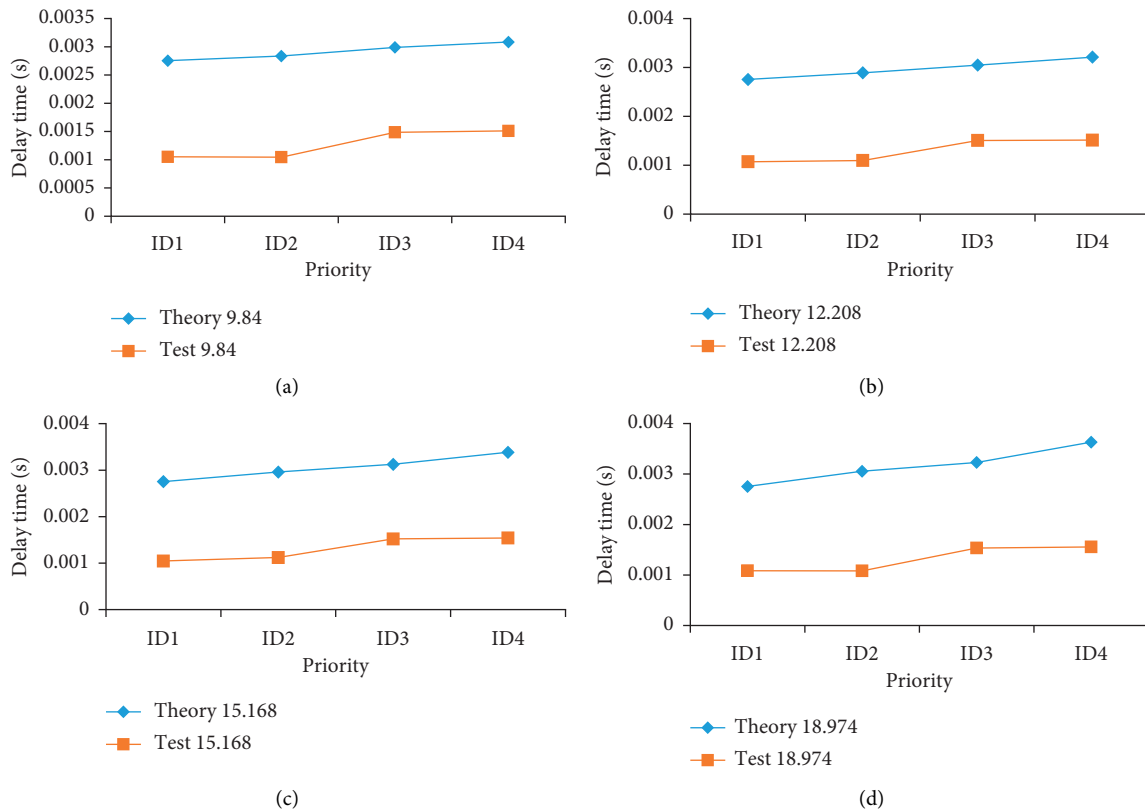
Figure 8: Results of theory and test. (a) Ratio = 9.84%. (b) Ratio = 12.208%. (c) Ratio = 15.168%. (d) Ratio = 18.974%.

6. Conclusions

This paper adopts the GI/G/1 queue system model to analyze the nonperiodic CAN messages time delay performance with nonpreemptive discrimination of priorities, and the experimental data reflect the reliability of the upper boundary of waiting time and the service time obtained by the bit-stuffing mechanism. The similarity between mathematical theory and the experiment about the trends of delay time in different ratios with different priorities also shows that the mathematical theory of the GI/G/1 queue system is feasible. Using the upper boundary of response time, the new model for the worse scenario of response time to handle the case of messages transmit in CAN bus will be investigated in the future.

Data Availability

The research data used to support the findings of this study are available from the corresponding author upon request.

Conflicts of Interest

The authors declare that they have no conflicts of interest.

Acknowledgments

References

[1] Y. Zhang, M. Chen, N. Guizani, D. Wu, and V. C. M. Leung, "Sovcan: safety-oriented vehicular controller area network," *IEEE Communications Magazine*, vol. 55, no. 8, pp. 94–99, 2017.

[2] R. Sato and S. Fukumoto, "Response-time analysis for controller area networks with randomly occurring messages," *IEEE Transactions on Vehicular Technology*, vol. 69, no. 4, pp. 3893–3902, 2020.

[3] X. Jin, J. Wang, S. Sun, S. Li, J. Yang, and Z. Yan, "Design of constrained robust controller for active suspension of in-wheel-drive electric vehicles," *Mathematics*, vol. 9, no. 3, 2021, https://www.mdpi.com/2227-7390/9/3/249.

[4] C. Young, J. Zambreno, H. Olufowobi, and G. Bloom, "Survey of automotive controller area network intrusion detection systems," *IEEE Design & Test*, vol. 36, no. 6, pp. 48–55, 2019.

[5] X. Jin, J. Yang, Y. Li, B. Zhu, and G. Yin, "Online estimation of inertial parameter for lightweight electric vehicle using dual unscented kalman filter approach," *IET Intelligent Transport Systems*, vol. 14, no. 5, 2020.

[6] G. Xie, G. Zeng, R. Kurachi et al., "WCRT analysis of can messages in gateway-integrated in-vehicle networks," *IEEE Transactions on Vehicular Technology*, vol. 66, no. 11, pp. 9623–9637, 2017.

[7] X. Ying, S. U. Sagong, A. Clark, L. Bushnell, and R. Poovendran, "Shape of the cloak: formal analysis of clock skew-based intrusion detection system in controller area networks," *IEEE Transactions on Information Forensics and Security*, vol. 14, no. 9, pp. 2300–2314, 2019.

[8] Y. Liu, X. Zhu, H. Zhang, and M. Basin, "Improved robust speed tracking controller design for an integrated motor-transmission powertrain system over controller area network," *IEEE/ASME Transactions on Mechatronics*, vol. 23, no. 3, pp. 1404–1414, 2018.

[9] S.-F. Lokman, A. T. Othman, and M.-H. Abu-Bakar, "Intrusion detection system for automotive controller area network (CAN) bus system: a review," *EURASIP Journal on Wireless Communications and Networking*, vol. 2019, no. 1, p. 184, 2019.

[10] H. Lim, G. Kim, S. Kim, and D. Kim, "Quantitative analysis of ringing in a controller area network with flexible data rate for reliable physical layer designs," *IEEE Transactions on Vehicular Technology*, vol. 68, no. 9, pp. 8906–8915, 2019.

[11] S. Mubeen, J. Mäki-Turja, and M. Sjödin, "Extending worst case response-time analysis for mixed messages in controller area network with priority and FIFO queues," *IEEE Access*, vol. 2, pp. 365–380, 2014.

[12] K. Wu, S. Srivathsan, and Y. Shen, "Three-moment approximation for the mean queue time of a GI/G/1 queue," *IISE Transactions*, vol. 50, no. 2, pp. 63–73, 2018.

[13] G. Giambene, "M/G/1 Queuing theory and applications," 2014.

[14] C. N. Nguyen, S. Hwang, and J.-S. Kim, "Making a case for the on-demand multiple distributed message queue system in a hadoop cluster," *Cluster Computing*, vol. 20, no. 3, pp. 2095–2106, 2017.

[15] H. H. Yang, Y. Wang, and T. Q. S. Quek, "Delay analysis of random scheduling and round robin in small cell networks," *IEEE Wireless Communications Letters*, vol. 7, no. 6, pp. 978–981, 2018.

[16] Y. Shen and K. Wu, "Stability of a GI/G/1 queue: a survey," *Asia-Pacific Journal of Operational Research*, vol. 35, no. 3, Article ID 1850015, 2018.

[17] A. A. Fredericks, "A class of approximations for the waiting time distribution in a GI/G/1 queueing system," *Bell System Technical Journal*, vol. 61, no. 3, pp. 295–325, 2014.

[18] G. I. Mary, Z. C. Alex, and L. Jenkins, "Response time analysis of messages in controller area network: a review," *Journal of Computer Networks and Communications*, vol. 2013, Article ID 148015, 11 pages, 2013.

[19] W. Grassmann and J. Tavakoli, "The distribution of the line length in a discrete time GI/G/1 queue," *Performance Evaluation*, vol. 131, pp. 43–53, 2019.

[20] S. Hu, D. Yue, X. Xie, Y. Ma, and X. Yin, "Stabilization of neural-network-based control systems via event-triggered control with nonperiodic sampled data," *IEEE Transactions on Neural Networks Learning Systems*, vol. 99, pp. 1–13, 2016.

Research Article

Game-Based Multiobjective Optimization of Suspension System for In-Wheel Motor Drive Electric Vehicle

Tang Feng [1,2] **and Lin Shu** [3]

[1]*Department of Automobile and Mechanical Engineering, Anhui Communications Vocational & Technical College, Hefei 230051, China*
[2]*School of Electrical Engineering and Automation, Hefei University of Technology, Hefei 230009, China*
[3]*School of Automotive and Transportation Engineering, Hefei University of Technology, Hefei 230009, China*

Correspondence should be addressed to Tang Feng; tfok@163.com

Since the driving motor is embedded in the wheel, the unsprung mass and the wheel rotational inertia of the in-wheel motor drive electric vehicle both increase, which not only affect the vehicle smoothness but also worsen the motor's working condition due to its own vertical vibration. The evaluation index of in-wheel motor's vertical vibration is introduced on the basis of vehicle smoothness analysis. The parameters' optimization of vibration absorber and suspension are carried out, respectively, and the optimization results show the contradictory relationship between smoothness objective and the motor's vertical vibration acceleration objective. Regarding the contradictory indices of the smoothness and the motor's vertical acceleration as the objective function, a multiobjective optimization scheme is designed. Then, the orthogonal experimentation and fuzzy clustering method are applied in the multiobjective optimized design based on the game decision analysis, and the Nash equilibrium and cooperative competition game theory are used to optimize the parameters of suspension and vibration absorber. The optimized results verify the game relation between the optimization variables, the game optimization obtains better optimized results than traditional linear weight sum method, and the in-wheel motor functional stability and the vehicle smoothness can be both achieved. Compared with the traditional complex iterative process and the manmade preassurance weight allocation, the game optimization has the advantages of less iterations, faster convergence, and less influence by human experience.

1. Introduction

New energy automobiles have become the forward-looking field in the car industry. The driven technology of the new energy automobiles and the traditional internal combustion engine cars shares a great deal of differences, among which the in-wheel motor drive electric vehicles embrace a promising prospect as a new car driven method. Compared with motor integrated power driven, the in-wheel motor drive has a big advantage, which is more flexible and has less complicated mechanic driven system. Nevertheless, it also has some disadvantages. The electric wheels in the in-wheel drive vehicles combine the electric machines, wheel hubs, retarding mechanisms, and brakes together, greatly increasing the unsprung mass and rotational inertia, worsening the vibration caused by the in-wheel motor drive, and causing the vibration between the neighbour parts and the rotors, which brings bad influence on the vehicles' smoothness and the safety of the tires touching the ground. How to reduce and even get rid of this kind of bad effect has become one of the key problems needed to be solved in the development of in-wheel drive electric vehicles.

Focusing on the above problems, currently, the scholars have already conducted initial research on the related questions to reduce the influence of the in-wheel drive motor on vehicle vibration. References [1–5] pointed out that, because of the introduction of the in-wheel motors, the

unsprung mass of the vehicle is increased clearly, promoting the dynamic load of the tires and the vibration acceleration of the car greatly to affect the ground-touching features of the tires and the smoothness of the vehicle. In order to suppress the in-wheel vibration and improve vehicle ride comfort, the in-wheel motor in [6] was considered as a dynamic vibration absorber, which was isolated from the unsprung mass by using a spring and a damper. A Rojas et al. [7] conducted a deep and thorough study on the active and passive suspensions of the in-wheel motor drive cars and the in-wheel motors including the damping suspension devices, and the study results revealed that the half and active suspension system could reduce the unsprung mass vertical vibration acceleration. But it did little improvement in the wheel ground-touching load, while the design of the motor suspension could effectively improve the wheel ground-touching load and the sprung mass vertical vibration acceleration. Guo-bao Ning et al. [8] from Tongji University analysed the transformation of the vehicle vertical vibration caused by the in-wheel motor system and put forward the idea of transferring the motor mass from the unsprung load with the method of mass transferring as the mass of the vibration absorbing unit to lower the wheel motor load. Scholars like Ma Ying [9] used the minimum root-mean-square value of the vehicle smoothness index as the optimized target and conduced optimization on the in-wheel motor suspension motors. The result showed that the optimized suspension structure of the in-wheel motor could not only eliminate the negative effect exerted on the vertical operation of the in-wheel motors but also improve the wheel ground-touching operations and improve the smoothness and safety of the electric cars.

However, with the development of the in-wheel motor technology, the orientation of the in-wheel motor drive cars is not limited to the travel tool in the city. Its optimized analysis is not limited to the traditional smoothness optimization. As the core part of the in-wheel motor electric cars, the operation, and condition of the in-wheel motor directly exert influences on the safety and cruising ability of the car. The research on in-wheel motor has gained more and more attention. Wei Tong et al. [10] used 1/4 vehicle motor force models to introduce the appraisal index of the vehicle smoothness and the motor vehicle vibration acceleration, based on the relative root-mean-square value and the transmission characteristics, among which the motor vehicle vibration is closely related to the features of the vehicle. It provides available ranges for matching the vehicle performances. In [11], it was proposed that the magnet gap deformation will lead to unbalanced magnetic force, which was a critical vibration source to the vehicle vertical dynamics. For this problem, an in-wheel-motor-driven electric vehicle without a speed reducer was considered as the research subject, and the results demonstrated that the magnetic force had an influence on vehicle vertical dynamics, which provided some theoretical basis for the design and optimization of the in-wheel motor drive electric vehicle.

Besides, the related optimized design analysis and research on in-wheel motors have progressed greatly [12, 13],

among which, the game theory is applied more and more often in recent years in engineering optimized design as a competitive nature-driven theory and method. Suheyla Özymldmrmm [14] put forward the optimized method based on the Nash equilibrium and noncompetition game theory in a relatively systematic way, realizing the optimization on the nonrenewable resource models, with calculating speedup by 90% compared with the traditional genetic algorithm. Periaux et al. [15] applied multiple-aimed Nash equilibrium game method in the numerous engineering examples of the airfoil aerodynamic promotion motor optimization, multiple-wing optimization design, and multiple-standard reverse power optimization. Zhong Chen et al. [16] adopted the competition and cooperation game models to conduct multiple-targeted optimized design on the Baihe Dam's shape, reaching a better design plan. Hong-bo Zhang et al. [17] applied Nash equilibrium on the collision analysis of automobiles, confronted with complicated automobile analysis problems, and the game optimization method presented good robustness, with faster convergence during the problem-solving process, meeting the multiple-targeted demands. It could be seen that the game analysis had solved many practical and effective engineering problems.

Many related solutions have been put forward to overcome the negative impact brought by the torque ripple of the in-wheel motors on electric automobiles. While the suspension vibration and the in-wheel motor vibration are both affected by each other. Only observing the vibration of the suspension to get good ride comfort may lead the in-wheel motor over vibration. Due to the limited space in the wheel for the motor, the over vibration of the vehicle motor will shorten its using lifetime; meanwhile, this also affects the other parts working in the wheel or the vehicle. In this paper, we will discuss different suspension types with the in-wheel motor. During different suspension types, suspension parameters selection will get different vibration performance. Thus, the parameter optimization method and strategy are very important to improve the suspension performance. In this paper, it is focused on the two optimized schemes on the in-wheel motor drive vehicle, which are suspension parameters optimization and vibration absorber optimization, respectively. Based on vehicle's smoothness analysis, the evaluation index of vertical vibration of the in-wheel motor is introduced. The parameters of suspension and vibration absorber are optimized, respectively, and the two optimization schemes are compared and analysed. Then, regarding the contradictory smoothness index and the in-wheel vertical acceleration as the two objective functions, the suspension parameters' multiobjective optimization scheme is carried out, which could better consider the smoothness of the whole vehicle and the stability of the motor vibration. Finally, the orthogonal experimentation and fuzzy clustering method are applied in the multiobjective optimization design based on the game decision analysis, realizing the transfer of the multiobjective optimization to game-related problems and the division of the game player side. The Nash equilibrium and the cooperation and competition equilibrium are adopted, respectively, to solve the best solution of the related parameters with the profit function as

optimization target. Compared with the traditional optimized result, the optimization of the game theory is further analysed, and the effect of the multiobjective optimization with the help of the game theory is validated.

2. Suspension Model of In-Wheel Motor Drive Vehicle

The torque ripple of the in-wheel motor exerts influences on various functional parameters of the suspension system, especially on the unsprung mass wheel, deteriorating the ground-catching ability of the wheels and harm to the smooth travel of the vehicles. At the same time, the vertical vibration of the in-wheel motor will also deteriorate the motor's working condition. In [18], the regular solutions were pointed out: (1) to conduct torque ripple control over the motor or to optimize the motor types; (2) to optimize or to reallocate the automobile suspension; (3) to design an in-wheel motor vibration absorbing system in particular. This paper mainly focuses on the influence exerted by the electric wheels on the vehicles' vertical motor forces, instead of the function of the motor itself. Therefore, the study primarily is on the latter two solutions in this paper. The suspension parameter optimization model and the vibration absorbing optimization model are established, respectively.

2.1. Suspension Parameter Optimization Model.
The simplified 1/4 vertical vibration model of the vehicle with the in-wheel motor is established as shown in Figure 1.

Because the tire damping is relatively low, the tire damping is neglected. The motion equation of the 1/4 vehicle vertical vibration model with in-wheel motor is built as follows:

$$
\begin{aligned}
(m_1 + m_3)\ddot{x}_1 + k_2(x_1 - x_2) + c_2(\dot{x}_1 - \dot{x}_2) + k_1(x_1 - x_0) &= 0, \\
m_2\ddot{x}_2 + k_2(x_2 - x_1) + c_2(\dot{x}_2 - \dot{x}_1) &= 0.
\end{aligned}
\tag{1}
$$

The root-mean-square value of the car body's acceleration is $\sigma_{\ddot{x}_2} = \sqrt{4\pi^2 G_q(n_0)n_0^2 u \int_0^\infty |H(j\omega)|^2_{\ddot{x}_2 \sim \dot{x}_0} \, df}$, the root-mean-square value of the suspension dynamic deflection is $\sigma_{f_d} = \sqrt{4\pi^2 G_q(n_0)n_0^2 u \int_0^\infty |H(j\omega)|^2_{f_d \sim \dot{x}_0} \, df}$, and the root-mean-square value of the wheels' relative loading is $\sigma_{F_d/G} = \sqrt{4\pi^2 G_q(n_0)n_0^2 u \int_0^\infty |H(j\omega)|^2_{F_d/G \sim \dot{x}_0} \, df}$.

In the above formula, $G_q(n_0)$ is the average value of the road spectrum, n_0 is the reference space frequency, and u is the vehicle speed. $|H(j\omega)|_{\ddot{x}_2 \sim \dot{x}_0}$ is the frequency characteristics of the acceleration of car body $\ddot{x}_2$ to the random road input speed $\dot{x}_0$, $|H(j\omega)|_{f_d \sim \dot{x}_0}$ is the amplitude-frequency characteristics of suspension dynamic deflection to the random road input speed $\dot{x}_0$, $|H(j\omega)|_{F_d/G \sim \dot{x}_0}$ is the amplitude-frequency characteristics of wheels' relative loading to random road input speed $\dot{x}_0$, x_0 is the input of the uneven degree of the road, x_j ($j = 1, 2, 3$) is the related mass position movement, m_1 is the unsprung mass (mass of the wheel), m_2 is the sprung mass (mass of the 1/4 car body), m_3 is the in-wheel motor mass, c_1 is the wheel damping coefficient, c_2 is
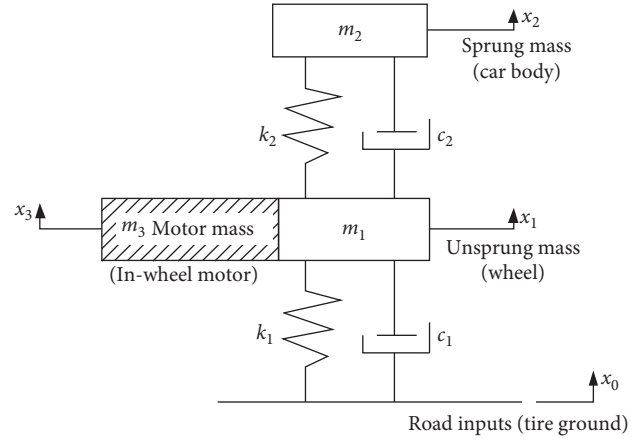
FIGURE 1: Vertical vibration model of 1/4 in-wheel motor drive electric vehicle.

the vehicle suspension damping coefficient, k_1 is the tire stiffness, and k_2 is the vehicle suspension stiffness. The system parameters of the target vehicle are shown in Table 1.

2.2. Vibration Absorbing Optimization Model.
The introduction of the in-wheel motor brings about the severe vertical negative effect on the vehicle. On the premise of not changing the suspension structure and parameters of the initial design in Section 2.1, the special in-wheel motor vibration absorbing system is installed. The 1/4 in-wheel motor vehicle vertical vibration model with vibration absorbing device [10, 19] is set up and shown in Figure 2.

The wheel, vehicle body, and in-wheel motor's vertical displacement are x_1, x_2, and x_3, respectively. With the origin of coordinates staying in the respective equilibrium points, the road displacement input is x_0 and its dynamic differential equation is

$$
M\begin{pmatrix} \ddot{x}_1\ \ddot{x}_2\ddot{x}_3 \end{pmatrix} + C\begin{pmatrix} \dot{x}_1 \\ \dot{x}_2 \\ \dot{x}_3 \end{pmatrix} + K\begin{pmatrix} x_1 \\ x_2 \\ x_3 \end{pmatrix} = \begin{pmatrix} c_1 \\ 0 \\ 0 \end{pmatrix} \dot{x}_0 + \begin{pmatrix} k_1 \\ 0 \\ 0 \end{pmatrix} x_0.
\tag{2}
$$

In the above formula, M is the quality matrix, C is the damping matrix, and K is the stiffness matrix.

$$
\begin{aligned}
M &= \begin{pmatrix} m_1 & 0 & 0 \\ 0 & m_2 & 0 \\ 0 & 0 & m_3 \end{pmatrix}, \\
C &= \begin{pmatrix} c_1 + c_2 + c_3 & -c_2 & -c_3 \\ -c_2 & c_2 & 0 \\ -c_3 & 0 & c_3 \end{pmatrix}, \\
K &= \begin{pmatrix} k_1 + k_2 + k_3 & -c_2 & -k_3 \\ -k_2 & k_2 & 0 \\ -k_3 & 0 & k_3 \end{pmatrix},
\end{aligned}
\tag{3}
$$

TABLE 1: System parameters of the target vehicle.

Parameter	m_1 (kg)	m_2 (kg)	m_3 (kg)	k_1 (N/m)	k_2 (N/m)	c_1 (N/(m/s))	c_2 (N/(m/s))
Value	45.4	317.5	50	192000	15000	50	1500
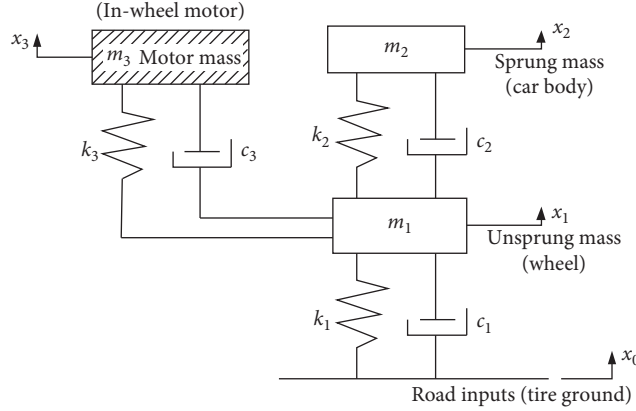
FIGURE 2: Vertical vibration model of the 1/4 in-wheel motor vehicle contained with vibration absorber.

where c_3 is the damping coefficient of vibration absorbing system between the motor and the wheel and k_3 is the spring stiffness between the motor and the wheel.

The in-wheel motor's vertical displacement and the in-wheel motor's vertical displacement relative to the wheel, that is, the root-mean-square value of the in-wheel motor dynamic deflection, are

$$\sigma_{x_3 \sim \dot{x}_0} = \sqrt{4\pi^2 G_q(n_0) n_0^2 u \int_0^\infty |H(j\omega)|^2_{x_3 \sim \dot{x}_0} df}, \qquad (4)$$

$$\sigma_{x_3 - x_1 \sim \dot{x}_0} = \sqrt{4\pi^2 G_q(n_0) n_0^2 u \int_0^\infty |H(j\omega)|^2_{x_3 - x_1 \sim \dot{x}_0} df}, \qquad (5)$$

where $|H(j\omega)_{x_3 \sim \dot{x}_0}|$ and $|H(j\omega)_{x_3 - x_1 \sim \dot{x}_0}|$ represent the frequency response of in-wheel motors' motion distance of x_3 and the relative motion distance of the in-wheel motor $x_3 - x_1$ to the vertical speed input $\dot{x}_0$, respectively.

3. Parameter Optimization of Suspension and Vibration Absorber

3.1. Suspension Parameter Optimization. Suspension could be used to buffer the impact on the in-wheel motor drive electric vehicle caused by the rough road and reduce the vibration to ensure the smooth travel of the vehicle. The suspension parameter optimization aims at fulfilling the realistic demand of the vehicle wheels to reach an optimal suspension parameter value. The in-wheel motor is the drive core of in-wheel motor drive electric vehicle. Its vertical vibration analysis is one of the crucial subjects in the research. The covibration frequency belt of the car-carried in-wheel motor has the characteristics of large changing range, big covibration peak, slow decreasing speed, and so on [20].

When matching the in-wheel vehicle parameters, the motor vibration's effect has to be noted particularly.

According to the standard GB/T 4970–1996, the car's smoothness relies on the random input of driving trial method. The suspension parameter optimization scheme is set as follows: selecting the road average spectrum $G_q (n_0)$ as 0.0000256 m^3 (level C) and the random road speed 80 km/h as working encouragement. The evaluation index of vertical vibration of the in-wheel motor $\sigma_{\ddot{x}_3}$ is introduced on the basis of vehicles' smoothness optimization index $J_{\text{vao}} = \sigma_{\ddot{x}_2} + \sigma_{f_d} + \sigma_{F_d/G}$, and the optimization is carried out for the model in Section 2.1 to get the optimal suspension damping and stiffness parameter. $\sigma_{\ddot{x}_2}$ is the root-mean-square value of the car body's acceleration, σ_{fd} is the root-mean-square value of the suspension dynamic deflection, and $\sigma_{F/G}$ is the root-mean-square value of the wheels' relative loading.

m_3 and m_2 are solid connections, so the vibration of m_3 is basically the same as m_2. Therefore, the vibration of m_3 is about the relative dynamic load of the wheel.

The variation range of the variables in the optimization process is $(1/2)k_2 \leq k_2 \leq (3/2)k_2$ and $(1/2)c_2 \leq c_2 \leq (3/2)c_2$. The suspension dynamic deflection f_d should be properly allocated with its limit distance $[f_d]$; otherwise, the suspension would constantly bump into the limited area. Thus, the restriction $0 \leq f_d \leq 0.1$ is added.

3.2. Vibration Absorber Optimization. The introduction of the in-wheel motors brings about the severe vertical negative effect on the vehicle. Adoption of the method in 3.1 could have some improvement, but the challenges are great in terms of the parameter adjustment and matching involved in the vehicle stability in the method [21]. To solve this problem, the in-wheel motor in [6] was considered as a dynamic vibration absorber, which was isolated from the wheel shaft and hub by using an in-wheel spring and a damper, whereby the rigid connections between the motor

and the hub were replaced by flexible connections. Based on the model in Section 2.2, the vibration absorber optimization scheme is designed in this section, and the vibration absorber parameters k_3 and c_3 are optimized by using the same working condition, evaluation index, and objective function as the suspension parameter optimization scheme.

The vertical vibration acceleration can be calculated by equation (4). Substituting the restriction of the suspension limit distance $0 \leq f_d \leq 0.1$ into formula (5), we obtain $\sigma_{x_3 - x_1 \sim \dot{x}_0} \leq 0.00287m$, and other restrictions keep the same with the suspension optimization scheme. Mark the smoothness optimization index as J_{vao}, and the optimization comparison results are shown in Table 2.

3.3. Comparison and Analysis of Optimization Results.
The comparison results of two optimization schemes show that the two schemes both improve the smoothness of electric vehicle. The vibration absorber optimization scheme is superior to the suspension parameter optimization scheme in terms of vehicle smoothness. In the suspension optimization, the in-wheel motor acceleration increased by 1.2% with a little deterioration, while in the vibration absorbing optimization, the in-wheel motor acceleration increased by 19.7% with bigger deterioration.

From the above analysis, it could be seen that the vibration absorbing scheme enjoys an obvious improvement in the vehicle's smoothness compared with the initial design. However, the condition of the in-wheel motor deteriorates greatly. In suspension parameter optimization, the smoothness improvement is not that obviously compared with the initial design and the corresponding working condition of the in-wheel motor in this scheme deteriorates only a little.

For this circumstance, reference [22] mentioned that this is caused by the newly installed vibration absorber. After installing the vibration absorber, the coupling relationship of the system increases, and the outer force leads to the covibration of the main system and the vibration absorbing system. Under the circumstance of the same input energy of the road, the vibration energy is separated by the main system and the vibration absorbing system. By adjusting the vibration absorber damping and spring, the vibration of the system comes near to the road vibration frequency and thus resonance happens as a result. The majority of the energy is absorbed and under the circumstance of the same input energy of the road, it reaches the goal of decreasing the energy of the main system. But compared with the time when the dynamic vibration absorber is not installed, m_3 is in the free vibration end and the system mass is reduced greatly compared with the former solid connection. Though part of the vibration is absorbed by damping and spring, generally speaking, the ability to resist the road input vibration is reduced. If the road input energy is large, the independent takeover of the vibration should be taken by m_3 but this would lead to worse working conditions.

Therefore, it is required to design a new multiobjective optimization of suspension parameter, by adjusting the parameters k_2, c_2, k_3, and c_3 to enable both the suspension system's smoothness and in-wheel motor vertical vibration acceleration in a better working condition.

TABLE 2: Comparison of the main evaluation indexes of three optimization schemes.

Index	Smoothness evaluation index, J_{vao}	Root-mean-square value of the in-wheel motor acceleration $\sigma_{\ddot{x}_3}$
Suspension parameter optimization	1.7577	0.3978
Vibration absorber optimization	1.1717	0.4765
Multiple-objective optimization	1.2009	0.4102

4. Multiple-Objective Optimal Design

Based on the analysis in Section 3.3, choosing the vehicle main suspension damping coefficient and stiffness, the damping coefficient and stiffness of the vibration absorbing system between motor and wheel as the optimization variables of the multiple-objective optimization, that is, the optimization variable, is $x = \{k_2, k_3, c_2, c_3\}$ in the optimization model. Considering the in-wheel motor drive electric vehicle's demand for smoothness and the working condition and lifespan of in-wheel motor, a multiple-objective optimal design is needed. Mark the multiple-objective optimization's smoothness evaluation index J_{vao} as the first optimal objective and the root-mean-square value of the in-wheel motor acceleration $\sigma_{\ddot{x}_3}$ as the second objective. To fully coordinate the conflicts and confrontation between the first and second optimization objective, the model in Section 2.2 is used as the optimization model, including the variables of k_2, c_2, k_3, and c_3. To better compare the optimization results, the initial design parameter $\{k_3, c_3\} = \{45000, 4500\}$ is set.

Firstly, the classic linear weight sum method is adopted to solve this multiple-objective optimization problem. It is shown as follows:

$$\begin{cases} \min z(x) = \sum_{i=1}^{k} q_i f_i(x), \\ s.t. x \in X. \end{cases} \tag{6}$$

In the above formula, q_i is the weight and $\sum_{i=1}^{k} q_i = 1$. By using different weight parameters to solve the above optimal problem, the solution could be reached as follows.

4.1. Objective Function.
The smoothness evaluation index J_{vao} and the root-mean-square values of in-wheel motor acceleration $\sigma_{\ddot{x}_3}$ are used that as the objective function in the multiple-objective optimization, which are expressed as $f_1(x)$ and $f_2(x)$, respectively. And we have the following formula:

$$z(x) = q_1 f_1(x) + q_2 f_2(x) \longrightarrow \min. \tag{7}$$

4.2. Restrictions.
The changing ranges of the optimization variables in the multiple-objective optimization process are as follows:

$$\frac{1}{2}k_2 \le k_2 \le \frac{3}{2}k_2,$$

$$\frac{1}{2}k_3 \le k_3 \le \frac{3}{2}k_3,$$

$$\frac{1}{2}c_2 \le c_2 \le \frac{3}{2}c_2,$$

$$\frac{1}{2}c_3 \le c_3 \le \frac{3}{2}c_3. \tag{8}$$

4.3. Optimization Result and Its Analysis.

Because there is not enough former theoretical support for solutions, it takes nine groups of different weight parameters for optimization, regarding the average value [23] as the optimal result shown in Table 2. As a representative, the nine groups of different weight parameters are selected for the multiple-objective optimization, shown in Table 3.

Compared with the suspension parameter optimization, the multiple-objective optimization smoothness evaluation index J_{vao} is reduced by 30%, and compared with the vibration absorbing optimization, it increased by 2%. Compared with the suspension parameter optimization, the in-wheel motor acceleration increased by 3%, and compared with the vibration absorbing optimization, it is reduced by 20%. Compared with the initial design, multiple-objective optimization smoothness evaluation index J_{vao} is reduced by 31%, and the in-wheel motor acceleration only increased by 4%. Compared with the suspension parameter optimization, the vibration absorbing optimization, and multiple-objective optimization, the solution of the multiobjective optimization scheme is more balanced, which is more comprehensive and reasonable than the original design.

5. Game Optimization

5.1. Basic Principles of Game Theory.

Game means an action competitive or with protesting nature. From the perspective of methodology, the game theory is a vector optimization consisting of objective function vector and strategic vector. From the perspective of countermeasure, the game mainly studies the decision when the decision-makers act with each other and the equilibrium formed by the decision under some restrictions [24].

From the above sections, it could be seen that, in the suspension parameter optimization, the improvement of the smoothness is smaller compared with the initial design. The in-wheel motor working condition is only deteriorated a little bit, while in the vibration absorbing optimization, the smoothness is obviously improved compared with the initial design and the corresponding in-wheel motor's working condition deteriorates greatly.

It could be seen that the smoothness evaluation index is in a relative resistance relation with the index, that is, the acceleration of in-wheel motors, meeting the requirement of the game equilibrium optimization. The optimization is actually to form an individual advantage and a decision-making process of taking profits separately from each side. By game decisions'

TABLE 3: Multiobjective optimization weighting parameters.

q_1	0.1	0.2	0.3	0.4	0.5	0.6	0.4	0.7	0.8	0.9
q_2	0.9	0.8	0.7	0.6	0.5	0.4	0.6	0.3	0.2	0.1

mutual compromise, the final optimization results eliminate the gaining contradictions between the two, thus forming an equilibrium scheme taking both the vehicle's smoothness and the motor's vibration smoothness into account.

5.2. Description of the Game Equilibrium Optimization.

Game equilibrium optimization is represented by Nash noncompetitive game and cooperation-competitive game, the main differences of which lie in whether the game individuals abide by the unified agreement. The cooperative competition game focuses more on the whole profit and team cooperation, rather than the cooperative competition game, which only considers its self-interest to realize the maximization of its profits [25]. In the specific formula, the cooperative competition game replaces the profit function of the Nash equilibrium game by the profit weighting function.

$$F_i = q_{ii}\frac{f_i\left(s_i^*, \bar{s}_i^{(0)}\right)}{f_i\left(s_i^{(0)}, \bar{s}_i^{(0)}\right)} + \sum_{j=1(j\ne i)}^{m} q_{ij}\frac{f_i\left(s_i^*, \bar{s}_i^{(0)}\right)}{f_i\left(s_i^{(0)}, \bar{s}_i^{(0)}\right)} \quad (i, j = 1, 2, \dots, m). \tag{9}$$

The Nash equilibrium game roughly consists of the following four steps [26]:

(1) By calculating the sensitivity of the variables in the game, it divides the optimization variables $X_1, X_2, \dots, X_m$ into the strategic combination $S = \{S_1, S_2, \dots, S_m\}$ in the game side, and then game contest is conducted.

(2) In the strategic combination S, the initial and feasible strategy combination $s^{(0)} = \{s_1^{(0)}, s_2^{(0)}, \dots, s_m^{(0)}\}$ is randomly generated.

(3) Mark $\bar{s}_1^{(0)}, \bar{s}_2^{(0)}, \dots, \bar{s}_m^{(0)}$ as the related complements of $s_1^{(0)}, s_2^{(0)}, \dots, s_m^{(0)}$ in $s^{(0)}$. The optimization targets F_1, F_2, ..., F_m are the profit functions of the game $f_1, f_2, \dots, f_m$, respectively; that is, $F_1(s) = f_1(s)$, ..., $F_m(s) = f_m(s)$. Fixing $\bar{s}_1^{(0)}, \bar{s}_2^{(0)}, \dots, \bar{s}_m^{(0)}$, the proper objective optimization game method (Nash equilibrium or Cooperative competition game) is selected to carry out the single objective optimization for strategic combination $S_1, S_2, \dots, S_m$. That is, the best decision s_i^* is solved for any i^{th} game side ($i = 1$, 2, ..., m), making the game gaining the profit $F_i(s_i^*, \bar{s}_i^{(0)}) \longrightarrow$ min and meeting the existing restrictions.

(4) Let $s^{(1)} = s_1^* \cup s_2^* \cup \dots \cup s_m^*$, and calculate the distance (norm) between the two (former and latter) strategic combinations to see if it meets the convergence criterion $\|s^{(1)} - s^{(0)}\| \le \varepsilon = 10^{-6}$. If it is satisfied, the game process is over; if not, use $s^{(1)}$ replacing $s^{(0)}$ and then transfer to step (3) to go over the process. The framework of Nash equilibrium game is shown in Figure 3.
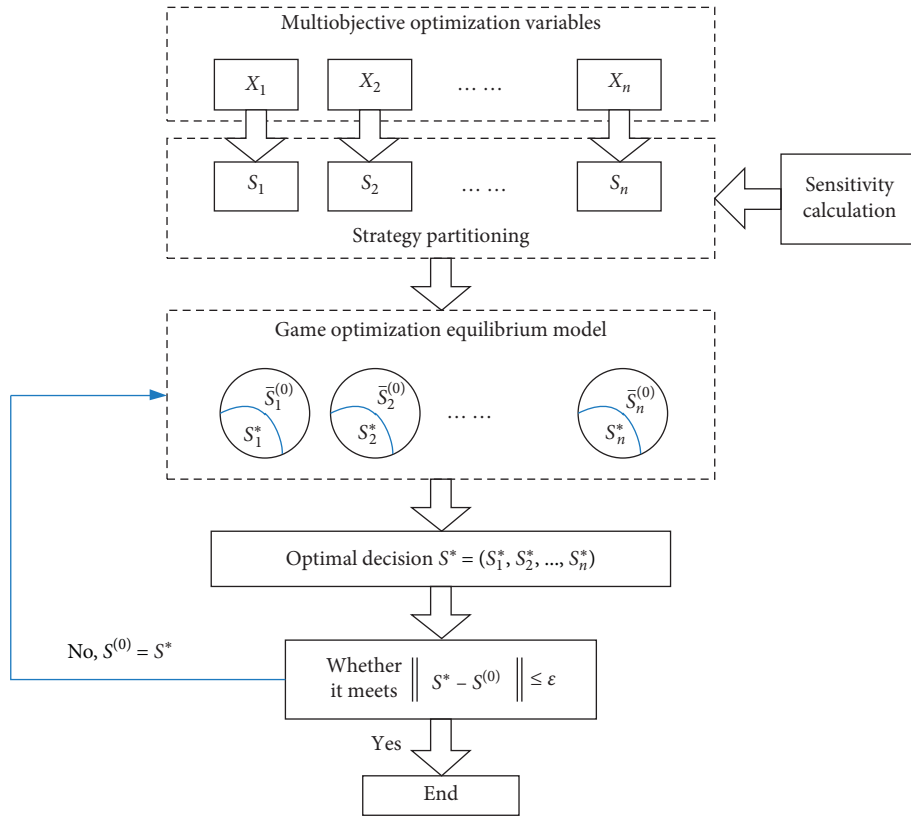
FIGURE 3: Framework of Nash equilibrium game.

5.3. Game Optimization Calculation.

Choosing the same multiobjective optimization model, optimization target, optimization function, and restrictions with those in Section 4 to set up game optimization model, mark the game optimization's smoothness evaluation index as J_{vao} for the game optimization calculation [27].

Firstly, conduct single objective optimization to the objective function J_{vao}, $\sigma_{\ddot{x}_3}$, respectively, and get Table 4.

The optimization target in this paper is the nonlinear optimization target, very sensitive to searching space. The calculation efficiency of using general strategy division is relatively low. Therefore, it uses the orthogonal test in the experimental division to calculate the sensitivity of the various optimization variables to the objective functions.

It is known that this optimization contains four variables and two objective functions. According to the orthogonal test rule [28], the orthogonal experiment table $L_8(2^7)$ is set up. The first five lists of the table are selected to arrange the orthogonal experiment. The calculation formula of the sensitivity is as follows:

$$\left| S_{ij} \right| \approx \left| R_j \right| / \left| \max\{x_{j1}, x_{j2}, \ldots\} - \min\{x_{j1}, x_{j2}, \ldots\} \right|, \quad (10)$$

where i is the number of factor level, j is the number of factor column, R_j is the range of factor x_j's average value $\overline{K}_{ij}$, $\overline{K}_{ij} = T_{ij}/a_j$, a_j is the number of horizontal repetitions of the scheduled factors in the jth column, and T_{ij} is the total value of the i level of the factor arranged in the jth column whose magnitude is the sum of the a_j test results at the jth level.

The orthogonal experiment table of the various objective functions is set up, getting the sensitivities of various optimization variables to each objective function shown in Tables 5–8 in detail.

We get the test variables x_1, x_2, x_3, and x_4, that is, optimization variables of k_2, c_2, k_3, and c_3, and the sensitivities to the two objective functions are separately shown as

$$S(J_{\text{min}}) = \left\{ 4.525 \times 10^{-5} \quad 1.6675 \times 10^{-4} \quad 3.25 \times 10^{-6} \quad -2.5 \times 10^{-7} \right\},$$
$$S(\sigma_{\ddot{x}_3}) = \left\{ -1.05 \times 10^{-5} \quad 0.0000205 \quad 0.0001165 \quad -9 \times 10^{-6} \right\}.$$
$$(11)$$

The sensitivity of each variable corresponds to one by one and influence factors $\Delta_1, \Delta_2, \Delta_3, \Delta_4$ are then extracted which are $\Delta_1 = \left\{ 4.525 \times 10^{-5} \quad -0.0000105 \right\}, \Delta_2 = \left\{ 1.6675 \times 10^{-4} \right.$ $\left. 0.0000205 \right\}, \Delta_3 = \left\{ 3.25 \times 10^{-6} \quad 0.0001165 \right\}, \Delta_4 = \left\{ -2.5 \times 10^{-7} \quad -9 \times 10^{-6} \right\}$.

Based on the fuzzy clustering method [29], the fuzzy similar equivalent matrix is obtained as follows:

$$I = \begin{bmatrix} 1.0000 & 0.9958 & 0.8136 & 1.0000 \\ 0.9958 & 1.0000 & 0.9017 & 0.9969 \\ 0.8136 & 0.9017 & 1.0000 & 0.8532 \\ 1.0000 & 0.9969 & 0.8532 & 1.0000 \end{bmatrix}. \quad (12)$$

Choose the confidence level 0.92 to divide the matrix. From the fuzzy clustering method, the strategic set of game

TABLE 4: Single objective optimization results.

Objective variables	J_{vao}	$\sigma_{\ddot{x}_3}$
Suspension stiffness, k_2 (N/m)	11000	13813
Suspension damping, c_2 (N/(m/s))	750	1493
Suspension stiffness, k_3 (N/m)	55336	25000
Suspension damping, c_3 (N/(m/s))	1292	4500
Root-mean-square value of the body's acceleration	0.9038	1.2995
Root-mean-square value of suspension dynamic deflection	0.0124	0.0081
Root-mean-square value of wheels' relative loading	0.2321	0.2633
Root-mean-square value of the in-wheel motor acceleration	0.5087	0.383
Objective function, J_{vao}	1.1484	1.5709

TABLE 5: Level table of J_{vao} optimization factors.

Factors	x_1	x_2	x_3	x_4
Level 1	10950	700	55286.58	1242.84
Level 2	11050	800	55386.58	1342.84

TABLE 6: Orthogonal experimental results of the J_{vao} optimization.

Factors	x_1	x_2	x_3	x_4	J_{gop}
Experiment 1	10950	700	55286.58	1242.836	1.1389
Experiment 2	10950	700	55286.58	1342.836	1.139
Experiment 3	10950	800	55386.58	1242.836	1.156
Experiment 4	10950	800	55386.58	1342.836	1.1559
Experiment 5	11050	700	55386.58	1242.836	1.1438
Experiment 6	11050	700	55386.58	1342.836	1.1438
Experiment 7	11050	800	55286.58	1242.836	1.1602
Experiment 8	11050	800	55286.58	1342.836	1.1601
K_{j1} (J_{gop})	1.14745	1.141375	1.14955	1.149725	—
K_{j2} (J_{gop})	1.151975	1.15805	1.149875	1.1497	—
R_j (J_{gop})	0.004525	0.016675	0.000325	−2.50E-05	—
S_j (J_{gop})	4.53E-05	0.00016675	3.25E-06	−2.50E-07	—

TABLE 7: Level table of $\sigma_{\ddot{x}_3}$ optimization factors.

Factors	x_1	x_2	x_3	x_4
Level 1	13763.02	1443.72	24950	4450
Level 2	13863.02	1543.72	25050	4550

TABLE 8: Orthogonal experimental results of the $\sigma_{\ddot{x}_3}$ optimization.

| Factors	x_1	x_2	x_3	x_4	J_{gop}
Experiment 1	13763.02	1443.72	24950	4450	0.3834
Experiment 2	13763.02	1443.72	24950	4550	0.3832
Experiment 3	13763.02	1543.72	25050	4450	0.394
Experiment 4	13763.02	1543.72	25050	4550	0.3938
Experiment 5	13863.02	1443.72	25050	4450	0.399
Experiment 6	13863.02	1443.72	25050	4550	0.395
Experiment 7	13863.02	1543.72	24950	4450	0.3839
Experiment 8	13863.02	1543.72	24950	4550	0.3847
K_{j1} ($\sigma_{\ddot{x}_3}$)	0.3886	0.3886	0.3838	0.390075	—
K_{j2} ($\sigma_{\ddot{x}_3}$)	0.3891	0.39065	0.39545	0.389175	—
R_j ($\sigma_{\ddot{x}_3}$)	−0.00105	0.00205	0.01165	−0.0009	—
S_j ($\sigma_{\ddot{x}_3}$)	−0.0000105	0.0000205	0.0001165	−9E-06	—

(a)

(b)

(c)

(d)
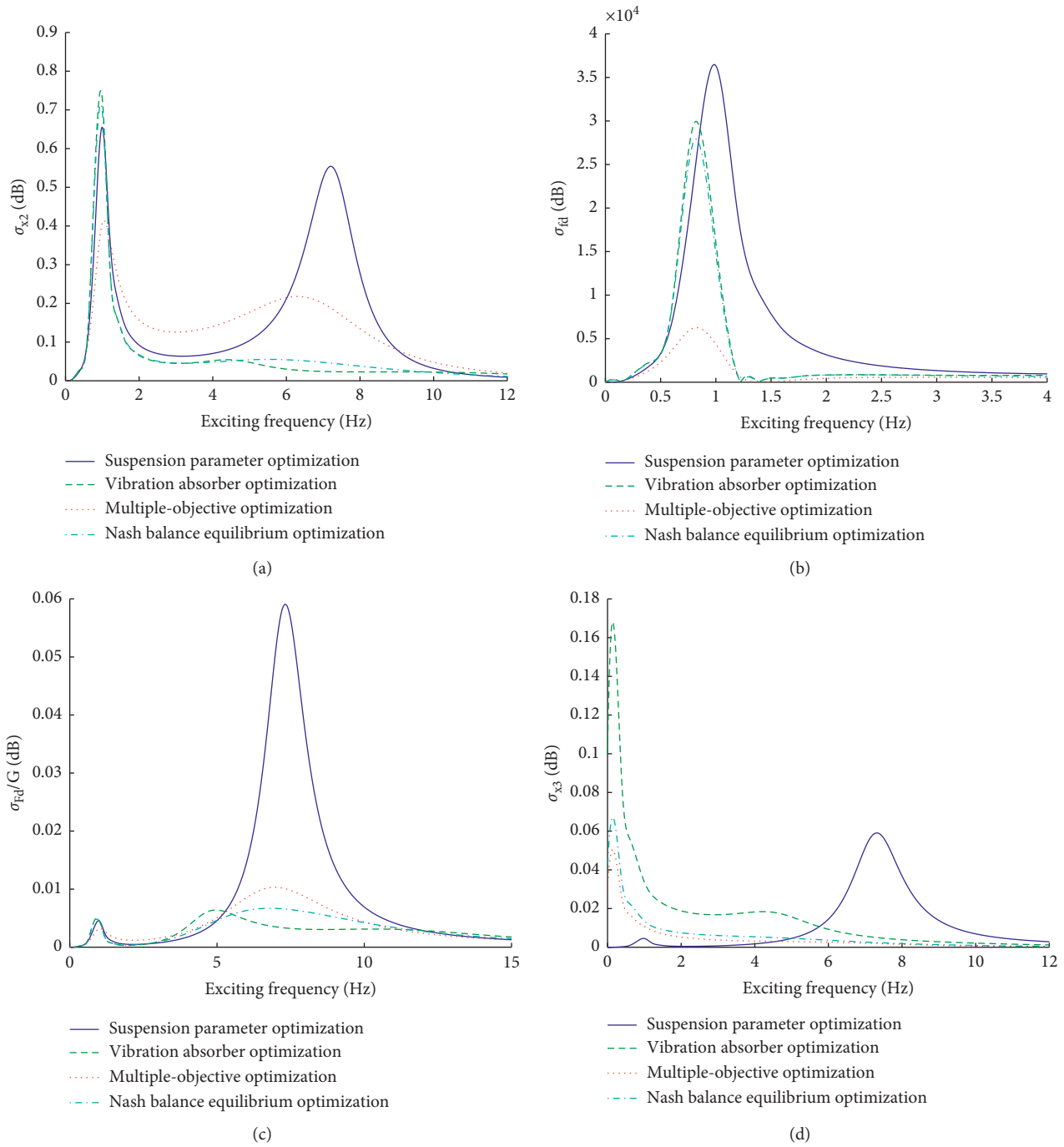
FIGURE 4: Optimization results of Nash equilibrium optimization. (a) Spectrometer of root-mean-square value of vehicle body acceleration. (b) Spectrometer of root-mean-square value of the suspension dynamic deflection. (c) Spectrometer of root-mean-square value of the wheel relative loading. (d) Spectrometer of root-mean-square value of motor acceleration.

side f_1 is $S_1 = \{x_1, x_2, x_4\}$, that is, $\{k_2, c_2, c_3\}$, and the strategic set of game side f_2 is $S_1 = \{x_3\}$, that is, $\{k_3\}$. The main parameters in the initial design are used as the initial and feasible strategy combination $s^{(0)} = \{s_1^{(0)}, s_2^{(0)}\} = \{15000 \ 1500 \ 45000 \ 4500\}$, which is the starting point of the iteration, where $s_1^{(0)} = \{x_1^{(0)}, x_2^{(0)}, x_4^{(0)}\} = \{k_2$

$(0), c_2^{(0)}, c_3^{(0)}\} = \{15000, 1500, 4500\}, s_2^{(0)} = \{x_3^{(0)}\} = \{45000\}$.

Thus, the complements of $s_1^{(0)}$ and $s_1^{(0)}$ in $s^{(0)}$ are $\bar{s}_1^{(0)} = s_2^{(0)} = \{45000\}$ and $\bar{s}_2^{(0)} = s_1^{(0)} = \{15000, 1500, 4500\}$, respectively.

According to step (3), construct the profit function $F_1(s) = f_1(s), \ldots, F_m(s) = f_m(s)$. The profit function $F_i(s_i^*, s_i^{(0)}) \longrightarrow$ min is used as the optimal game objective to

TABLE 9: Results comparison by various optimization schemes.

| Evaluation index	Suspension parameter optimization	Vibration absorber optimization	Multiobjective optimization	Nash equilibrium	Cooperative competition
Suspension stiffness, k_2 (N/m)	11437	15000	11002	11600	11061
Suspension damping, c_2 (N/(m/s))	1236	1500	750	1414.2	778
Vibration absorber stiffness, k_3 (N/m)	—	56631	45773	53232	45403
Vibration absorber damping, c_3 (N/(m/s))	—	1325	2857	1398	2182
Root-mean-square value of the body's acceleration $\sigma_{\ddot{x}_2}$	1.3418	0.9264	0.9283	0.9274	0.9303
Root-mean-square value of suspension dynamic deflection σ_{fd}	0.0181	0.0125	0.0126	0.0129	0.0122
Root-mean-square value of wheels' relative loading $\sigma_{Fd/G}$	0.3978	0.2328	0.2599	0.233	0.2456
Root-mean-square value of the in-wheel motor acceleration $\sigma_{\ddot{x}_3}$	0.3978	0.4765	0.4102	0.4221	0.4028
Smoothness J_{vao}	1.7577	1.1717	1.2009	1.1734	1.1881
Iterations	—	—	—	7	11

(a)

(b)
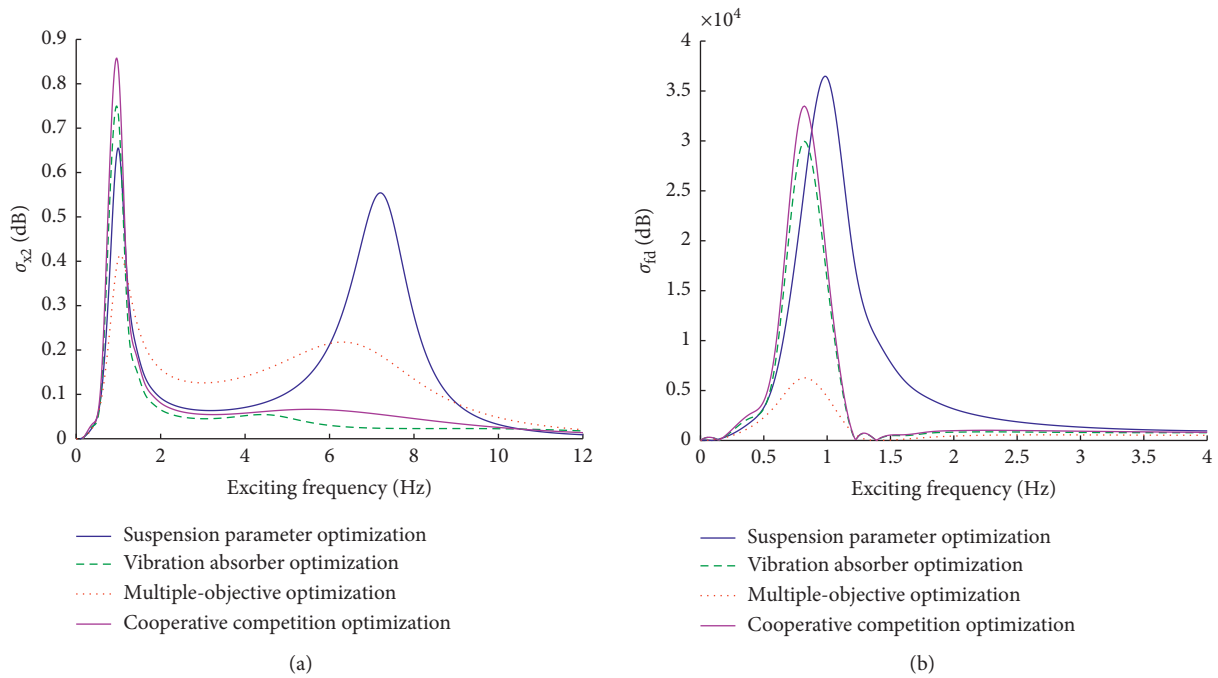
FIGURE 5: Continued.
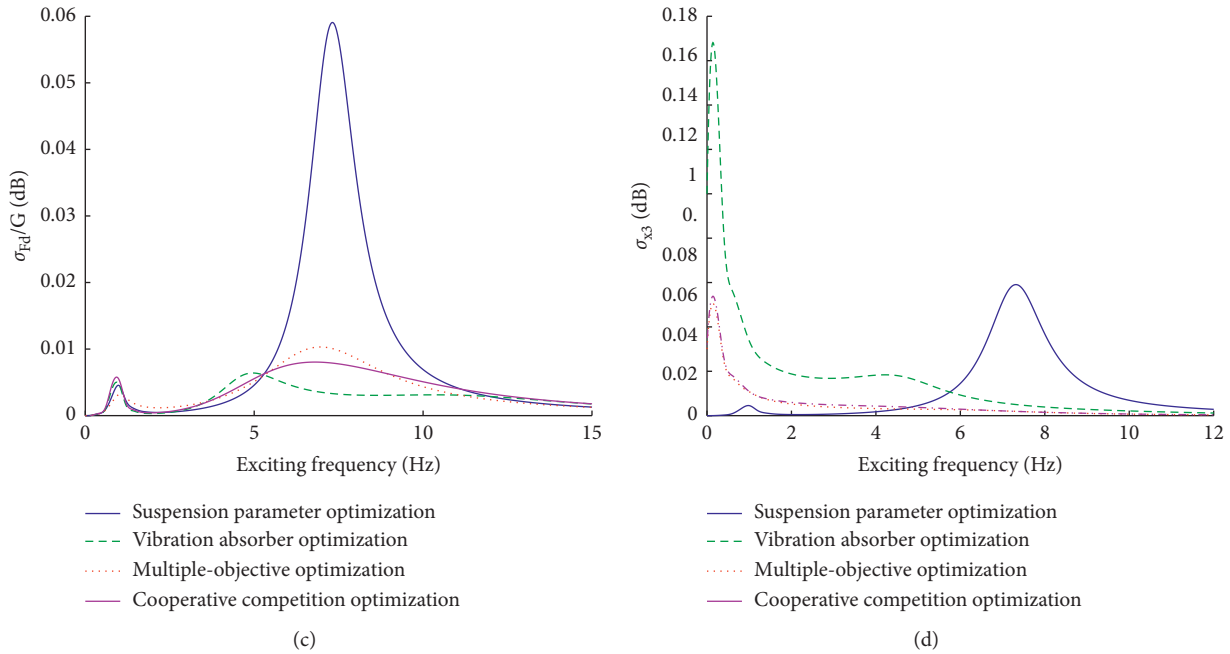
FIGURE 5: Results of cooperative competition game optimization. (a) Spectrometer of root-mean-square value of vehicle body acceleration. (b) Spectrometer of root-mean-square value of the suspension dynamic deflection, (c) Spectrometer of root-mean-square value of the wheel relative loading, and (d) Spectrometer of root-mean-square value of motor acceleration.

conduct Nash equilibrium optimization. The results are shown in Table 9 and Figure 4.

The cooperative competition game optimization is conducted using formula (9) as the profit function of the game optimization and the results are shown in Table 9 and Figure 5.

5.4. Optimization Result Comparison and Analysis Based on the Game.

According to the above results' comparison, the evaluation index presents more reasonable equilibrium relative to the suspension parameter and vibration absorber optimization, which are more close to multiple-objective optimization, that is, the traditional weighting optimization scheme. But compared with the traditional and complex iterative process and the manmade preassurance weight allocation, the game optimization has the advantages of less iterations, faster convergence, and less influenced by human factor, which is more efficient. Meanwhile, vertically comparing the optimization parameters in the different optimizations, it is easy to find that although the game optimization results are similar, the optimization parameters k_2, c_2, k_3, and c_3 are not close to each other.

The basic optimal parameters k_2, c_2, k_3, and c_3 in Nash equilibrium optimization are basically those values between the suspension parameter optimization and the vibration absorber optimization or close to that of either group of parameters. In Nash equilibrium optimization, the specific comparison results k_2 ($11437 < 11600 < 15000$), c_2 ($1236 < 1414 < 1500$), k_3, and c_3 are close to those in vibration

absorber optimization, while the optimization parameters k_2, c_2, k_3, and c_3 in the cooperative competition optimization are more close to those in multiobjective optimization, which is due to the different profits focused by the game sides. In Nash equilibrium strategy, the game sides do not have a favour towards the objectives and they only focus on their own profits and the competition relations among the various objectives.

Nash equilibrium optimization, suspension parameters, and vibration absorber optimization have the same optimal parameters k_2, c_2, k_3, and c_3 and the same profits (optimization objective), but they adopt different optimization strategies (suspension optimization and vibration absorber optimization), leading to the profits of each side conflict to each other (smoothness evaluation index and in-wheel motor acceleration have formed a certain contrast). Therefore, the Nash equilibrium could be totally seen as the competition and game between two game strategies of suspension parameters optimization and vibration absorber optimization, and the parameters allocation stays between the two values of the two optimizations. In cooperative competition equilibrium game strategy, the game sides focus on the whole profit of all the game sides and the objectives remain as cooperative and competitive relationship. The parameters are coordinated better. Similar to the idea of the traditional weight allocation, the parameters' allocation is close to the multiobjective optimization naturally.

To view in a comprehensive way, Nash equilibrium game strategy and cooperative competition game strategy both

achieve the optimization design effect of the in-wheel motor, fulfilling the complex design demand of the in-wheel motors and revealing the effectiveness and efficiency of game optimization.

6. Conclusions

The two common in-wheel motor smoothness optimization models, the suspension parameter optimization model and vibration absorber optimization model, are set up. Based on vehicle's smoothness analysis, the evaluation index of in-wheel motors' vertical vibration is introduced. The suspension stiffness and damping parameters are optimized for the suspension parameter optimization model, and the stiffness and damping parameters of the vibration absorber are optimized for the vibration absorber optimization model. The comparison and analysis of two optimization results show that, compared with the suspension parameter optimization scheme, the vibration absorber optimization scheme can better improve vehicle smoothness, but the corresponding vertical vibration acceleration deterioration of in-wheel motor worsens more.

Comparison analysis between the suspension optimization scheme and the vibration absorber optimization scheme is conducted. On this basis, a multiple-objective optimization scheme is designed. The linear weighting method is used to weigh the smoothness index and the in-wheel motors' vibration acceleration index, and the parameters of suspension stiffness k_2, suspension damping c_2, vibration absorber stiffness k_3, and the vibration absorber damping c_3 are optimized by multiple-objective optimization scheme. The results show that the two optimization objectives are adjusted in a great balance to enable the vehicle in-wheel motor to work in the stable condition while maintaining the good smoothness of the vehicle.

The game optimization is applied to deal with the conflict of the two optimization objectives. Taking advantage of the orthogonal experiment combined with fuzzy clustering method, the multiple-objective optimization is converted to game equilibrium optimization. Based on the sensitivity of the optimization variables to optimization objectives, the different game strategic combinations are divided to conduct game confrontation. Using the main suspension and vibration absorber stiffness and damping coefficients as the optimization variables and the minimum profit function as objective function, the Nash equilibrium and cooperative competition game optimizations are adopted to optimize the parameters of suspension and vibration absorber, and the results are more ideal than that by linear weighting multiobjective optimization.

Combined with the game theory, the internal game relation between different optimization results is analysed. The game optimization has the advantages of the greater convergence and high efficiency. The different optimal equilibriums of the suspension vibration and in-wheel motor vibration have been achieved by the two different game strategies. Compared with the traditional linear weighting method, this method does not require the weighting of different objectives, which has greater value applied in engineering. Although the optimization design can significantly promote the in-wheel motor drive vehicle vertical vibration performance, the parameters in the system cannot be dynamically regulated according to the vehicle driving conditions. To design the controllers to achieve the suspension and absorber parameters' real-time regulation while driving can further reduce the vehicle vertical vibration. Meanwhile, the motor vibration has the coupling with the suspension system vertical vibration, so paying attention to the coordinated controller design of the motor and suspension considering their characteristics, so as to further reduce the in-wheel motor drive vehicle vertical vibration and improve the system comprehensive performance, is especially worth studying.

Data Availability

The data used to support the findings of this study are available from the corresponding author upon request.

Conflicts of Interest

The authors declare that they have no conflicts of interest.

Acknowledgments

References

[1] X. X. Shao, F. Naghdy, and H. P. Du, "Reliable fuzzy H-infinity control for active suspension of in-wheel motor driven electric vehicles with dynamic damping," *Mechanical Systems and Signal Processing*, vol. 87, pp. 21–25, 2017.

[2] Z. Li, L. Zheng, W. Gao, and Z. Zhan, "Electromechanical coupling mechanism and control strategy for in-wheel-motor-driven electric vehicles," *Institute of Electrical and Electronics Engineers Transactions on Industrial Electronics*, vol. 66, no. 6, pp. 4524–4533, 2019.

[3] B. Xu, C. Xiang, Y. Qin, P. Ding, and M. Dong, "Semi-active vibration control for in-wheel switched reluctance motor driven electric vehicle with dynamic vibration absorbing structures: concept and validation," *Institute of Electrical and Electronics Engineers Access*, vol. 6, no. 2018, pp. 60274–60285, 2018.

[4] S. Nie, Y. Zhuang, F. Chen, Y. Wang, and S. Liu, "A method to eliminate unsprung adverse effect of in-wheel motor-driven vehicles," *Journal of Low Frequency Noise, Vibration and Active Control*, vol. 37, no. 4, pp. 955–976, 2018.

[5] Z. Wang, C. Yong, Z. Li et al., "Simulation analysis and optimization of ride quality of in-wheel motor electric

vehicle," *Advances in Mechanical Engineering*, vol. 10, no. 5, pp. 1–10, 2018.

[6] M. Liu, F. Gu, J. Huang, C. Wang, and M. Cao, "Integration design and optimization control of a dynamic vibration absorber for electric wheels with in-wheel motor," *Energies*, vol. 10, no. 12, pp. 2069–2091, 2017.

[7] A. E. Rojas Rojas, H. Niederkofler, and J. Willberger, "Comfort and safety enhancement of passenger vehicles with in-wheel motors," *SAE Technical Papers*, vol. 10, pp. 4–6, 2010.

[8] G. B. Ning and G. Wan, "The present research situation of the influences on vehicle vertical performances induced by direct wheel drives system," *Automobile Technology*, vol. 3, pp. 21–25, 2007.

[9] Y. Ma, Z. X. Deng, and D. Xie, "Analysis and optimization of in-wheel motor suspension configuration," *Journal of Central South University (Science and Technology)*, vol. 9, no. 45, pp. 3008–3014, 2013.

[10] W. Tong and Z. C. Hou, "Analyses on the vertical characteristics and motor vibration of an electric vehicle with motor-in-wheel drive," *Automobile Engineering*, vol. 4, no. 36, pp. 398–403, 2013.

[11] D. Tan and C. Lu, "The influence of the Magnetic force generated by the in-wheel motor on the vertical and lateral coupling dynamics of electric vehicles," *Institute of Electrical and Electronics Engineers Transactions on Vehicular Technology*, vol. 65, no. 6, pp. 4655–4668, 2016.

[12] D. Tan, *Dynamics and Structure Optimization of the In-Wheel Motor System with Rubber Bushing*, South China University of Technology, Guangzhou, China, 2013.

[13] Z. Li and L. Zheng, "Integrated design of active suspension parameters for solving negative vibration effects of switched reluctance-in-wheel motor electrical vehicles based on multi-objective particle swarm optimization," *Journal of Vibration and Control*, vol. 25, no. 3, pp. 639–654, 2019.

[14] S. Özyıldırım and N. Alemdar, "Learning the optimum as a Nash equilibrium," *Journal of Economic Dynamics & Control*, vol. 24, pp. 483–499, 2000.

[15] J. Periaux, H. Q. Chen, B. Mantel, M. Sefrioui, and H. T. Sui, "Combining game theory and genetic algorithms with application to DDM-nozzle optimization problems," *Finite Elements in Analysis and Design*, vol. 37, no. 5, pp. 417–429, 2001.

[16] Z. Li, N. G. Xie, and Y. M. Zhang, "Cooperative game method for structural optimization with multiple objectives," *Engineering Mechanics*, vol. 4, no. 26, pp. 32–37, 2009.

[17] H. B. Zhang, L. Gu, and Y. Z. Xu, "Vehicle crashworthiness multi-objective optimization based on game theory," *Automotive Engineering*, vol. 7, no. 30, pp. 553–556, 2008.

[18] T. F. Ma, N. W. Xue, Z. X. Li et al., "The analysis of the influence factors of vehicle handling and stability and study and evaluation on handling and stability," *Machinery Design & Manufacture*, vol. 4, pp. 122-123, 2005.

[19] R. He and R. J. Zhang, "Research and development of in-wheel motor drive technology," *Journal of Chongqing University of Technology (Natural Science)*, vol. 7, no. 29, pp. 10–18, 2015.

[20] Y. M. Sun, *Study on Suspension Vertical Mechanical-Electrical Coupled Vibration of In-Wheel Motor Electrical Vehicle*, Anhui Polytechnic University, Wuhu, China, 2015.

[21] W. Tong, *Research on the Vertical Performance and Motor Vibration of Electrical Vehicle Driven by In-Wheel Motors*, Tsinghua University, Beijing, China, 2013.

[22] Y. E. Zhao, J. W. Zhang, and X. Han, "Design and study on the dynamic-damper mechanism for an in-wheel motor individual drive electric vehicle," *Mechanical Science and*

[23] *Technology for Aerospace Engineering*, vol. 3, no. 27, pp. 395–398, 2008.

[23] H. W. Tang, *Practical Methods of Optimization*, Dalian University of Technology Press, Dalian, China, 2004.

[24] R. G. Fan, *Game Theory*, Wuhan University Press, Wuhan, China, 2011.

[25] XG. Na, *Game and Decision-Making*, Foreign Language Teaching and Research Press, Beijing, China, 2011.

[26] J. Tan and L. Wang, "A game-theoretic framework for vehicle-to-grid frequency regulation considering smart charging mechanism," *Institute of Electrical and Electronics Engineers Transactions on Smart Grid*, vol. 8, no. 5, pp. 2358–2369, 2017.

[27] Z. R. Shen, *The Research and Application of Multi-Objective Optimization Design Method Based on Game Theory*, Zhejiang University, Hangzhou, China, 2013.

[28] L. Q. Ren, *Optimum Design and Analysis of Experiments*, Higher Education Press, Beijing, China, 2001.